BRICS
Workshop on Biophotonics-2023

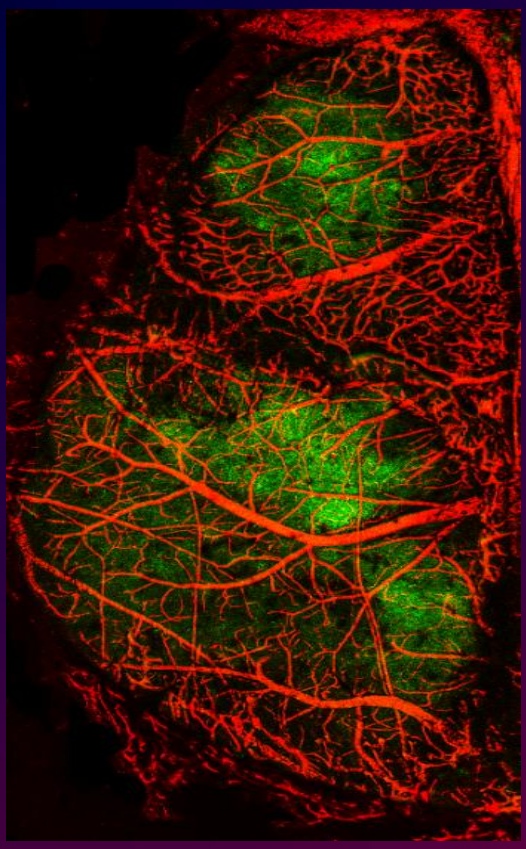

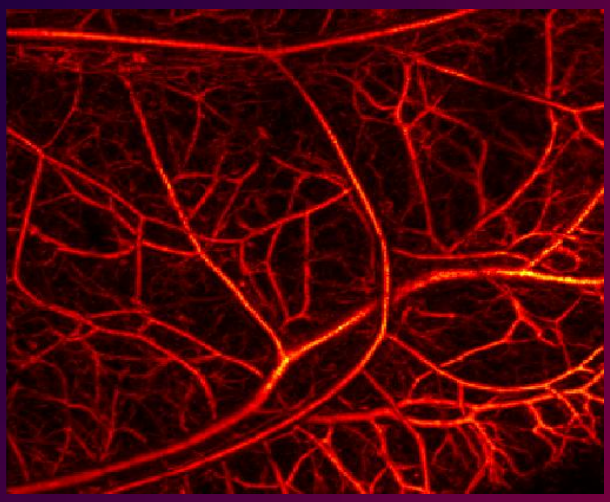

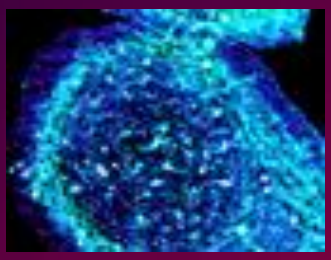

SEPTEMBER 27 – 29, 2023
SARATOV STATE UNIVERSITY, SARATOV, RUSSIA
HAINAN UNIVERSITY, CHINA
UNIVERSITY OF SÃO PAULO, BRAZIL
MANIPAL ACADEMY OF HIGHER EDUCATION, INDIA
UNIVERSITY OF JOHANNESBURG, RSA

SARATOV FALL MEETING

OPTICA Formerly OSA

MANIPAL ACADEMY of HIGHER EDUCATION
(Deemed to be University under Section 3 of the UGC Act, 1956)

HUAZHONG UNIVERSITY OF SCIENCE AND TECHNOLOGY

HAINAN UNIVERSITY 1958

SSU

USP Universidade de São Paulo

UNIVERSITY OF JOHANNESBURG

ИНЖЕКТ
РОСАТОМ

ООО НПП
Наноструктурная Технология Стекла

Saratov State University (National Research University of Russia)

BRICS Workshop on Biophotonics-2023
Proceedings of BRICS Workshop

Edited by Polina A. Dyachenko, Qingming Luo,
Vanderlei Salvador Bagnato, Santhosh Chidangil,
Heidi Abrahamse and Valery V. Tuchin

SEPTEMBER 27 – 29, 2023

SARATOV

Семинар БРИКС по Биофотонике-2023

Сборник материалов семинара БРИКС
под редакцией Полины А. Дьяченко, Цинмин Ло,
Вандерлея Сальвадора Баньято, Сантоша Чидангила,
Хайди Абрахамс и Валерия В. Тучина

27 – 29 СЕНТЯБРЯ 2023 Г.

САРАТОВ

УДК 535.8:577.3(082)
ББК 22.34
Б 87

BRICS Workshop on Biophotonics -2023. Proceedings of BRICS Workshop / Edited by P.A. Dyachenko, V.V. Tuchin – Russian Federation, Qingming Luo – China, Vanderlei Salvador Bagnato – Brazil, Santhosh Chidangil – India, Heidi Abrahamse – RSA. – Saratov, Russian Federation: Publishing house "Saratov source", 2023. – 200 p.

ISBN 978-5-6051304-1-3

The collection includes extended proceedings of lectures and reports of the participants of the BRICS Workshop on Biophotonics -2023, held online as part of the Saratov Fall Meeting 2023.

Семинар БРИКС по биофотонике – 2023. Сборник материалов семинара БРИКС / Под редакцией П.А. Дьяченко, В.В. Тучина – Российская Федерация, Цинмин Ло – Китай, Вандерлея Сальвадора Баньято – Бразилия, Сантоша Чидангила – Индия, Хайди Абрахамса – ЮАР. – Саратов, Российская Федерация. Издательство "Саратовский источник", 2023. – 200 с.

Сборник включает расширенные материалы лекций и докладов участников семинара БРИКС по биофотонике – 2023, проходившего онлайн в рамках осенней встречи в Саратове 2023.

Saratov State University (National Research University of Russia), 410012, Saratov, Astrakhan str., 83

Саратовский национальный исследовательский государственный университет имени Н. Г. Чернышевского, 410012, Саратов, улица Астраханская, 83

УДК 535.8:577.3(082)
ББК 22.34

Contents

BRICS Workshop on Biophotonics -2023
SEPTEMBER 27 –29, 2023, SARATOV, RUSSIA

BRICS Workshop on Biophotonics - 2023 was held online, on 27-29, Sept. 2023, and is intended to bring together scientists, engineers and clinical researchers from the BRICS countries of various fields of science involved in the application of optics, photonics and imaging technologies to solve urgent problems of biology and medicine. The scope of this Forum ranges from basic research to instrumentation, preclinical and clinical research, mainly in those areas where researchers from the BRICS countries are world leaders. The topics are extensive and will cover (but are not limited to) the following:

- ✓ **Optical Interactions in Tissue and Cells**
- ✓ **Biomedical Spectroscopy, Microscopy and Imaging**
- ✓ **Advanced Optical Techniques for Clinical Medicine**
- ✓ **Multimodal Biomedical Imaging**
- ✓ **Nano/Biophotonics**
- ✓ **Photonic Therapeutics, Diagnostics and Instrumentations**
- ✓ **Tissue Optical Clearing and Drug Delivery**
- ✓ **Antimicrobial and Antivirus Phototherapies**

Chairs:
Valery V Tuchin, Saratov State University, Russia
Qingming Luo, Hainan University, China
Vanderlei Salvador Bagnato, University of São Paulo, Brazil
Santhosh Chidangil, Manipal Academy of Higher Education, India
Heidi Abrahamse, University of Johannesburg, RSA

Secretaries:
Polina A. Dyachenko, SSU, Russia
Dongyu Li, HUST, China
Lilian Moriyama & Natalia M. Inada, University of São Paulo, Brazil
Renu John, Indian Institute of Technology, Hyderabad, India

DOI 10.24412/cl-37136-2023-1-7-15

ORGAN-PAM: PHOTOACOUSTIC MICROSCOPY OF WHOLE-ORGAN MULTISET VESSEL SYSTEMS

JUNNING ZHANG [1], DINGLU PENG[1], WEI QIN[1], WEIZHI QI[1], XIAOYA LIU[1], YUCHENG LUO[1], QIONGYU GUO[1] AND LEI XI1, [2, 3]

[1] *Department of Biomedical Engineering, Southern University of Science and Technology, China*
[2]*Guangdong Provincial Key Laboratory of Advanced Biomaterials, Southern University of Science and Technology, China*
[3]*Shenzhen Bay Laboratory, China*

xilei@sustech.edu.cn

ABSTRACT

Organs maintain their unique functions through a variety of distinctive vessel systems. However, examination of multiset vessels over the entire organ still remains challenging due to the difficulties of assigning multiple vessel systems and labor-intensive imaging reconstruction technologies [1-3].

Micro X-ray computed tomography (μCT) is one of the most used non-optical imaging modalities for *in vitro* visualization and analysis of organ vessel systems due to its high spatial resolution three-dimensional (3D) imaging capability [4]. However, the drawbacks of μCT are its insufficient signal-to-noise ratio (SNR) and field of view (FOV) as well as the complicated angiographic and data processing protocols [5]. Optical-based imaging modalities also show promising application in revealing organ vessel systems due to their superior resolution and sensitivity. Whole-organ optical clearing technique combined with cutting-edge optical microscopies, such as light-sheet microscopies, can resolve organ vessel systems with cellular-level spatial resolution [6]. Nevertheless, the complex and time-consuming organ optical clearing protocols as well as the tradeoff among temporal resolution, imaging FOV and spatial resolution remains major challenges. Sectioning tomography assisted by tissue microtomy technique can also achieve cellular-level imaging of whole-organ vessel systems [7]. However, correction of unavoidable distortions on the sectioning surfaces, complicated labeling and the unavoidable trade-off between spatial resolution, temporal resolution and imaging scale remain unsolved. Briefly, current commonly applied organ vessel system imaging platforms still face shared technical barriers: (1) unbalance between large-scale organ compatibility, spatial resolution and temporal resolution and (2) complex labeling procedures, complicated labor-assist-required segmentation algorithms and resource-consuming post-imaging processes in distinguishing multiset vessel systems. So far, an organ vessel system imaging platform with a good balance between spatial resolution, temporal resolution and multiscale-organ compatibility that applies simplified protocols to easily distinguish multiset vessel systems has not yet been reported.

Photoacoustic imaging (PAI), an emerging hybrid imaging modality utilize the phenomenon of generating ultrasound waves from a pulsed laser-excited optical absorber, exhibits the advantageous capability of vasculature characterization due to its rich optical imaging contrast and deep ultrasound sensing depth [8]. Photoacoustic microscopy (PAM), a major sub-modality of PAI, features a high spatial resolution of microns, rich optical absorption sensitivity, and 3D imaging ability, making it accessible and promising to investigate vessel systems in organs [8]. However, there remains several major challenges for PAM to achieve whole-organ multiset vessel system imaging: (1) the severe optical scattering of biological tissues limits the penetration depth to ~1.5 mm, preventing PAM from reaching the whole-organ depth [8]; (2) the limited spatial FOVs of existing PAMs, especially the axial FOV, are insufficient for imaging organs of large rodents, non-human primates, and humans; and (3) it is difficult for PAM to differentiate different vessel systems in the organ. As a result, so far, there is no systematic description of using the superior imaging capabilities of PAM to achieve whole-organ imaging of vessel systems.

In this study, we resolved such challenges hindering the feasibility of whole-organ vessel system visualization using PAM and further overcome the technical barriers of imaging scale and multiset vessel

distinguish complexity faced by current approaches. We developed an organ-level photoacoustic microscopic imaging platform (Organ-PAM), which utilizes a fast optical-clearing-assisted organ decellularization technique, a dual-illuminant ultra-large FOV optical-resolution PAM system, and a well-designed photoacoustic angiographic imaging protocol.

The detailed design of the imaging interface of our designed dual-illuminant ultra-large FOV optical-resolution PAM system consists of four separate units from top to bottom (Figure 1a), both the upper-side and bottom-side excitation units are made up of a 532 nm pulsed laser to induce photoacoustic waves, a two-dimensional galvanometer to perform rotary scanning of the light beam, and an F-theta lens to converge the light beam into the sample. The transducer rotates coordinately with the light scanning via a specially designed rotary scanning mechanism to achieve an effective imaging domain with a diameter of 4 cm in lateral (Figure 1b), the unit of the motorized sample holder moves the oversized sample in a raster pattern to obtain an extended lateral FOV *via* an imaging stitching algorithm (Figure 1c). We achieved a lateral resolution perpendicular to the acoustic beam of ~12.1 μm and an axial resolution along the acoustic axis of ~172.8 μm with the dual-illuminant ultra-large FOV optical-resolution PAM system (Figure 1d) and the current maximum lateral FOV can be achieved up to ~81 cm^2. Based on the distribution and a tolerable spatial resolution limit of 25 μm as the worst resolution (Figure 1e), we estimated the best double-sided illumination scenario where an axial FOV of ~12 mm can be achieved with an acceptable lateral resolution (Figure 1f).

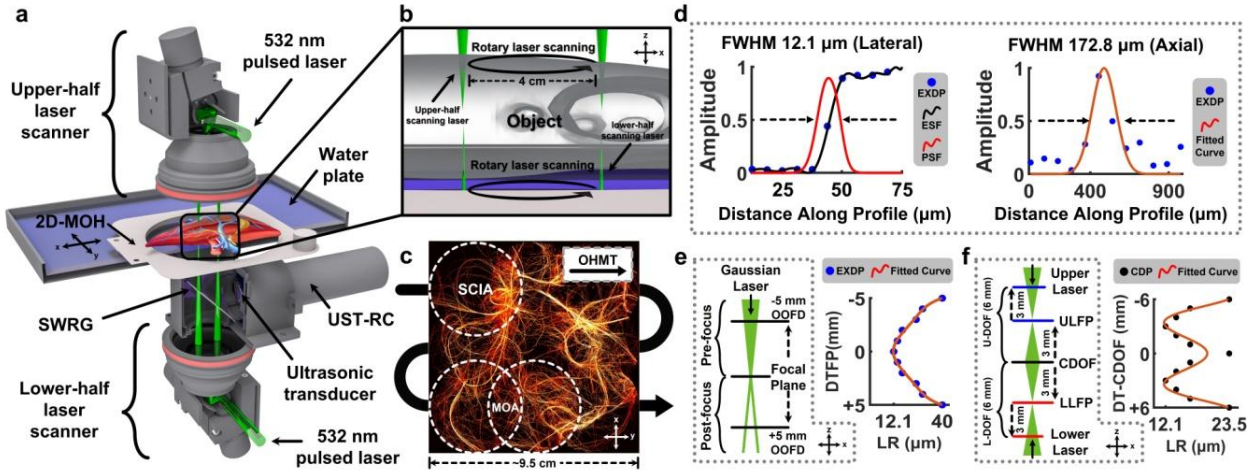

Figure 1: *Organ-PAM imaging interface configuration and lateral and axial FOVs. (a) 3D rendered configuration of the Organ-PAM imaging interface. (b) Close-up schematic of imaging target placed on the object holder and rotationally scanned by dual-sided scanning laser beams axially oriented to each other. (c) Maximum lateral FOV evaluation using an ultra-large planner phantom. (d) The best lateral and axial resolution of Organ-PAM. (e) The distribution of Organ-PAM's lateral resolution in the off-focus range of -5 mm to +5 mm along the axial direction. (f) The calculated Organ-PAM's lateral resolutions over the axial FOV of ~12 mm. 2D-MOH, two-dimensional movable object holder; SWRG, sound wave reflection glass; UST-RC, ultrasonic transducer rotation chamber; MOA, mutual overlap area; OHMT, object holder moving trajectory; SCIA, single circular imaging area; ESF, edge spread function; EXDP, experimental data point; PSF, point spread function; DTFP, distance to focal plane; LR, lateral resolution; OOFD, out-of-focus distance; CDOF, the center of depth-of-focus; CDP, calculated data point; DT-CDOF, distance to the center of depth-of-focus; L-DOF, lower side laser depth-of-focus; LLFP, lower side laser focal plane; U-DOF, upper side laser depth-of-focus; ULFP, upper side laser focal plane.*

A photoacoustic gradient concentration differential angiography was proposed for the first time to enable complex-procedure-free labeling, imaging, and segmentation of multi-set vessel systems. This angiography is developed based on a fundamental photoacoustic phenomenon, which presents the amplitude of a photoacoustic wave linearly proportional to the concentration of the chromophore inside the absorber. According to the photoacoustic effect, samples labeled with different concentrations of chromophore can be distinguished by linear mapping between chromophore concentration and photoacoustic amplitude. By imaging a five-channel microfluidic chip injected using photoacoustic

contrast agents with different concentration, we observed varying photoacoustic intensities for different channels (Figure 2a-f). Based on the microfluidic phantom experiment and combined with organ decellularization clearing technique to produce acellular organs with enhanced optical transmittance following a decellularization protocol, we developed photoacoustic gradient concentration differential angiography for imaging multiple vessel systems in a single organ (Figure 2g-h).

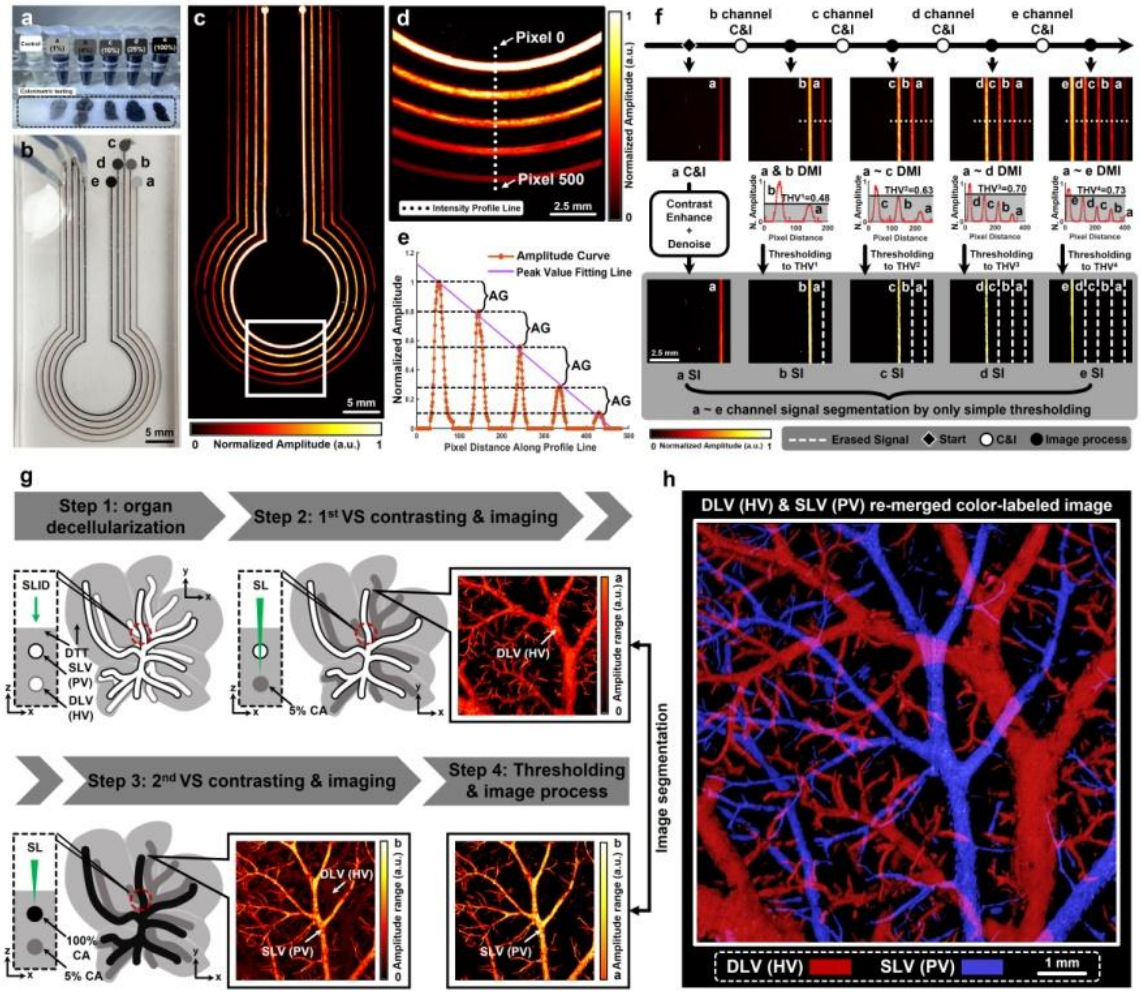

Figure 2: *Performance demonstration of photoacoustic gradient concentration differential angiography. (a) Colorimetric test of solvent soybean oil and five PAI contrast agents with gradient concentration formulated by mixing soybean oil and black oily ink in different ratios. (b) The PAI contrast agents were injected into the corresponding channels on a vessel phantom. (c) Amplitude normalized imaging results of the contrasted vessel phantom using Organ-PAM. (d) The zoomed-in visualization of the area within the white square in (c). (e) The normalized amplitude profile corresponds to the white dotted profile line marked in (d) with AG indicated. (f) The workflow of applying photoacoustic concentration differential angiography to segment PAI signal from the five contrasted microfluidic channels in a vessel phantom. (g) A demonstration workflow of applying the photoacoustic gradient concentration differential angiographic method to imaging and separate PAI signals from two vessel systems located at different depths inside an organ. (h) Re-merged color-labeled image of two vessel systems separated through the workflow shown in (g). AG, amplitude gap; C&I, contrast-and-imaging; DMI, denoised merged image; N. Amplitude, normalized amplitude; SI, segmented image; THV, threshold value; CA, contrast agent; DLV, deep-layer vessel system; DTT, decellularized transparent tissue; SL, scanning laser; SLID, scanning laser incident direction; SLV, shallow-layer vessel system; VS, vessel system.*

Utilizing our dual-illuminant ultra-large FOV optical-resolution PAM system and photoacoustic gradient concentration differential angiography organ multiple vessel systems imaging workflow, we first achieved panoramic visualization of the hepatic vein (HV), portal vein (PV), hepatic artery (HA), and bile duct (BD) systems in a rat liver. We sequentially infused the oil-based ink solutions with increasing concentrations of 1%, 4%, 20%, and 100% into HV, PV, BD, and HA, respectively, and carried out Organ-

PAM scans after each infusion (Figure 3). To show the detailed 3D spatial distribution of these vessel systems, we zoomed in on three sub-views from different lobes of the liver with a FOV of 5 mm × 5 mm × 4 mm (x-, y- and z-axis, respectively), shown in Figure 3f, and observed the portal triad of PV, BD, and HA as well as the discrete HV in the three corresponding cross-sectional slices (Figure 3g).

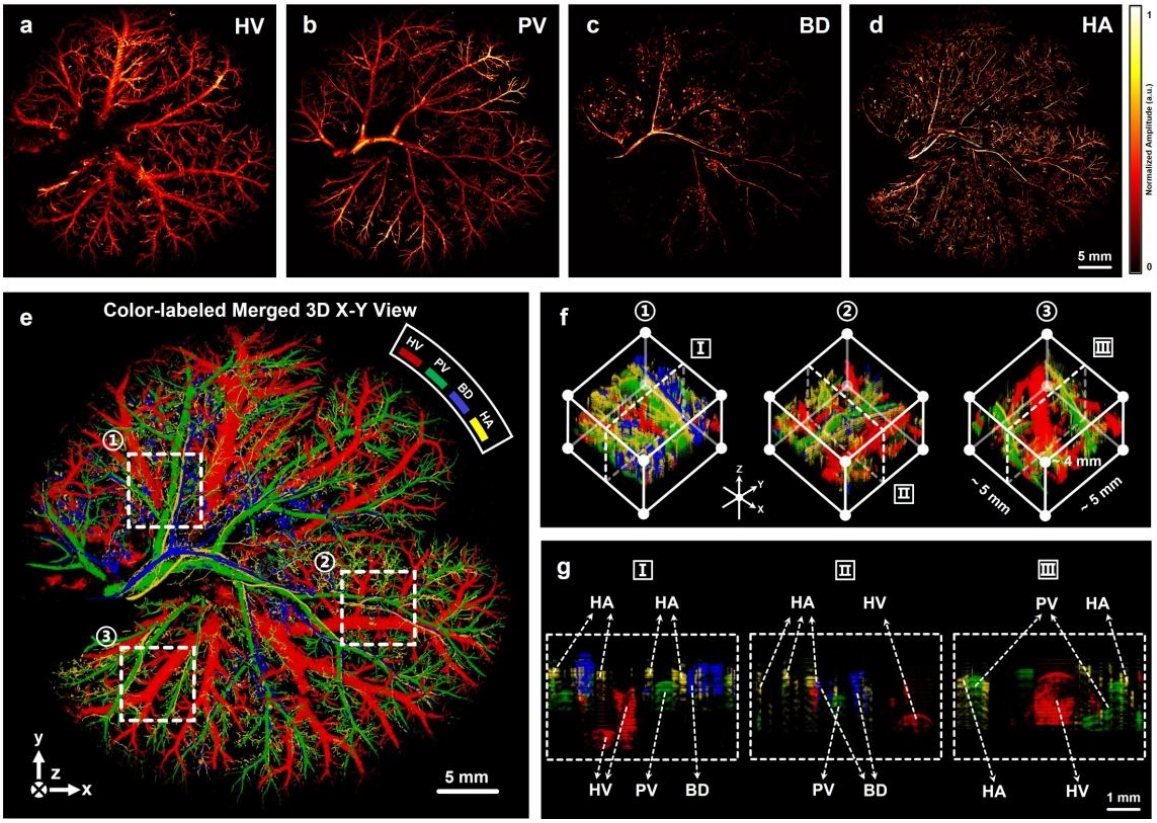

Figure 3: *2D and 3D visualization of hepatic vessel systems inside an SD rat liver using Organ-PAM. Amplitude normalized 2D MAP images of (a) hepatic vein, (b) portal vein, (c) bile duct, and (d) hepatic artery. (e) 3D color-labeled and merged reconstruction results of whole-liver vessel systems. (f) Close-up volumetric view of three sections corresponding to the dashed white squares marked in (e). (g) Selected longitudinal cross-section reconstructions corresponding to the area within the dashed white rectangles in (f). BD, bile duct; HA, hepatic artery; HV, hepatic vein; PV, portal vein.*

The lateral FOV is essential for Organ-PAM to investigate the vessel systems inside organs of large animals and even humans. To show the ultra-large FOV of Organ-PAM, we harvested a New Zealand rabbit liver with a size of 12 cm × 12 cm and decellularized the entire organ. Due to the fact that the size of the liver is far beyond the one-scan FOV (4 cm in diameter) of Organ-PAM, we divided the liver into nine partially overlapping circular regions (Dia. 4 cm) that covered the entire liver (Figure 4). Following the nine single-scans of the divided regions, the image registration algorithm recognizes the overlapped areas between adjacent images and achieves image tiling by matching the overlapped areas (Figure 4b). Using photoacoustic concentration differential angiography, we achieved the visualization and segmentation of whole-set HV and PV systems of the healthy rabbit liver (Figure 4c).

For organs with planar sides that can be flattened on the imaging plane, such as the liver, lung, and spleen, as well as organs from small animals that possess relatively thin tissue, single-sided illumination is sufficient to cover the entire organ in depth. Unfortunately, the thickness of some important organs, such as the heart, stomach and kidney, are beyond the best effective axial FOV of single-sided illumination. The Organ-PAM we designed can achieve a doubled axial FOV of up to ~30 mm using a specially designed double-sided illumination. To highlight the superiority of the extended axial FOV, we tested the panoramic volumetric visualization of whole-set renal artery (RA) and renal vein (RV) systems of a rabbit kidney with a thickness of 11 mm (Figure 5).

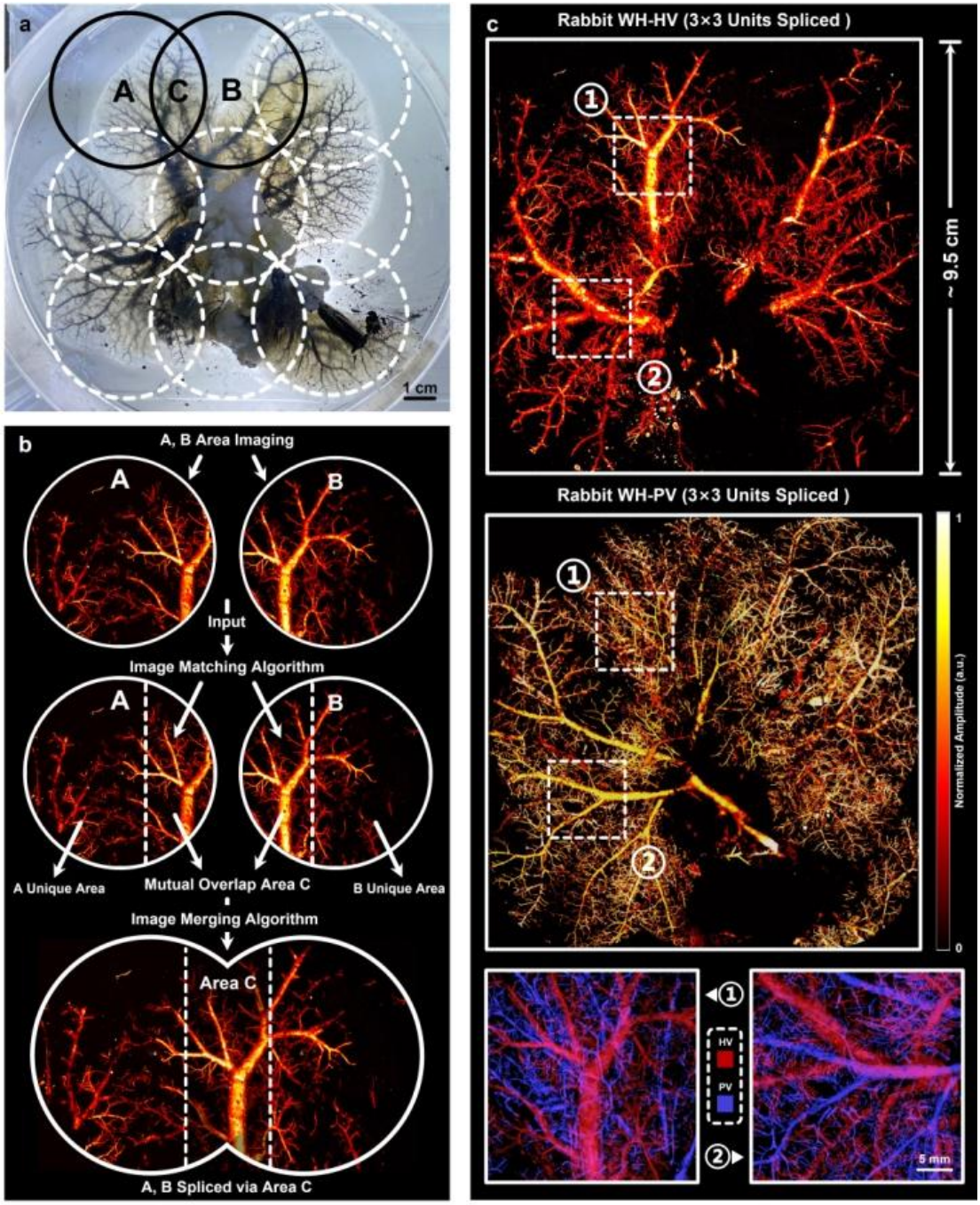

Figure 4: *Visualization of large-scale whole-hepatic vein systems inside a New Zealand rabbit liver by Organ-PAM. (a) Multi-regional imaging of large-scale New Zealand rabbit liver to reconstruct complete vessel system visualization. (b) Image tiling workflow demonstration of two adjacent imaging units corresponding to the imaging regions marked by black circles in (a). (c) The complete 2D reconstruction of the large-scale New Zealand rabbit liver whole-hepatic HV and PV and two ROI images were obtained by re-merging and color-labeling the two vessel systems inside the areas corresponding to the areas within the dotted white squares. HV, hepatic vein; PV, portal vein; WH-HV, whole-hepatic HV; WH-PV, whole-hepatic PV.*

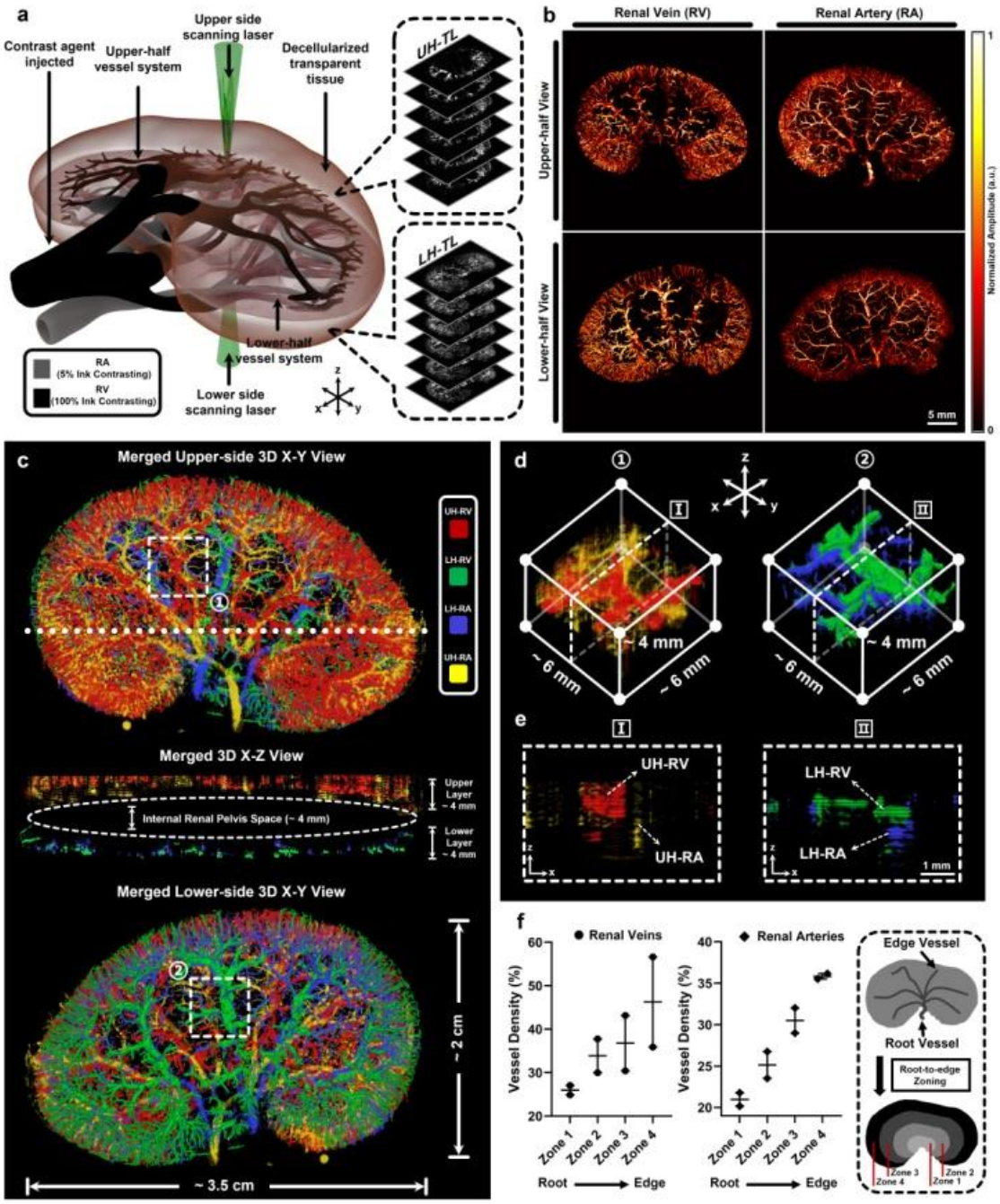

Figure 5: *2D and 3D visualization of whole-renal vessel systems using Organ-PAM. (a) The schematic of whole-renal concentration differential angiography with Organ-PAM. (b) 2D MAP images of RV and RA of each half of the kidney. (c) 3D color-labeled complete visualizations of RV and RA. (d) Close-up volumetric view of two sub-sections corresponding to the dashed white boxes marked in (c). (e) The selected longitudinal cross-sections of the sub-visualizations correspond to the dashed white rectangles in (d). (f) Quantification of RV and RA vascular density (%) according to the imaging data of both halves within four zones equidistantly divided from the root vessel original point to the renal edge. RA, renal artery; RV, renal vein; LH-RA, lower-half renal artery; LH-RV, lower-half renal vein; UH-RA, upper-half renal artery; UH-RV, upper-half renal vein.*

Unlike kidneys and livers, lungs are highly ductile organs with more complex extracellular matrix (ECM) structures rich in various structural proteins, resulting in more structural proteins in decellularized lung tissue and thus more light scattering and less tissue transparency. Hence, it is quite challenging to achieve sufficient light penetration at thick tissue regions of decellularized lungs. To address such limitation, we combined decellularization with a unique intra-organ-perfusion-style optical clearing (OC), which enables faster and better transparency of lungs. To further demonstrate the non-vascular vessel system visualization capability and the multi-organ compatibility of Organ-PAM, we visualized the PT and

pulmonary artery (PA) systems panoramically within a rat lung treated with both decellularization and intra-organ-perfusion-style OC (Figure 6).

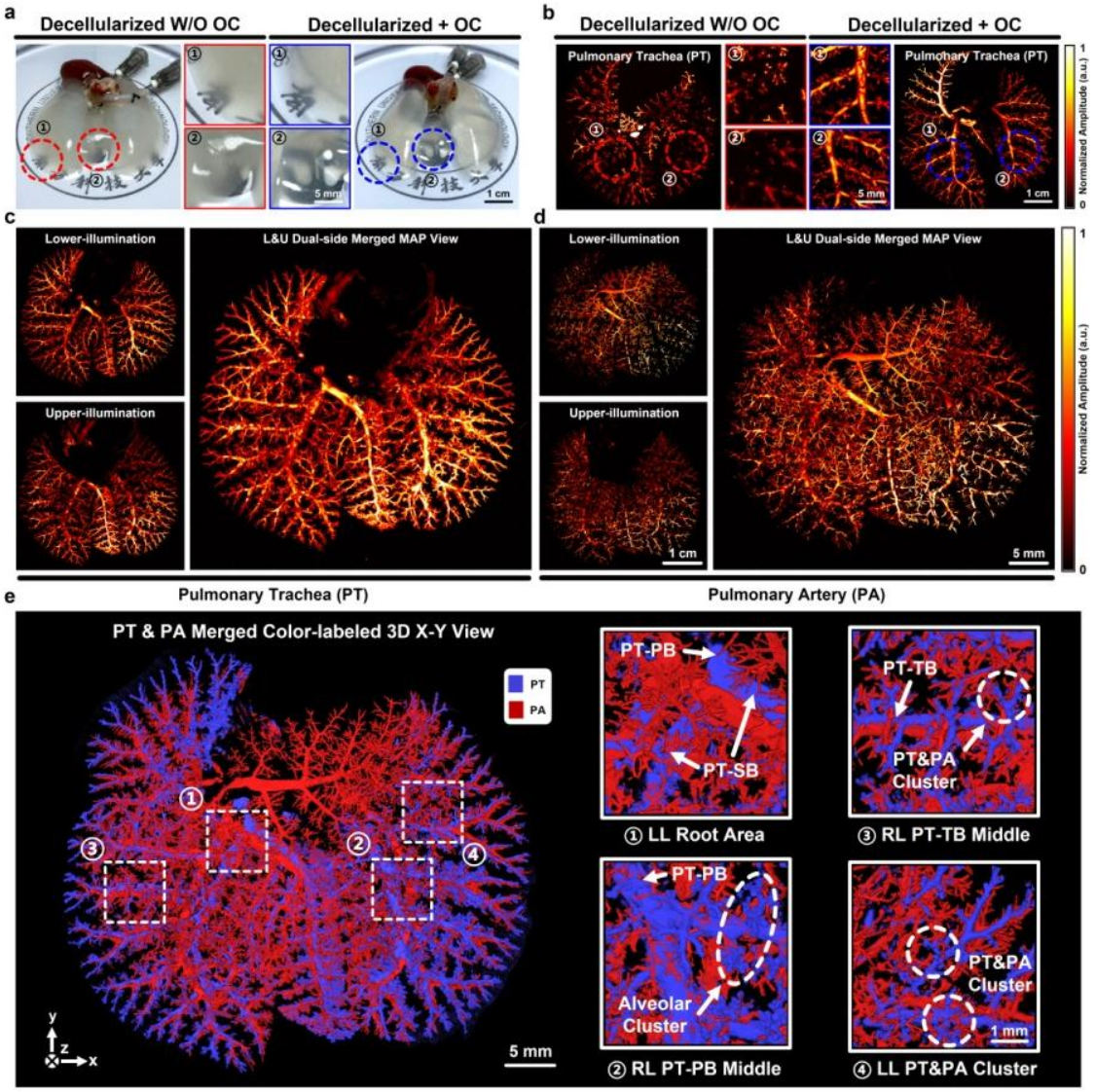

Figure 6: *Fast optical-clearing-assisted decellularized tissue transparency and the visualization of pulmonary trachea (PT) and pulmonary artery (PA) systems within a rat lung using Organ-PAM. (a)-(b) The comparation of tissue transparency and imaging performance between decellularized rat lung and optical clearing enhanced decellularized rat lung. (c)-(d) The 2D MAP visualizations of segmented PT and PA. Visualizations captured using both lower and upper illuminations and merged visualizations are provided. (e) 3D color-labeled visualization of PT and PA with four representative areas selected for zoom-in views. OC, optical clearing; W/O, without; L&U, lower and upper; LL, left lung; PA, pulmonary artery; PT, pulmonary trachea; PT-PB, pulmonary trachea primary bronchi; PT-SB, pulmonary trachea secondary bronchi; PT-TB, pulmonary trachea tertiary bronchi.*

We further utilized the Organ-PAM to probe the pathological vessel systems in primary rat liver cancers at distinct stages (Figure 7). The three sets of vasculatures (i.e., HV, PV, and HA) in the decellularized cancerous livers were contrasted and imaged to investigate the role of blood vessels during cancer progression. We further derived the vascular density ratio (VDR, normalized indicator of vascular density), branch point quantity (BPQ) and vessel length (VL) to quantify the difference between cancers at different stages. We note that the artery system shows an increase, while the vein systems reveal decreases from the marginal area to the center area. All the quantification results demonstrate that the artery system plays a significant role in the metabolic activity of hepatic tumor compared with the vein systems.

Overall, we present an organ-level photoacoustic microscopic imaging platform, named Organ-PAM, with a micron-scale spatial resolution and ultra-large field of views (FOVs), which can achieve a lateral

and axial FOV of up to ~81 cm2 and ~30 mm, respectively. With the assistance of whole-organ decellularization, optical clearing and a specifically designed photoacoustic gradient concentration differential angiographic pipeline, we successfully achieve the visualization of up to four-set vessel systems inside diversified organs with multiple scales. In addition, we conduct quantitative analyses of vessel systems in both healthy livers and kidneys as well as cancerous livers with exogenous transplanted tumor at different stages. Thus, the platform enables high-efficiency multiset vessel imaging, recognition, and quantification of different organs, providing critical insights into distinct vessel systems under varying pathological conditions.

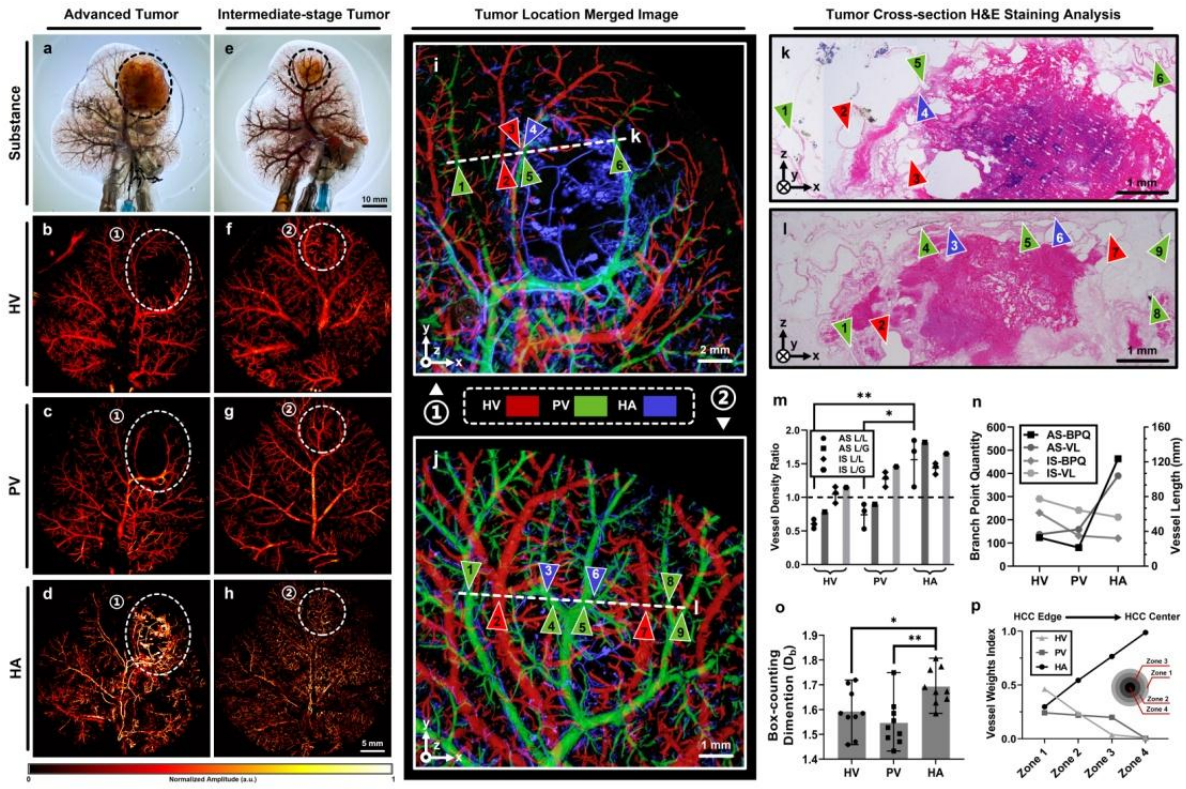

Figure 7: *Visualization and quantitative analysis of whole-hepatic vessel systems inside SD rat livers with exogenous transplanted tumors using Organ-PAM. The substance photos ((a) and (e)) and amplitude normalized 2D MAP images of HV ((b) and (f)), PV ((c) and (g)), and HA ((d) and (h)) of two cancerous rat livers at advanced and intermediate stages, respectively, with dotted circles indicating the cancer locations. The color-labeled and merged vessel systems inside the cancer regions at advanced (i) and intermediate stages (j). Histological analysis of the advanced cancer (k) and intermediate-stage cancer (l) using H&E staining with corresponding sectioning location indicated in (i) and (j). The triangle markers in (i), (j), (k) and (l) indicate vessels can be identified and located mutually in both PAM images ((i) and (j)) and the histological images ((k) and (l)). (m) Local-to-local and local-to-global vascular density ratios of both cancerous livers. (n) Quantification of branch point quantity and vessel length of the vessel systems at cancer sites in both cancerous livers. (o) Quantification of vessel system complexity for advanced liver cancers using box-counting. (p) The visualization showing the changing trend of vessel weights for the vessel systems inside the advanced stage liver cancer from margin to center. HA, hepatic artery; HV, hepatic vein; PV, portal vein; AS, advanced stage; IS, intermediate-stage; L/L, local-to-local vascular density ratio; L/G, local-to-global vascular density ratio; BPQ, branch point quantity; VL, vessel length.*

REFERENCES

[1] Collaboration GBoDLC, The Burden of Primary Liver Cancer and Underlying Etiologies From 1990 to 2015 at the Global, Regional, and National Level: Results From the Global Burden of Disease Study 2015, JAMA Oncology, 2017;3(12):1683-91.

[2] Lafci B, Hadjihambi A, Konstantinou C, Herraiz JL, Pellerin L, Burton NC, et al, Multimodal Assessment of Non-Alcoholic Fatty Liver Disease with Transmission-Reflection Optoacoustic Ultrasound, bioRxiv, 2022:2022.08.16.504139.

[3] Lugano R, Ramachandran M, Dimberg A, Tumor angiogenesis: causes, consequences, challenges and opportunities, Cellular and Molecular Life Sciences, 2020;77(9):1745-70.
[4] Epah J, Palfi K, Dienst FL, Malacarne PF, Bremer R, Salamon M, et al, 3D Imaging and Quantitative Analysis of Vascular Networks: A Comparison of Ultramicroscopy and Micro-Computed Tomography, Theranostics, 2018;8(8):2117-33.
[5] Elkhoury JE, Shankar R, Ramakrishnan TS, Resolution and Limitations of X-Ray Micro-CT with Applications to Sandstones and Limestones, Transport in Porous Media, 2019;129(1):413-25.
[6] Yang L, Feuchtinger A, Moller W, Ding Y, Kutschke D, Moller G, et al, Three-Dimensional Quantitative Co-Mapping of Pulmonary Morphology and Nanoparticle Distribution with Cellular Resolution in Nondissected Murine Lungs, ACS Nano, 2019;13(2):1029-41.
[7] Zheng T, Feng Z, Wang X, Jiang T, Jin R, Zhao P, et al, Zheng T, Feng Z, Wang X, Jiang T, Jin R, Zhao P, et al. Review of micro-optical sectioning tomography (MOST): technology and applications for whole-brain optical imaging [Invited], Biomed Opt Express, 2019;10(8):4075-96.
[8] Wang LV, Yao J, A practical guide to photoacoustic tomography in the life sciences, Nat Methods, 2016;13(8):627-38.

DOI 10.24412/cl-37136-2023-1-16-18

MACHINE LEARNING-BASED RECONSTRUCTION OF BLOOD OXYGEN SATURATION: PILOT STUDY

ALEKSANDR KHILOV[1], DARIA KURAKINA[1], MIKHAIL KIRILLIN[1] AND VALERIYA PEREKATOVA[1]

[1] *Federal Research Center A.V. Gaponov-Grekhov Institute of Applied Physics of the Russian Academy of Sciences, Russia*

alhil@inbox.ru

ABSTRACT

The problem of the determination of blood oxygen saturation (sO_2) is important for a number of biomedical applications [1]. Methods of diffuse optical spectroscopy (DOS) are traditionally used for sO_2 measurements. DOS employs the difference in spectra of oxy- and deoxyhemoglobin at two probing wavelengths. However, the resolution of this method is not vessel level, but for particular applications, for example, tumor response to treatment monitoring [2], one may need the mapping of sO_2 within tissue. To achieve this goal hybrid techniques can serve as an optimal solution.

Optoacoustic (OA) imaging [3, 4] is one of such hybrid methods. OA imaging is based on the detection of ultrasonic waves generated in the studied biological tissue due to the absorption of probing laser pulses by optical inhomogeneities. As different chromophores have their own absorption spectra, spectral OA measurements allow for the reconstruction of chromophores concentrations. The main blood components, oxy- and deoxyhemoglobin, are the strongest absorbers in the visible wavelength range, which makes it possible to use optoacoustic method to obtain angiographic images. OA imaging combines benefits of optical and ultrasound imaging resulting in high spatial resolution, contrast and functional imaging. One of the most promising directions of OA imaging application is the 3D mapping of sO_2 based on OA spectroscopy data, owing to significant difference in oxy- and deoxyhemoglobin absorption spectra, which makes it possible to use OA for various biomedical applications. However, biological tissues are optically inhomogeneous, and their optical properties are a priori unknown, which requires the development of customized approaches for the extraction of physiological parameters. Current trend consists in the application of machine learning techniques [5, 6] using large sets of synthetic OA data, which requires numerical solutions of both optical and acoustic problems. We report on the employment of machine learning based approaches in pixel-by-pixel 3D reconstruction of sO_2.

Usually, quantitative OA imaging research aims to achieve an absolute quantification of the absorption coefficient μ_a, from measured OA signals. In OA imaging, quantification of μ_a involves a solution of two ill-posed inverse problems: acoustic reconstruction yielding images of the OA signal $p(r,\lambda)$ for each measurement wavelength

$$p(r,\lambda) = \Gamma H(r,\lambda) \quad (1)$$

and the estimation of μ_a from absorbed energy spectrum $H(r,\lambda)$, which can be written as

$$H(r,\lambda) = \mu_a(r,\lambda)\Phi(r,\lambda) \quad (2)$$

where $\Phi(r,\lambda)$ is distribution of local light fluence.

In this study we trained machine learning algorithm on in silico data generated through Monte Carlo (MC) simulation of absorbed light distribution in model tissue and than estimated sO_2 from in vivo OA data. A custom developed MATLAB-based implementation of MC algorithm [7-9] was employed for the generation of absorption maps characterized by the distribution of the absorbed dose in a tissue-like medium containing blood vessels with varying diameters and depths within morphological range. In this study we consider 2 wavelengths and simplified model of rabbit ear, containing 4 blood vessels with different diameters and location depths. Absorption maps were calculated for different configuration of model tissue (vessel diameters and depths) and also different sO_2 level.

Calculated absorption maps for different vessel configurations at 532 and 1064 nm were normalized and converted in pixel-wise dataset with ground truth sO_2 and embedding depth labels. 800000 samples were divided on train and test datasets and used for training Gradient Boosting Regressor (GBR) [10]. Raw OA data obtained from OA microscope were reconstructed by delay-and-sum reconstruction [11]. Reconstructed OA data with accounting for the tissue surface were also normalized and converted in pixel-wise dataset for presenting to trained model and estimation of sO_2. The data normalization was performed by matching the signal ranges from OA and MC data.

The machine learning algorithm was tested on the set of experimental data acquired on rabbit ear in vivo [12] in the course of temperature stimulation (cooling down to 15 °C followed by heating up to 43 °C) of arteriovenous anastomosis (AVA) resulting in the variation of blood saturation level in vessels. Maximum intensity projection (MIP) OA images obtained at 532 nm are similar in both temperature regimes (Fig. 1a), while in cold regime AVA phenomenon (Fig. 1b) and its interruption (Fig. 1c) are visible on OA images obtained at probing wavelengths 1064 nm. This set of in vivo data was employed for testing the developed algorithm (Fig. 2).

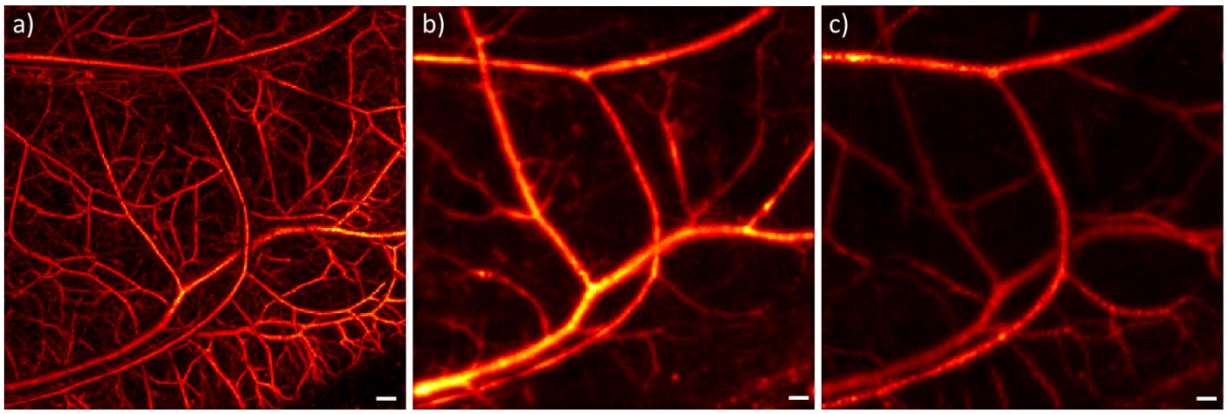

Figure 1: *MIP of OA reconstructed images obtained at 532 nm (a) and 1064 nm (b-c) at immersion chamber temperature of 15 °C (a,b) and 43 °C (c). All bars are 1 mm.*

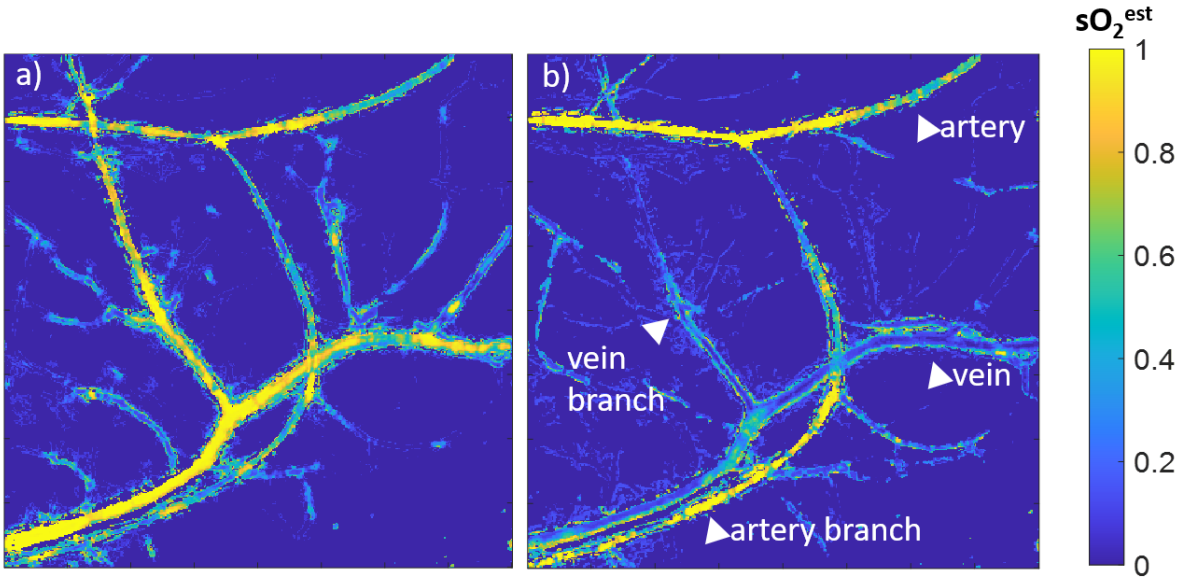

Figure 2: *MIP of reconstructed saturation maps at immersion chamber temperature of 15 °C (a) and 43 °C (b).*

Results of machine learning-based sO_2 reconstruction from MIP OA images visualize AVA appearance and interruption (Fig. 2). It shows clear difference in sO_2 values obtained in veins in cold and warm regimes. Veins are connected with arteries at 15 °C, which leads to exchange of oxygenated blood between them (Fig.

2a) and high sO_2 values in both arteries and veins, while the interruption of AVA at 43 °C leaves only low oxygenated blood in veins (Fig. 2b).

Thus, the developed algorithm demonstrates high potential for sO_2 mapping from MIP OA images without accounting for vessel embedding depth. It has obvious perspectives to be employed for different biomedical applications in quantitative OA imaging.

ACKNOWLEDGEMENTS

The study is supported by supported by Russian Science Foundation (project no. 22-29-00074).

REFERENCES

[1] H.-W. Wang, M.E. Putt, M.J. Emanuele, D.B. Shin, E. Glatstein, A.G. Yodh, T.M. Busch, Treatment-induced changes in tumor oxygenation predict photodynamic therapy outcome, Cancer Res. 64(20), 7553, 2004.

[2] L. Xiang, D. Xing, H. Gu, D. Yang, S. Yang, L. Zeng, W.R. Chen, Real-time optoacoustic monitoring of vascular damage during photodynamic therapy treatment of tumor. J. Biomed. Opt. 12(1), 014001, 2007.

[3] A. Taruttis, V. Ntziachristos, Advances in real-time multispectral optoacoustic imaging and its applications, Nat. Photonics 9(4), 219, 2015.

[4] X.L. Deán- Ben, D. Razansky, Optoacoustic imaging of the skin, Exp. Dermatol. 30(11), 1598, 2021.

[5] J, Gröhl, M. Schellenberg, K. Dreher, L. Maier-Hein, Deep learning for biomedical photoacoustic imaging: A review, Photoacoustics 22, 100241, 2021.

[6] C. Bench, A. Hauptmann, B. Cox, Toward accurate quantitative photoacoustic imaging: learning vascular blood oxygen saturation in three dimensions, J. Biomed. Opt. 25(8), 085003, 2020.

[7] M. Kirillin, A. Khilov, D. Kurakina, A. Orlova, V. Perekatova, V. Shishkova, A. Malygina, A. Mironycheva, I. Shlivko, S. Gamayunov, I. Turchin, E. Sergeeva, Dual-Wavelength Fluorescence Monitoring of Photodynamic Therapy: From Analytical Models to Clinical Studies, Cancers 13(22), 5807, 2021.

[8] D. Kurakina, M. Kirillin, V. Perekatova, V. Plekhanov, A. Orlova, E. Sergeeva, A. Khilov, A. Nerush, P. Subochev, S. Mallidi, I. Turchin, T. Hasan, owards Bimodal Optical Monitoring of Photodynamic Therapy with Targeted Nanoconstructs: A Phantom Study, Appl. Sci. 9(9), 1918, 2019.

[9] V. Perekatova, D. Kurakina, A. Khilov, M. Kirillin, Combined Monte Carlo and k-Wave Simulations for Reconstruction of Blood Oxygen Saturation in Optoacoustics: A Pilot Study, J. Biomed. Photonics Eng. 8(4), 40511, 2022.

[10] P. Prettenhofer, G. Louppe, Gradient boosted regression trees in scikit-learn, in PyData 2014, 2014.

[11] P. Subochev, F. Spadin, V. Perekatova, A. Khilov, A. Kovalchuk, K. Pavlova, A. Kurnikov, M. Frenz, M. Jaeger, Toward Real-Time Giga-Voxel Optoacoustic/Photoacoustic Microscopy: GPU-Accelerated Fourier Reconstruction with Quasi-3D Implementation, Photonics 9(1), 15, 2022.

[12] V. Perekatova, S. Nemirova, A. Orlova, M. Kirillin, A. Kurnikov, K. Pavlova, A. Khilov, A. Kovalchuk, P. Subochev, Three-dimensional dual-wavelength optoacoustic angiography reveals arteriovenous anastomoses, Las. Phys. Lett. 18(4), 045601, 2021.

DOI 10.24412/cl-37136-2023-1-19-21

PHOTODYNAMIC THERAPY AND COMBINED TREATMENTS

AMANDA SURUR[1], ANDREI DABUL[1] AND CARLA FONTANA[1]

[1]*School of Pharmaceutical Sciences, São Paulo State University, Brazil*

amanda.koberstain@unesp.br
nicoli.dabul@unesp.br

ABSTRACT

Antimicrobial photodynamic therapy (aPDT) is a noninvasive form of therapy used in the treatment of diseases in various fields of medicine, such as dermatology [1,2], oncology [3,4] and urology [5,6]. Such treatment produces excellent therapeutic results alone, but there is also the possibility of applying combined therapy of aPDT with other therapeutic protocols aiming to improve the outcome [7]. aPDT still presents the advantage of being well tolerated by patients due to its selective action [8].

aPDT is based on the local or systemic application of a photosensitizing compound (PS), which is intensely accumulated in target tissues. Light at a specific wavelength then activates the PS from its ground state to the excited state, which will react with nearby molecules by transfer of energy or charges in two possible reactions: type I or type II (Fig. 1). Both pathways can cause oxidation of various cellular components, resulting in cell death. In the type I reaction there is production of free radicals, such as $HO^{\bullet}$, which reacts with either biomolecules or with other $HO^{\bullet}$ radicals, originating the cytotoxic compound hydrogen peroxide, besides lipoperoxide, leading to lipid peroxidation. In the type II reaction, energy is transferred to oxygen, inducing the production of $^1O_2$, which leads to the oxidation of proteins, nucleic acids and lipids [7].

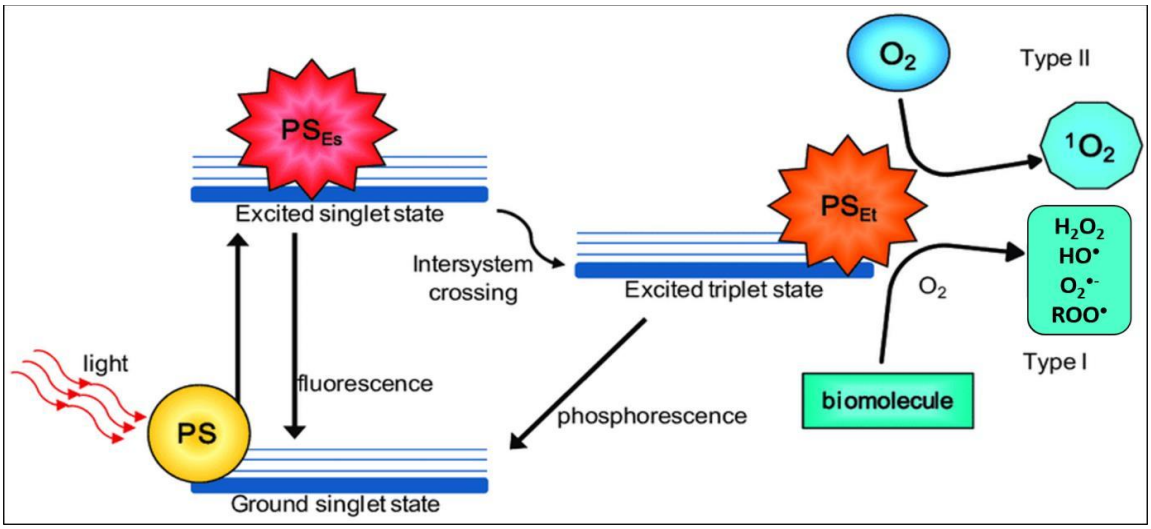

Figure 1: *Jablonski's Diagram for the mechanism of action of PDT type I and II reactions. PS: photosensitizer; PSEs: photosensitizer in excited singlet state; PSEt: triplet excited state photosensitizer; $^1O_2$: singlet oxygen. Adapted from* [9].

One of the possible combined treatments mentioned is the employment of enzymatic inhibitors with subsequent photodynamic treatment. Recently, our research group was able to demonstrate that methylene blue-mediated aPDT in association with a superoxide dismutase inhibitor was effective in reducing the microbial viability of *E. coli* cultured both in planktonic and biofilm forms, characterizing a synergistic phenomenon. Thus, further studies evaluating this combined treatment against other pathogens that have

enzymatic mechanisms for oxidative damage prevention via reactive oxygen species production will be strengthened [10].

Another possibility of combined treatment would be the use of glycoside hydrolases to degrade the polysaccharidic fraction of the extracellular matrix of the microbial biofilm, and then applying aPDT in order to reduce the viability of the microbial cells.

It is estimated that most microorganisms on the planet live in the form of biofilms, allowing them to survive in inhospitable environments. In the case of human pathogens, this feature is particularly important, as it makes the action of antimicrobials even more difficult. Furthermore, exposure to antimicrobial concentration gradients within the biofilm may facilitate the development of resistance [11]. Biofilms are communities of microorganisms that attach to biotic or abiotic surfaces through a polymeric extracellular matrix, which may contain polysaccharides, proteins, extracellular DNA and lipids, in addition to other biomolecules, with polysaccharides being the most abundant in most microorganisms [12].

There are several strategies to inhibit the formation of bacterial biofilms, or even to destroy preformed biofilms, and one of them is the use of enzymes that target the polymers of the extracellular matrix of biofilms, such as the glycoside hydrolases aiming the polysaccharides [13].

This is a very recent research line implemented in our laboratory, in collaboration with another research group, who already demonstrated the ability of these enzymes to eradicate bacterial biofilms. Thus, we intend to evaluate the action of several glycoside hydrolases on several microbial biofilms and further investigate their combination with aPDT aiming a deeper effect.

REFERENCES

[1] S.R. de Annunzio, L.M. de Freitas, A.L. Blanco, M.M. da Costa, C.C. Carmona-Vargas, K.T. de Oliveira, C.R. Fontana, Susceptibility of *Enterococcus faecalis* and *Propionibacterium acnes* to antimicrobial photodynamic therapy, J Photochem Photobiol B. 178, 545–550, 2018.

[2] A.M. Mackay, The evolution of clinical guidelines for antimicrobial photodynamic therapy of skin, Photochemical & Photobiological Sciences. 2022.

[3] V. Karimnia, F.J. Slack, J.P. Celli, Photodynamic Therapy for Pancreatic Ductal Adenocarcinoma, Cancers. 13, 2021.

[4] N. Yu, X. Luo, T. Wei, Q. Zhang, J. Yu, L. Wu, J. Su, M. Chen, K. Huang, F. Li, Y. Xie, F. Fang, L. Zhang, R. He, X. Chen, S. Zhao, W. Bu, Dermabrasion combined with photodynamic therapy: a new option for the treatment of non-melanoma skin cancer, Lasers Med Sci. 2021.

[5] A. V Kustov, N.L. Smirnova, O.A. Privalov, T.M. Moryganova, A.I. Strelnikov, P.K. Morshnev, O.I. Koifman, A. V Lyubimtsev, T. V Kustova, D.B. Berezin, Transurethral Resection of Non-Muscle Invasive Bladder Tumors Combined with Fluorescence Diagnosis and Photodynamic Therapy with Chlorin e6-Type Photosensitizers, Journal of Clinical Medicine . 11, 2022.

[6] D. Tichaczek-Goska, M. Gleńsk, D. Wojnicz, The Enhancement of the Photodynamic Therapy and Ciprofloxacin Activity against Uropathogenic *Escherichia coli* Strains by Polypodium vulgare Rhizome Aqueous Extract, Pathogens. 10, 2021.

[7] S. Kwiatkowski, B. Knap, D. Przystupski, J. Saczko, E. Kędzierska, K. Knap-Czop, J. Kotlińska, O. Michel, K. Kotowski, J. Kulbacka, Photodynamic therapy – mechanisms, photosensitizers and combinations, Biomedicine & Pharmacotherapy. 106, 1098–1107, 2018.

[8] J. O'Neill, Tackling drug-resistant infections globally: final report and recommendations, 2016.

[9] G. Calixto, J. Bernegossi, L. de Freitas, C. Fontana, M. Chorilli, Nanotechnology-Based Drug Delivery Systems for Photodynamic Therapy of Cancer: A Review, Molecules. 21, 342, 2016.

[10] A.K. Surur, V.M. Momesso, P.M. Lopes, T.M. Ferrisse, C.R. Fontana, Assessment of synergism between enzyme inhibition of Cu/Zn-SOD and antimicrobial photodynamic therapy in suspension and *E. coli* biofilm, Photodiagnosis Photodyn Ther. 41, 103185, 2023.

[11] C. Uruén, G. Chopo-Escuin, J. Tommassen, R.C. Mainar-Jaime, J. Arenas, Biofilms as Promoters of Bacterial Antibiotic Resistance and Tolerance, Antibiotics (Basel). 10, 1-36, 2020.

[12] L. Karygianni, Z. Ren, H. Koo, T. Thurnheer, Biofilm Matrixome: Extracellular Components in Structured Microbial Communities, Trends Microbiol. 28, 668–681, 2020.
[13] W.K. Redman, G.S. Welch, K.P. Rumbaugh, Differential Efficacy of Glycoside Hydrolases to Disperse Biofilms, Front Cell Infect Microbiol. 10, 379, 2020.

DOI 10.24412/cl-37136-2023-1-22-24

TUNABLE INFRARED LASERS FOR BIOMEDICAL AND ENVIRONMENTAL APPLICATIONS

IGOR GOLYAK[1], IGOR FUFURIN[1], ANDREY MOROZOV[1], PAVEL DEMKIN[1], DMITRIY ANFIMOV[1] AND DMITRY NAZAROV[2]

[1]Department of physics, Bauman Moscow State Technical University, Russia
[2]Science and Education Center for Photonics and IR-Technology, Bauman Moscow State Technical University, Russia

dimananfimov97@gmail.com

ABSTRACT

This paper discusses the development of an infrared quantum cascade laser emitting in the range from 9.6 to 12.5 μm. The laser is made according to a circuit with an external cavity (Littrow scheme). It is shown that the selected laser design, its energy characteristics (peak pulse power 150 mW and 8 average radiation power mW), wide tuning range (from 9.6 to 12.5 μm), tuning step 2 cm^{-1}, linewidth of 2 cm^{-1}, which allows the developed device to be used in a wide range of applications in the field of spectroscopy.

INTRODUCTION

The analysis of chemical compounds in a solid or liquid state is one of the most important tasks, which has not only fundamental but also applied significance. At the same time, analysis methods are largely determined by the final goal of the study, the conditions of the experiment and the time allotted for it.

At the moment, there are many common methods for solving problems of identifying liquid and solid substances. The most common approach is Raman spectroscopy [1, 2]. Due to the high selectivity of Raman spectra, as well as the ability to study substances even through transparent packaging, this method has become widespread.

Methods for identifying powder samples without prior sample preparation include diffuse reflectance Fourier transform infrared spectroscopy (DRIFTS). The sample is placed in a special cup, then the IR radiation incident on the sample is reflected to varying degrees through the sample. Diffuse reflectance is collected on a parabolic mirror and enters a photodetector. DRIFTS is convenient to use in laboratory settings [3].

Another classical spectral method used in the analysis of chemical compounds is absorption spectroscopy. This method has become especially widespread for the analysis of substances in the gas phase, in particular for the identification of vapors in an open atmosphere using the passive method of FTIR spectroscopy [4, 5].

Currently, significant progress has been made in the development of quantum cascade lasers (QCLs) [6]. QCLs are unipolar semiconductor lasers with the ability to tunable wavelengths over a wide spectral range. Some QCLs are capable of tuning in a range of more than 1000 cm^{-1} and, operating in a pulsed mode, generate peak power up to 150 mW. The use of such lasers makes it possible to obtain fairly informative spectra of diffuse reflection of substances and, as a result, to successfully identify chemical compounds [7].

RESULTS

The developed quantum cascade laser (Fig. 1) generates radiation in the wavelength range 9.6-12.5 μm with a tuning step of 2 cm^{-1} and an output peak power of up to 200 mW, a pulse duration of 300 ns. The laser is built according to the Littrow scheme (external cavity quantum cascade laser).

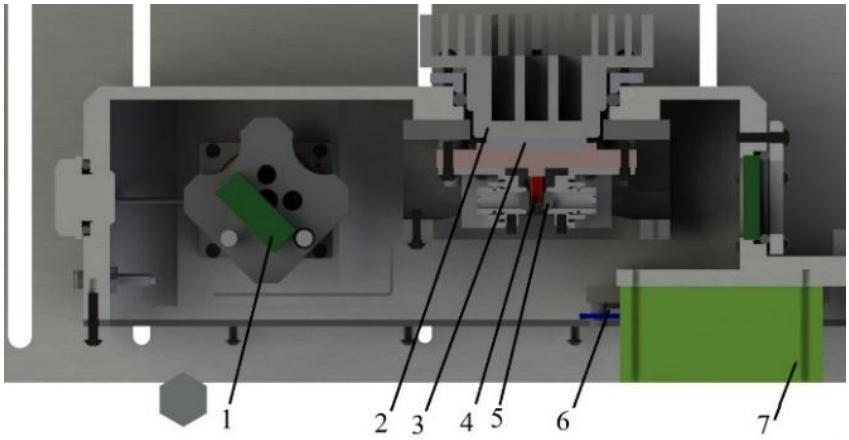

Figure 1: *Quantum-cascade laser. 1 – diffraction grating; 2 – radiator; 3 – Peltier element; 4 – QC chip; 5 – aspherical collimating lens; 6 – control board for the CC chip; 7 – cooling control board.*

To record the signal, a thermoelectrically cooled mercury cadmium telluride (MCT TE) photodetector is used. The system is equipped with a 24-bit analog-to-digital converter.

The developed laser has the following technical characteristics (Table 1).

Table 1. Technical characteristics of a quantum cascade laser.

Radiation range	μm	9,6-12,5
Maximum average radiation power	mW	8,0
Maximum peak pulse power	mW	150
Pulse duration	ns	300
Time interval between radiation pulses	μs	5,7
Tuning step, no more	cm^{-1}	2
Spectral pulse width, no more	cm^{-1}	2
Beam divergence, no more	mrad	5
Output beam size	mm	3,5x5,0
Power consumption (220 V 50 Hz)	W	50
Overall dimensions (LxWxH)	mm	130x150x250
Weight	kg	6

In Figure 2 shows the spectral characteristic of the output power of a quantum cascade laser.

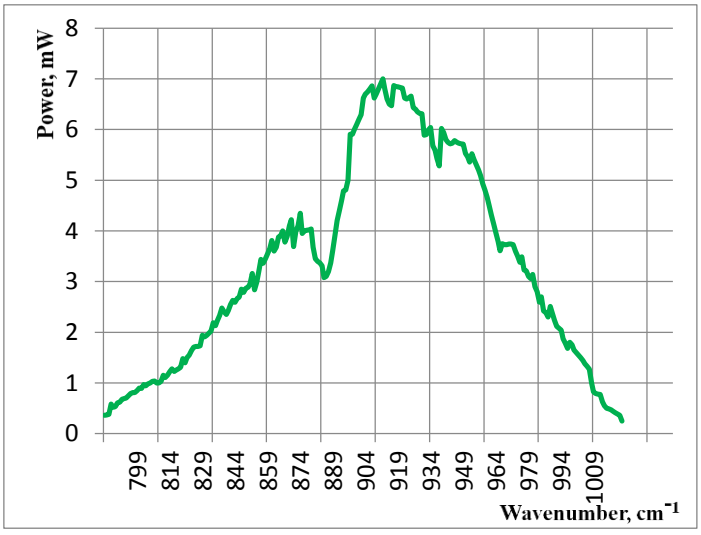

Figure 2: *Dependence of output optical power on wavenumber T= 18°C, Pulse ratio 5%, 14 V.*

CONCLUSIONS

This work presents a prototype of a quantum cascade laser in the range from 9.6 to 12.5 μm. The design features and technical characteristics of the laser are presented. The paper presents a diagram of an

experimental setup, namely a laser spectrometer, for research in the field of diffuse reflectance spectroscopy [8, 9] (as an alternative to Raman spectroscopy [10]) and laser absorption spectroscopy.

The developed experimental setup can be used in the chemical industry [11], pharmacology, medicine, industrial production, ensuring chemical [12] and biological safety, and inspection activities.

The work was carried out within the framework of the Priority 2030 program.

REFERENCES

[1] Gorelik, V., Bi, D., Fei, G. T., Xu, S. H., and Gao, X. D., «Raman scattering in nanocomposite photonic crystals», Inorganic Materials 55(4), 355–364 (2019).
[2] Portnov, A., Rosenwaks, S., and Bar, I., «Detection of particles of explosives via backward coherent antistokes raman spectroscopy», Applied Physics Letters 93(4), 041115 (2008).
[3] Fanning, P. E. and Vannice, M. A., «A DRIFTS study of the formation of surface groups on carbon by oxidation», Carbon 31(5), 721–730 (1993).
[4] Bashkin, S., Karfidov, A., Kornienko, V., Lelkov, M., Mironov, A., Morozov, A., Svetlichnyi, S., Tabalin, S., and Fufurin, I., «An imaging Fourier transform spectroradiometer with a multi-element photodetector for the spectral range of 7–14 μm», Optics and Spectroscopy 121(3), 449–454 (2016).
[5] Golubkov, G. V., Manzhelii, M. I., Berlin, A. A., Eppelbaum, L. V., Lushnikov, A. A., Morozov, I. I. Dmitriev, A. V., Adamson, S. O., Dyakov, Y. A., Morozov, A. N., et al., «The problems of passive remote sensing of the earth's surface in the range of 1.2–1.6 GHz», Atmosphere 11(6), 650 (2020).
[6] Capasso, F., Tredicucci, A., Gmachl, C., Sivco, D. L., Hutchinson, A. L., Cho, A. Y., and Scamarcio, G., «High-performance superlattice quantum cascade lasers», IEEE Journal of selected Topics In quantum electronics 5(3), 792–807 (1999).
[7] Ghorbani, R. and Schmidt, F. M., «Real-time breath gas analysis of co and co 2 using an EC-QCL», Applied Physics B 123(5), 144 (2017).
[8] Anfimov, D. R., Golyak, I. S., Nebritova, O. A., & Fufurin, I. L. (2022). Dispersion Analysis of Diffuse Scattering Spectra Obtained by a Quantum-Cascade Laser as a Means of Substance Identification. Russian Journal of Physical Chemistry B, 16(5), 834-838.
[9] Golyak, I. S., Morozov, A. N., Svetlichnyi, S. I., Tabalina, A. S., & Fufurin, I. L. (2019). Identification of chemical compounds by the reflected spectra in the range of 5.3–12.8 μm using a tunable quantum cascade laser. Russian Journal of Physical Chemistry B, 13, 557-564.
[10] Vintaykin, I. B., Golyak, I. S., Golyak, I. S., Esakov, A. A., Morozov, A. N., & Tabalin, S. E. (2020). The Use of Raman Spectroscopy for the Rapid Analysis of Chemical Compounds. Russian Journal of Physical Chemistry B, 14, 752-759.
[11] Fufurin, I. L., Tabalina, A. S., Morozov, A. N., Golyak, I. S., Svetlichnyi, S. I., Anfimov, D. R., & Kochikov, I. V. (2020). Identification of substances from diffuse reflectance spectra of a broadband quantum cascade laser using Kramers–Kronig relations. Optical Engineering, 59(6), 061621-061621.
[12] Anfimov, D. R., Fufurin, I. L., Golyak, I. S., & Morozov, A. N. (2021, April). Design of an analyzer based on a quantum cascade laser for substance identification by infrared reflected radiation. In Integrated Optics: Design, Devices, Systems and Applications VI (Vol. 11775, pp. 115-122). SPIE.

DOI 10.24412/cl-37136-2023-1-25-29

STUDY OF CHANGES IN THE ATTENUATION COEFFICIENT OF TISSUE WITH DEFORMATION ACCORDING TO OCT DATA

EVGENY SHERSTNEV[1], ALEXANDER MOISEEV[1] AND GRIGORY GELIKONOV[1]

[1]*A.V. Gaponov-Grekhov Institute of Applied Physics of the Russian Academy of Sciences, Russia*
jenya.sherstniov@yandex.ru

ABSTRACT

Optical coherence tomography (OCT) is an interferometric method for visualizing the structure of objects. One of the implementations of OCT is spectral-domain OCT. In this method, the source light is split into two parts. One of them is directed to the reference mirror, and the second to the object under study. Light reflects off both the mirror and the object. Then the spectrum of the sum of the reflected signals is recorded by a spectrometer, which, as a rule, is based on a diffraction grating (Fig. 1). The constant component is removed from the resulting spectrum. After that, the Fourier transform is performed. The result will be a depth distribution of the reflected signal.

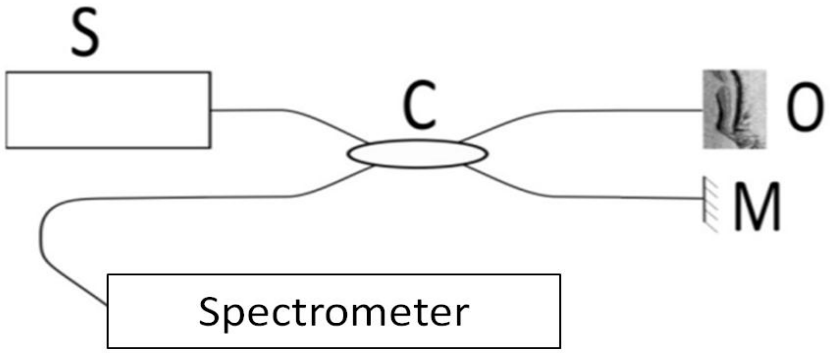

Figure 1: *Simplified OCT setup with spectrometer. S—low-coherent light source; C—coupler; M—reference mirror; O—object.*

The main application of OCT is non-invasive imaging of biological tissues in medical applications. OCT is most widely used in ophthalmology, but other applications are being developed. For example, it can be applied in otorhinolaryngology, neurosurgery, dermatology, etc.

One of the additions to OCT is elastographic studies. There are several implementations of optical coherent elastography. One of them is compression OCE (C-OCE). The probe exerts axial pressure on the sample. To determine the pressure, an additional layer of silicone is used, which is placed between the probe and the object. Young's modulus for this silicone is known, its deformation is determined together with the deformation of the object (Fig. 2).

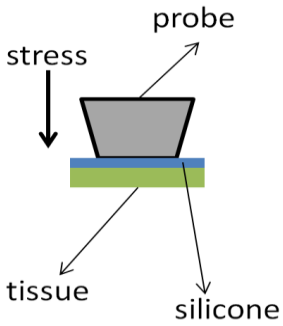

Figure 2: *Standard C-OCE experiment.*

Observation of OCT data, which contain amplitude and phase components, is taken as the basis. Firstly, a frame without pressure is recorded, then axial pressure is applied to the sample, and the next frame is recorded. The phase difference between two frames is calculated. The phase difference is linearly related to the local displacement of points in the image. At the same time, the determination of the phase shift makes it possible to detect even small subpixel shifts. Displacement of local points allows you to determine the local relative deformation. Strain and pressure make it possible to evaluate the stiffness of the material. To determine the pressure, an additional layer of silicone is used, which is placed between the probe and the object. Young's modulus for this silicone is known, its deformation is determined together with the deformation of the object from the phase difference in the image (Fig.3)

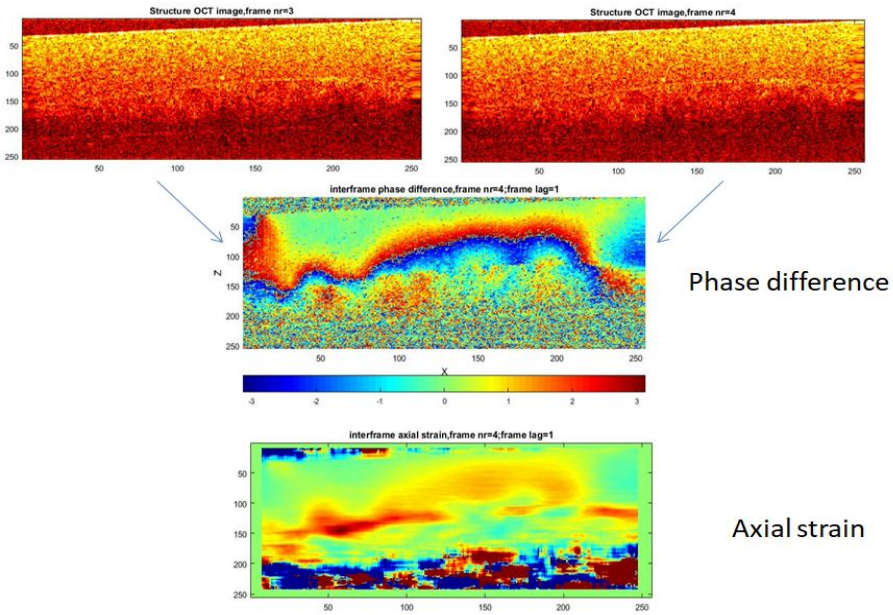

Figure 3: *The principle of image processing in C-OCE.*

In this case, an assessment of the change in the optical characteristics of an object during its deformation may be of interest as a source of additional information about the object. It is logical to assume that the change in the optical characteristics of an object during deformation is related to its hardness. Thus, the evaluation of changes in optical characteristics has the potential to determine the elastic characteristics of the sample without the use of phase calculations, which require high system stability. The purpose of this work is to evaluate the change in the optical characteristics of several samples with obviously different mechanical properties.

The attenuation coefficient of sample is an optical property of tissue that can be estimated from optical coherence tomography data. The attenuation coefficient calculation is used to study the properties of white matter [1], as well as in ophthalmology to improve the definition of certain pathologies [2].

There are two main methods for estimating the attenuation coefficient of a sample. For homogeneous tissues, the signal attenuation can be approximated by an exponential function. The second method was first proposed in [3]. It allows you to calculate the attenuation coefficient with depth resolution

$$\mu_{est}[i] \approx \frac{I[i]}{2 \cdot \Delta \cdot \sum_{j=i+1}^{\infty} I[j]}, \quad (1)$$

where I is the signal intensity, μ_{est} is the attenuation coefficient. The attenuation coefficient is estimated as the ratio of the signal intensity at a point to the sum of the signal intensities at all subsequent points. This method of calculating the attenuation coefficient has a number of requirements for the correctness of the calculation. Firstly, the calculation will be correct if the object under study has a homogeneous directional diagram in

depth. This condition cannot be guaranteed. The second condition is the need for complete attenuation of the signal by the end of the image. If part of the signal does not decay towards the end of the image, then the sum of the intensities in the denominator of eq.1 will be evaluated incorrectly. This causes a calculation error that increases with depth. The fulfillment of this condition can be assessed from the OCT image. The third requirement is the absence of noise in the OCT image. This requirement is not met. To correct the error caused by the presence of noise, the filtering method proposed by our group in [4]:

$$\begin{gathered}\mu[i] = \frac{H[i]\cdot SNR^{\mu}[i]}{|H[i]|^2\cdot SNR^{\mu}[i]+1}\cdot \mu_{est}[i],\\ H[i] = 1-\frac{\sum_{j=i+1}^{\infty} N[j]}{\sum_{j=i+1}^{\infty}(I[j]+N[j])} = 1-\frac{\langle N\rangle\cdot(i_{max}-i)}{\sum_{j=i+1}^{i_{max}}(I[j]+N[j])},\\ SNR^{\mu}[i] = \sum_{x_i,z_i\in W}\frac{|\mu_{est}[i]|^2-|N^{\mu}[i]|^2}{|N^{\mu}[i]|^2},\\ N^{\mu}[i] = \frac{N[i]}{2\cdot\Delta\cdot\sum_{j=i+1}^{\infty}(I[j]+N[j])} = \frac{\langle N\rangle}{2\cdot\Delta\cdot\sum_{j=i+1}^{i_{max}}(I[j]+N[j])},\end{gathered} \tag{2}$$

where $\langle N\rangle$ is the mean noise amplitude, SNR^{μ} is the local signal-to-noise ratio, (Ij+Nj) is the measured OCT signal. Δ – pixel axial size, i - axial measurement number, i_{max} - total number of pixels in axial direction, $\mu_{est}[i]$ – attenuation coefficient value, estimated according to [Vermeer].

Four different samples were selected for the study. There are two plastic phantoms and two biological tissues. Chicken skin and chicken muscle tissue were chosen as biological samples.

The experimental scheme is similar to the C-OCE scheme (Fig. 2). The probe was vertically fixed above the sample. The pressure was exerted due to the upward movement of the surface on which the sample was located. A layer of silicone was placed between the probe and the sample to measure the pressure. The same silicone was used in all four experiments. We assumed that the pressure is directly proportional to the deformation of the silicone. At the current stage, we have limited ourselves to measuring the deformation of silicone. As the pressure changed, OCT images were recorded. To assess the change in the attenuation coefficient, regions near the silicone-sample interface were selected. The areas in each image were divided into 64 rectangular pieces of equal size. The attenuation coefficient was averaged over these rectangles. It should be noted that the condition of complete signal attenuation by the end of the image is not met for plastic phantoms, which can cause some error in estimating the attenuation coefficient for these samples.

To estimate the magnitude of the change in the attenuation coefficient, a scatterplot of the dependence of the attenuation coefficient on the relative deformation of the additional layer was plotted. A linear approximation of this dependence was carried out according to

$$\mu = \alpha\cdot d + \beta, \tag{3}$$

where α and β are the coefficients that are determined during the approximation. α is a slope parameter that characterizes the amount of change in the attenuation coefficient. d is deformation of silicone layer, μ is attenuation coefficient.

The resulting dependencies and their approximation are shown in Fig. 4. The image also shows the value of the slope parameter for each of the samples. The α parameter is 0.26 1/mm for the hard phantom, 0.49 1/mm for the soft phantom, 0.69 1/mm for chicken muscle tissue, and 1.78 1/mm for chicken skin. The rate of change of the attenuation coefficient is the fastest for chicken skin and the lowest slope parameter corresponds to hard plastic.

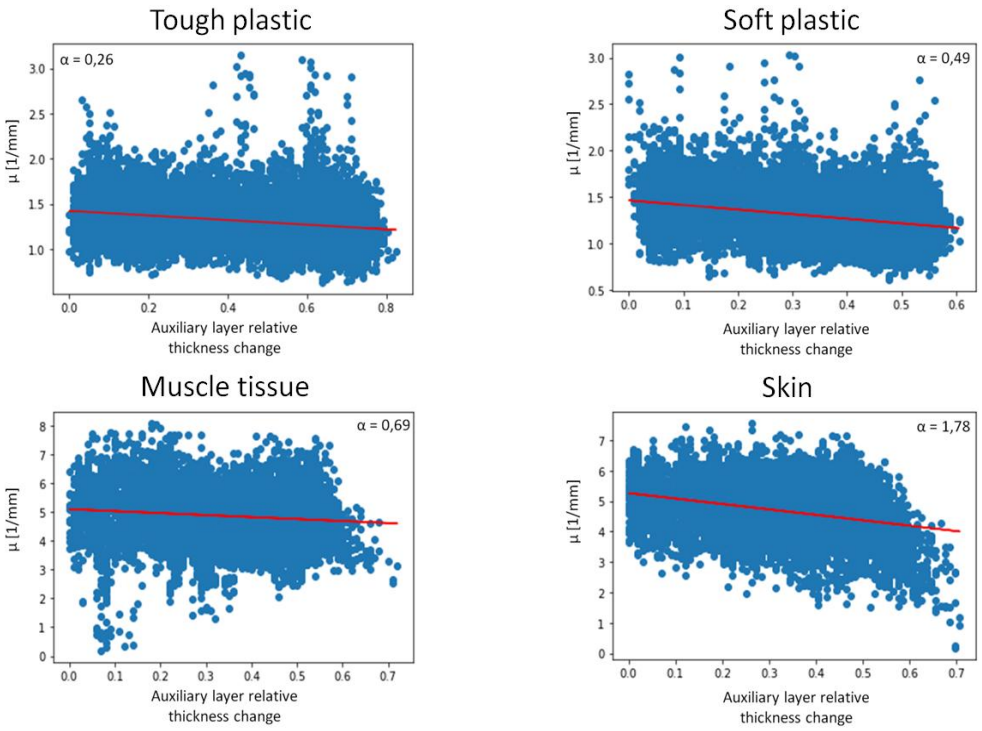

Figure 4: *Experimental dependence of the attenuation coefficient on the deformation of the additional layer for four samples: hard and soft phantoms, chicken muscle tissue and chicken skin*

The data obtained show that the attenuation coefficient varies differently for objects with different stiffness. The plastic phantoms turn out to be close to each other both in terms of the average damping coefficient and in the rate of change of the damping coefficient under pressure. In this case, the biological samples turn out to be close in terms of the average attenuation coefficient. At the same time, muscle tissue shows a rate of change in the attenuation coefficient closer to phantoms than to skin. The rate of change in the attenuation coefficient for chicken skin is noticeably higher than for all other samples. Two parameters can be selected to differentiate different samples. By using the rate of change of the attenuation factor and the average value of the damping factor, a sample map can be generated containing the magnitude of these two parameters and the margin of error (Fig.5).

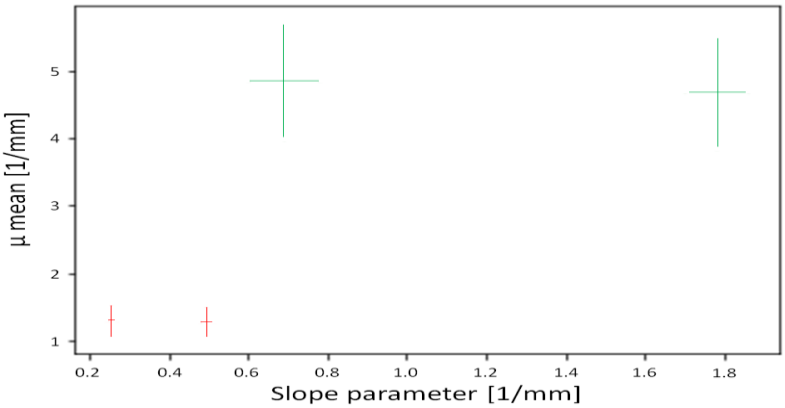

Figure 5: *Parameter map. The vertical axis shows the average attenuation coefficient, and the horizontal axis shows the slope of the linear approximation of the experimental data. Plastic samples are shown in red, biological samples are shown in green.*

The obtained results show the possibility of differentiating objects by the rate of change of the attenuation coefficient, however, at the moment it cannot be guaranteed that the rate of change of the damping coefficient is uniquely related to the hardness of the sample. The next step in the study will be to study the stiffness of the samples and compare the characteristics

REFERENCES

[1] A.A. Moiseev, K.A. Achkasova, E.B. Kiseleva, K.S. Yashin, A.L. Potapov, E.L. Bederina, S.S. Kuznetsov, E.P. Sherstnev, D.V. Shabanov, G.V. Gelikonov, Y.V. Ostrovskaya, and N.D. Gladkova, Brain white matter morphological structure correlation with its optical properties estimated from optical coherence tomography (OCT) data, Biomed. Opt. Express 13, 2393-2413, 2022.

[2] H. Zhou, J. Liu, R. Laiginhas, Y. Shi, M. Shen, G. Gregori, K. Chen, P. Rosenfeld, R. Wang, Depth-resolved visualization and quantification of hyper-reflective foci on OCT scans using optical attenuation coefficients, Biomedical Optics Express, 13(8):4175-4189, 2022

[3] K. Vermeer, J. Mo, J. Weda, H. Lemij, J. De Boer, Depth-resolved model-based reconstruction of attenuation coefficients in optical coherence tomography, Biomed. Opt. Express, 5 322–37, 2014

[4] E. Gubarkova, A. Moiseev, E. Kiseleva , D. Vorontsov, S. Kuznetsov, A. Vorontsov, G. Gelikonov, M. Sirotkina, N. Gladkova, Tissue optical properties estimation from cross-polarization OCT data for breast cancer margin assessment, Laser Phys. Lett. 17 075602 (7pp), 2020.

DOI 10.24412/cl-37136-2023-1-30-34

ALUMINIUM PHTHALOCYANINE-GOLD NANOPARTICLE CONJUGATES ENHANCE THE THERAPEUTIC EFFECT OF PDT IN OESOPHAGEAL CANCER.

ONYISI CHRISTIANA DIDAMSON[1], RAHUL CHANDRAN[1] AND HEIDI ABRAHAMSE [1]

[1] *Laser Research Centre, Faculty of Health Sciences, University of Johannesburg South Africa*
christydidamson@gmail.com

ABSTRACT

BACKGROUND

Gold nanoparticles mediated photodynamic therapy (PDT) have been reported to boost the efficiency and specificity of cancer treatment on various tumour (1-5), however, their impact on oesophageal cancer is limited. In this study, we performed an in vitro assessment of aluminium phthalocyanine (AlPcS4Cl)-gold nanoparticle (AuNPs) mediated PDT targeting oesophageal cancer cells.

METHOD

The AlPcS4Cl-AuNPs conjugate was synthesis through a non-covalent method. The synthesized AlPcS4Cl-AuNPs was confirmed by ultraviolet-visible (UV–vis) absorption spectral analysis and high-resolution transmission electron microscopy. In vitro effects of AlPcS4Cl-AuNPs based PDT in an oesophageal cancer cell line (HKESC-1) such as cell viability, cellular proliferation, and cytotoxicity were assessed by MTT assay, ATP cell proliferation assay, and lactate dehydrogenase (LDH) assay respectively. Fluorescent microscopy was used to determine the internalisation of the conjugates in cellular organelles. Furthermore, Mitochondrial membrane potential (MMP) integrity, and reactive oxygen species (ROS) generation indications of cell death were also examined.

RESULTS

$AlPcS_4Cl$-AuNP Synthesis and Characterization

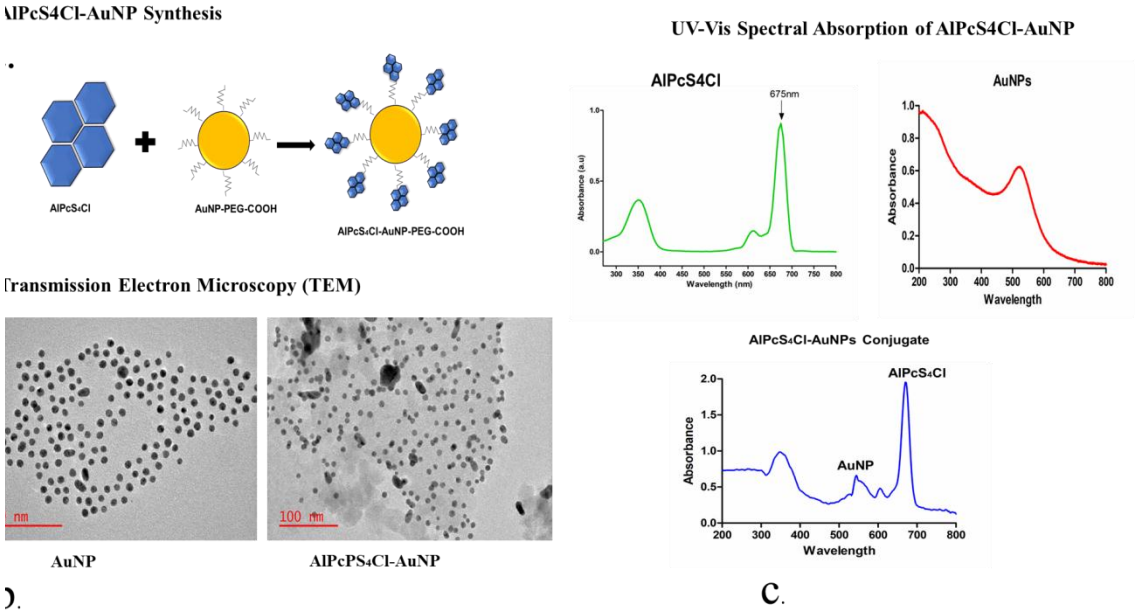

Figure 1: *a) The AlPcS4Cl-AuNPs conjugates was synthesized using a non-covalent conjugation method. b) Transmission electron microscopy images of AuNP and AlPcS4Cl-AuNPs. Scale bars, 100 nm. c) UV-Vis spectral characterization of AuNP, AlPcS4Cl and AlPcS4Cl-AuNPs Conjugate.*

Subcellular Localisation of $AlPcS_4Cl$-AuNPs in oesophageal cancer

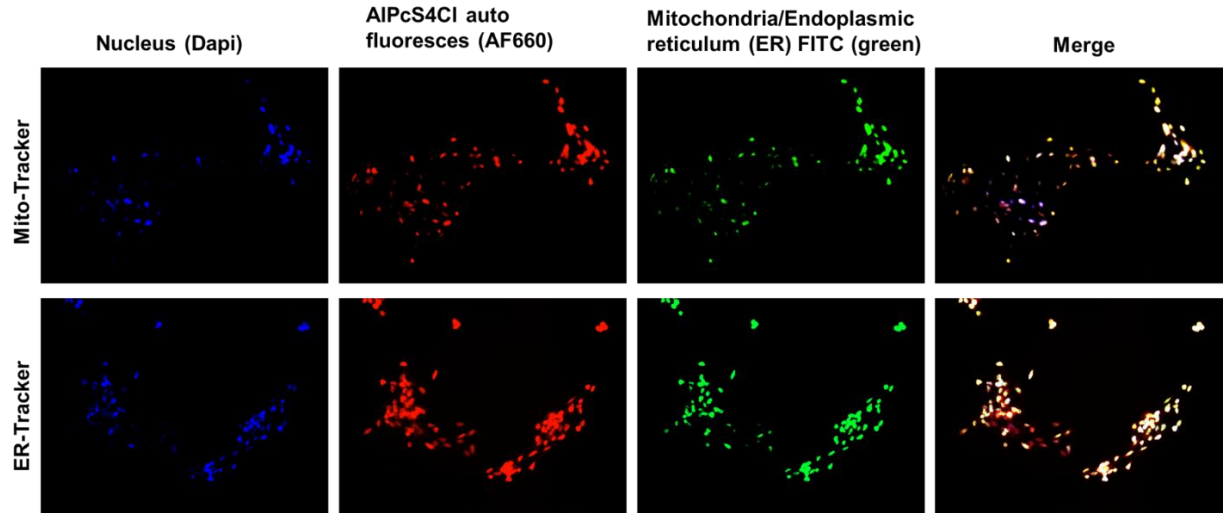

Figure 2: *The nuclei are counterstained with DAPI (blue), mitochondria, ER stained with FITC (green), and AlPcS4Cl-AuNPs auto fluoresces (red). The merged yellow/white and pink colour showed accumulation of AlPcS4Cl-AuNPs the mitochondria, ER and the nucleus.*

In Vitro Effects of AlPcS4Cl-AuNPs Conjugates Mediated PDT on Oesophageal Cancer

Dose-Response Evaluation of AlPcS4Cl-AuNPs Conjugates

Dose response was performed on HKESC-1 cells to obtain the appropriate concentration of $AlPcS_4Cl$, and the conjugates required for downstream application of PDT on HKESC-1 cells. The IC50 values was evaluated by using MTT cell viability assay post 24 h treatment with increasing concentrations of $AlPcS_4Cl$ and of AlPcS4Cl-AuNPs (1.25, 2.5, 5, 10, and 20µM).

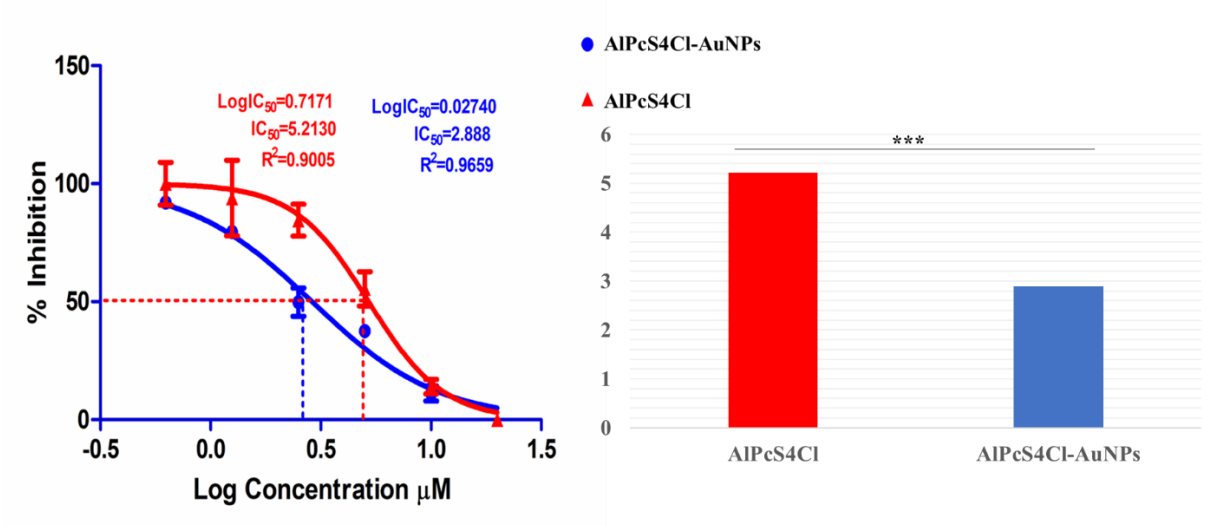

Figure 3*: Determination of 50% inhibitory concentration (IC50) using MTT Cell Viability assay of AlPcS4Cl-AuNPs and the free AlPcS4Cl in Oesophageal cancer. The results are depicted as ± SEM (n = 3); (**p < 0.01, ***p <0.001).*

Cytotoxicity Evaluation

Cytotoxicity assay was performed by evaluating the quantity of lactate dehydrogenase (LDH) enzyme leakage in the cell culture media. Cells that have damaged cell membrane integrity leaks out LDH indicative of cytotoxicity.

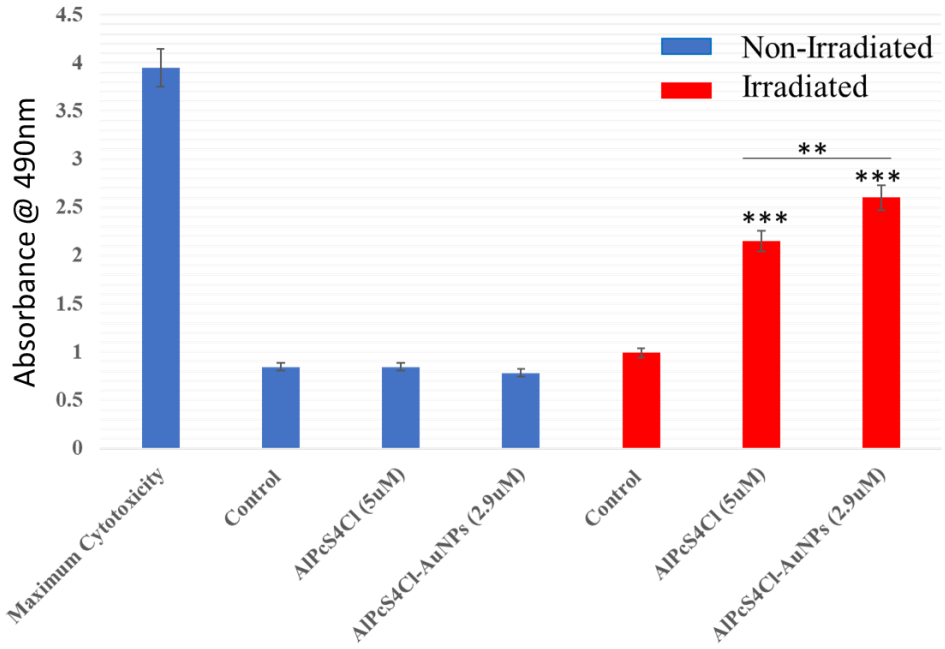

Figure 4: *The cytotoxic effects of AlPcS4Cl-AuNPs and AlPcS4Cl were determined by LDH release cytotoxicity assay. The amount of LDH release after AlPcS4Cl-AuNPs and AlPcS4Cl with 5 J/cm2 irradiation, with AlPcS4Cl-AuNPs conjugate showing increased LDH release compared to AlPcS4Cl and the control. The results are depicted as ± SEM (n = 3); (**p < 0.01, ***p <0.001).*

ATP Cellular Proliferation Assessment

Oesophageal cancer cells were evaluated for cellular proliferation ability with and without photoactivation using ATP proliferation assay. Proliferation results showed that the non-irradiated cancer cells displayed high proliferation activity with increased ATP levels. While the irradiated cells at 5 J/cm^2 showed significant decrease of ATP activities in the cells administered with the AlPcS$_4$Cl-AuNPs conjugate and AlPcS$_4$Cl, with the conjugate showing a more ATP inactivity.

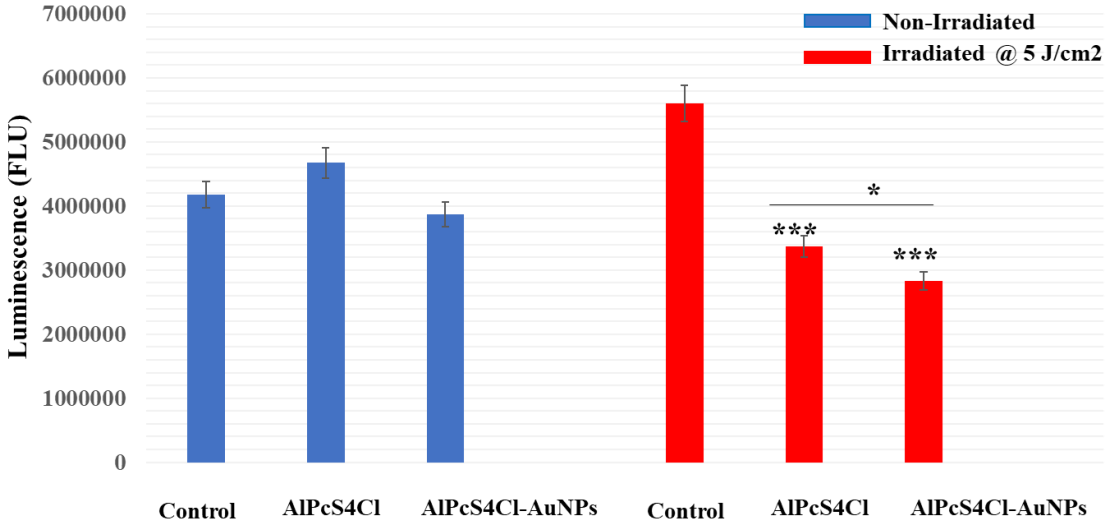

Figure 5: *The cellular proliferative effects of AlPcS4Cl-AuNPs and AlPcS4Cl on oesophageal cancer cells. Blue: the non-irradiated cells showed increase proliferative ATP activities with no significant difference between the control cells and cells administered with AlPcS4Cl and the conjugate. Red: the irradiated cells at 5 J/cm2 demonstrated reduced proliferative actions with reduced ATP levels between conjugate and the free PS (*p < 0.05 ***p < 0.001). The values shown are ± SEM (standard error of the mean) (n=3).*

Mitochondrial Membrane potential (MMP) Integrity

Mitochondrial membrane potential (MMP) was estimated using rhodamine-123. The HKESC-1 oesophageal cancer cells treated with AlPcS4Cl-AuNPs conjugate and AlPcS4Cl showed different effects on the

MMP integrity. AlPcS4Cl-AuNPs conjugate significantly alter the MMP of the HKESC-1 cells compared to the free AlPcS4Cl.

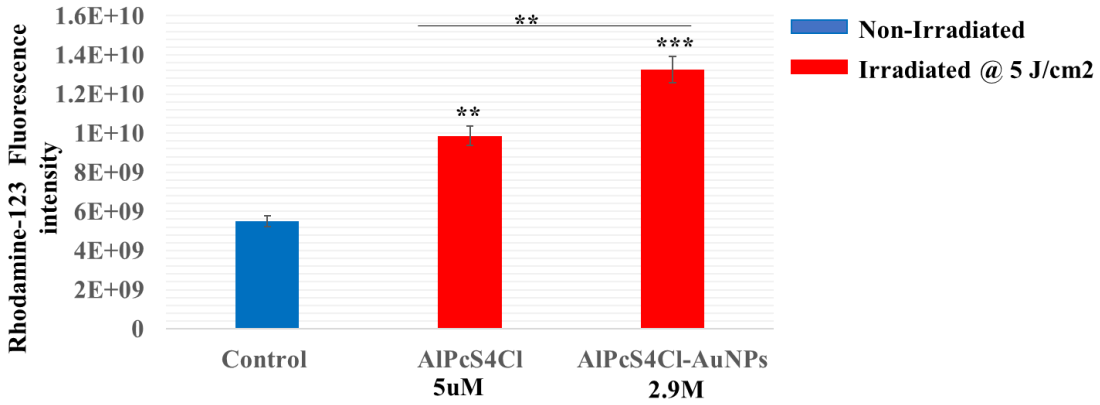

Figure 6: *AlPcS4Cl-AuNPs conjugate and AlPcS4Cl mediated PDT effects on Mitochondrial Membrane potential (MMP) Integrity of oesophageal cancer cells. Blue: the non-irradiated control cells showed decrease MMP impairment. Red: the irradiated cells treated with AlPcS4Cl-AuNPs conjugate and AlPcS4Cl at 5 J/cm^2 demonstrated significant MMP alterations (**p < 0.01 ***p < 0.001). The values shown are ± SEM (standard error of the mean) (n=3).*

Measurement of Reactive oxygen Species (ROS)

Fluorescent probe 2′,7′-dichlorofluorescein diacetate (DCFDA/H2DCFD), cellular reactive oxygen species (ROS) probe was used to quantify intracellular ROS generation of AlPcS4Cl-AuNPs conjugate and AlPcS4Cl based PDT in HKESC-1 cells.

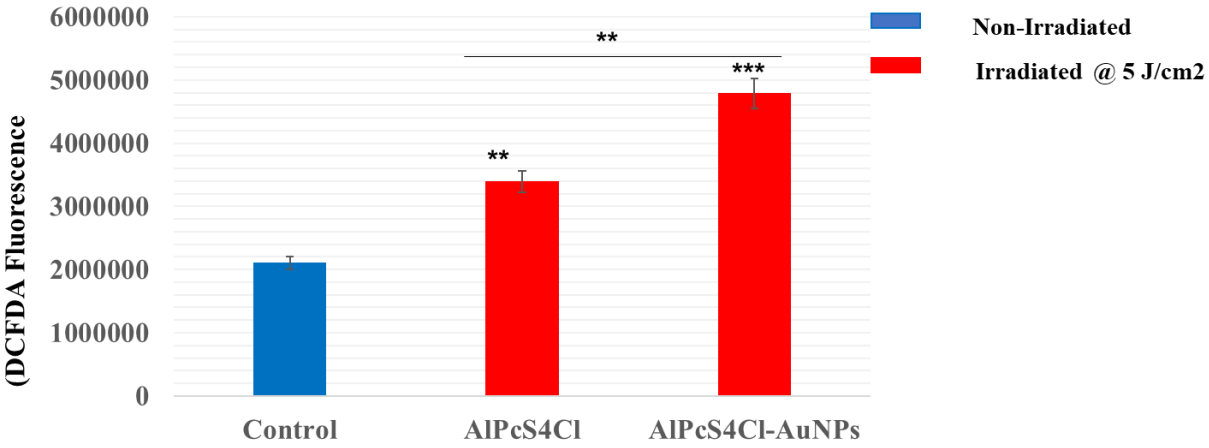

Figure 7*: Intracellular ROS production of AlPcS4Cl-AuNPs conjugate and AlPcS4Cl mediated PDT in HKESC-1oesophageal cancer cells. Blue: the non-irradiated control cells showed decrease ROS generation. Red: the irradiated cells treated with AlPcS4Cl-AuNPs conjugate and AlPcS4Cl at 5 J/cm^2 increase ROS generation (**p < 0.01 ***p < 0.001). The values shown are ± SEM (standard error of the mean) (n=3).*

DISCUSSION AND CONCLUSION

The findings showed that PDT with aluminium (III) phthalocyanine chloride tetra sulfonic acid (AlPcS4Cl) conjugated gold nanoparticle (AuNPs)(AlPcS4Cl-AuNPs) significantly inhibit cell viability/cellular proliferation, increase cytotoxicity, and ROS generation. Fluorescent microscopy revealed that (AlPcS4Cl-AuNPs) was localized in the mitochondria and Endoplasmic reticulum (ER) suggesting the biochemical cell death pathways induction could be mitochondria and ER dependent. More importantly, AlPcS4Cl-AuNPs significantly altered the mitochondrial membrane integrity in HKESC-1 cells. Further confirming the mitochondria dependent cell death pathway. In conclusion, our findings demonstrated that AlPcS4Cl-AuNPs conjugates improved the anti-cancer effects of PDT in oesophageal cancer cells, proposing a better measure to boost the therapeutic efficiency of PDT in oesophageal cancer.

REFERENCES

[1] Chi Y-f, Qin J-j, Li Z, Ge Q, Zeng W-h. Enhanced anti-tumor efficacy of 5-aminolevulinic acid-gold nanoparticles-mediated photodynamic therapy in cutaneous squamous cell carcinoma cells. Brazilian Journal of Medical and Biological Research. 2020;53.

[2] Crous A, Abrahamse H. Photodynamic Therapy with an AlPcS4Cl Gold Nanoparticle Conjugate Decreases Lung Cancer's Metastatic Potential. Coatings. 2022;12(2):199.

[3] Didamson OC, Chandran R, Abrahamse H. A Gold Nanoparticle Bioconjugate Delivery System for Active Targeted Photodynamic Therapy of Cancer and Cancer Stem Cells. Cancers. 2022;14(19):4558.

[4] Mkhobongo B, Chandran R, Abrahamse H. In Vitro Photodynamic Treatment Modality for A375 Melanoma Cell Line Using a Sulphonated Aluminum Phthalocyanine Chloride-Photosensitizer-Gold Nanoparticle Conjugate. Pharmaceutics. 2022;14(11).

[5] Mokoena D, George BP, Abrahamse H. Conjugation of Hypericin to Gold Nanoparticles for Enhancement of Photodynamic Therapy in MCF-7 Breast Cancer Cells. Pharmaceutics. 2022;14(10):2212.

DOI 10.24412/cl-37136-2023-1-35-38

OPTICAL TECHNOLOGIES FOR ORGAN TRANSPLANTATION PROCEDURES

JOSÉ VOLLET-FILHO[1] , LORAINE GOENAGA-MAFUD[1] , YORDANIA GÁMEZ1 , SOFIA SANTOS1[2] , NATALIA INADA[1] , ORLANDO CASTRO-E-SILVA[3] , CRISTINA KURACHI[1] , AND VANDERLEI BAGNATO[1,4]

[1]Sao Carlos Institute of Physics, University of Sao Paulo, Brazil [2] Institute of Geosciences and Exact Sciences, Sao Paulo State University "Julio de Mesquita Filho", Brazil [3]Ribeirao Preto Medical School, University of Sao Paulo, Brazil [4]Department of Biomedical Engineering, Texas A&M University, United States

volletfilho@usp.br

TRANSPLANTATION PROCEDURES

Transplantation is a surgical procedure that is effective in treating advanced-stage organ failure. It involves replacing a dysfunctional organ or tissue of a recipient with a compatible organ or tissue from a live or deceased donor. Its main objective is to restore organ functionality and ensure the survival of the recipient. There are two types of transplant: living donor transplant and deceased donor transplant. Living donor transplant is only possible for certain organs, such as the kidney, liver, lung, and bone marrow. According to the law, only relatives up to the fourth degree and spouses can be donors in this case. Non-relatives can donate only with judicial authorization. Deceased donor transplant is considered only when the donor has been diagnosed with brain death, and the target organ to be donated is physiologically normal, in addition to having the consent of the family and the recipient. Solid organ transplantation is the preferred treatment for improving the quality of life of people with irreversible chronic diseases that affect organs such as the kidney, pancreas, liver, heart, and lungs. The demand for solid organ transplants is growing rapidly worldwide due to the increase in diseases that cause terminal organ failure, such as terminal heart failure, chronic obstructive pulmonary disease, chronic liver cirrhosis and fibrosis, hepatic encephalopathy, hemorrhagic esophageal varices, acute liver failure, hepatitis/fulminant necrosis, and malignant diseases such as hepatocellular carcinoma, hepatoblastoma, hemangioendothelioma, cholangiocarcinoma, non-alcoholic steatohepatitis (NASH), alcoholic cirrhosis, hepatitis C, chronic renal failure, glomerulonephritis, polycystic kidney disease, congenital malformations, and lupus, among others. In these cases, organ transplantation may be the only treatment option for the patient's survival [1-5]. In 2019, 153,863 solid organs were transplanted globally, including kidneys, livers, hearts, lungs, pancreases, and intestines, but this only represents approximately 10% of the global demand, according to the Global Observatory on Donation and Transplantation (GODT). In Brazil, as of December 2020, there were 43,642 patients on the waiting list for organ transplantation, with the highest number of registered patients in São Paulo [6, 7]. Ex vivo perfusion is used for dynamic preservation of different solid organs, allowing continuous evaluation of transplant viability and the preservation of marginal organs. This technique expands the donor pool, reduces the risk of primary non-function, and extends the safe preservation period. However, organ transplantation is still challenging due to long waiting lists, infections, incompatibility between donor and recipient, and organ availability, which is a major limitation leading to an increased mortality rate of patients on the waiting list. To expand the number of organs available for transplantation, many transplant programs have expanded their donor acceptance criteria, including the use of marginal or borderline grafts [6, 7]. Optical techniques are promising regarding its use to investigate, monitor and enhance transplantation organ procedures, as both monitoring and therapeutical procedures can be improved by using light as a tool. Here, we present some of the possible approaches under development with contribution of our research group: assessment tools involving fluorescence spectroscopy for transplanted organs and therapeutical/preparing optical procedures for the enhancement or enabling of organ grafts for transplantation [8].

FLUORESCENCE SPECTROSCOPY FOR TRANSPLANTATION ASSESSMENT AND MONITORING

Fluorescence emission of biomolecules, both endogenous and exogenous, is a widely used technique in biophotonics for diagnosis and therapy. This is due to the characteristic emissions in visible and near-infrared ranges of the electromagnetic spectrum. Fluorescence is a phenomenon where light emission is obtained from electronic state transitions between an excited state and a more fundamental state of the same spin. This is observed in a variety of biological molecules, including human tissue molecules and photosensitizers. Fluorescence techniques depend on the concentration and characteristics of the electronic state available in molecules, which depend on their constitution, structure, and environment. Therefore, information that identifies biological molecules and tissues can be obtained through fluorescence, allowing for the detection and monitoring of specific biological processes. Fluorescence spectroscopy is a specific technique regarding spectral resolution, allowing for the identification of fluorescent molecules and changes in tissue characteristics. It has been used for decades in the monitoring of tissue characteristics and changes. Differently from fluorescence imaging, which allows for wider applications as it enables wide-field and microscopy detection, fluorescence spectroscopy increases the spectral resolution of information. Spectroscopy has been investigated as a tool to identify lesions using endogenous fluorescence differences or exogenous biomarkers. It can also monitor biological processes such as photosensitizers' pharmacokinetics, which involves monitoring their distribution, accumulation, and clearance at cells and tissues over time. Spectroscopy demands the use of lasers for excitation and optical fibers to deliver light and collect fluorescence, making it limited as a point-by-point detection but increasing the resolution of spectral information [9-14]. Since fluorescence spectroscopy can be utilized to identify tissues based on their characteristic spectra, it thus allows determining whether organ grafts are suitable for transplantation or to which extent changes they undergo during a transplantation procedure can be tolerated for viable organs. This approach is currently under development and is based on the principle that the optical properties of viable biological tissues depend on their molecular composition, concentration, and tissue structure. Any abnormalities that may arise in the tissue will produce differences in optical characteristics such as fluorescence emission and light propagation. By identifying patterns of normality or abnormality in tissues classified by accepted clinical standards (Fig. 1), an effective method can be provided for the detection of organ issues that might predict complications leading to death after transplantation. This approach can help surgeons make judgments on organ grafts with borderline acceptability, and greatly contribute to clinical practice. It has been shown that changes in the intensity and/or shape of fluorescence emission bands can be correlated to the preservation solution perfusion and blood reperfusion during liver transplantation procedures, where any complication may lead to an inefficient preservation of the graft and thus severe risk to transplanted patients [15-18].

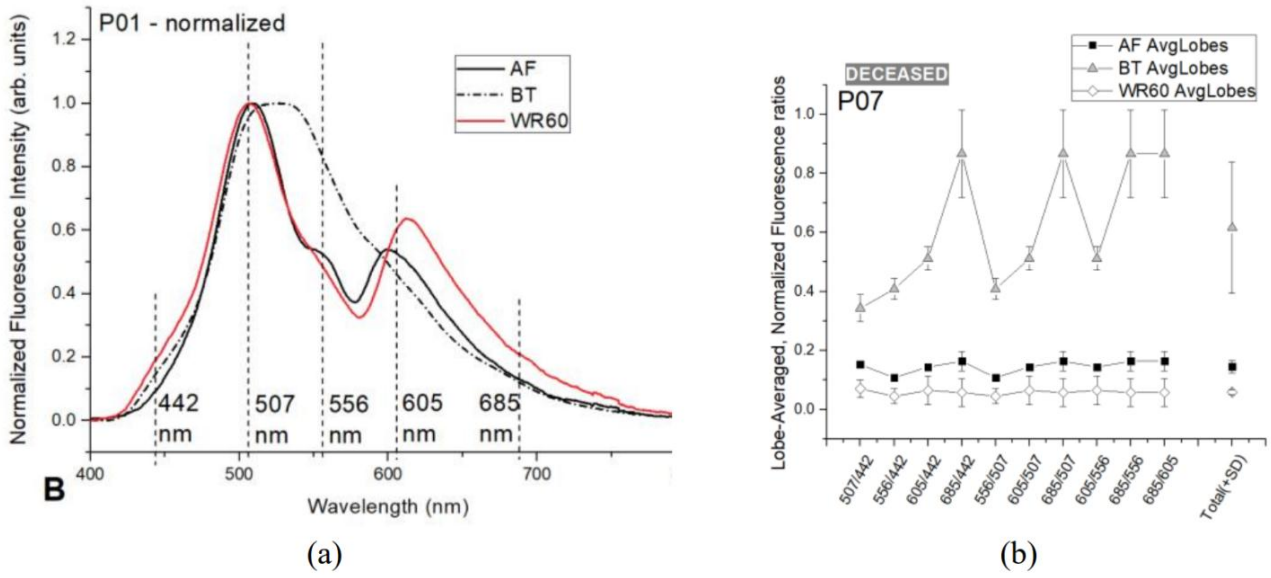

Figure 1: *Fluorescence spectra and variation of standards. (a) Fluorescence spectra at 408 nm excitation for different transplant stages (AF = autofluorescence; BT = backtable; WR60 = 60 min after warm reperfusion). (b) Example of abnormality of fluorescence ratios in spectra for non-surviving patients - spectral profile changes, indicating degeneration in the organ (adapted from [16]).*

OPTICAL TECHNIQUES FOR MICROBIOLOGICAL CONTROL IN TRANSPLANTATION ORGANS

The colonization or infection by microorganisms presents another challenge for organ transplantation, and potentially infected donor organs are usually discarded, further decreasing the available number of organs for transplantation. Thus, another promising approach of optical techniques for transplants involves their use to reduce the microbiological load of microorganisms in organs that would otherwise be eligible for transplantation [6, 19-22]. Microbiological contamination is often found in patients with severe morbidities, and organs are usually discarded for donation. The emergence of antimicrobial resistance and multi-drug resistant (MDR) microorganisms, especially in hospital settings, highlights the need for alternative methods to antibiotic use for decontaminating organs. Microorganisms of concern for antimicrobial resistance include methicillin-resistant Staphylococcus aureus (MRSA) and vancomycin-resistant S. aureus (VRSA), Klebsiella pneumoniae carbapenemase (KPC), NDM-1, MDR-TB (multi-drug resistant tuberculosis), Actinetobacter baumannii, Pseudomonas aeruginosa, Enterococcus faecium, and Proteus sp. However, the development of new generations of antibiotics to combat these superbugs is unlikely in the near future. Therefore, reducing the indiscriminate use of antibiotics and exploring alternative treatments is crucial. Ultraviolet C irradiation (UV-C) showed to be an alternative with microbiological reduction effects that can inactivate microorganisms without the use of chemicals. With the appropriate fluence and wavelength (commonly centered circa 254 nm), UV-C can dimmerize DNA and disrupt nucleic molecules of the target, preventing them from reproducing, and directly inactivate them by destroying their cell walls and membranes. The high photon energy of UV-C can damage all biomolecules, particularly lipids, proteins, and nucleic acids, leading to non-specific biological target action. UV-C has shown effectiveness in water treatment, food and surface disinfection, and can be a promising method for decontaminating organs [23-38]. An initiative has recently shown that lung transplantation could be greatly benefited by decontaminating the preservation solution during ongoing circulation through the organ with UV irradiation prior to the procedure. This approach reduced the microbiological load of the organ and contributed to better quality results of the procedure. Currently, the same approach is being investigated for kidney and liver transplantation using similar processes, both with UV irradiation and proposing a photodynamic inactivation approach [39]. Combining ex vivo organ perfusion with ultraviolet C radiation (Fig. 2) may therefore provide an alternative treatment for contaminated grafts. The perfusate is directly irradiated with UV-C, which eliminates the microbial load without damaging the organ itself. Studies have shown that ex vivo organ perfusion improves graft metabolic conditions and transplant success. Our group recently reported on the development of an ex vivo lung and kidney perfusion machine, which includes a UV-C irradiation protocol. Another option of optical technique for this approach is exploring photodynamic effects in microbiological control (namely photodynamic inctivation or PDI). PDI involves using a photosensitizer (PS) that generates reactive oxygen species (ROS) when activated by light at a specific wavelength and in the presence of oxygen. It has been successful in destroying tumor cells and treating microbial infections. PDI offers advantages over uv-C, particularly by providing a technique that do not demand ultraviolet radiation, thus offering lower light absorption by non-targeted structures and thus avoiding undesired damage to tissue [40].

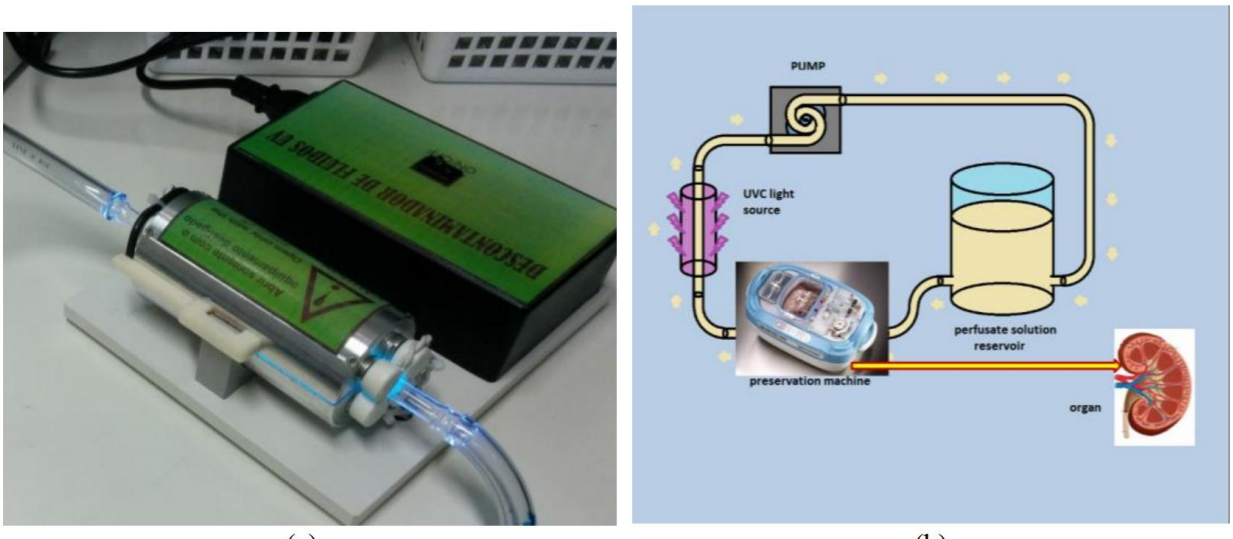

Figure 2: *UV-C decontamination of circulating perfusate - proo-of-principle. (a) UV-C irradiation device, with quartz tube among UV-C lamps, irradiating the circulating solution. (b) Representation of the decontamination process - preservation solution is perfused through the organ, and irradiated externally by UV-C light.*

PHOTOBIOMODULATION FOR THE IMPROVEMENT OF PROCEDURES

Optical techniques have not only been investigated for clinical approaches to transplantation procedures but also for phototherapeutic techniques. Recent studies have explored whether phototherapy protocols can aid in the preservation and maintenance of organ grafts before, during, and/or after transplantation. Promising results were observed in rat livers where the administration of 660 nm laser irradiation protocols prevented certain aspects of lesions caused by ischemia and blood reperfusion. These findings suggest that specific light delivery to organs undergoing transplantation can offer significant protection and may improve transplantation outcomes [41-43].

REFERENCES

[1] Scheuher, C. A review of organ transplantation. Crit. Care Nurs. Q., 39(3), 199-206, 2016.
[2] Hartert, M., et al. Lung transplantation: a treatment option in end-stage lung disease. Dtsch. Arztebl. Int., 111(7), 107-116, 2014.
[3] Tsochatzis, E. A., Bosch, J., Burroughs, A. K. Liver cirrhosis. Lancet, v. 383, n. 9930, p. 1749-1761, 2014.
[4] Rudow, D. L., Goldstein, M. J. Critical care management of the liver transplant recipient. Critical Care Nursing Quarterly, v. 31, n. 3, p. 232-243, 2008.
[5] Kwong, A. J., Fix, O. K. Update on the management of liver transplant patient. Current Opinion in Gastroenterology, v. 31, p. 224-232, 2015. DOI:10.1097/MOG.0000000000000173.
[6] World Health Organization. Activities global observatory on Donation & Transplantation. 2019. Available at: . Acess on: Jul. 3, 2021.
[7] Associação Brasileira de Transplante de Orgãos. Dimensionamento dos transplantes no Brasil e em cada estado (2013-2020). Registro Brasileiro de Transplantes, v. 26, n. 4, p. 1-88, 2020.

DOI 10.24412/cl-37136-2023-1-39-46

SYNERGIC VASCULAR PHOTODYNAMIC ACTIVITY BY METHYLENE BLUE-CURCUMIN SUPRAMOLECULAR ASSEMBLY

RODRIGO SILVA[1,2], HILDE BUZZÁ[3,4], ELI SILVEIRA-ALVES[1], KLEBER OLIVEIRA[2], VANDERLEI BAGNATO[3,5], GUILHERME SOUZA[6], LUCIANE ALMEIDA[7] AND PABLO GONÇALVES[1,8]*.

[1]Instituto de Química, Universidade Federal de Goiás (UFG), Brazil [2]Departamento de Química, Universidade Federal de São Carlos (UFSCar), Brazil [3]Instituto de Física de São Carlos, Universidade de São Paulo, (IFSC, USP), Brazil [4]Instituto de Física, Pontificia Universidad Católica de Chile, Chile
[5]Hagler Fellow, Texas A&M University, College Station, United States
[6]Instituto de Ciências Biológicas, Universidade Federal de Goiás (UFG), Brazil
[7]Universidade Estadual de Goiás (UEG), Campus Anápolis de Ciências Exatas e Tecnológicas, Brazil
[8]Instituto de Física, Universidade Federal de Goiás (UFG), Brazil

rcosta2609@gmail.com

ABSTRACT

A supramolecular assembly was obtained by combining methylene blue (MB) with a natural plant extract curcumin (Curc) in a stoichiometric ratio of 1:4 in aqueous solution (90% PBS + 10% ethanol) at room temperature. The MB-Curc supramolecular assembly was evidenced by absorption and fluorescence spectroscopies and the stoichiometry and bonding constant were obtained using Cielen´s model. Its stability and photostability were evaluated by chromatographic analyzes and UV-Vis absorption. The MB-Curc avoids the aggregation of both isolated compounds and was efficient to produce singlet oxygen ($\Phi\Delta = 0.52 \pm 0.03$). Its potential for photodynamic antiangiogenic treatments was evaluated through vascular effect observed in chicken chorioallantoic membrane (CAM) assay. The results showed intense damage in CAM vascular network by MB-Curc after irradiation, which is higher than the effect of isolated compounds, showing a synergic vascular effect. This combination can be important to avoid cancer revascularization after photodynamic application, and improve this approach's efficacy. The characteristics shown by MB-Curc make it a potential candidate for use in cancer treatments by photodynamic antiangiogenic therapy

INTRODUCTION

The combination of PDT with antiangiogenic therapy has been proposed to avoid cancer revascularization after PDT.[1] Basically, antiangiogenic therapy consists of the use of some drugs to cutting off the blood supply to tumor micro- regions, resulting in hypoxia and necrosis within solid tumor tissues and consequently its death by nutrition starvation.[2] Antiangiogenic therapy also is an alternative for cancer treatment and is effective for some types of cancer, such as metastatic renal cell carcinoma, but not for others, such as breast cancer, melanoma, pancreas and prostate cancers.[3] Another disadvantage of antiangiogenic therapy is the cost, some antiangiogenic drugs commercially available are monoclonal antibodies such as bevacizumab (Avastin®) and DC101, which are very expensive. An alternative to those drugs is the use of natural compounds extracted from plants, which has the advantage of low cost compared to conventional antiangiogenic drugs. Compounds extracted from the rhizomes of the plant *Curcuma longa* L called curcuminoids, which are composed of curcumin, demethoxy-curcumin and bis-demethoxy-curcumin, are natural products with a wide biological activity, such as antiangiogenics,[4] so on.

We hypothesized that Curc combined with MB could form a supramolecular structure combining the antiangiogenic and photosensitizing properties of Curc and MB. PDT combined with antiangiogenic therapy may result in a synergistic anti-tumor effect that would destroy the tumor and prevent its recurrence. This strategy could be an alternative low cost and efficient for antiangiogenic photodynamic therapy. Herein, we characterized the chemical interaction between these molecules, the formation of a MB-Cur supramolecular complex, evaluated the photo-stability of this complex, and its potential for photodynamic antiangiogenic treatments, which was evaluated through vascular effect caused in chicken chorioallantoic membrane (CAM) assay. We

selected this method because it provides quick results, is cost-effective, simple, has high reproducibility, and presents easy dynamic observation.[5]

RESULTS AND DISCUSSION

Figure 1A shows the effects of Curc presence on the MB absorption spectra. It is possible to observe that the increases of Curc concentration linearly quenches the main absorption band of MB at 664 nm (inset of Fig 1A). Differential UV-Vis spectra were obtained using the solution of MB (4 μM) as the background of experiments (Fig 1B). In this case, it is possible to see a new redshift band formation at 704 nm for a 1:4 molar ratio between MB and Curc, respectively (inset of Fig 1B). The isosbestic point at 590 nm and the new redshifted band suggests the formation of an MB-Curc complex. On the other hand, the increases of MB concentration (0 – 40 μM) in Curc solution (4 μM) did not cause observable changes in the absorption behavior of the Curc band. Possibly, this can be attributed to stoichiometry of the complex. While MB is affected by 4 molecules of curcumin, the curcumin absorption is disturbed by just 25% of this effect (data not shown).

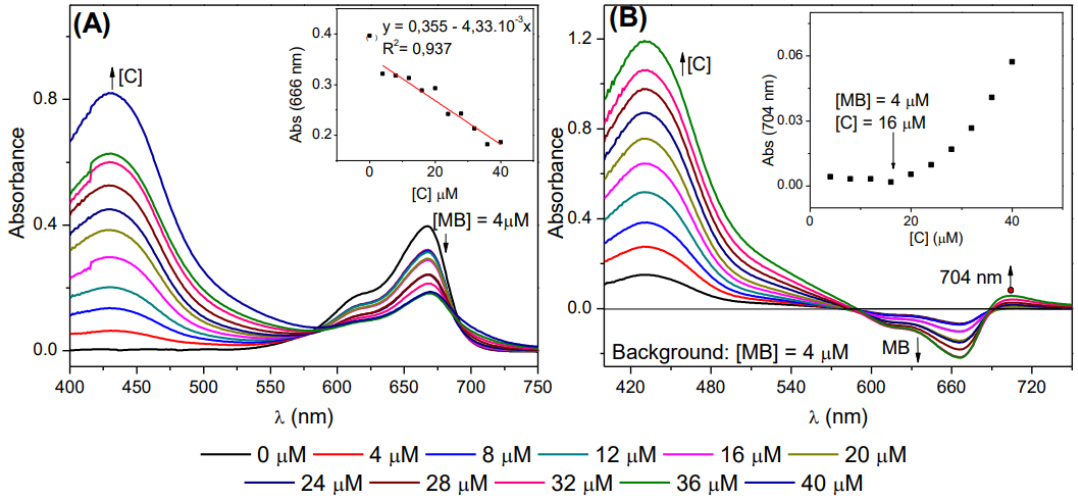

Figure 1: *A) UV-Vis absorption spectra for mixtures of MB (4 μM) with Curc (0-40 μM). Inset highlight the decrease of MB absorption band at 665 nm. B) Differential UV-Vis spectra for mixtures of MB (4 μM) with Curc (0-40 μM). Inset highlight the band intensity at 704 nm.*

Stoichiometry and bonding interaction

The MB-Cur complex formation was evaluated by fluorimetric titration using a multiple binding model developed by Ciele et. al 1998.[6]

$$\log\frac{F-F_{min}}{F_{max}-F} = -logK_d + nlog[B] \qquad (3)$$

F is the fluorescence signal at [B], while F_{min} and F_{max} denote the fluorescence signal at minimal [B] (absence of B) and maximal [B] (solution is saturated with B in excess), respectively. In a plot of left side of eqn (3) as a function of log [B], the slope provides n, while intersection with abscissa corresponds to $logK_d$. Finally, the binding constant (K_b) can be obtained from a reciprocal relation between K_b and K_d (K_b = 1/).

MB solution shows a fluorescence emission band centered at 690 nm, which is quenched by curcumin addition (Fig 3A). The absorbance value of the initial MB solution (in absence of Curc) at the excitation wavelength (630 nm) was adjusted to less than 0.1 to avoid the possible contribution of intermediate complexes to the fluorescence intensity. The fitting of the Hill plot (inset of Fig 2A) provides the n = 4.08 and K_b= 3.98×10^5 M^{-4}, suggesting a stoichiometry 1:4, corresponding to the binding of 4 molecules of Curc to 1 MB (Fig 2B), which is in accordance with data presented in Fig 2.

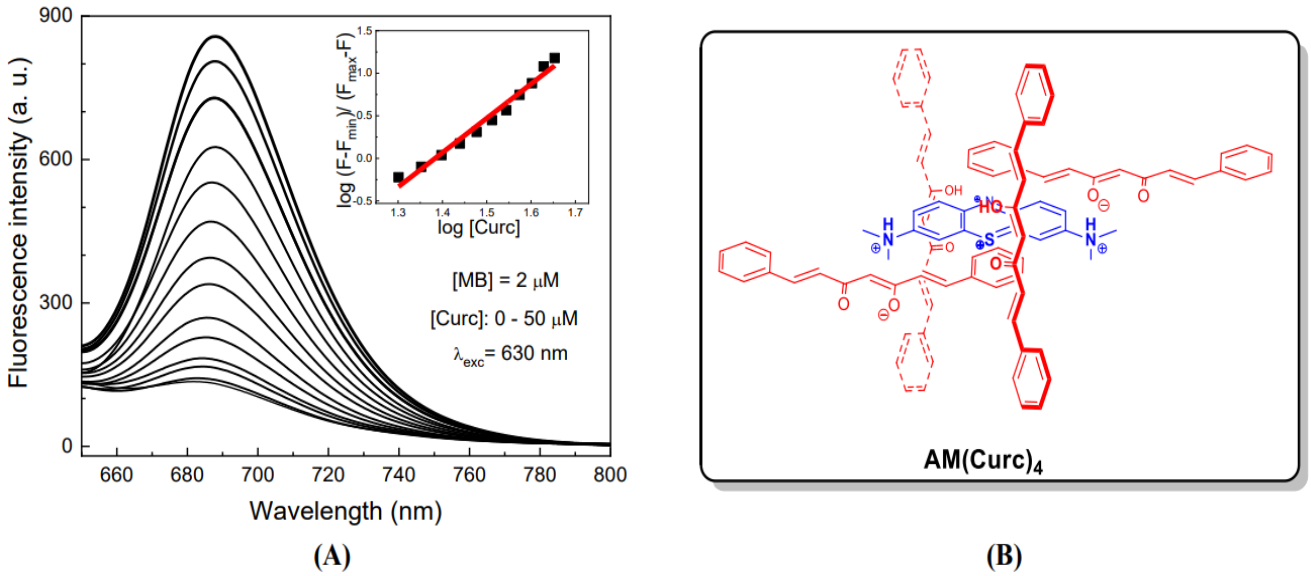

Figure 2: *A) Fluoresce emission spectra of MB (2 μM) as a function of Curc concentration (from 0 to 50 μM). Inset: Hill plot. B) Structure proposal of the MB-Curc complex.*

Stability of the Curc-MB complex in solution

The variation of the concentration of the species in solution was measured as a function of time to characterize the stability of the Curc-MB complex in solution. MB-Curc complex solution was prepared in PBS (pH 7.4) at 10% of ethanol in a ratio 1:4 of MB (6 μM) with Curc (24 μM), respectively. The concentrations were analyzed every 20 minutes for 5 hours to evaluate the stability of these species in solution by HPLC analysis.

The concentration of all species decreased during the experiment (Figure 3A-D). Interestingly, the MB retention time in the MB-Curc complex solution shifted to a shorter retention time during the first 40 minutes of analysis. Subsequently, the retention time of MB in MB-Curc complex solution was similar to the retention time obtained for MB solution, probably due to degradation of the complex in solution. The shorter retention time of MB in the MB-Curc complex solution suggests that the formation of the complex provides a character more hydrophilic to MB.

The concentration of Curc solution reduce of (23.5 ± 0.5) μM for (11.3 ± 0.5) μM, degradation of (52.0 ± 1.1)% (Figure 3A) while the concentration of Curc in MB-Curc complex solution reduce of (22.6 ± 0.1) μM for (14.3 ± 0.1) μM, reduction of (36.7 ± 0.2)% (Figure 3C). These results demonstrated that the MB-Curc complex has high Curc stability in solution at about 30%. However, the MB stability has low from (10.1 ± 0.1)% in MB solution (Figure 3B) to (22.5 ± 0.7)% in MB-Curc complex solution (Figure 3D), decreasing by 126%, which is about 4 times the increase of stability observed for Curc in MB-Curc complex solution.

The low stability of Curc in buffer systems at neutral-basic conditions has been reported [7]. Studies suggest that the maintaining of the conjugated diene moiety of the Curc, which is observed for both acid pH conditions and metal complexes, may contribute to increasing Curc stability [8]. Thus, our results suggest that the β-ketoenol moieties of Curc could be the site of complexation between Curc and MB.

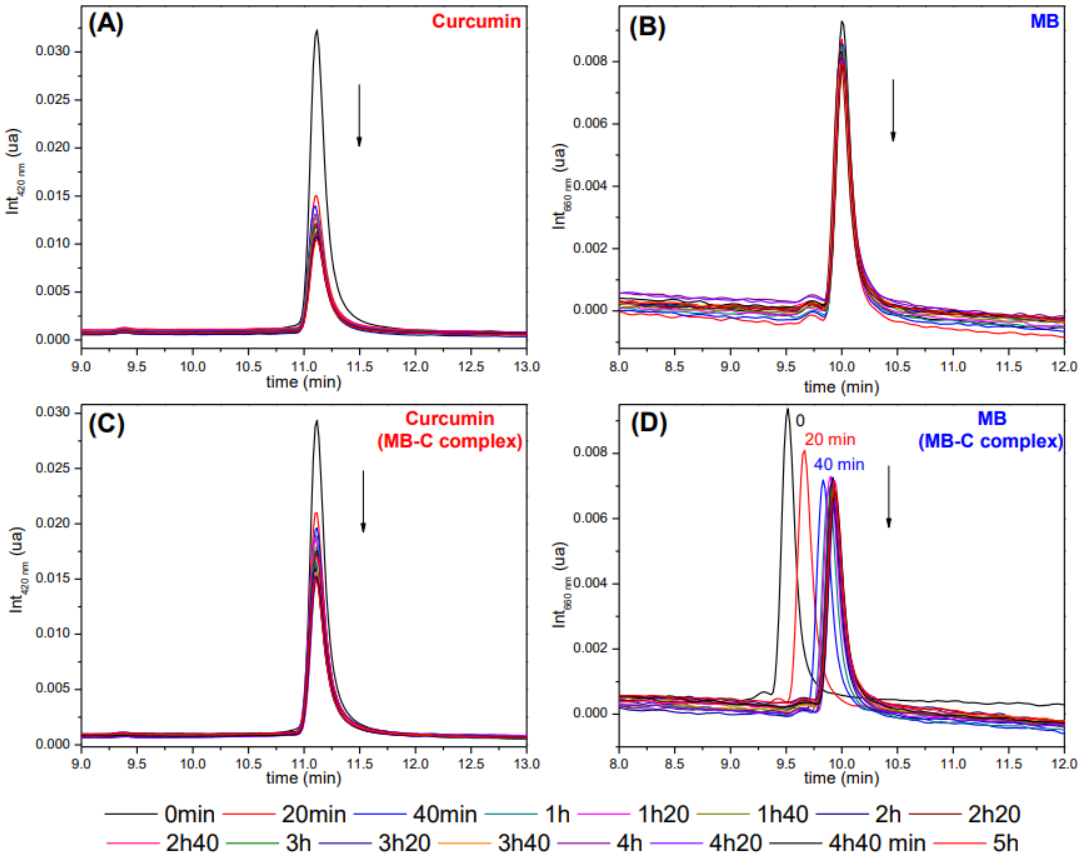

Figure 3: *Chromatogram recorded every 20 min for 5 hours for A) Curc, B) methylene blue, C) Curc in the MB-Curc complex solution and D) methylene blue in the MB-Curc complex solution.*

MB-Cur complex and aggregation

In solution, the π-stacking interaction between organic molecules of high electronic conjugation can cause the formation of aggregate. Aggregation is a process molecular that affects the properties of monomeric compounds and can reduce their therapeutic activity[9] and then it should be avoided. The formation of the aggregates of Curc was evaluated by the variation of the concentration of ethanol in the PBS buffer using UV-Vis spectroscopy. Thus, solutions of Curc (20 µM) were prepared in a mixture of PBS buffer and ethanol (10-100%). The data recorded has shown that the decrease of ethanol concentration lesser than 40% induced the appearance of a new blue-shift absorption band of Curc at 370 nm, characteristic of type-H aggregate (Figure 4).

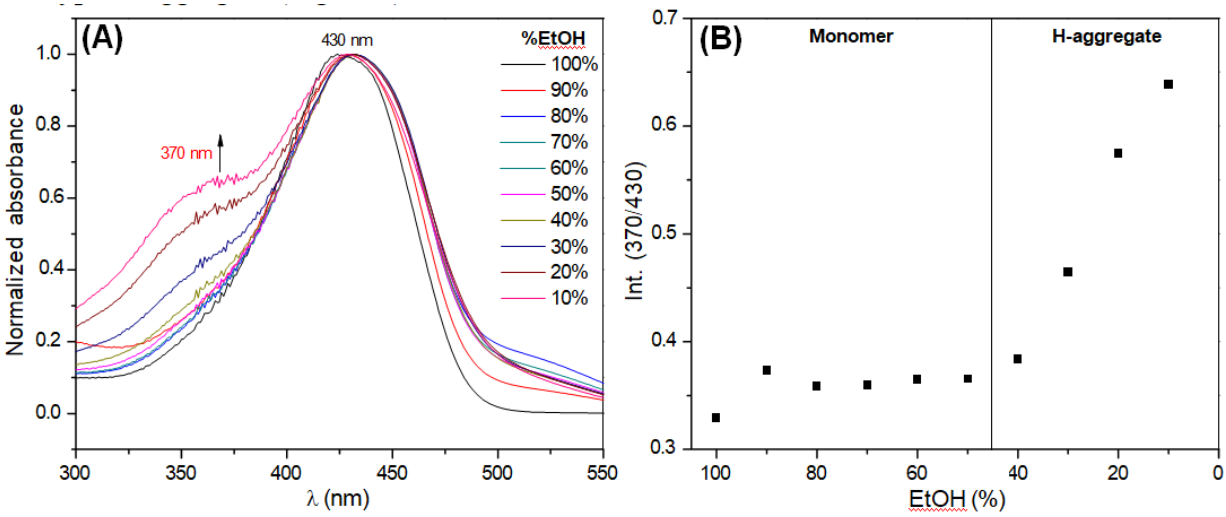

Figure 4: A) *UV-Vis spectroscopy of Curc (20 µM) in a mixture of PBS buffer and ethanol (10-100%).* ***B)*** *Relative intensity of new blue-shift absorption band at 370 nm concerning monomer Curc band at 430 nm.*

Subsequently, solutions of Curc (20 µM) and MB (1-10 µM) in a mixture of PBS buffer and ethanol at 10% were prepared to evaluate the influence of the MB-Curc complex in the trend of formation of type-H aggregate. The data recorded has shown that the increase of MB concentration in solution causes the disappearance of Curc aggregate band, at 370 nm (Figure 5), suggesting that the complex formation decreases the trend of the aggregation of Curc in solution.

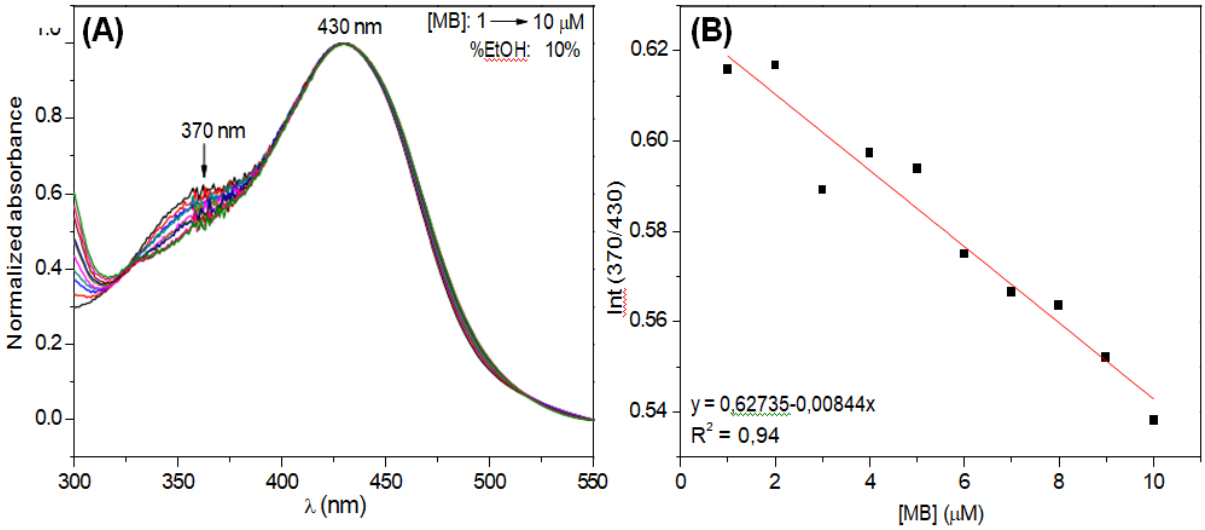

Figure 5: A) *UV-Vis spectroscopy of Curc (20 µM) and MB (1-10 µM) in a mixture of PBS buffer and ethanol (10%).* ***B)*** *Relative intensity of new blue-shift absorption band at 370 nm concerning monomer Curc band at 430 nm.*

Photochemical behavior

Singlet oxygen production by MB, Cur and MB-Cur complex was evaluated by the indirect method using uric acid (UA) as a quencher[10]. Figure 7 shows the effects of visible irradiation on the absorption spectra of compounds in the presence of UA, and the emission spectra of LEDs used as the light source. It is possible to see that blue LED irradiation (peak at 450 nm) overlaps the main absorption band of Curc, while red LED (632 nm) overlaps the main band of MB.

The blue LED irradiation practically did not induce any changes in the absorption band of UA as for isolate Curc as MB-Curc complex, indicating no production of singlet oxygen by both samples (Figure 6A and C). Studies have shown that Curc can produce both singlet oxygen and radical species, but when Curc is irradiated by light sources in the continuous mode (CW) a higher singlet oxygen production is observed [11]. However, this production is dependent on the environmental conditions[12] and appropriate formulations are required[13]. In the conditions used in the present work, no reactive oxygen species were produced which explains the negligible UA photodegradation observed.

Photobleaching of Curc was observed in both samples (Curc and complex) when irradiated by a blue LED. However, the photodegradation rate was higher for MB-Curc complex (4.01×10^{-3} s^{-1}, Figure 6A) than isolate Curc (1.63×10^{-3} s^{-1}, Figure 6C). On the other hand, MB in the complex kept stable when irradiated with blue LED. Photobleaching of Curc, observed for MB-Curc complex concerning Curc solution, suggests another Curc photodegradation mechanism should be involved such as electron transfer between complex species.

Red LED irradiation of MB solution confirms the singlet oxygen production by reduction of the absorption band of UA at 291 nm (Figure 6D). However, for MB-Curc complex, the red irradiation provided a series of photochemical processes in the complex (Figure 6B). In addition to the reduction of the UA absorption band, Curc was photodegraded while the MB absorption band undergoes a slight increase. The increase in the MB band suggests that irradiation could release MB from the MB-Curc complex (Figure 1). Furthermore, the Curc photodegradation constant was about 3.5 times higher (1.41×10^{-2} s^{-1}, Figure 6B) than obtained using blue LED irradiation (4.01×10^{-3} s^{-1}, Figure 6A).

MB-Curc presented a Φ_Δ of 0.52 ± 0.03, which was the same value found for isolate MB solution (0.52)[14]. These results suggest that the higher Curc photodegradation is not due to an increase of the reactive oxygen species

generation in solution, but is probably due to an electron transfer mechanism between MB and Curc.

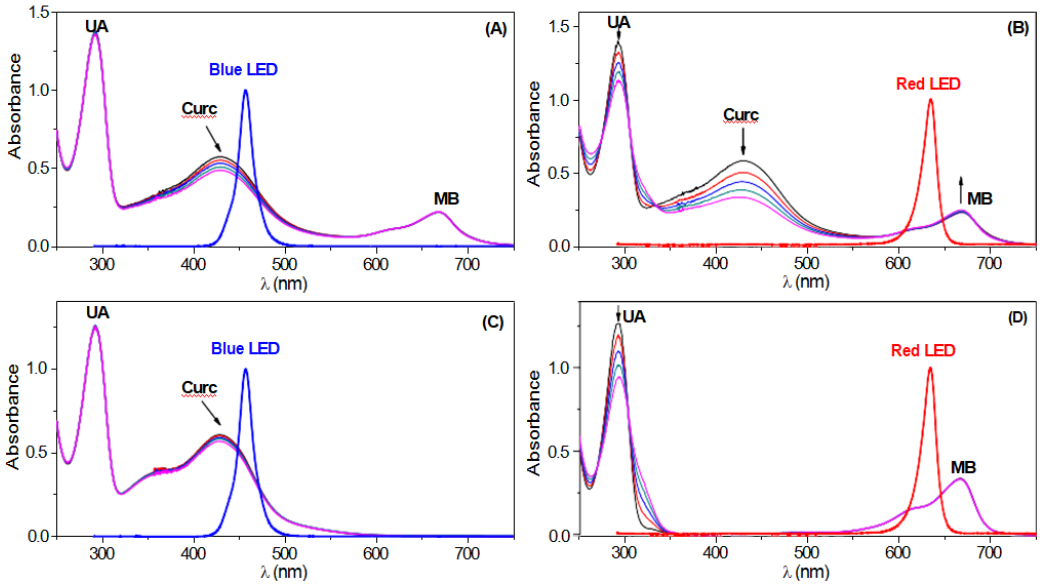

Figure 6: *UV-Vis spectroscopy data recorded every 10 seconds of irradiation for A) MB-Curc complex irradiated with blue LED, B) MB-Curc complex irradiated with red LED, C) Curc solution irradiated with blue LED, and D) MB solution irradiated with red LED. Normalized emission spectra of ligth sources are presented: a blue LED (peak at 450 nm) and a red LED (632 nm).*

Vascular effect of the methylene blue-Curc complex

The vascular response of CAM was calculated by the ratio between the number of black pixels and total pixels of the processed image normalized by the vascular network immediately before treatment. The control groups, solvent and red light, did not present any effect on blood vessels (data not shown). On the other hand, the other groups showed different vascular effects over time (Figure 7).

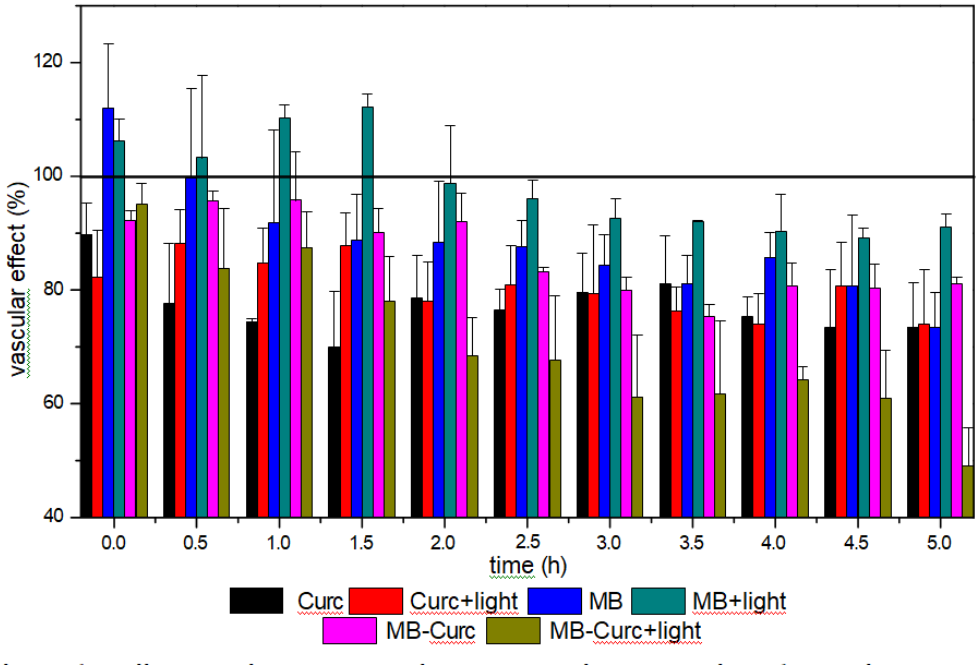

Figure 7: *Evolution of vascular effect as a function time of monitoring after 5 min of irradiation for: curcumin in the dark (Curc); curcumin under irradiation (Curc + red light); methylene blue in dark (MB); methylene blue under irradiation (MB + red light); MB- Curc complex in dark (MB-Curc); and MB-Curc complex under irradiation (MB-Curc + red light). The studied concentrations were: [MB] = 100 μM, [Curc] = 400 μM and for [MB-Curc]: [MB] = 100 μM and [Curc] = 400 μM, respectively.*

Regarding the curcumin groups (Curc and Curc+light, Figure 7), CAM vasoconstriction was observed in the dark and after irradiation with red LED. In this case, vasoconstriction cannot be attributed to irradiation, since: (i)

the Curc absorbs in spectral range (320 to 550 nm) different (Fig. 1) of LED emission (570 to 670 nm); (ii) there is no significant difference between the dark and light treatments results, and (iii) no reactive oxygen species were observed when irradiated with red and blue LEDs. Therefore, the intrinsic antiangiogenic activity of curcumin is most likely responsible for the vasoconstriction effect observed in these groups.

Concerning the methylene blue groups (MB and MB+light, Figure 7), it was also observed CAM vasoconstriction in the dark and after irradiation. In the dark, MB causes initial vasodilation followed by a vasoconstrictor effect that reaches a value close to 25% after 5 h of monitoring. This vasoconstriction effect of MB in the dark was previously reported in the literature, and it was attributed to the inhibition of NO synthase enzymatic activity.[15–17] Under irradiation conditions, is observed initially vasodilation (up to 2 hours after irradiation) followed by vasoconstriction (10%) at the end of monitoring (after 5 h). This effect had already been described for Photoditazine® and was attributed to ischemia of superficial blood vessels due to high oxidative stress, resulting in increased blood flow from internal microvessels.[18]

For the MB-Curc complex groups (MB-Curc, MB-Curc+light), the maximum vasoconstriction in the dark was 20%. No statistically significant difference among the vasoconstriction of MB-Curc complex and the other experiments performed in dark (Curc and MB) was observed. After irradiation, the MB-Curc complex group presented a higher reduction of the vascular network (50% of vasoconstriction). This result can be explained based on a synergistic effect between the photodynamic activities of singlet oxygen generated by the MB and the antiangiogenic activity of curcumin. In addition, it was not observed increase of the vascular effect in the first 2 hours of monitoring after irradiation of MB- Curc complex, suggesting that the complex avoided the ischemia of superficial blood vessels induced by the oxidative stress of the PDT.

Curc and MB present different affinities in the cell environment, Curc has a great affinity for the cell membrane due to its high lipophilicity,[19] while MB is positively charged and binds to negatively charged parts of the cells, such as mitochondria.[20] Because of this, the vasoconstrictor effects of these species are performed at different active sites since the curcumin inhibits VEGF and its VEGFR receptors[21] and methylene blue inhibits NO synthase.[15] However, it is probable that it persists in the cellular environment since i) failure to observe the synergistic effect of MB and Curc in the dark and ii) the synergistic effect of photodynamic therapy for MB and antiangiogenic effect of Curc under irradiation.

CONCLUSION

Although methylene blue (MB) and curcumin (Curc) have been employed as photosensitizers agents in photodynamic applications, in the present work we obtained a supramolecular structure (MBCurc). The assembly was formed in a molar ratio of 1:4 in an aqueous solution, reduced the aggregation tendency of isolated compounds, increased the stability of curcumin in solution, without affecting the singlet oxygen quantum yield by methylene blue, and presented a high vascular effect. Under irradiation, a vasoconstriction was 50% was observed after 5 h of monitoring. It was attributed to the synergistic effect of the photodynamic activity of MB with the antiangiogenic of curcumin. The excellent vascular response of the MB-Curc makes it a potential candidate for use in cancer treatments by photodynamic antiangiogenic therapy. It is important to note that these compounds are inexpensive, non-toxic, and, in the case of curcumin, a natural product.

ACKNOWLEDGEMENTS

The authors gratefully acknowledge financial support from Fundação de Amparo à Pesquisa do Estado de Goiás (FAPEG); Conselho Nacional de Desenvolvimento Científico e Tecnológico (CNPq); Fundação de Amparo à Pesquisa do Estado de São Paulo (FAPESP); Coordenação de Aperfeiçoamento de Pessoal de Nível Superior (CAPES)

REFERENCES

[1] K. Ichikawa, Y. Takeuchi, S. Yonezawa, T. Hikita, K. Kurohane, Y. Namba, N. Oku, *Cancer Lett.* 2004, *205*, 39–48.
[2] L. M. Sherwood, E. E. Parris, J. Folkman, *N. Engl. J. Med.* 1971, *285*, 1182–1186.
[3] N. S. Vasudev, A. R. Reynolds, *Angiogenesis* 2014, *17*, 471–494.
[4] G. P. Nagaraju, S. Zhu, J. E. Ko, N. Ashritha, R. Kandimalla, J. P. Snyder, M. Shoji, B. F. El-Rayes, *Cancer Lett.* 2015, *357*, 557–565.
[5] A. Weiss, J. R. van Beijnum, D. Bonvin, P. Jichlinski, P. J. Dyson, A. W. Griffioen, P. Nowak-Sliwinska, *J. Cell. Mol. Med.* 2014, *18*, 480–491.

[6] E. Cielen, A. Tahri, K. Ver Heyen, G. J. Hoornaert, F. C. De Schryver, N. Boens, *J. Chem. Soc. Perkin Trans. 2* 1998, 1573– 1580.
[7] E. Pfeiffer, S. Höhle, A. M. Solyom, M. Metzler, *J. Food Eng.* 2003, *56*, 257–259.
[8] B. Zebib, Z. Mouloungui, V. Noirot, *Bioinorg. Chem. Appl.* 2010, *2010*, 1–8.
[9] P. J. Gonçalves, N. M. Barbosa Neto, G. G. Parra, L. De Boni, L. P. F. Aggarwal, J. P. Siqueira, L. Misoguti, I. E. Borissevitch, S. C. Zílio, *Opt. Mater. (Amst).* 2012, *34*, 741–747.
[10] P. J. Gonçalves, F. C. Bezzerra, A. V. Teles, L. B. Menezes, K. M. Alves, L. Alonso, A. Alonso, M. A. Andrade, I. E. Borissevitch, G. R. L. Souza, B. A. Iglesias, *J. Photochem. Photobiol. A Chem.* 2020, *391*, 112375.
[11] L. S. Sampaio, S. R. de Annunzio, L. M. de Freitas, L. O. Dantas, L. de Boni, M. C. Donatoni, K. T. de Oliveira, C. R. Fontana, *Photodiagnosis Photodyn. Ther.* 2020, *31*, 101925.
[12] C. F. Chignell, P. Bilskj, K. J. Reszka, A. G. Motten, R. H. Sik, T. A. Dahl, *Photochem. Photobiol.* 1994, *59*, 295–302.
[13] L. M. Ailioaie, C. Ailioaie, G. Litscher, *Pharmaceutics* 2021, *13*, 1562.
[14] B. R. Rabello, A. P. Gerola, D. S. Pellosi, A. L. Tessaro, J. L. Aparício, W. Caetano, N. Hioka, *J. Photochem. Photobiol. A Chem.* 2012, *238*, 53–62.
[15] B. Mayer, F. Brunner, K. Schmidt, *Biochem. Pharmacol.* 1993, *45*, 367–374.
[16] M. Rey-Funes, I. M. Larrayoz, J. C. Fernández, D. S. Contartese, F. Rolón, P. I. F. Inserra, R. Martínez-Murillo, J. J. López- Costa, V. B. Dorfman, A. Martínez, C. F. Loidl, *Am. J. Physiol. Integr. Comp. Physiol.* 2016, *310*, R1011–R1019.
[17] N. Zacharakis, P. Tone, C. S. Flordellis, M. E. Maragoudakis, N. E. Tsopanoglou, *J. Cell. Mol. Med.* 2006, *10*, 493–498.
[18] H. H. Buzzá, L. V. Silva, L. T. Moriyama, V. S. Bagnato, C. Kurachi, *J. Photochem. Photobiol. B Biol.* 2014, *138*, 1–7.
[19] H. Tsuchiya, *Molecules* 2015, *20*, 18923–18966.
[20] C. S. Oliveira, R. Turchiello, A. J. Kowaltowski, G. L. Indig, M. S. Baptista, *Free Radic. Biol. Med.* 2011, *51*, 824–833.
[21] A. E. Gururaj, M. Belakavadi, D. A. Venkatesh, D. Marmé, B. P. Salimath, *Biochem. Biophys. Res. Commun.* 2002, *297*, 934–942.

DOI 10.24412/cl-37136-2023-1-47-52

CYTOTOXICITY OF *SENNA DIDYMOBOTRYA* LEAVES GREEN- SYNTHESIZED SILVER NANOPARTICLES AND PHOTOTHERAPY AGAINST A375 MELANOMA CELLS

MEHAK ZAHRA[1], HEIDI ABRAHAMSE[1], BLASSAN P. GEORGE [1*]

[1]*Laser Research Centre, Faculty of Health Sciences, University of Johannesburg, Doornfontein, South Africa*

[*]E-mail: blassang@uj.ac.za

ABSTRACT

Cancer is a term used to describe a collection of illnesses where the cells within the body undergo unregulated growth and multiplication. It is also worth noting that cancerous cells have the potential of entering the metastatic phase and this allows them of invading adjacent body organs. Currently, there are at least five known conventional treatment modalities for cancer treatment. However, these therapies have been reported of playing a significant role in the induction of tumor recurrence. To address this critical issue, this study anti-proliferative effects of green synthesized silver nanoparticles (AgNPs). The A375 melanoma cell line was employed as the experimental model, and a range of AgNPs concentrations (2, 4, 8, 16 and 32 µg/mL) was applied. Subsequently, the treated cells were subjected to irradiation using a 525 nm diode laser, at a light dose of 10 J/cm², and the morphological changes in cells were observed using a light inverted microscope. Collectively, the results unveiled a dose-dependent reduction in cell proliferation in response to the AgNPs treatment. Taken together, the findings from this study suggests that green-synthesized AgNPs poses significant therapeutic properties as a novel therapeutic approach for the treatment of different forms of cancer, thus offering an effective and eco-friendly therapeutic approach in cancer therapy. The schematic representation of the adopted synthesis and treatment methodology as depicted in the graphical abstract Figure 1.

Graphical abstract

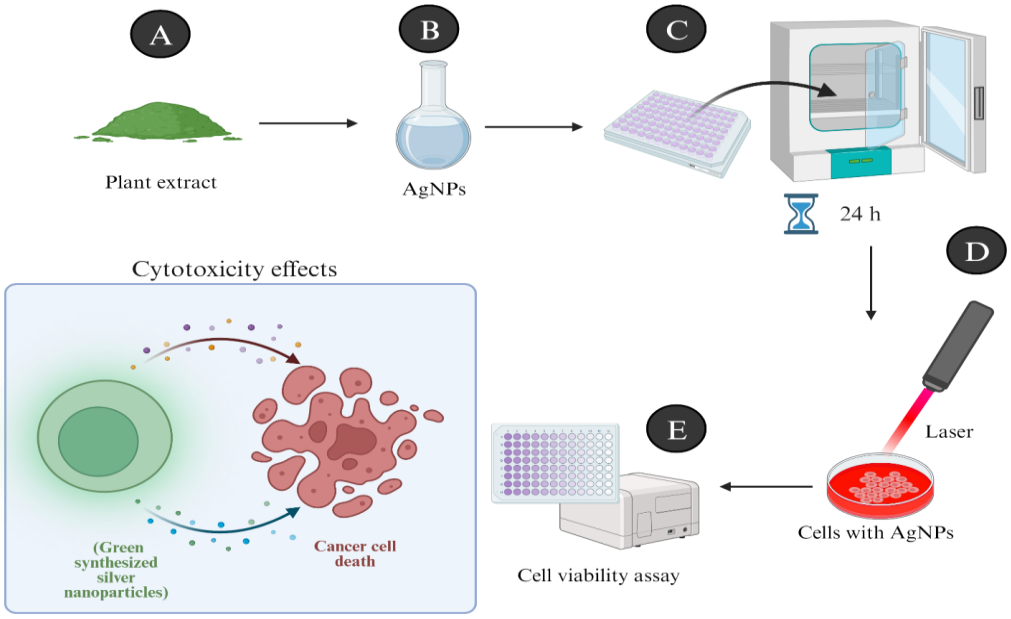

Figure 1: *A general overview of the methodology adopted for the present study. Ethanol leaf plant extraction using a Soxhlet extractor (A), wet chemistry synthesis of AgNPs using the "bottom-up approach (B), 24 h incubation post-treatment (C), 525 nm laser irradiation (D) and cell viability analysis (E).*

INTRODUCTION

Melanoma of the skin presents as a metastatic condition known for its challenging resistance to treatment, and its global incidence has notably surged in recent years. A comprehensive understanding of the initiation, advancement, and spreading of tumors is imperative to address the existing knowledge gaps in melanoma biology. Tumors can manifest on various body surfaces, including the skin, ocular membranes, retroperitoneal space, parenchymatous organs, and various mucosal areas [1]. However, a significant majority, approximately 95%, of all melanoma cases are primarily found on the skin. It's noteworthy that despite their common cellular origin, melanomas should be regarded as a diverse group of diseases rather than a single tumor entity, given their distinct causes, development processes, behaviors, and progression patterns, which can vary based on their location [2]. Despite substantial advancements in comprehending the mechanisms driving melanoma development and progression, there remains a need for deeper mechanistic insights and the exploration of alternative therapeutic strategies [3]. Most importantly, the selection of these treatments depends on the stage and advancement of the tumor. To mitigate some of these adverse effects, numerous researchers are actively investigating fresh therapeutic approaches, such as the integration of photodynamic therapy (PDT) with chemotherapy drugs and phototherapy (PTT). Photodynamic therapy (PDT) represents an emerging treatment modality that employs the use of non-ionizing radiation to induce tumor cell death in different types of cancer [4]. This therapy entails the administration or intravenous delivery of photosensitive drugs, commonly referred to as photosensitizers (PSs), to areas of the body affected by the condition, such as the skin. The fundamental concept underlying PDT relies on the molecular interactions between these photosensitizers, which tend to preferentially accumulate within specific locations of tumor cells, and laser light in conjunction with the presence of molecular oxygen (O_2). This interaction subsequently triggers the production of cytotoxic reactive oxygen species (ROS) [5]. This study explores the cytotoxic effects of eco-friendly green synthesized AgNPs against A375 melanoma cells using a 525 nm diode laser a light dose of $10J/cm^2$. Our results demonstrated a clear dose- dependent reduction in cell proliferation. As the concentration of the treatment agent increased, we observed a corresponding decrease in cell growth. Alongside the decrease in cell proliferation, we also noted dose-dependent morphological alterations. These changes in cell appearance were consistent with the reduction in cell growth, suggesting a direct correlation. The dose-dependent reduction in cell proliferation and associated morphological changes suggest that the treatment, involving green synthesized silver nanoparticles and phototherapy, holds promise as a potential therapeutic approach for cancer treatment.

METHODS AND METERIALS

The plant *Senna didymobotrya* leaves were gathered within the campus premises of the University of KwaZulu-Natal. The plant's leaves were first cleansed and air-dried in the shade. Subsequently, the dried leaf material was finely ground into a powder using a blender. Following this step, the powdered plant material underwent an extraction process using a Soxhlet extractor. This extraction was performed with the aim of synthesizing green silver nanoparticles (AgNPs). To summarize, approximately 10 mL of *Senna didymobotrya* leaf extract stock solution was introduced into a 1 mM AgNO3 solution dissolved in 90 mL of deionized water. This mixture was agitated at a rate of 150 rpm at room temperature. After 6 hours, a noticeable change in the solution's color was observed, indicating a successful reaction. Subsequently, the homogenous mixture was subjected to centrifugation at 12,000 rpm for 10 minutes. The stock solution, which was initially prepared in 0.5% dimethyl sulfoxide (DMSO), was stored at -20°C for future experiments. To confirm the formation of silver nanoparticles (AgNPs), UV-vis is spectroscopy was employed. The UV/Vis analysis covered a spectral range of 300-800 nm and was conducted using a Jenway Genova spectrophotometer.

Figure 2: *Senna Didymobotrya – a visual representation of the plant specimen*

A375 melanoma cells were cultivated in Dulbecco's Modified Eagle's medium (DMEM) supplemented with 10% (v/v) fetal bovine serum (FBS), 0.1% (v/v) penicillin-streptomycin, and 0.1% (v/v) amphotericin-β. These cells were maintained at a temperature of 37°C in an environment with 5% CO_2. For in vitro investigations, a seeding density of 3 x 10^5 cells/mL was used for cell plating, and 3.4 cm² culture plates were employed. In this study, two experimental groups were utilized: one comprising cell that did not undergo PtT treatment (referred to as "dark toxicity"), and the other consisting of cells subjected to PTT. Both groups were treated with AgNPs and incubated for 24 hours post-treatment. Various concentrations were applied, encompassing AgNPs (2, 4, 8, 16, and 32 µg/mL) and mediated PTT (2, 4, 8, 16, and 32 µg/mL).

Ultraviolet-visible (UV-vis) spectroscopy is a scientific method that utilizes light to investigate the characteristics and behaviors of substances within the UV-vis range of the electromagnetic spectrum. This technique offers valuable insights into phenomena such as electronic transitions in various molecules and their absorption characteristics. To analyze the absorbance spectra of both the plant extract and the silver nanoparticles synthesized through environmentally friendly methods, we employed UV-vis emission spectroscopy. We utilized a UV-Vis Spectrophotometer, specifically the Genova 7315 Life Science Spectrophotometer from JENWAY located at the University of Johannesburg, Laser Research Centre. This instrument was used to measure absorption across the spectral range of 300-800 nm at rtp,

Morphological changes were investigated using an Olympus CKX 41 inverted light microscope, which was equipped with an Olympus C5060-ADUS digital camera. The assessment of viable and non-viable A375 cells 24 hours after treatment with AgNPs and AgNPs-mediated PTT. Briefly, cells were subjected to a thrice wash by the using HBSS prior to visualization.

In the current study, we employed the CellTiter-Glo® ATP luminescence assay kit (Promega, G968A). To outline the procedure briefly, approximately 50 µL of a cell suspension was combined with an equal volume of reconstituted ATP reagent. This mixture was thoroughly mixed and allowed to incubate for 10 minutes at room temperature and atmospheric pressure. Following the incubation period, the resulting homogenous colorimetric mixture was then subjected to ATP luminescence measurement using the PerkinElmer VICTOR Nivo™ instrument.
The experiments were conducted in triplicate (n=3). Data analysis was carried out using IBM SPSS version 27 software to assess the mean differences and determine the statistical significance between the control and experimental groups. The mean values were presented as mean ± standard error (SE), and statistical significance was denoted as follows: $p < 0.001$ (a).

RESULTS AND DISCUSSION

To investigate the absorbance spectra of both the plant extract and the green synthesized AgNPs by *Senna didymobotrya.* we utilized UV-vis emission spectroscopy. The results obtained from this analysis revealed a prominent surface plasmon resonance peak at approximately 517 nm, as illustrated in Figure 3A, whereas the plant extract has no peak in the therapeutic window of PTT. The UV-vis spectrometry results in our study align closely with those reported by Sytu *et al.*, [7].

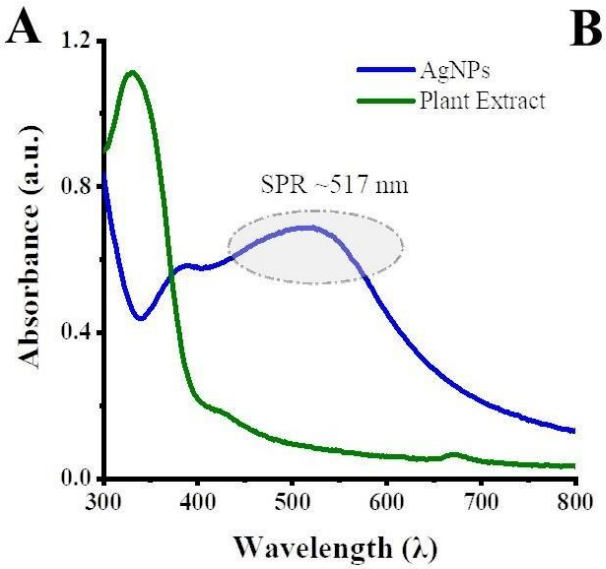

NAME	PARAMETERS
Drug	AgNPs
Light Source	Diode Laser
Wavelength	525 nm
Wave Emission	Continuous
Spectrum	Blue (Visible)
Fluency	10 J/cm^2

Figure 3: *UV-vis spectrometry of plant extract (green colour) and AgNPs (blue colour) in the spectra range of 300-800 nm (A) and laser parameters (B).*

The morphology of both untreated and treated A375 cells is depicted in Figure 4A. After a 24-hour post-treatment period, an analysis of morphological changes in A375 melanoma cells was conducted. When contrasted with the control group, cells subjected to laser light exhibited no significant morphological changes observed. However, when treated cells exposed to dark toxicity and those treated with the 525 nm laser in combination with AgNPs exhibited dose-dependent alterations in cellular morphology. Furthermore, a dose-dependent reduction in ATP proliferation was observed in both the dark toxicity and photothermal therapy (PTT) groups. Particularly, alterations in cell morphology were evident in A375 cells treated with AgNPs and AgNPs-mediated PTT. Even more intriguingly, our findings closely resemble those of another study conducted by Khoza *et al.*, [8].

The energy levels in both untreated and treated A375 cells were assessed by measuring ATP luminescence levels. In cells subjected to AgNPs-mediated PTT treatment, a dose-dependent reduction in cell proliferation was evident, as depicted in Figure 4B. A simple linear regression analysis demonstrated a negative correlation between relative light units and concentration. This observation strongly indicates that as the concentration increases, the relative light units (%) decrease. However, it's noteworthy that ATP levels were found to be higher in A375 cells that received laser treatment alone. In research conducted by Sriram and colleagues [9], it was demonstrated that silver nanoparticles (AgNPs) possess the ability to differentiate between cancerous and healthy cells. Moreover, they exhibited the capability to trigger anti-tumor effects through the activation of caspase 3, a group of cysteine proteases that play crucial roles in cellular apoptosis pathways. This activation, in turn, resulted in a regenerative response and a subsequent reduction in tumor volume [10]. In a prior study that closely resembles our own research, it was observed that the application of laser irradiation alone or silver nanoparticles (AgNPs) alone did not result in a significant decrease in cell proliferation in the tested cell lines. However, when both laser irradiation and AgNPs were combined in phototherapy (PTT), their synergistic effects led to a notable reduction in cell proliferation within the cancer cell lines [10].

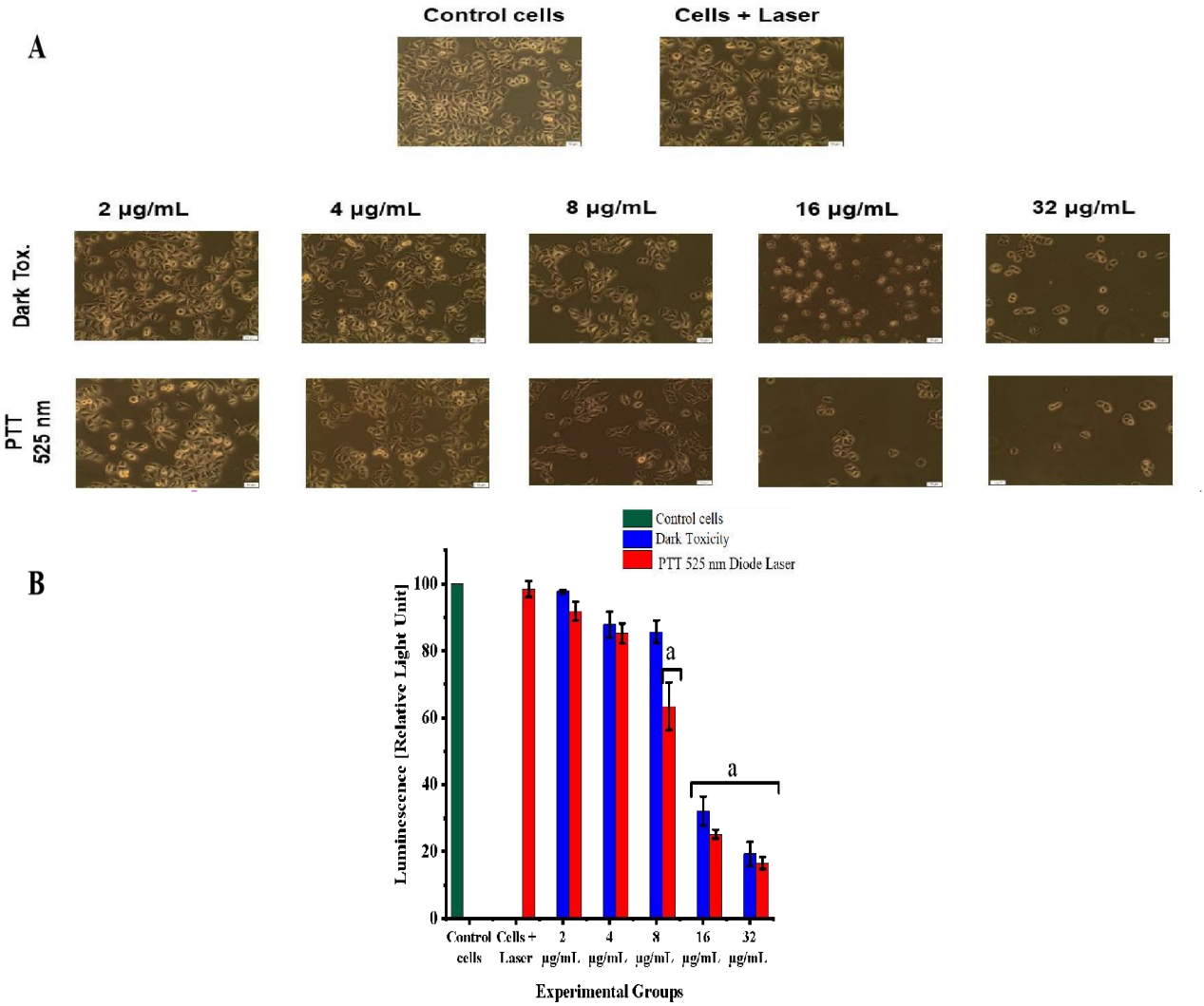

Figure 4: *Morphological (A) and ATP Viability analysis (B) of A375 melanoma cells 24 h post treatment. When compared to control cells, cells treated with laser light did not any significant alterations in morphology. Dark toxicity and 525 nm laser treated cells incubated with AgNPs displayed a dose dependent change in cellular morphology (A) (10X magnification). A dose dependent decrease in ATP viability was observed in both dark toxicity and PTT (B). Significant differences depicted in the graph are denotated as p < 0.001(a).*

CONCLUSION

In conclusion, our study focused on evaluating the anti-proliferative effects of green synthesized AgNPs in combination with phototherapy against A375 melanoma cells. In our investigation, we used AgNPs at varying concentrations in conjunction with phototherapy using a 525 nm diode laser with a light dose of 10 J/cm². The morphological changes observed through light microscopy demonstrated a dose-dependent reduction in cell proliferation following AgNPs treatment. This promising outcome suggests that green-synthesized AgNPs hold significant therapeutic potential as a novel approach for combating various forms of cancer. Our findings point toward the exciting prospect of utilizing green synthesized AgNPs as an effective and eco-friendly therapeutic strategy in cancer treatment. By leveraging the combination of AgNPs and phototherapy, we may be moving closer to a more efficient and targeted approach to combatting cancer, ultimately offering hope for improved outcomes in cancer therapy. Further research and clinical studies are warranted to validate and expand upon these promising results.

ACKNOWLEDGEMENTS

The authors sincerely thank the South African Research Chairs initiative of the Department of Science and Technology and the National Research Foundation (NRF) of South Africa, Global Excellence Stature (GES) for doctoral bursary, South African Medical Research Council (SAMRC), University Research Committee (URC), and Laser Research Centre (LRC), University of Johannesburg. The research reported in this review

article was supported by the South African Medical Research Council (SAMRC) through its Division of Research Capacity Development under the Research Capacity Development Initiative from funding received from the South African National Treasury. The content and findings reported/illustrated are the sole deduction, view, and responsibility of the researchers and do not reflect the official position and sentiments of the SAMRC.

FUNDING

This work is based on the research funded by the South African Research Chairs initiative of the Department of science and technology and National Research Foundation (NRF) of South Africa (Grant No. 98337), South African Medical research Council (Grant No. SAMRC EIP007/2021), as well as grants received from the NRF Research Development Grants for Y-Rated Researchers (Grant No: 137788), University Research Committee (URC), African Laser Centre (ALC), University of Johannesburg, and the Council for Scientific Industrial Research (CSIR)-National Laser Centre (NLC).

REFERENCES

[1] Avram, S.; Coricovac, D.-E.; Pavel, I.Z.; Pinzaru, I.; Ghiulai, R.; Baderca, F.; Soica, C.; Muntean, D.; Branisteanu, D.E.; Spandidos, D.A.; et al. Standardization of A375 Human Melanoma Models on Chicken Embryo Chorioallantoic Membrane and Balb/c Nude Mice. *Oncol Rep* **2017**, *38*, 89–99, doi:10.3892/or.2017.5658.

[2] Potrony, M.; Badenas, C.; Aguilera, P.; Puig-Butille, J.A.; Carrera, C.; Malvehy, J.; Puig, S. Update in Genetic Susceptibility in Melanoma. *Ann Transl Med* **2015**, *3*, 210, doi:10.3978/j.issn.2305-5839.2015.08.11.

[3] Chalkiadaki, G.; Nikitovic, D.; Katonis, P.; Berdiaki, A.; Tsatsakis, A.; Kotsikogianni, I.; Karamanos, N.K.; Tzanakakis, G.N. Low Molecular Weight Heparin Inhibits Melanoma Cell Adhesion and Migration through a PKCa/JNK Signaling Pathway Inducing Actin Cytoskeleton Changes. *Cancer Lett* **2011**, *312*, 235–244, doi:10.1016/j.canlet.2011.08.016.

[4] Wang, K.; Yu, B.; Pathak, J.L. An Update in Clinical Utilization of Photodynamic Therapy for Lung Cancer. *J Cancer* **2021**, *12*, 1154–1160, doi:10.7150/jca.51537.

[5] Li, J.; Meng, X.; Deng, J.; Lu, D.; Zhang, X.; Chen, Y.; Zhu, J.; Fan, A.; Ding, D.; Kong, D.; et al. Multifunctional Micelles Dually Responsive to Hypoxia and Singlet Oxygen: Enhanced Photodynamic Therapy via Interactively Triggered Photosensitizer Delivery. *ACS Appl Mater Interfaces* **2018**, *10*, 17117–17128, doi:10.1021/acsami.8b06299.

[6] Jaca, T.; Condy, G. Senna Didymobotrya (Fabaceae: Caesalpinioideae): Northwestern, East and Southern Africa, and Madagascar.
Flowering Plants of Africa **2017**, *65*, 68–75.

[7] Sytu, M.R.C.; Camacho, D.H. Green Synthesis of Silver Nanoparticles (AgNPs) from Lenzites Betulina and the Potential Synergistic Effect of AgNP and Capping Biomolecules in Enhancing Antioxidant Activity. *BioNanoSci.* **2018**, *8*, 835–844, doi:10.1007/s12668-018-0548-x.

[8] Khoza, P.; Ndhundhuma, I.; Karsten, A.; Nyokong, T. Photodynamic Therapy Activity of Phthalocyanine-Silver Nanoparticles on Melanoma Cancer Cells. *Journal of Nanoscience and Nanotechnology* **2020**, *20*, 3097–3104, doi:10.1166/jnn.2020.17398.

[9] Sriram, M.I.; Kanth, S.B.M.; Kalishwaralal, K.; Gurunathan, S. Antitumor Activity of Silver Nanoparticles in Dalton's Lymphoma Ascites Tumor Model. *International Journal of Nanomedicine* **2010**, *5*, 753–762, doi:10.2147/IJN.S11727.

[10] Mfouo-Tynga, I.; Hussein, A.E.-; Abdel-Harith, M.; Abrahamse, H. Photodynamic Ability of Silver Nanoparticles in Inducing Cytotoxic Effects in Breast and Lung Cancer Cell Lines. *International Journal of Nanomedicine* **2014**, *9*, 3771–3781.

DOI 10.24412/cl-37136-2023-1-53-54

ENHANCED PHOTODYNAMIC THERAPY

BUHONG LI [1,*], YI SHEN[2] AND XUEJIAO SONG[3]

[1]*School of Science, Hainan University, China*

[2]*Key Laboratory of OptoElectronic Science and Technology for Medicine of Ministry of Education, Fujian Normal University, China*

[3]*Key Laboratory of Flexible Electronics and Institute of Advanced Materials, Nanjing Technology University, China*

ABSTRACT

Photodynamic therapy (PDT), a minimally invasive therapeutic modality, utilizes photosensitizers (PSs) together with irradiation light of specific wavelength interacting with molecular oxygen in tissue to generate cytotoxic reactive oxygen species (ROS), thereby destroying malignant and nonmalignant diseases. Most recently, the applications of PDT have been extended to the treatment of anti-microbial infections, such as bacterial, fungal and virus. For clinical PDT, PS, light and oxygen are the three important components for effective photodynamic activity.

Firstly, several novel PSs, including C_{60}, black phosphorus, graphene quantum dots and PSs with aggregation-induced emission, have been developed to improve the quantum yield of singlet oxygen. The delivery efficiency of PSs has been improved by the different PS delivery strategies and the tumor-microenvironment-responsive release scheme. The absorption of PSs has been enhanced by organelle targeting and photochemical internalization, while the hypoxia resistance of PSs has been resolved through loading with oxygen carriers or oxygen-generating reactants. Moreover, the development of PSs with synergistic therapeutic function will be used to further enhance PDT efficacy.

Secondly, solar light, broad-spectrum lamps, lasers, light-emitting diodes (LEDs), X-ray sources, ultrasonic sources and *in vivo* self-excited light sources capable of bioluminescence, chemiluminescence and Cherenkov light, have been widely studied as PDT excitation sources. In clinical practice, LEDs and lasers are the most popular light sources. In particular, wearable, implantable, and disposable PDT light sources have greatly progressed through the development of inorganic LED array, flexible LEDs, and wireless driven LEDs. *In vivo* self-excited light source has been studied to avoid the absorption and scattering of light by biological tissues. Additionally, to ensure the oxygen supply during PDT treatment, new illumination schemes of light fractionation PDT and metronomic PDT have been proposed.

Moreover, oxygen carrier with strong oxygen storage capacity or the chemical reaction substance could be delivered to the target lesion for *in situ* oxygen generation, which is the most popular methods to enhance the oxygen supply for PDT. In addition, hypoxia-activated linkers or prodrugs have been applied to compensate for the low efficacy caused by hypoxia. Meanwhile, the reduction of oxygen consumption during PDT could be achieved by limiting certain oxygen-consuming intracellular chemical reactions or reducing oxygen dependence by using type I or type III PDT.

Finally, PDT has been combined with clinical surgery, radiotherapy, chemotherapy, photothermal therapy, sonodynamic therapy, magnetic hyperthermia and immunotherapy in order to improve the therapeutic efficacy. In addition, Multi-modes for synergistic treatment with PDT will be presented. Meanwhile, the simultaneous employment of two PSs targeting at different subcellular organelle also employed to improve PDT efficacy.

REFERENCES

[1] L Lin, X Song, X Dong, B Li. Nano-photosenitizers for enhanced photodynamic therapy. *Photodiagnosis and Photodynamic Therapy*. 2021, 36:102597.

[2] B Li, L Lilge. Introduction to the special issue on enhanced photodynamic therapy. *Journal of Innovative Optical Health Sciences*. 2022, 15(4), 2202002.

[3] B Li, L Lilge. Special issue on enhanced photodynamic therapy: Part II. *Journal of Innovative Optical Health Sciences*. 2022, 15(6): 2202003.

[4] B Li, L Lin. Internal light source for deep photodynamic therapy. *Light: Science & Applications*. 2022, 11: 85.
[5] B Li, T Chen, L Lin, B Chen, H Qiu, Y Gu. Recent progress in photodynamic therapy: from fundamental research to clinical applications. *Chinese Jouranl of Lasers*. 2022, 49(5): 507101.
[6] J Zhu, A Jiao, Q Li, X Lv, X Wang, X Song, B Li, Y Zhang, X Dong. Mitochondrial Ca^{2+}-overloading by oxygen/glutathione depletion-boosted photodynamic therapy based on a $CaCO_3$ nanoplatform for tumor synergistic therapy. *Acta Biomaterialia*. 2022,137: 252-261.
[7] B Li and L Lin (2023) Enhanced photodynamic therapy. *In Biomedical Photonic Technologies* (Edited by M Z Zhang, S Jiang, B Li.), pp. 165–199. WILEY-VCH GmbH,Weinheim, Germany.

DOI 10.24412/cl-37136-2023-1-55-55

PHOTODYNAMIC INACTIVATION OF VEGETATIVE AND DORMANT FORMS OF THE CAUSATIVE AGENT OF TUBERCULOSIS *IN VITRO* AND INSIDE MACROPHAGES IN THE PRESENCE OF 5-AMINOLEVULINIC ACID.

M.O. SHLEEVA [1], I.A. LINGE [2], I.A. GLIGONOV [1], G.N. VOSTROKNUTOVA [1], A.S. APT [2], A.S. KAPRELYANTS[1], A.P. SAVITSKY [1]

[1]*A.N. Bach Institute of Biochemistry, Federal Research Center "Fundamentals of Biotechnology" of the Russian Academy of Sciences, Moscow, Russia*

[2]*Laboratory of Immunogenetics, Central Institute for Tuberculosis of the Russian Academy of Sciences, Moscow, Russia*

The problem of effective treatment of tuberculosis in the clinic is the prevalence of antibiotic-resistant strains of the pathogen *Mycobacterium tuberculosis* (Mtb). About a quarter of the world's human population is latently infected, due to the transition of Mtb to a dormant state. Known anti-tuberculosis drugs used in medical practice are not active against dormant Mtb. Antimicrobial photodynamic inactivation (aPDI) is one of the alternatives to antibiotic therapy that can inactivate bacteria, including those with extensive and multidrug resistance. A promising direction is the use of endogenous photosensitizers of mycobacteria, in particular porphyrins.

The aim of this work was to study approaches to stimulate the accumulation of endogenous porphyrins in the cells of the causative agent of tuberculosis and to evaluate the possibility of photoinactivation of vegetative and dormant forms of Mtb.

The dormant forms of Mtb contained 6 times more porphyrins compared to vegetative cells. In the presence of 5-aminolevulinic acid (ALA) in the growth medium, an 85-fold increase in the amount of porphyrins in dormant Mtb cells was observed. An unusual derivative of coproporphyrin, tetramethyl ester of coproporphyrin (CPMe4), has been identified in dormant forms of Mtb. The accumulated porphyrins in mycobacteria were presented in the form of water-soluble compounds (uroporphyrin, coproporphyrin) and tetramethyl esters of coproporphyrin and its Zn complexes. The synergistic action of zinc and magnesium (10 μM and 25 mM, respectively) led to an even greater increase in the production of porphyrins. Transcriptome analysis revealed an increase in the activity of a number of genes during cell growth in the presence of ALA, which is associated with the pathways of synthesis and metabolism of porphyrins and precorrins. Mycobacteria grown in the presence of ALA showed very high photosensitivity (about 99.99% of bacteria died) both *in vitro* and in macrophages. At the same time, the primary effect of light exposure was a sharp decrease in the activity of bacterial DPI reductase, down to zero.

Thus, successful photoinactivation *in vitro* and *ex vivo* of both metabolically active and dormant forms of the tuberculosis pathogen due to the accumulation of endogenous porphyrins when 5-aminolevulinic acid is added to the growth medium has been demonstrated. Data on the strategy of stimulating the synthesis of porphyrins and other fluorescent tetrapyrroles in mycobacteria have been obtained, which can later be used in the treatment of tuberculosis, including latent and multidrug-resistant tuberculosis, for the irradiation of the pathogen in order to prevent recurrence of this disease.

DOI 10.24412/cl-37136-2023-1-56-56

PHOTODYNAMIC FOR MICROBIOLOGICAL CONTROL AND BREAKDOWN OF RESISTANCE TO ANTIBIOTIC

VANDERLEI S. BAGNATO

Instituto de Fisica de São Carlos – Universidade de São Paulo – BRAZIL
Biomedical Eng. – Texas A&M University – College Station - Texas - USA

vander@ifsc.usp.br
http://cepof.ifsc.usp.br

ABSTRACT

The use of photodynamic action to combat microorganisms is a well-established field of great importance for microbiological control, including antibiotic-resistant bacteria. In situations where the basic elements for the relationship of the photodynamic annihilation of microorganisms can be applied: light, oxygen and photosensitization, the treatment with photodynamic reaction for microbial elimination works very well. In cases where these elements cannot be assured, we still depend on the action of the antibiotic. In this work, we demonstrate the use of oxidative stress caused by photodynamic action to reduce antibiotic resistance in resistant bacteria, allowing the antibiotic action to be reestablished.

Many different aspects of this demonstration and experimental realization are presented in this work. That includes the possibility to detect spectroscopically the bacteria resistance previously to treatment. This work has the participation of K. Blanco, T. Quatrine, J. M. Soares, Claudia P. Patino . Support from FAPESP, CNPq - Brazil and program CEPRIT – Texas – USA.

REFERENCES

[1] J. M.Soares et al – Physiochemical mechanisms of bacterial response in photodynamic potentiation of antibiotic effecs – Scientific Report 2022, 12, 2146

[2] J. A. Willis et al – Breaking down antibiotic resistance in methicillin-resistant S. Aureus – Proceeding of the National Academy of Science – PNAS 2022, 119, 2208378119

DOI 10.24412/cl-37136-2023-1-57-57

THE FORCES OF INTERACTION OF RED BLOOD CELLS AND ENDOTHELIUM: A REVISED STUDY BY LASER TWEEZERS

PETR B. ERMOLINSKIY[1]*, MATVEY K. MAXIMOV[1], ANDREI E. LUGOVTSOV[1], OLGA N. SCHEGLOVITOVA[2] AND ALEXANDER V. PRIEZZHEV[1]

[1]Faculty of Physics, Lomonosov Moscow State University, Moscow, Russia
[2]N.F. Gamaleya National Research Center for Epidemiology and Microbiology, Moscow, Russia
** Correspondence:*
peter.ermolinskiy@biomedphotonics.ru

ABSTRACT

Blood microbiology is essentially determined by the properties of blood plasma and the interaction between blood cells, i.e., the aggregation of red blood cells (RBCs), the interaction between different blood cells and endothelium, etc. [1]. Endothelial cells do not only act as an insulating layer between blood and tissues, but also play an important role in controlling the blood flow and influence blood cell properties, e.g., RBCs aggregation. RBCs can reversibly interact with each other under low shear stress forces forming linear and more complex structures. RBCs aggregation is mainly responsible for the non-Newtonian behavior of blood and regulates the microcirculation of blood in human body.

In this work, we studied the interaction between the endothelial monolayer and RBCs. Previously, we studied the interaction between single endothelial cells and single RBCs. However, a single endothelial cell and an endothelial cell in a monolayer have different properties.

The aim of this study was to investigate the interaction between endothelium cells in a monolayer and RBCs of healthy volunteers at different concentrations of fibrinogen at the level of individual cells in vitro. Laser tweezers were used to manipulate individual cells without mechanical contact, as well as to measure the forces of their interaction [2].

Blood for the study was drawn from the cubital veins of four healthy donors. Endothelial cells were grown at 37°C (CO_2 environment) on round glass slides and formed a cell monolayer. The blood sample was a small amount of blood and autologous serum with added fibrinogen under the concentrations of 0, 2, 4, 6, 8 mg/ml. The blood sample was placed in a microcuvette with endothelium isolated from the air and the interaction forces between the cells were measured.

It was shown that the interaction force between RBCs and endothelial cells increases with fibrinogen concentration and reaches the saturation level of 4 pN at the concentration of 4 mg/ml. This force value is comparable with the interaction forces between individual RBCs in autological plasma.

This work was supported by the Development program of the Interdisciplinary Scientific and Educational School of Lomonosov Moscow State University «Photonic and Quantum Technologies. Digital medicine».

REFERENCES

[1] Furst E.M., Squires T.M. “Microrheology” Oxford University Press, United Kingdom (2017).
[2] Kapkov A.A., Semenov A.N., Ermolinskiy P.B., Lugovtsov A.E., Priezzhev A.V. “Forces of RBC interaction with single endothelial cells in stationary conditions: Measurements with laser tweezers”. Journal of Innovative Optical Health Sciences. 14(5), 2142005 (2021).

DOI 10.24412/cl-37136-2023-1-58-62

PHOTODYNAMIC THERAPY ENHANCES THE BERBERINE INDUCED CYTOTOXICITY IN LUNG CANCER CELLS

PAROMITA SARBADHIKARY[1], BLASSAN P GEORGE[1] AND HEIDI ABRAHAMSE[1]

Laser Research Centre, Faculty of Health Sciences, University of Johannesburg, South Africa

paromitas@uj.ac.za

ABSTRACT

Even with a thorough understanding of the molecular causes of cancer and enormous strides in cancer therapy and diagnosis, cancer still poses a serious health risk and it is the second leading cause of death worldwide. According to the GLOBOCON report 2020, lung cancer continues to be the second most common cancer diagnosed, with an estimated 2.3 million new cases worldwide. According to reports, the global incidence rate of lung cancer in people of both sexes is 11.4% across all other cancer types with the highest mortality rate of 18% (1). Additionally, lung cancer is the deadliest disease due to its high metastatic potential, whereby nearly 70% of patients start receiving their diagnosis and treatment in advanced stages III or IV of the disease (2). Phytochemicals present a promising alternative to conventional therapies for improving treatment effectiveness in lung cancer patients, by overcoming the drawbacks of severe induced side effects and induction of resistance [3].

Among several different potent and safer antineoplastic phytochemicals, Berberine (BBR) (Fig. 1) is a phytochemical that has been used in traditional medicine with promising antitumor activity by inhibiting cell proliferation, angiogenesis, metastasis and inducing apoptosis by regulating different signaling pathways [4]. Moreover, BBR is reported to be a naturally occurring phototoxic alkaloid, which can be activated by near-ultraviolet light (NUV) and far-UV (FUV) to generate Reactive Oxygen Species (ROS) to induce a photosensitizing effect in cancer cells [5,6]. However, due to its poor aqueous solubility, very low bioavailability and membrane permeability, BBR can only induce its chemotoxic potential at very high concentrations [4,7]. However, combining the chemotoxic potential with the toxic effect of photogenerated ROS during photodynamic therapy (PDT) has the potential to induce strong phototoxic effects even at lower BBR concentrations. The purpose of this study is to evaluate the potential of BBR as a synergic chemo and phototoxic agent and observe the effects produced by this combination in lung carcinoma cells.

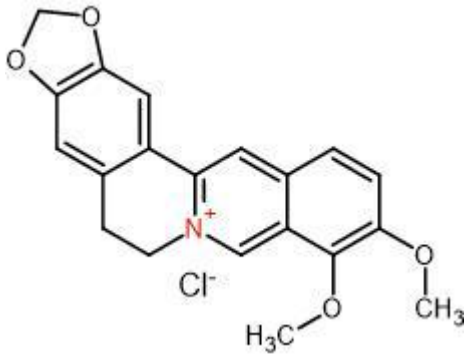

Figure 1: *Chemical Structure of Berberine Chloride*

The human epithelial lung cancer cells A549 (ATCC® CCL-185TM) obtained from American Type Culture Collection (ATCC) was maintained in Roswell Park Memorial Institute 1640 medium (RPMI) containing 1% antibiotics (penicillin/streptomycin) and 10% fetal bovine serum (FBS). The cells were grown at 37 ℃ in an 85% humified incubator under 5% CO_2. For assessment of the chemotoxic potential of BBR, A549

cells were plated in 96 well plate and treated with BBR concentrations range from 2.5 to 320 μM for 24 h. BBR induced phototoxicity and/or combined cytotoxicity was evaluated by treating the cells with a BBR concentration range of 2.5 to 63 μM for 24 h. Following this, cells were irradiated with a 405 nm blue light semiconductor laser diode at light dose of 2 J/cm^2. 24 h post treatment and irradiation the BBR induced chemotoxicity, phototoxicity and/or combined cytotoxicity was determined using Adenosine Triphosphate Assay (ATP) quantification assay using CellTiter-Glo® 3D Cell Viability Kit (Promega G9681). Briefly, following the treatment period, cells were washed twice with Hank's Balanced Salt Solution (HBSS). Following this, 50 μL ATP reagent was added in each well containing 50 μL of HBBS then mixed thoroughly and incubated at room temperature for 25 min. Post-incubation, the resultant ATP luminescence was recorded using a plate reader PerkinElmer, VICTOR Nivo^{TM}. The percentage viability for experimental groups was calculated with respect to the luminescence value in the control untreated group. Cellular damage post treatment was visualized by phase contrast inverted light microscope (Wirsam, Olympus CKX 41) attached to a digital camera (Olympus C5060-ADUS) at 200X magnification. The qualitative analysis of cell viability following treatment was carried out by staining the cells with a LIVE/DEAD cytotoxicity kit (Invitrogen L3224). All the experiments were performed in triplicates and independently repeated thrice. SigmaPlot version 14.0 software was used to analyze the mean and standard error (SE) values for each experimental group. Data points are represented as mean ± standard error (SE), and the difference between the control and experimental groups were statistically analyzed by Student's *t*-test, with a 95% confidence interval.

Fig. 2 shows the chemotoxic effect of BBR on the cell viability of A549 lung cancer cells treated for 24 h. Results showed BBR induced cytotoxicity in a concentration-dependent manner (Fig. 2 (a)). The IC_{50} value determined from the sigmoidal concentration-response curve is 63 μM (Fig. 2 (b)).

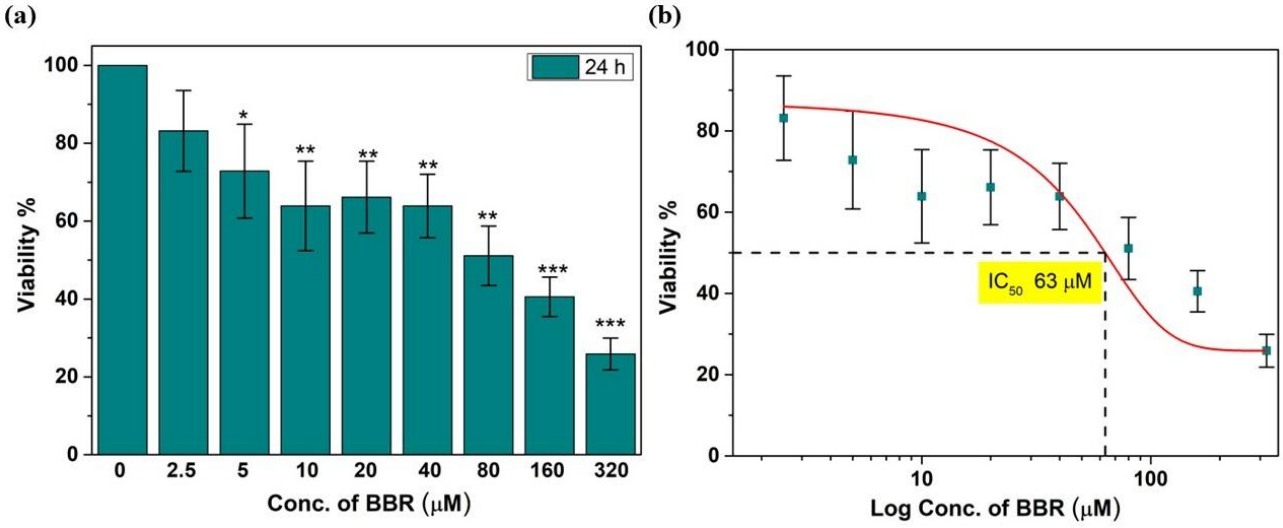

Figure 2: *(a) Cytotoxicity induced by different concentrations (0, 2.5,5, 10, 20, 40, 80 160 and 320 □M) of Berberine (BBR) in A549 lung cancer cells treated for 24 h and determined by ATP proliferation assay, (b) sigmoidal concentration-response curve of BBR treatment. Data points in the graphs are represented as mean ± standard errors from experiments repeated in triplicates.*
(p <0.05), **(p <0.01), *(p < 0.005) indicate significant differences.*

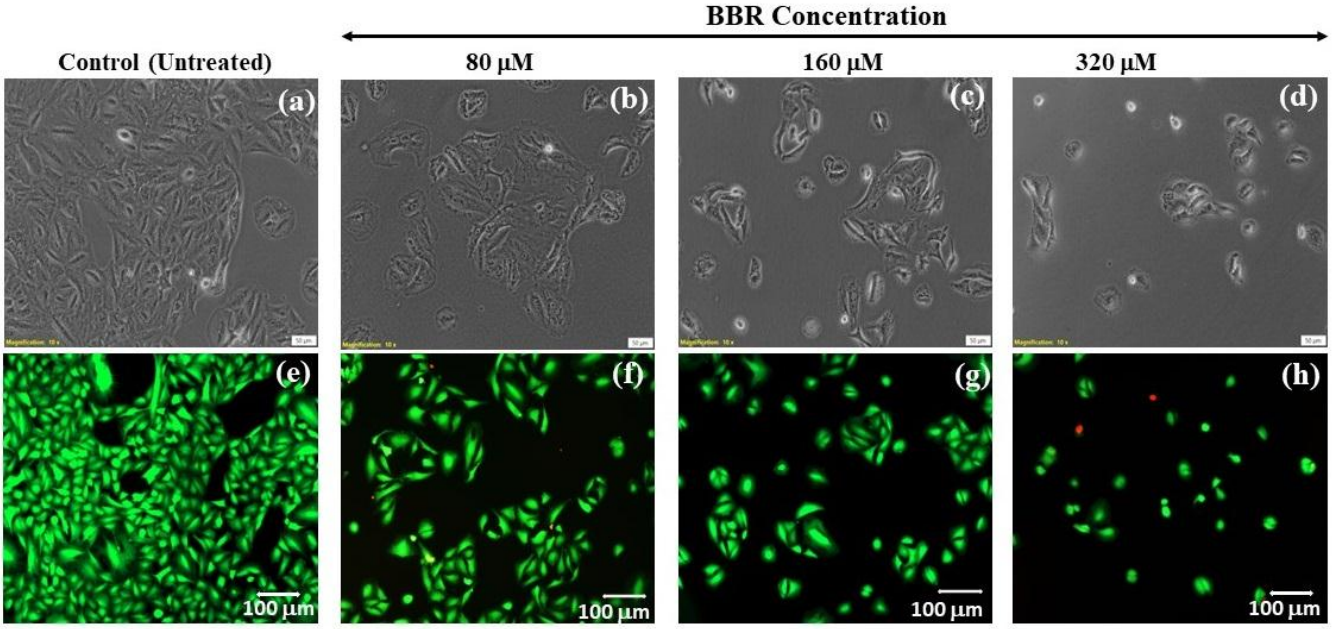

Figure 3: *Phase contrast and LIVE DEAD fluorescence micrographs showing cellular morphology and live and dead A549 cells in (a) and (e) control untreated, 24 h post treatment with (b) and (f) 80 µM, (c) and (g) 160 µM and (d) and (h) 320 µM concentrations of Berberine. (200x Magnification). Green Calcein fluorescence represents Live cells and red EthD-1-stained nucleus represents dead cells.*

The morphological changes in A549 cells after BBR induced chemotoxicity are shown in Fig 3. The control untreated cells (Fig. 3 (a) and (e)) showed healthy morphology with intact cell membrane. The number of cells in BBR treated group, showed gradual decrease in cell population at 80 µM and 160 µM (Fig. 3 (b) (c), (f) and (g)), with many cells showing rounded off morphology at the highest concentration of 320 µM (Fig. 3 (d) and (h)).

As shown in Fig. 4 (a), treatment of A549 cells with various concentrations of BBR followed by light exposure at fixed light dose of 2 J/cm^2 led to concentration dependent increase in cytotoxicity as compared to respective BBR unirradiated treatment groups. The IC_{50} and IC_{90} doses of ~ 11 µM and 52 µM is determined for irradiated groups (Fig. 4 (b)).

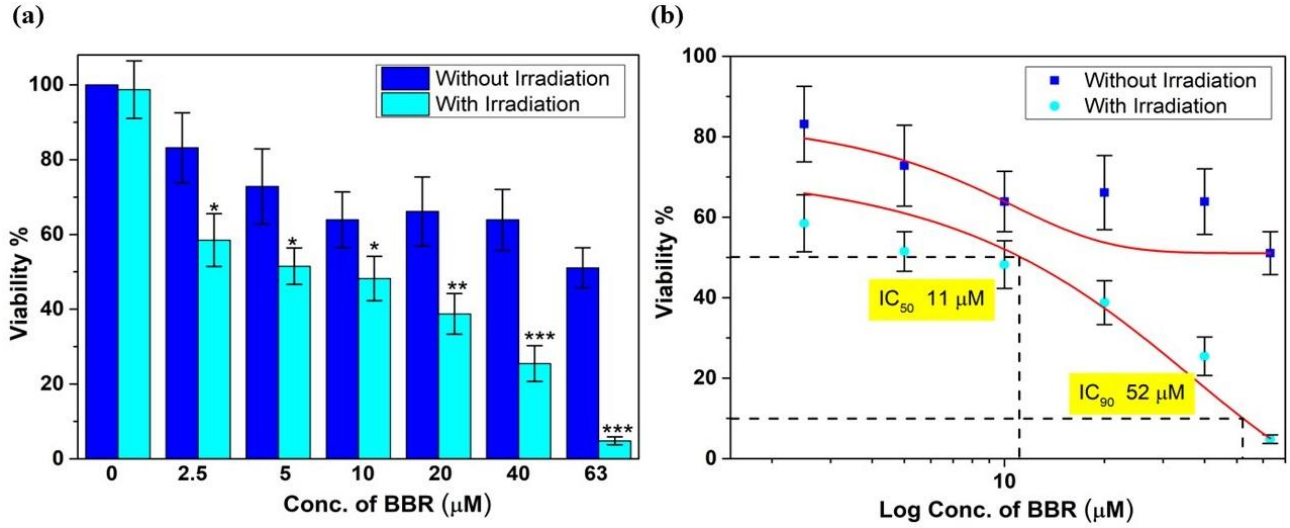

Figure 4: *(a) Concentration dependent (0, 2.5, 5, 10, 20, 40 and 63 µM) phototoxicity induced by Berberine (BBR) in A549 cells at a fixed light dose of 2 J/cm^2 with 405 nm blue laser, determined by ATP proliferation assay (b) sigmoidal concentration-response curve of BBR treatment with and without light irradiation. Data points in the graphs are represented as mean ± standard errors from experiments repeated in*

*triplicates. *(p <0.05), **(p <0.01), ***(p < 0.005) indicate significant difference. In graph (a) statistical significance is determined between irradiated and unirradiated groups of each BBR concentration.*

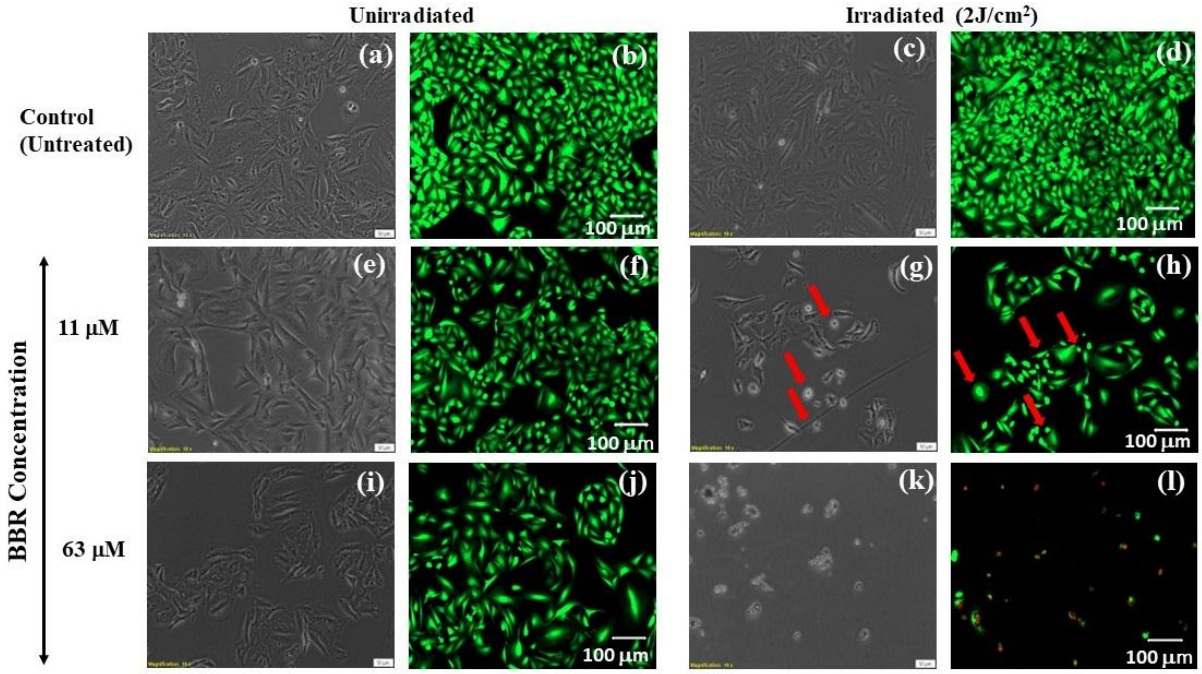

Figure 5: *Representative phase contrast and LIVE DEAD fluorescence micrographs showing cellular morphology, live and dead A549 cells in control untreated and unirradiated (a) and (b), control untreated and irradiated (c) and (d), 24 h post treatment with 11 μM of Berberine (BBR) unirradiated (e) and (f) and irradiated (g) and (h), 63 μM of Berberine (BBR) unirradiated (i) and (j) and irradiated (k) and (l). (200x Magnification). Green Calcein fluorescence represents live cells and red EthD-1-stained nucleus represents dead cells. Red arrows show rounded and damaged cells.*

The changes in cellular morphology and viability observed with and without irradiated following BBR treatment is shown in Fig. 5. The irradiated group at BBR IC_{50} concentration (~11 μM) showed rounded up cellular morphology in certain cell population representing early signs of cell death (Fig. 5 (g) and (h)). While 63 μM BBR concentration upon irradiation showed significant morphological changes with cells showing rounding up, detachment from culture plates, membrane damage and strong red fluorescent nuclei representing cell death (Fig. 5 (k) and (l)).

In the present study, ATP assay results demonstrate that the combined chemo and phototoxicity with BBR treatment at 63 μM concentration resulted in ~95% loss in cancer cell viability in comparison to the 320 μM BBR unirradiated group which showed a loss of cell viability by only 75%. Even the IC_{50} dose in the irradiated group is significantly low (~11 μM) compared to the unirradiated group (63 μM). Further, the morphological and viability analysis (Fig 5) also showed significant cell damage and death in large cell population of irradiated groups in comparison to unirradiated group. Thus, our preliminary results suggested, the combination of chemotoxic potential of BBR with its induced phototoxicity instigates an effective cytotoxic effect against lung cancer cells at very low concentrations which cannot be achieved without PDT.

In summary, plant-based compound BBR is a potential candidate to augment the anticancer action in combined chemo and phototoxic treatment and thus offers the advantage of its application as natural product-based cancer prevention and therapy. However, further research is warranted to provide mechanistic insights at protein, gene, and transcriptome levels to identify the exact cell death signaling pathway induced by the combination therapy.

ACKNOWLEDGEMENTS

The authors sincerely thank the South African Research Chairs initiative of the Department of science and technology and National Research Foundation (NRF) of South Africa, South African Medical Research Council (SAMRC) and Laser Re-search Centre (LRC), University of Johannesburg.

Research reported in this review article was supported by the South African Medical Research Council (SAMRC) through its Division of Research Capacity Development under the Research Capacity Development Initiative from funding received from the South African National Treasury. The content and findings reported/ illustrated are the sole deduction, view and responsibility of the researcher and do not reflect the official position and sentiments of the SAMRC.

FUNDING

This work is supported by the South African Research Chairs initiative of the Department of science and technology and National Research Foundation of South Africa (Grant No 98337), South African Medical Research Council (Grant No. SAMRC EIP007/2021), NRF Research Development Grants for Y-Rated Researchers (Grant No: 137788) as well as grants received from the University Research Committee (URC), University of Johannesburg and the Council for Scientific and Industrial Research (CSIR)-National Laser Centre (NLC).

CONFLICTS OF INTEREST

The authors declare no conflict of interest.

REFERENCES

[1] Sung H, Ferlay J, Siegel RL, Laversanne M, Soerjomataram I, Jemal A, et al. Global cancer statistics 2020: GLOBOCAN estimates of incidence and mortality worldwide for 36 cancers in 185 countries. CA Cancer J Clin. 2021;

[2] Ellis PM, Vandermeer R. Delays in the diagnosis of lung cancer. J Thorac Dis. 2011;3(3).

[3] Daga A, Ansari A, Patel S, Mirza S, Rawal R, Umrania V. Current drugs and drug targets in non-small cell lung cancer: Limitations and opportunities. Vol. 16, Asian Pacific Journal of Cancer Prevention. 2015.

[4] Mirhadi E, Rezaee M, Malaekeh-Nikouei B. Nano strategies for berberine delivery, a natural alkaloid of Berberis. Vol. 104, Biomedicine and Pharmacotherapy. 2018.

[5] Wang MX, Huo LM, Yang HC, Gao YJ, E Z. An experimental study on the photodynamic activity of berberine in vitro on cancer cells. J Tradit Chin Med. 1986;6(2).

[6] An YW, Jin HT, Yuan B, Wang JC, Wang C, Liu HQ. Research progress of berberine mediated photodynamic therapy (Review). Vol. 21, Oncology Letters. 2021.

[7] Javed Iqbal M, Quispe C, Javed Z, Sadia H, Qadri QR, Raza S, et al. Nanotechnology-Based Strategies for Berberine Delivery System in Cancer Treatment: Pulling Strings to Keep Berberine in Power. Vol. 7, Frontiers in Molecular Biosciences. 2021.

DOI 10.24412/cl-37136-2023-1-63-68

MODULATION OF CELLULAR RESPONSES TO IONISING RADIATION BY RADIOFREQUENCY FIELDS: POTENTIAL MECHANISMS

ANGELA CHINHENGO AND JOHN AKUDUGU

Division of Radiobiology, Department of Medical Imaging and Clinical Oncology, Stellenbosch University, South Africa

jakudugu@sun.ac.za

ABSTRACT

Radiotherapy is one of the most used treatment options for different kinds of cancer and its main goal is to kill tumour cells while minimising toxicity normal tissue. A sure means of killing cancers is to increase the dose radiation that is administered to patients, but dose escalation may lead to adverse normal tissue toxicity. Hence, the need to develop noninvasive ways to sensitise tumour cells to low doses of radiation. Pharmaceuticals have been used to partly address this need, but systemic side effects pose another challenge. Electromagnetic fields (EMF) which largely thought to be nonhazardous have long been shown to have wide ranging benefits in the treatment of disorders as diverse as fractures, wounds, depression, and cancer [1- 3]. However, EMF have equally exhibited both desirable and undesirable effects and their anticancer and cancer-promoting properties have been demonstrated [4]. These effects have been observed for EMF frequencies ranging from fractions of a hertz (Hz) to several petahertz (PHz).

Specifically, radiofrequency fields (RF) have received significant attention in the clinic. For instance, they have been extensively used in radiofrequency ablation of hepatocellular carcinoma [5-7], early-stage renal cell carcinoma [8], non-small cell lung cancer [9], and melanoma [10-12]. Radiofrequency ablation typically employs a frequency of ~500 MHz which falls within the medium radio wave range, and the desired biological effect of this procedure is mediated by induction of molecular frictional heating in the target tissue by the radio wave [13]. The technique is minimally invasive (electrodes and probes inserted into target tissue) and is thought to be more superior than surgery. An informed combination of radiofrequency fields with radiotherapy could prove beneficial in cancer management. In a series of studies, we sought to evaluate the effect of low frequency radio waves on the sensitivity *in vitro* cell cultures to X-ray irradiation. The main objectives of these investigations were to confirm the capacity of RF to modulate cellular radiosensitivity and identify potential underlying mechanisms for such modulation. For this, Chinese hamster lung fibroblasts (V79) and human melanoma cells (MeWo) were remotely exposed to radiofrequency fields prior to or post irradiation with X-rays and processed for colony forming cell survival [14,15]. The radiofrequencies were generated from an EMEM oscillator amplifier (EMEM Devices Rife Machine, Model No. 1-2012B, Boulder, CO, USA; Fig. 1) with a carrier frequency of 27.125 MHz, square amplitude modulated at 100 and 1000 Hz. The modulating frequencies were injected from a GME frequency generator (GME Technology, Model No. SG-10, Panoma, CA, USA). In the cell cultures, the RF-induced magnetic flux densities were estimated to range between 0.05 and 0.25 μT. The X-ray irradiation was performed using a Faxitron MultiRad 160 X-ray irradiator (Faxitron Bioptics, Tucson, AZ, USA). The irradiation was performed at a dose rate of 1 Gy/min. Radiofrequency field and X-ray exposures were carried out at room temperature (20°C).

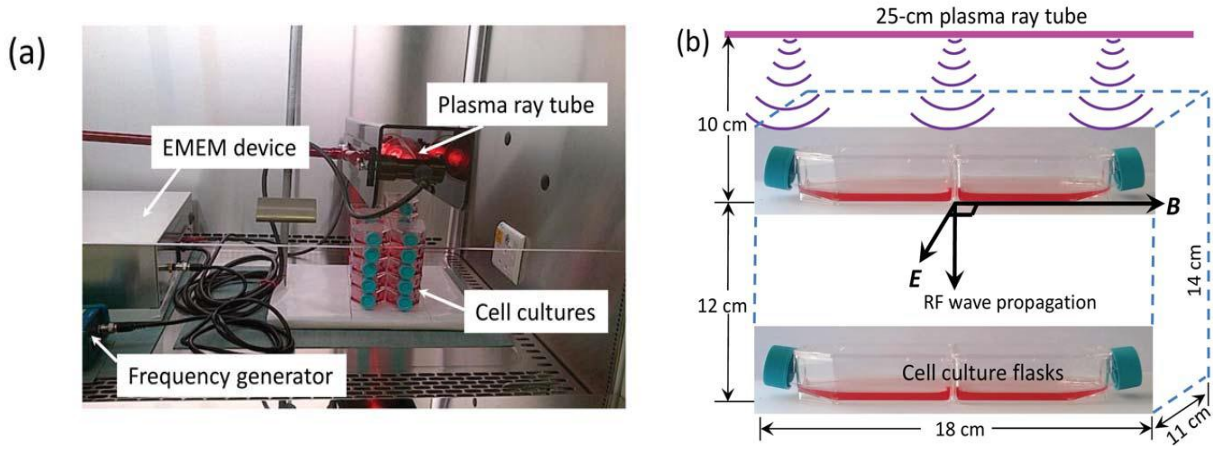

Figure 1: *(a) Photograph of the EMEM Devices radiofrequency field (RF) exposure system. (b) Schematic showing the top and bottom cell culture planes of a 2 × 2 × 6 flask matrix. Plasma ray tube centred horizontally above the cell culture flasks. Induced magnetic field (B) and electric field in the culture medium (E) are parallel to the length and width of the flasks, respectively [14].*

No cytotoxicity was apparent when cell cultures were exposed to radiofrequency field alone. It was found that the radiosensitising effect of the 1000 Hz-modulated field was more prominent than that of the 100 Hz-modulated field when the interval between X-ray and RF exposures was 4 h [14]. Pre-exposure of the "apparently normal" V79 cells to the 100 and 1000 Hz-modulated fields, 2 h prior X-ray irradiation did not affect the sensitivity of the cells to X-rays. However, the malignant MeWo cells were respectively protected and sensitised by the 100 and 1000 Hz-modulated fields at all time points. On the other hand, the 1000 Hz-modulated field protected the fibroblasts when RF exposure was performed 1 h prior to X-ray irradiation. These findings suggest that RF modulation of cellular radiosensitivity is not only frequency dependent but also reliant on the sequence in which the exposures occur. Also, the observation that the different cell lines do not respond in a similar fashion to the different frequencies may be may be attributed to the notion of the existence cell-specific resonant frequencies at which cells could be rendered sensitive to the X-ray insult [15]. To further investigate the potential of radiofrequency fields in radiotherapy dose reduction, cell survival following an acute (3 Gy), a split dose (1.5 Gy + 1.5 Gy) of X-rays, and 2 Gy given with radiofrequency fields were compared. The key findings are highlighted in Fig. 2 [16]. Cell exposure to RF modulated at 1000 Hz 6 h prior to treatment with 2 Gy of X-rays sensitises the malignant melanoma cells (MeWo) and protects "apparently normal" fibroblasts from the effects of ionising radiation. When compared with 3-Gy treatments, this suggests that use of a radiofrequency field modulated at 1000 Hz can assist in reducing radiation dose by up to 50% without compromising therapeutic benefit. The radioprotective and radiosensitising properties of the RF field seen here corroborate the finding of our earlier study [14].

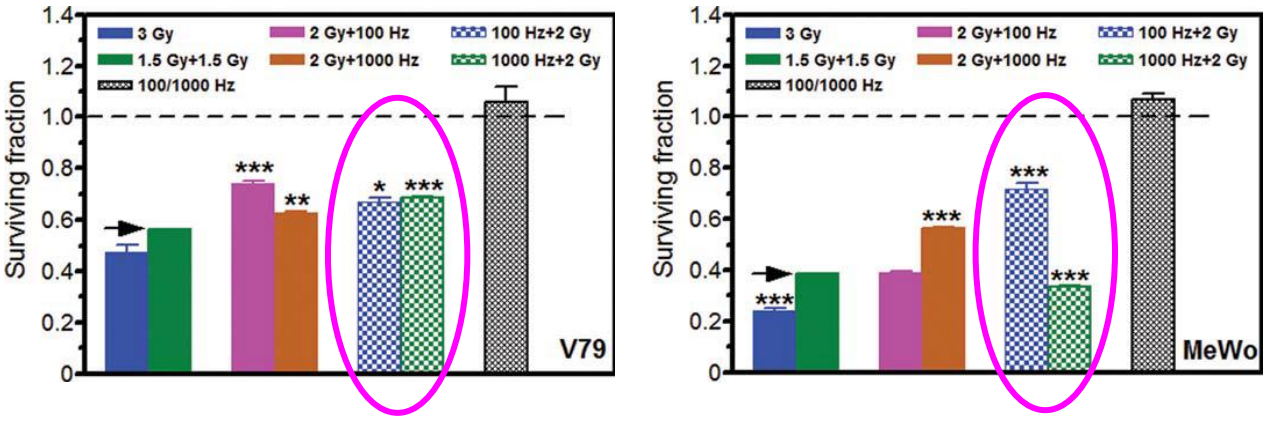

Figure 2: *Surviving fractions for V79 and MeWo cells following various treatment protocols: acute dose of 3 Gy of X-rays, RF exposure alone, and split dose of X-rays (1.5 Gy/fraction) or combination of RF exposure*

and 2 Gy of X-rays given 6 h prior to or after each other. Surviving fractions of untreated cell cultures (dashed lines), arrowheads (split dose survival with which survival after combination treatments were compared), pink ovals are for easy comparison between the 'apparently normal" and malignant cells [16].

In a sequel of studies intended to elucidate possible mechanisms underlying the observed modulation of radiosensitivity by the low frequency RF used here, an extended of four human cell lines (melanomas: MeWo - p53 mutant and Be11 - p53 wild-type; prostate carcinoma: DU145 - p53 mutant; normal lung fibroblasts - p53 wild-type) were used [17-21]. Due to a breakdown of the EMEM radiofrequency generation system [14] and our inability to make contact with the supplier (Teli Enterprises LLC), RF exposure for these studies was performed using a PERL M^+ oscillator amplifier (Resonant Light Technology Inc., Courtenay, Canada; Serial # PM 171116) [17,18; Fig. 3]. A ProGen II frequency generator (Serial No. PG 171211) was used to generate the modulating frequencies. In this set-up, the estimate induced magnetic flux densities ranged from 6.74 to 22.43 μT.

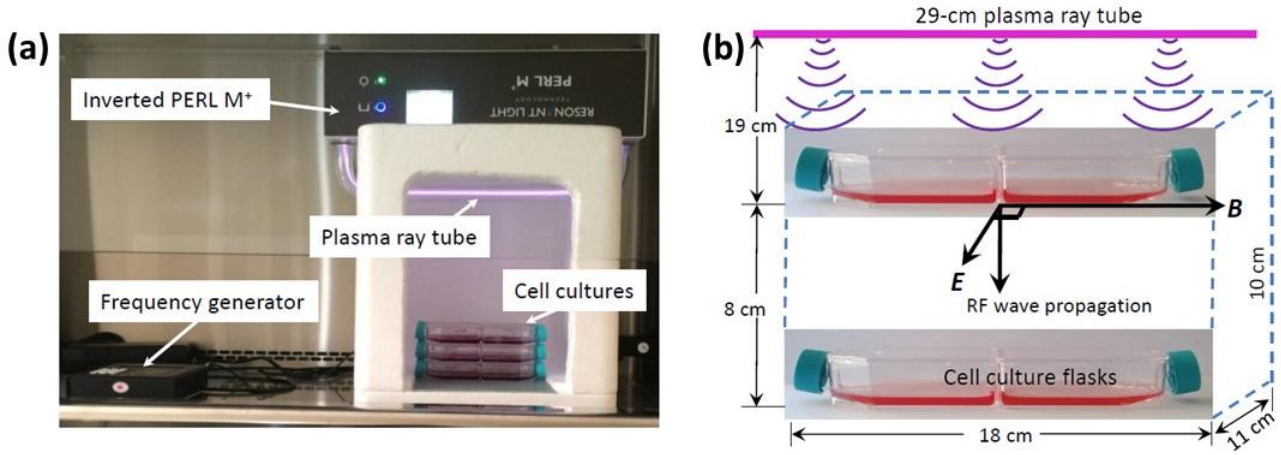

Figure 3: *(a) Photograph of the Resonant Light Technology radiofrequency field (RF) exposure system, with the PERL M^+ inverted on a cut Styrofoam box. (b) Schematic showing the top and bottom cell culture planes of a 2 × 2 × 4 flask matrix. Plasma ray tube centred horizontally above the cell culture flasks. Induced magnetic field (B) and electric field in the culture medium (E) are parallel to the length and width of the flasks, respectively [17,18].*

Factors that were investigated for their potential role in radiosensitivity modulation by radiofrequency fields were: (a) p53 status, (b) DNA damage processing and proliferative activity, (c) metabolic activity, and (d) induction of reactive oxygen species (ROS). The modulation of radiosensitivity by radiofrequency fields that was previously demonstrated was confirmed. In the following, the findings on the potential mechanisms underlying RF-mediated alterations of radiosensitivity *in vitro* are summarised:

p53 status: The effect of a 27.125 MHz field modulated at 100, 1000, 2000, and 4000 Hz on the radiosensitivity of the four human cell lines (MeWo, Be11, DU145, and L132) was assessed on the basis of colony forming capacity. The wide range of RF-induced magnetic flux density for the different radiofrequency generation systems did not seem to significantly affect RF-modulation of radiosensitivity [14,17,18]. The modulation cellular radiosensitivity by radiofrequency fields was confirmed and appeared to be frequency- and cell-type-dependent [17]. Extending the modulating frequencies to include 2000 and 4000 Hz showed that the extent of RF-mediated radiosensitisation does not steadily increase with increasing the modulating frequency. The demonstrated frequency and cell type-dependence of radiofrequency field modulation of cellular sensitivity to X-ray treatment is consistent with the finding of the earlier studies [14,16]. In the panel of cell lines used here, the p53 wild-type cells showed the highest radiosensitisation and which peaked at a modulating frequency of 1000 Hz, especially when cells were irradiated to 6 Gy [18]. This is consistent with the earlier observation that the sensitisation of the "apparently normal" V79 cells was minimal [14]. These rodent cells possess a non-functional and mutated p53 [22]. This finding shows that a radiofrequency field of 27.125 MHz modulated at 1000 Hz is more efficient in modulating large fractional doses of ionising radiation and may be beneficial in

hypofractionated radiotherapy where large doses are administered fraction. Specifically, this could be the case for patients with tumours exhibiting low alpha/beta ratios, like those presenting with prostate cancer. Expanding the panel of cell lines may help in confirming the potential role of low frequency radio waves and cellular gene profiles in the use of radiofrequency fields as radiation protectors and sensitisers. The role of p53 status in the radiofrequency modulation of cellular sensitivity to ionising radiation is also warrants further investigation.

DNA damage processing and proliferative activity: Cellular DNA processing was evaluated using the cytokinesis-blocked micronucleus formation assay. The yield of binucleated cell in the cytokinesis-blocked cultures was used as an indicator of proliferation. The yields of micronuclei (marker of DNA damage) and binucleated cells (marker of proliferation) were correlated with the cellular radiosensitisation that was conferred by 100- and 1000-Hz modulated radiofrequency fields [19]. Binucleation can be used represent cell proliferation, as an elevated binucleation index is indicative of a large proportion of actively progressing cells through the cell cycle [23-25]. An elevated micronucleus yield was linked to a higher degree of radiosensitisation by radiofrequency fields. This correlation was independent of modulating frequency. While an increased proliferative index was correlated with a marked radiosensitisation by the 100-Hz modulated field, a raised proliferative capacity was linked to a slight radiosensitisation when cells were exposed to the 1000-Hz modulated field. From these findings, it can be inferred that that radiofrequency fields interfere with the capacity of cells to process ionising radiation-induced DNA damage and their ability to progress in the cell cycle. Interaction between ionising radiation and radiofrequency fields may have significant ramifications in radiation protection, radiotherapy, and wound healing following preoperative radiotherapy. Although fibroblast proliferation is a precursor of good wound healing, enhanced proliferation in irradiated fibroblasts does not always promote efficient wound healing [26]. Therefore, further validation of these findings in a large panel of cell lines and preclinical systems is of merit.

Metabolic activity: Changes in the metabolic activity of the cell lines was determined using the 3-(4,5-dimethylthiazol-2-yl)-2,5-diphenyltetrazolium bromide assay. Cell lines that displayed larger reductions in metabolic activity emerged more radiosensitised by radiofrequency exposure, relative to when they were treated with radiation alone [20]. This was independent of whether RF exposure occurred prior to or after X-ray irradiation. The finding that metabolic activity in surviving cells remained raised following a combined treatment of X-rays and radiofrequency fields for up to 18 h suggests that radiofrequency fields trigger alterations in metabolic activity to support DNA repair and subsequent cell survival. Changes in cellular metabolic activity in X-ray treated cells following radiofrequency exposure might have significant implications for cellular responses to ionising radiation in the ambience of radiofrequency fields. The sustained metabolic activity observed in X-ray treated cells concomitantly exposed to the radiofrequency may be attributed to the RF fields inducing dormant cells to enter and progress through the cell cycle. This could explain the enhance cell proliferation eluded to earlier [19]. An enhanced proliferation is a reflection of increased G_2/M activity [27,28]. As cells G_2/M are more radiosensitive would be more susceptible to the radiation insult, thus giving rise to elevated radiosensitisation. This phenomenon requires further elucidation in a large panel of cell lines and preclinical models, if radiofrequency fields of the kind studied here are to be routinely used in radiotherapy as adjuvants.

Induction of reactive oxygen species (ROS): ROS expression was assessed by measurement of cytosolic superoxide dismutase activity in the cell lines following the various treatments. On average, radiation-induced ROS activity was consistently increased by radiofrequency field exposure in all cell lines. However, the degree to which RF exposure enhanced ROS activity did not correlate with the level of radiosensitisation [21]. The finding that ROS activity is elevated by radiofrequency field exposure supports other studies that have demonstrated that electromagnetic fields have a strong influence ROS production in cellular systems [29-31]. The absence of clear link between RF-induction of ROS radiosensitivity is not entirely unexpected as reactive oxygen species are known to play multiple and opposing roles in biological systems. ROS can initiate oxidative stress that leads to cell death or promote malignant cancer acclimatisation to low oxygen tension, cell propagation, and survival [32-34]. Similar studies on an expanded panel of cell lines and preclinical systems are required in order to confirm the potential role of reactive oxygen species in radiofrequency-mediated radiosensitisation.

Acknowledgements

These finding are based on research supported by the National Research Foundation of South Africa (Grant Nos.: 85703, 92741, 100157, 107703) and funding from the Faculty of Medicine and Health Sciences (Stellenbosch University), the Harry Crossley Foundation, and the Cancer Association of South Africa.

REFERENCES

[1] D. Janigro, C. Perju, V. Fazio, K. Hallene, G. Dini, M.K. Agarwal, L. Cucullo, Alternating current electrical stimulation enhanced chemotherapy: a novel strategy to bypass multidrug resistance in tumor cells, BMC Cancer 6(1):1-12, 2006.

[2] Verginadis, I., Velalopoulou, A., Karagounis, I., Simos, Y., Peschos, D., Karkabounas, S. and Evangelou, A., Beneficial effects of electromagnetic radiation in cancer. In: Bashir SO, Editor, Electromagnetic Radiation, Shanghai, Intech, p. 249-268, 2012.

[3] A.C. Francisco, S.A.M. del Mar, C. Irene, R.A. Sandra, L. Josefa, R.M. Elisa, O. Nicolás, N.M. Isabel, Could radiotherapy effectiveness be enhanced by electromagnetic field treatment?, Int. J. Mol. Sci. 14(7):14974-14995, 2013.

[4] D.K. Meijer, H.J. Geesink, Favourable and unfavourable EMF frequency patterns in cancer: perspectives for improved therapy and prevention, J. Cancer Ther. 9(3):188-230, 2018.

[5] N. Kim, J. Cheng, I. Jung, J. Der Liang, Y.L. Shih, W.Y. Huang, T. Kimura, V.H. Lee, Z.C. Zeng, R. Zhenggan, C.S. Kay, Stereotactic body radiation therapy vs. radiofrequency ablation in Asian patients with hepatocellular carcinoma, J. Hepatol. 73:121-129, 2020

[6] N. Kim, H.J. Kim, J.Y. Won, K.H. Han, I. Jung, J. Seong, Retrospective analysis of stereotactic body radiation therapy efficacy over radiofrequency ablation for hepatocellular carcinoma, Radiother. Oncol. 131:81-87, 2019.

A. Cacciola, S. Parisi, C. Tamburella, S. Lillo, G. Ferini, L. Molino, G. Iatì, A. Pontoriero, A. Bottari, S. Mazziotti, G. Cicero, Stereotactic body radiation therapy and radiofrequency ablation for the treatment of liver metastases: How and when?, Rep. Pract. Oncol. Radiother. 25:299-306, 2020.

[7] E.K. Donovan, F. Xie, A.V. Louie, W. Chu, S. Siva, A. Kapoor, A. Swaminath, Cost effectiveness analysis of radiofrequency ablation (RFA) versus stereotactic body radiotherapy (SBRT) for early stage renal cell carcinoma (RCC), Clin. Genitourin. Cancer, 20:e353-e361, 2022.

[8] H. Bilal, S. Mahmood, B. Rajashanker, R. Shah, Is radiofrequency ablation more effective than stereotactic ablative radiotherapy in patients with early stage medically inoperable non-small cell lung cancer?, Interact. CardioVasc. Thorac. Surg. 15:258-265, 2012.

[9] P. Mariani, M.M. Almubarak, M. Kollen, M. Wagner, C. Plancher, R. Audollent, S. Piperno-Neumann, N. Cassoux, V. Servois, Radiofrequency ablation and surgical resection of liver metastases from uveal melanoma, Eur. J. Surg. Oncol. (EJSO) 42:706e712, 2016.

[10] R. Bale, P. Schullian, M. Schmuth, G. Widmann, W. Jaschke, G. Weinlich, Stereotactic radiofrequency ablation for metastatic melanoma to the liver, Cardiovasc. Intervent. Radiol. 39:1128-1135, 2016.

[11] Shashank, M. Shehata, D.L. Morris, J.F. Thompson, Radiofrequency ablation in metastatic melanoma, J. Surg. Oncol. 109:366-369, 2014.

[12] Y. Ni, S. Mulier, Y. Miao, L. Michel, G. Marchal, A review of the general aspects of radiofrequency ablation, Abdom. Imaging 30:381-400, 2005.

[13] Chinhengo, A.M. Serafin, Hamman B, J. Akudugu, Electromagnetic fields induce frequency-dependent radioprotection and radiosensitization in *in vitro* cell cultures. Plasma Med. 8(2):163-175, 2018.

[14] J.W. Zimmerman, H. Jimenez, M.J. Pennison, I. Brezovich, D. Morgan, A. Mudry, F.P. Costa, A. Barbault, B. Pasche, Targeted treatment of cancer with radiofrequency electromagnetic fields amplitude-modulated at tumor-specific frequencies, Chin. J. Cancer, *32*(11):573-581, 2013.

[15] Chinhengo, A.M. Serafin, J. Akudugu, Comparison of cellular sensitivity to a split radiation dose and a combination of a single radiation dose and electromagnetic field exposure. Plasma Med. 9(1):15-22, 2019.

[16] Chinhengo, A.M. Serafin, J. Akudugu, Radiofrequency fields preferentially enhance *in vitro* cellular radiosensitivity to large fractional doses in a p53-dependent manner. Plasma Med. 9(2):147-166, 2019.

[17] Chinhengo, A.M. Serafin, J. Akudugu, Radiosensitization by low-frequency radiofrequency fields is dependent on the magnitude of the modulating frequency, Plasma Med. 12(2):27-36, 2022.

[18] Chinhengo, A.M. Serafin, J. Akudugu, Radiosensitization by radiofrequency fields is correlated with micronucleus yield and proliferative index. Plasma Med. 10(1):27-43, 2020.

[19] Chinhengo, A.M. Serafin, J. Akudugu, Radiofrequency field–induced radiosensitization is related to reductions in metabolic activity. Plasma Med. 9(2):177-190, 2019.

[20] Chinhengo, A.M. Serafin, J. Akudugu, Radiofrequency field–induced radiosensitization is not correlated with induction of reactive oxygen species. Plasma Med. 9(2):167-176, 2019.

[21] W. Chaung, L.-J. Mi, RJ. Boorstein, The p53 status of Chinese hamster V79 cells frequently used for studies on DNA damage and DNA repair, Nucleic. Acids Res. 25:992-994, 1997.

[22] J.M. Akudugu, T. Theron, A. Serafin, L. Böhm, Influence of DNA double-strand break rejoining on clonogenic survival and micronucleus yield in human cell lines, Int. J. Radiat. Biol. 80:93-104, 2004.

[23] Y. Shibamoto, C. Streffer, Estimation of the dividing fraction and potential doubling time of tumors using cytochalasin B, Cancer Res. 51:5134-5138, 1991.

[24] Y. Shibamoto, T. Shibata, S. Miyatake, Y. Oda, T. Manabe, G. Ohshio, K. Yagi, C. Streffer, M. Takahashi, M. Abe, Assessment of the proliferative activity and radiosensitivity of human tumours using the cytokinesis-block assay. Br. J. Cancer 70:67-71, 1994.

[25] J.M. Akudugu, R.S. Bell, C. Catton, A.M. Davis, B. O'Sullivan, J. Waldron, J.S. Wunder, RP. Hill, Clonogenic survival and cytokinesis-blocked binucleation of skin fibroblasts and normal tissue complications in soft tissue sarcoma patients treated with preoperative radiotherapy, Radiother. Oncol. 72:103-12, 2004.

[26] S. Velizarov, P. Raskmark, S. Kwee, The effects of radiofrequency fields on cell proliferation are non-thermal, Bioelectrochem. Bioenerg. 48:177-780, 1999.

[27] L.-Y. Sun, D.-K. Hsieh, T.-C. Yu, H.-T. Chiu, S.-F. Lu, G.-H. Luo, T.K. Kuo, O.K. Lee, T-W. Chiou, Effect of pulsed electromagnetic field on the proliferation and differentiation potential of human bone marrow mesenchymal stem cells, Bioelectromagnetics 30:251-260, 2009.

[28] H.C. Lai, N.P. Singh, Medical applications of electromagnetic fields. In Electromagnetic Phenomena and Health - A Continuing Controversy? IOP Conference Series: Earth and Environmental Science, IOP Publishing (UK), 10:012006, 2010.

[29] Morabito, S. Guarnieri, G. Fanò, M.A. Mariggiò, Effects of acute and chronic low frequency electromagnetic field exposure on PC12 cells during neuronal differentiation, Cell. Physiol. Biochem. 24:947-958, 2010.

[30] P. Kovacic, R. Somanathan, Electromagnetic fields: mechanism, cell signaling, other bioprocesses, toxicity, radicals, antioxidants and beneficial effects, J. Recept. Sig. Transd. 30:214-226, 2010.

[31] M. López-Lózaro, Dual role of hydrogen peroxide in cancer: Possible relevance to cancer chemoprevention and therapy, Cancer Lett. 252:1-8, 2007.

[32] J.-S. Pan, M.-Z. Hong, J.-L. Ren, Reactive oxygen species: A double-edged sword in oncogenesis, World J. Gastroenterol. 15:1702-1707, 2009.

[33] S.C. Gupta, D. Hevia, S. Patchva, B. Park, W. Koh, B.B. Aggarwal, Upsides and downsides of reactive oxygen species for cancer: The roles of reactive oxygen species in tumorigenesis, prevention, and therapy, Antioxid. Redox. Signal. 16:1295-1322, 2012.

DOI 10.24412/cl-37136-2023-1-69-70

SCIENCE AND INNOVATIONS IN NON-INVASIVE DIAGNOSTICS THROUGH HUMAN EXHALED BREATH ANALYSIS

MANIK PRADHAN

Department of Chemical and Biological Sciences, S. N. Bose national Centre for Basic Science, India

manik.pradhan@bose.res.in

ABSTRACT

Human breath contains a very large number of trace volatile organic compounds (VOCs) with concentrations parts per billion (ppb) to parts per trillion (ppt) levels. Some of the molecular species are strongly associated with the pathogenesis of the disease. Elevated concentrations of these molecules, or of specific isotopologues, can be markers for particular medical conditions, and the breath analysis provides a non-invasive and rapid diagnostic method. The conventional endoscopic and biopsy-based invasive methods are not only suitable for early diagnosis, but also inappropriate for widespread population-screening including infants, children, pregnant women and seniors. Moreover, the invasive and relentless nature of the endoscopic procedure limits its suitability for large-scale screening.

In this workshop, I will talk about some important medical-social problems in the domain of laser spectroscopy and photonics such as *H. pylori* bacterial infection in human stomach, peptic ulcer disease, various gastric disorders, diabetes and IBS that has received special attention all over the world. For this study, we have used high-resolution and ultra-sensitive optical cavity ring-down spectroscopy (CRDS) coupled with diode and quantum cascade lasers (QCLs) in the IR region [1,2]. We have investigated various rovibronic spectroscopic signatures by shining the laser beam on human exhaled molecules. We explored some unique patterns of exhaled molecular species and their isotopes through light-matter interactions that might be considered as potential markers or so-called "breathprints" for non-invasive diagnosis and precise classification of several complex diseases as mentioned above without the need for painful invasive endoscopy and biopsy tests.

Using a high-resolution CRD spectroscopy, we have developed a novel strategy for early detection of type 1 diabetes (T1D) and to precisely distinguish T1D from type 2 diabetes (T2D). Our findings suggest that the exhaled oxygen-18 of CO_2 may act as a potential biomarker for non-invasive assessment of T2D and thus may open a new method for treating T2D [3,4]. In another study by employing high-resolution laser spectroscopy, we have explored the triple-isotopic compositions of water isotopes in the gastrointestinal tract and found that human the deuterium-enriched exhaled semi-heavy water, i.e., $HD^{16}O$ is a new marker of the noninvasive assessment of the ulcer-causing *H. pylori* gastric pathogen [5]. We have also established that there is a potential link between *H. pylori* infection and type 2 diabetes. We established these observations through the isotopic fractionations of carbon-13 and oxygen-18 in exhaled breath CO_2 in response to glucose metabolism [6]. Moreover, in a recent investigation, using QCL spectroscopy we have shown a strong physiological link between exhaled N_2O and bacterial infection in the stomach, providing important insights into the biological activities of human-associated microorganisms [7]. Finally, I will talk about our recent technological innovation on "Pyro-breath" product and its potential for large-scale non-invasive screening purposes.

REFERENCES

[1] A. De, G. D. Banik, A. Maity, M. Pal, S. Ghosh, M. Pradhan, Continuous wave external-cavity quantum cascade laser-based high-resolution cavity ring-down spectrometer for ultrasensitive trace gas detection, Optics Letters, 41 (9), 1949-1952, 2016.

[2] G. D. Banik, A. Maity, S. Som, M. Pal, M. Pradhan, An external-cavity quantum cascade laser operating near 5.2 μm combined with cavity ring-down spectroscopy for multi-component chemical sensing, Laser Physics, 28, 045701, 2018.
[3] C. Ghosh, S. Mandal, G. D. Banik, A. Maity, P. Mukhopadhyay, S. Ghosh, M. Pradhan, Targeting erythrocyte carbonic anhydrase and oxygen-18 isotope of breath CO_2 for sorting out Type 1 and Type 2 diabetes, Scientific Reports, 6, 35836, 2016.
[4] C. Ghosh, G. Banik, A. Maity, S. Som, A. Chakraborty, C. Selvan, S. Ghosh, S. Chowdhury, M. Pradhan. Oxygen-18 isotope of breath CO2 linking to erythrocytes carbonic anhydrase activity: a biomarker for pre-diabetes and type 2 diabetes, Scientific Reports, 5, 11959, 2015.
[5] M. Pal, S. Bhattacharya, A. Maity, S. Chaudhuri, M. Pradhan. Exploring triple-isotopic signatures of water in human exhaled breath, gastric fluid, and drinking water using integrated cavity output spectroscopy, Anal. Chem. 92, 8, 5717-5723, 2020.
[6] S. Som, G.D. Banik, S. Chaudhuri and M. Pradhan, Non-invasive diagnosis of Helicobacter pylori infection and type 2 diabetes simultaneously using isotope-specific infrared absorption measurements, Isotopes in Environment and Health Studies, 54, 435-445, 2018.
[7] M. Pal, S. Maithani, A. Maity, S. Chaudhuri, M. Pradhan, Exploring the physiological link of breath N_2O through nitrification and denitrification processes in human gastric juice, Journal of Breath Research, 13, 016002, 2018.

DOI 10.24412/cl-37136-2023-1-71-75

3D PRINTABLE SOFT ARTIFICIAL OPTICAL SKIN FOR HEALTHCARE APPLICATION

ABHIJIT CHANDRA ROY[1], NAVIN KUMAR[1], SHREYAS B S[1], ANANYA GUPTA[1], ALOKE KUMAR[2], AVEEK BID[1], AND V. VENKATARAMAN[1]

[1]Department of Physics, Indian Institute of Science, Bangalore, Karnataka, India-560012
[2]Department of Mechanical Engineering, Indian Institute of Science, Bangalore, Karnataka, India-560012

ABSTRACT

The human skin being the largest and most exposed organ in the body provides various essential information including touch, temperature, pressure, vibration, and humidity of the surrounding for smooth and safe functioning of our body. Similarly, artificial soft electronic skin, like human skin, perceives various environmental stimuli by transducing them into an electrical signal. Soft artificial optical skin capable of sensing touch and pressure is essential in many applications, including social robotics, healthcare, and augmented reality. However, several hurdles remain challenging, such as highly complex and expensive fabrication processes, instability in long-term use, and difficulty producing large areas and mass production. Here, we present a robust 3D printable large area soft artificial optical skin made of a soft and resilient polymer capable of detecting touch, load, and bending with extreme sensitivity to touch and load, 750 times higher than earlier work. The soft artificial optical skin shows excellent long-term stability and consistent performance up to almost a year. In addition, we describe a fabrication process capable of producing large areas, large numbers, yet cost-effective. The soft artificial optical skin consists of a uniquely designed optical waveguide and a layer of a soft membrane with an array of soft structures which work as passive sensing nodes. The use of a soft structure provides the freedom of stretching to the soft artificial optical skin without considering the disjoints among the sensing nodes. The soft artificial optical skin's operation has been shown using a variety of techniques.

INTRODUCTION

Soft artificial skin similar to human natural skin perceives various surrounding stimuli by transducing them into an electrical signal through various methods. Soft artificial skin has earned overwhelming consideration in recent time due to the rise of diversified fields of science and technologies including the social interactive robots[1] internet of 'action' (Iowa)[2], modern health-monitoring technologies[3] prosthetics[4] and augmented reality, etc. In spite of several endeavor in developing soft artificial skin, there are still several considerable hurdles to make soft-ao-skin suitable for practical use and industrial-scale production. For instance, most of the earlier works on soft-ao-skin at least have one or the other inadequacies such as highly complex and expensive fabrication process, consume high power, low sensitivity, shows instability at long-term, high response time and short operational bandwidths etc.

Therefore, we have attempts to resolve those issues by exploiting a novel design of the soft optical waveguide with a strong promise of mass production and improved sensitivity i.e. possible to attain sensitivity more than 750 times higher than the sensitivity of earlier work based on optical waveguide strategy[5] and longer stability, less response time ~ 63 ms.

WORKING OF THE SOFT-AO-SKIN

Figure 1a and b depict the soft artificial optical skin cell (SAOS-Cell), where soft hemispherical lens (SHL) is without and with the contact of soft Dove prism (SDP) respectively. Clearly, with no contact as in Figure 1a, light from an LED in air medium (air RI ~1) parallel to the longitudinal axis of the prism enters one sloped side of the SDP, get total internal reflection (TIR) from the top surfaces and refract back to a photodetector (PT) without loss. On the other hand, in Figure 1b, a fraction of the light ray escapes from getting TIR from the top surface of the SDP where both lens and SDP are in physical contact. The contact between SHL and SDP creates a bridge of homogeneous circular area of same refractive index (RI) through which light passes and reaches to the edge of the SHL Figure 1b. Figure 1c shows the schematic representation of the arrangement

of array of light source and the array of array of photodetector to make a complete soft-ao-skin. Figure 1e shows image of a complete soft-ao-skin. The light sources and the photodetectors are attached to the soft waveguide by using 3D printed cages.

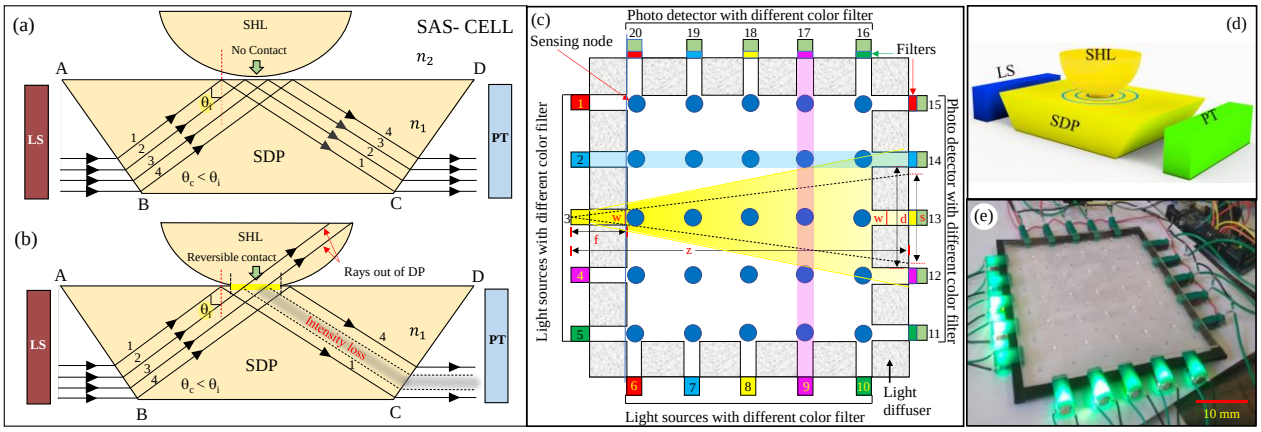

Figure 1*. Schematic representation of the working principle of electronic skin (soft-ao-skin). (a) Schematic diagram of soft-ao-skin unit cell (SAOS-Cell), a soft hemispherical lens (SHL) before touching a Dove prism shaped soft slab kept between light source (LS) and the photodetector (PT). Light passes through the SAOS-Cell from the LS to the PT without loss due to total internal reflection of light ray (TIRL). (b) SHL touches the surface of the SAOS-Cell, creates a circular contact area, light otherwise totally reflected, passes through the contact area in the expanse of lowering output intensity. (c) Schematic representation of soft-ao-skin with light sources and the array of detectors. (d) 3D representation of SAOS-Cell. (e)Image of the soft-ao-skin. (SDP- soft dove prism, SAOS- soft artificial optical skin).*

RESULTS

Figure 2a shows the schematic representation of a custom-designed instrument to calibrate the SAOS-Cell in terms of load and voltage. The PDMS soft hemispherical lens made using a hemispherical mold (with a diameter of 3 mm) is attached to a computer-controlled micro-stage to exert load on the PDMS SDP. Optical images were recorded from the top during the application of loads 0, 0.13, 0.53,1.17, and 2 N on the SDP through a soft hemispherical lens (Figure 2c-g). Figure 2c show that no light appears at the edge of the soft hemispherical lens at zero applied load, i.e., light rays travel through the SDP without any loss (barring negligible losses due to absorption by the PDMS) and reach the photodetector. As a result, the PT shows maximum intensity at the output. However, with increasing applied load, the intensity at the edge of the soft hemispherical lens increases (Figure 2c-g), and that at the output decreases proportionally. The contact formation between the soft hemispherical lens and the SDP is depicted by capturing the images at various loads by replacing PT with an optical camera (Figure 2h-l). These optical images also confirm that the contact area between the SDP and soft hemispherical lens increases with increased load.

Figure 3a shows a plot of the output voltage versus the applied load for SAOS-Cell made of various soft hemispherical lenses like PDMS, Ecoflex, and PDMS oligomer-filled hemispherical lens (OFHL). In all cases, for small, applied loads, a linear relationship is observed between the applied load through the soft hemispherical lens on the SDP and the cubic power of the output intensity (V_n^3). This can be explained through the solid-solid contact deformation model introduced by Johnson, Kendall, and Roberts in 1971, popularly known as the JKR model [6]. Briefly, the relation among the contact radius (a), work of adhesion (W), elastic modulus (E), and applied load (P) is as follows:

$$a^3 = \frac{R}{K}\{P + 3\pi WR + [6\pi WRP + (3\pi WR)^2]^{0.5}\} \quad (1)$$

Here,

$$\frac{1}{K} = (3/4)\left\{\frac{1-n_1^2}{E_1} + \frac{1-n_2^2}{E_2}\right\} \quad (2)$$

$$\frac{1}{R} = \frac{1}{R_1} + \frac{1}{R_2} \quad (3)$$

P is an external load, n_1 and n_2 are Poisson ratios of the materials, R is the radius of curvature of the soft hemispherical lens. Note that the result shows a linear relation between V_n and a, (SI, Figure S4a, measured for PDMS soft hemispherical lens), implying a linear relationship between F and V_n^3 up to a specific load.

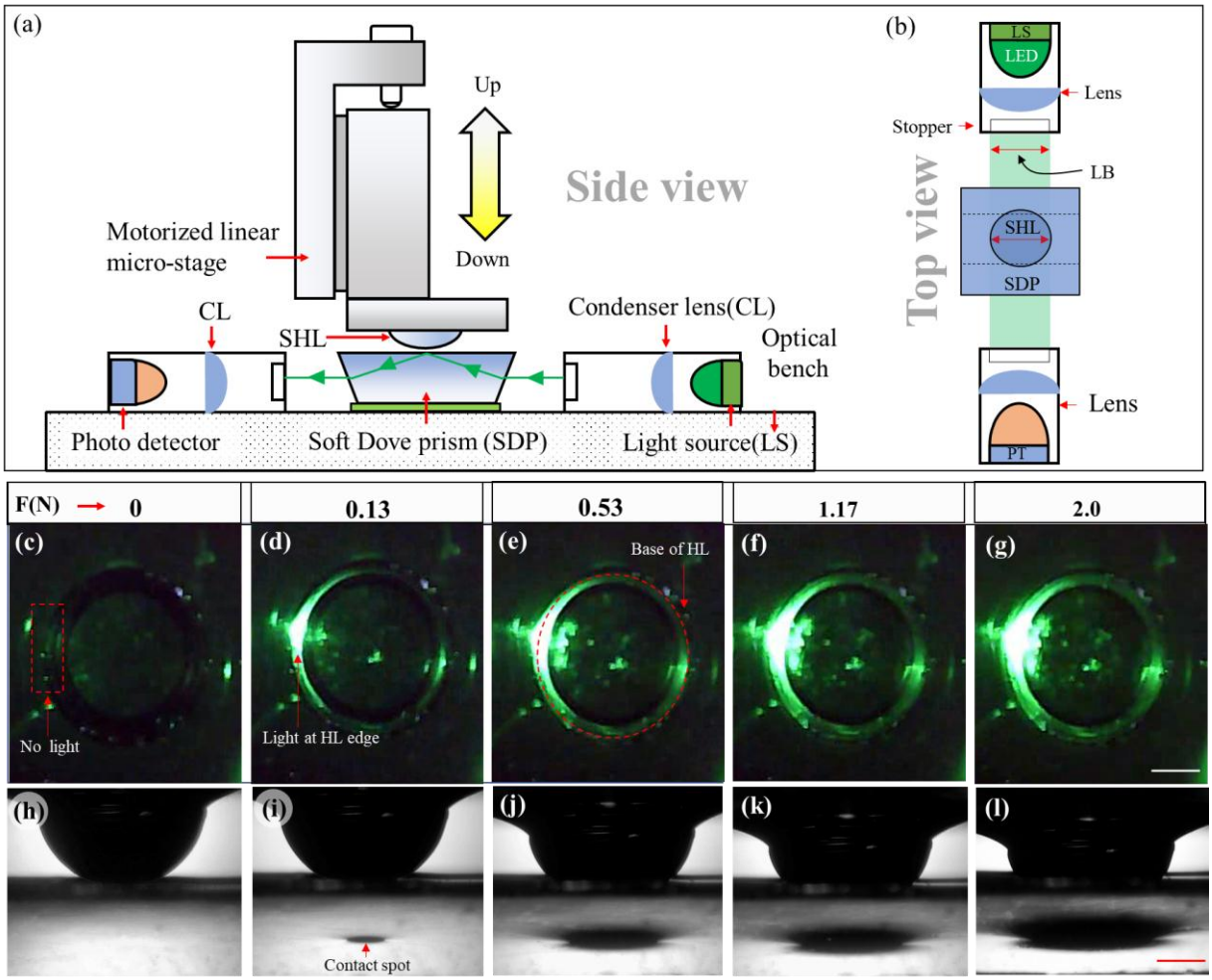

***Figure 2**: Characterization of the soft-ao-skin. (a) Schematic diagram from the side view of a custom-made characterization tool for a soft-ao-skin. (b) Top view schematic of the experimental setup. (c-g) Images captured from the top of the soft hemispherical lens (SHL) during the application of loads of 0, 0.13, 0.53,1.17, and 2 N, respectively, on the SHL. (h-l) Optical images corresponding to the loads 0, 0.13, 0.53,1.17, and 2 N, respectively, on SHL when viewed from the side (a camera replaces PT). The scale bar is 1 mm.*

PDMS SHL of diameter 3 mm shows excellent linear relation of applied load with V_n^3 up to ~1.2 N, however, beyond that load it follows nonlinearity. Within the linear region, the SAOS-units with SHL diameter 3mm show sensitivity as high as ~4.1, 13, and 21.2 $kPa^{-1}$for PDMS, Ecoflex and OFHL soft hemispherical lens respectively. The results show the sensitivity of the soft-ao-skin can be improved more than 3, and 5 folds when the PDMS SHL is replaced by material of lower modulus Ecoflex SHL and OFHL respectively. Figure 3b shows the voltage output with respect to various applied step loads. Figure 2c insert image shows the graph for finding the response time of the soft-ao-skin. The measurement shows the response time of SAOS is ~63 ms. Figure 3c the calibration estimation of the SAOS at various time to shows the robustness and durability of the SAOS. The experiment from 2 to 5 depict the calibration of the SAOS after 10 months and experiment 1 represent the calibration of the SAOS before 10 months. The results show the SAOS exhibits excellent reproducibility in terms of calibration with an accuracy of more than 99.56%. This result shows a superior long-term stability of the SAOS compared to many soft artificial skins reported earlier[7].

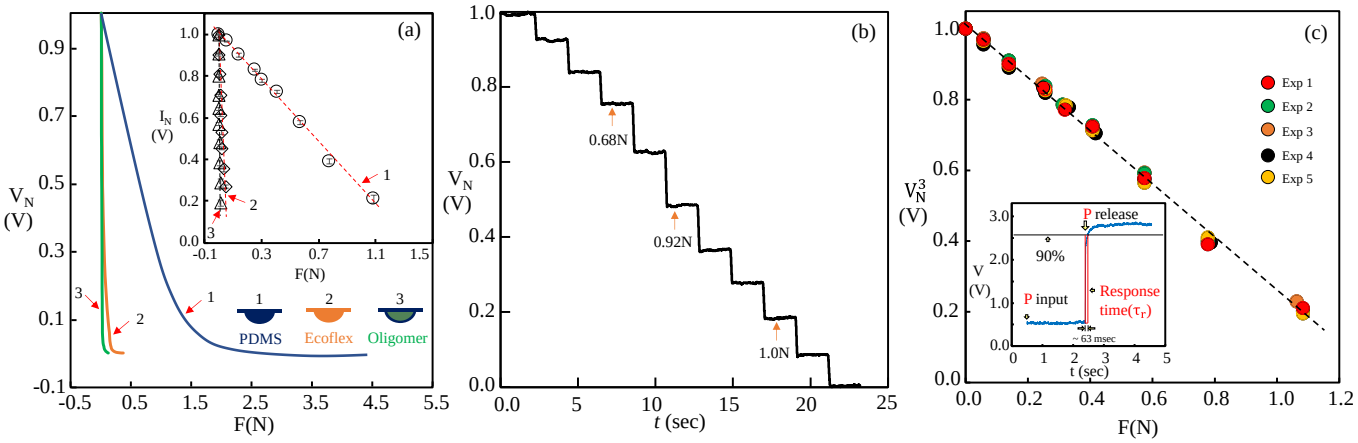

Figure 3*. Characterization of the soft-ao-skin unit node. (a) The plot shows the calibration between distance and load for various hemispherical lens of similar diameter 3mm. The curves 1, 2, and 3 depict SHL of 3 mm diameter made of PDMS, Ecoflex and PDMS membrane SHL filled with PDMS oligomer. (b) Step response in terms of normalized voltage at various applied loads and unloads. (c) Long term stability test in terms of soft-ao-skin calibration and response time (insert image). PDMS- Polydimethylsiloxane.*

DISCUSSION

The results show that the shape, *i.e.,* the curvature (κ), height (h), conic constant (k) of the hemispherical structure above the soft optical waveguide (SOW) plays an important role in determining the sensitivity (S) and the pressure detection range of the soft-ao-skin. The modulus of the soft hemispherical lens (considering other constant parameters) is also crucial in determining the sensitivity and pressure detection range of the soft-ao-skin. Another important finding from this work reveals that the waveguide design plays an important role in detecting the bending and spatial resolution of the soft-ao-skin. Results show that the sensitivity of the soft-ao-skin made of Ecoflex (Ecoflex-00-30) SHL with a mold-based technique and having a modulus ~ 0.07MPa is three times higher than soft-ao-skin made of PDMS SHL (PDMS: Crosslinking ratio;10:1) with modulus ~ 2MPa. Further, for a soft hemispherical lens made of the oligomer-filled hemispherical lens (OFHL, membrane thickness ~20 μm), a fivefold increment of sensitivity of the soft-ao-skin has been observed. However, this was accompanied by a reduction of pressure detection range from 350 kPa to 26 kPa. In the case of a 3D printed soft hemispherical lens, a sensitivity of 30kPa^{-1} is achieved, which in the case of oligomer filled SHL will lead to the maximum sensitivity of 150kPa^{-1} with a limit of detection (LoD) ~0.056 kPa(SI for LoD, Figure S10). In real-world applications, the sensor with ultra-high sensitivity at lower load regime and low sensitivity at higher load is desirable. The size of the sensing nodes will also play a role in the detection limit of the soft-e-skin. The smaller the sensing node's size, the lesser the detection limits would be. The waveguide design is important in determining the sensitivity, pressure detection range, the sensor nodes' spatial density, and the bendability of the soft-ao-skin. Using the LASER diode as a light source can give the advantage of not using a condenser lens in constructing soft-ao-skin. The result shows that if the soft-ao-skin is transparent, stray light may affect the performance of the soft-ao-skin depending upon the presence of environmental/stray light. Therefore, to overcome such a problem, an approach consists of a completely flexible opaque top membrane to obstruct the stray light can be deployed. Another attractive prospect of our soft-ao-skin is the use of SHLs as passive sensing elements rather than electrically connecting active/passive elements 6,29,31, which is usually vulnerable to disjointing. Hence, using the passive soft hemispherical lens gives the freedom to stretch the soft-ao-skin until the material fails. Considering the overall fabrication process of the soft-ao-skin, both the mold-based technique and 3D printing technique have their advantages and limitations; however, the 3D printing technique gives more freedom in tuning parameters of SHLs, and that gives the liberty to fine-tuning of soft-ao-skin parameters within a size limit of SHL. Also, the 3D printing technique is cost-effective compared to making new molds. One important issue with this soft-ao-skin is maintaining the position of the light source and photodetector unaltered after multiple uses by using 3D printed external holders. However, this issue can be addressed by introducing organic light-emitting diode (OLEDs) and organic photodetectors attached directly to the soft skin rather than attaching 3D printed holders.

In summary, many previous works have been reported on soft-ao-skin, however, most of them partially satisfy the criteria to be a complete realistically useable product for real-world use. For example, many previously reported soft-ao-skins show superior sensitivity but show long response time and instability in long term, etc. On the contrary, this work focuses on the realization of a practical, robust, suitable for industrial-scale production and easily scalable (3D printable) large-area soft artificial skin without compromising quality *i.e.* highly sensitive (750 times more sensitive), quick response time, bendability, stretchability etc. This reliable soft artificial skin is made by using a specially designed soft optical waveguide and soft hemispherical structure as a sensing node placed on the top of the waveguide. In addition, we have achieved significantly improved *i.e.* possible to attain sensitivity as high as 150 kPa^{-1} with a quick response of 63ms. The multifold increase in sensitivity is the outcome of a special design of the soft optical waveguide, and the unique aspherical soft hemispherical structures and their material property *e.g.* elastic modulus of the material. Moreover, we have observed the consistent performance of the soft-ao-skin up to almost a year, an indication of better reliability of the soft-ao-skin. Also, we have demonstrated a very convenient and cost-effective process of making the soft electronic skin by involving ultrafast liquid 3D printing technique (specially designed for this purpose) capable of printing large area with an ability of mass production.

ACKNOWLEDGEMENTS

The authors acknowledge funding from the Department of Science and Technology, DST, India and IISc Bangalore, India.

REFERENCES

[1] R. S. Dahiya, G. Metta, M. Valle, and G. Sandini, Tactile sensing-from humans to humanoids, IEEE Trans. Robot., vol. 26, no. 1, pp. 1–20, 2010.

[2] Q. Hua et al., Skin-inspired highly stretchable and conformable matrix networks for multifunctional sensing, Nat. Commun., vol. 9, no. 1, pp. 1–11, 2018.

[3] H. Keum, M. Mccormick, P. Liu, Y. Zhang, and F. G. Omenetto, RESEARCH ARTICLES Epidermal Electronics, vol. 333, 2011.

[4] A. Chortos, J. Liu, and Z. Bao, Pursuing prosthetic electronic skin, Nat. Mater., vol. 15, no. 9, pp. 937–950, 2016.

[5] M. Ramuz, B. C. K. Tee, J. B. H. Tok, and Z. Bao, Transparent, optical, pressure-sensitive artificial skin for large-area stretchable electronics, Adv. Mater., vol. 24, no. 24, pp. 3223–3227, 2012.

[6] Jo and and A. D. R. nson, L.L., K.Kendall, Surface energy and the contact of elastic solids, Proc. R. Soc. London. A. Math. Phys. Sci., vol. 324, no. 1558, pp. 301–313, Sep. 1971.

[7] T. Someya, T. Sekitani, S. Iba, Y. Kato, H. Kawaguchi, and T. Sakurai, A large-area, flexible pressure sensor matrix with organic field-effect transistors for artificial skin applications, Proc. Natl. Acad. Sci. U. S. A., vol. 101, no. 27, pp. 9966–9970, 2004.

DOI 10.24412/cl-37136-2023-1-76-81

PHOTOBIOMODULATION AT 660 NM PROMOTES CELL PROLIFERATION THROUGH THE RELEASE OF BASIC FIBROBLAST GROWTH FACTOR AND ACTIVATION OF THE GSK3B PATHWAY IN DIABETIC WOUNDED FIBROBLAST CELLS *IN VITRO*

SANDY JERE[1] AND NICOLETTE HOURELD[1]

[1] *Laser Research Centre, Faculty of Health Sciences, University of Johannesburg, South Africa.*

sandyj@uj.ac.za

ABSTRACT

Basic fibroblast growth factor (bFGF) is broadly used in the management of cutaneous wounds. Glycogen synthase kinase 3 beta (GSK3β) is a serine/threonine kinase and plays a major role in the control of β-catenin signalling. bFGF is a multipotent growth factor that stimulates cellular signalling for cell growth, proliferation, and migration in various cell types, including fibroblasts. Diabetes mellitus (DM) has been linked to atypical cell signalling processes thereby promoting the alteration of key cellular regulatory factors, membrane receptor proteins, and development of slow to heal wounds. Wound chronicity is common in DM, and is the main cause of non-traumatic limb amputation. Photobiomodulation (PBM) involves exposing wounds to light from lasers or light emitting diodes (LEDs) to induce healing. However, its mechanisms on fibroblast cellular proliferation remain unclear. In this investigation, WS1 skin fibroblast cells were split into diabetic (D) and diabetic wounded (DW) cell models, and were subjected to a continuous wave diode laser at a wavelength of 660 nm, power density of 11 mW/cm^2, and fluence of 5 J/cm^2. Non-treated cells (0 J/cm²) were used as controls. Following irradiation, cells were incubated for 48 h and evaluated for cell proliferation using the dimethylthiazol-diphenyltetrazolium bromide (MTT) assay, and the release of bFGF, phosphorylation of GSK3β, and β-catenin using the Enzyme-linked immunosorbent assay (ELISA). PBM significantly affected cell proliferation, the release of bFGF and activation of the GSK3β/β-catenin pathway in diabetic wounded fibroblast cells *in vitro*, suggesting that PBM at 660 nm with 5 J/cm^2 may be used to augment diabetic wound healing.

INTRODUCTION

Proliferation involves a series of events that take place within the cell and is regulated by growth factors that bind to their specific cell surface receptors. Cell surface receptors, also known as receptor tyrosine kinases (RTKs), are coupled to intracellular signalling proteins, including transcription factors [1]. The activation of RTKs initiates different signalling pathways that stimulate the expression of proteins to interact with other intracellular factors for cell proliferation. Cells proliferate or remain inactive using signalling pathways that communicate about their environment. Activation of the signalling pathways stimulates progression through the typical cell cycle. Signals initiated by growth factors, deoxyribonucleic acid (DNA) damage, and several other developmental indicators, influence the decision for DNA replication and cell proliferation. Deregulated activation of cell signalling is frequently accompanied with diseases such as diabetes and cancer [2, 3]. Basic fibroblast growth factor (bFGF) signalling advances proliferative, anti-apoptotic, anti-inflammatory, and migration progression in dermal fibroblasts during the wound healing process. In acute wound healing, bFGF and β-catenin interaction advances wound regeneration. The phosphorylation of GSK3β inhibits the degradation of β-catenin, causing cytoplasmic accumulation and nuclear translocation of active β-catenin for gene transcription [4, 5].

Diabetes mellitus (DM) refers to a group of metabolic diseases characterised by elevated blood sugar (hyperglycaemia) due to deficiencies in insulin action, secretion, or both, and over time, may lead to damage of the heart, eyes, blood vessels, kidneys, and nerves [6]. DM has become an increasingly prevalent disease worldwide. According to the International Diabetes Federation (IDF), approximately 540 million adults aged 20-80 (10%) were diabetic in 2021, and this number is expected to rise to approximately 645 million (11%) by 2030, and 785 million (12%) by 2045 [7]. Diminished healing of wounds affects approximately 25% of all

patients with DM, often leading to amputation of a lower limb [8]. Wound chronicity in diabetic patients develops due to several factors induced by high blood glucose (Fig 1). The presence of imbalanced matrix metalloproteinases (MMPs) and tissue inhibitors of metalloproteinases (TIMP) affects the release and function of growth factors and blocks several signalling pathways, leading to poor wound and tissue restoration [9]. Treatment of chronic diabetic wounds with synthetic growth factors have the potential to mediate wound healing at different phases of the healing process, stimulating changes in molecular and cellular reactions including the formation of granulation tissue, angiogenesis, and re-epithelization. However, their bioavailability and action in the wound milieu is diminished due to increased action of MMPs which continuously degrade both growth factors and their cell surface receptors [10].

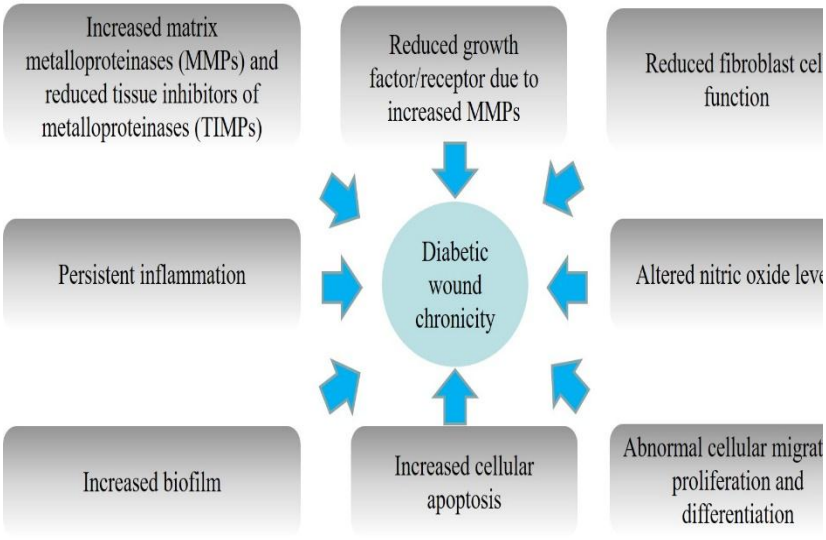

Figure 1: *Factors affecting wound healing in diabetic patients.*

Photobiomodulation (PBM) is initiated by low-level light from lasers or light emitting diodes (LEDs) or both, and interacts with cellular chromophores to stimulate or inhibit biological activities [9]. The explanation of the effect and mechanism of PBM at a molecular, cellular, and tissue level remains indefinable. It is proposed however, that its impact is affected by the fluence, wavelength, output power, and time. Photoreceptors in the mitochondria, such as cytochrome c oxidase, and other cellular partitions absorb the light, converting it into photochemical energy with a subsequent increase in the production of adenosine triphosphate (ATP), synthesis of proteins, and cell proliferation [11]. PBM has shown to have stimulatory, anaesthetic, and anti-inflammatory effects in tissue and wound regeneration [12]. In addition, PBM is capable of altering the action of MMPs and enhance collagen production in chronic diabetic wounds [13]. Ayuk *et al*., [14] reported a significant rise in cell proliferation and viability in diabetic wounded cells irradiated at a wavelength of 660 nm with a fluence of 5 J/cm^2 *in vitro*. The aim of this study was to assess the effect of PBM at a wavelength of 660 nm and a fluence of 5 J/cm^2 on proliferation, the release of bFGF, and activation of the GSK3β/β-catenin pathway in diabetic wounded fibroblast cells *in vitro*.

METHODOLOGY

WS1 human skin fibroblast cells (ATCC®, CRL-1502™) were cultivated using standard culture procedures. Two cell models were used in the study, namely diabetic (D) and diabetic wounded (DW). An *in vitro* diabetic model was achieved by continuously cultivating WS1 cells in supplemented minimum essential medium (MEM) with an additional 17 mM D-glucose, thereby mimicking a hyperglycaemic condition [15]. To perform experiments, cells (6 X 10^5) were cultivated in 3.4 cm diameter tissue culture plates and incubated at 37°C in 5% CO_2 for attachment. After 24 h, a central scratch was performed 30 min pre-irradiation in the wounded cell model (DW), thereby creating a cell free zone bordered by cells on both sides of the "wound" in the confluent monolayer [16]. Cell culture plates, with the lids off, were exposed to laser light from above in the dark. Table 1 shows the laser parameters used. Cells were irradiated at a wavelength of 660 nm and a fluence of

5 J/cm^2, after which cells were incubated for 48 h. Cells were analysed for cell proliferation using the dimethylthiazol-diphenyltetrazolium bromide (MTT) assay (Sigma Aldrich, 11465007001), and the release of bFGF into the culture media (Human FGF basic ELISA Kit (FGF2), BIOCOM Africa, Abcam, ab99979), phosphorylation of GSK3β (p-GSK3 beta (Ser9) InstantOne ELISA™ Kit, ThermoFisher Scientific, 85-86172), and β-catenin (Human Beta Catenin ELISA Kit, BIOCOM Africa, Abcam, ab275100) using the enzyme-linked immunosorbent assay (ELISA). Unirradiated cells were used as controls (0 J/cm^2). All experiments were repeated three times (n=3), and for ELISA, tests were done in duplicate, the average of which was used. SigmaPlot version 14 (Systat Software, Inc.) was used for statistical analysis. Statistical differences between groups was determined by the Student *t* test. Analysis of variance (ANOVA) followed by Dunnett's test was used to compare differences between D and DW cell models. Results are shown as standard error of the mean (SEM), and statistical significance is shown in the graphs as *p<0.05, **p<0.01 and ***p<0.001.

Table 1. *Laser parameters.*

Light source	Diode laser
Wavelength (nm)	660
Emission	Continuous wave
Power output (mW)	101
Power density (mW/cm^2)	11
Spot size (cm^2)	9.1
Energy density (J/cm^2)	5
Irradiation time	7 min 35 s
Energy (J)	46

RESULTS

In this study, PBM at a wavelength of 660 nm with a fluence of 5 J/cm^2 significantly reduced cellular proliferation in PBM treated D cells (p<0.01) and significantly increased proliferation in DW cells (p<0.05) when compared to their control cells at 48 h. There was a significantly increased cellular release of bFGF in PBM treated D cells (p<0.05) and DW cells (p<0.01) when compared to their control cells at 48 h (Figure 1). When compared to non-treated D cells using ANOVA, a significant decrease in proliferation was noted in non-treated DW cells (p<0.01), and a significant increase in treated DW cells when compared to treated D cells (p<0.05). There was no difference in the release of bFGF in non-treated and treated DW cells when compared to non-treated and treated D cells, respectively.

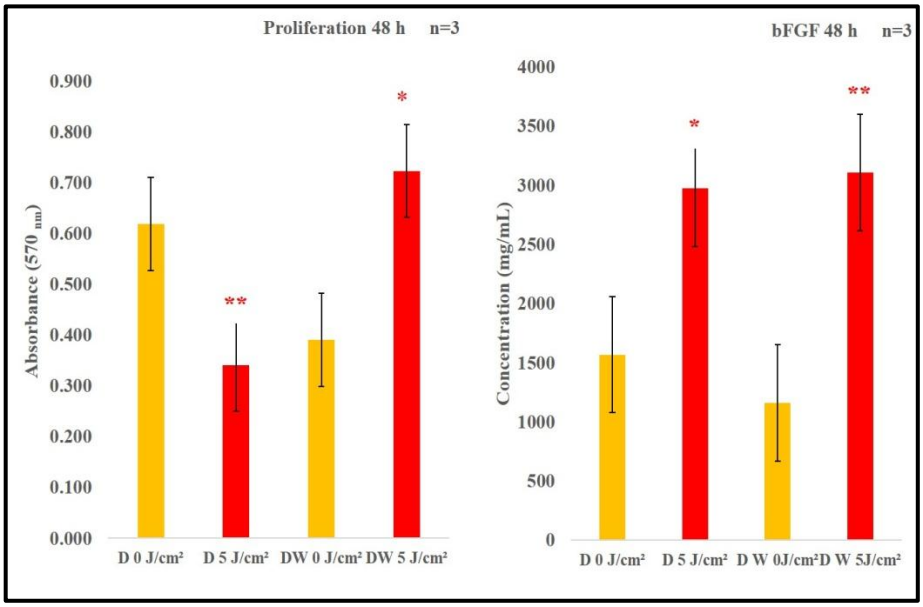

Figure 1: *Cell proliferation and the release of basic fibroblast growth factor (bFGF) in the media were assessed by the dimethylthiazol-diphenyltetrazolium bromide (MTT) assay and the enzyme-linked immunosorbent assay (ELISA), respectively at 48 h in non-treated (0 J/cm^2) and photobiomodulation (PBM) treated (5 J/cm^2) diabetic (D 0 J/cm^2; D 5 J/cm^2) and diabetic wounded (DW 0 J/cm^2; DW 5 J/cm^2) cells. Significant probability is shown as **P<0.01 and *P<0.05 ±SEM.*

PBM at a wavelength of 660 nm with a fluence of 5 J/cm^2 significantly increased the inactive form of GSK3β in PBM treated D cells ($p<0.05$) and DW cells ($p<0.001$) when compared to their non-treated control cells at 48 h. There was also a significant increase in total β-catenin in PBM treated D cells and DW cells ($p<0.05$) (Figure 2). When compared to non-treated D cells using ANOVA, a significantly decreased inactivated form of GSK3β was noted in non-treated DW cells ($p<0.01$), and no significant difference was noted in treated DW cells when compared to treated D cells. There was no difference in total β-catenin in both non-treated and treated DW cells when compared to non-treated and treated D cells, respectively.

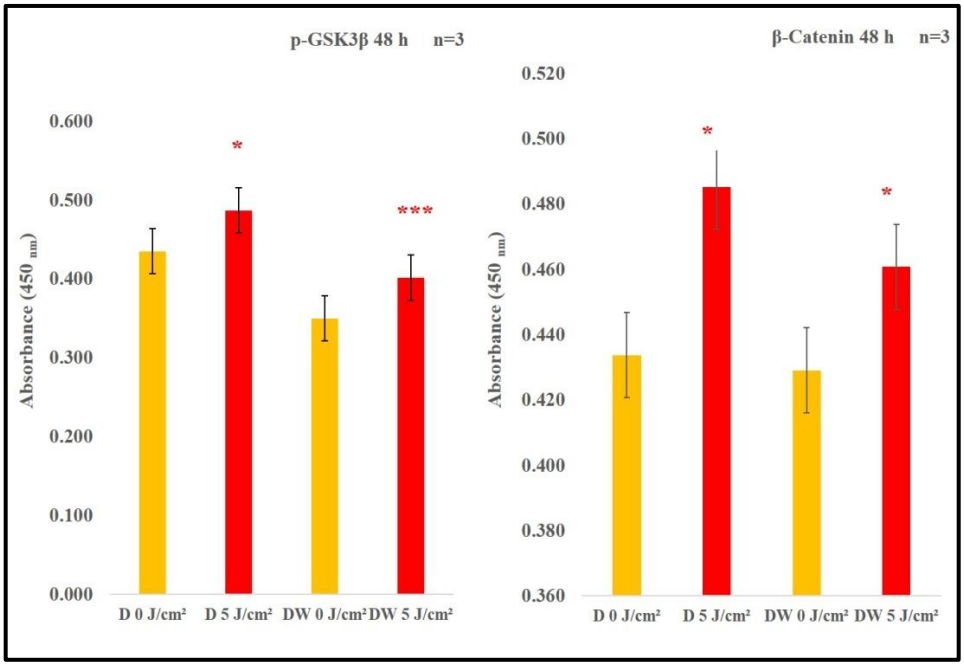

Figure 2: *Phosphorylated (inactivated) glycogen synthase kinase 3 beta (p-GSK3β), and beta (β-) catenin were determined by the enzyme-linked immunosorbent assay (ELISA) 48 h post-photobiomodulation (PBM) in non-treated (0 J/cm^2) and PBM treated (5 J/cm^2) diabetic (D 0 J/cm^2; D 5 J/cm^2) and diabetic wounded (DW 0 J/cm^2; DW 5 J/cm^2) cells. Significant probability is shown as ***P<0.001 and *P<0.05 ±SEM.*

DISCUSSION AND CONCLUSION

The cellular environment dictates whether cells proliferate or remain inactive via different cellular signalling pathways that initiate the cell cycle. The decision to enter the synthesis (S) phase of the cell cycle, in which DNA is replicated, is mostly influenced by growth factors, DNA damage, and developmental signals [17]. During cell proliferation, cells divide and increase in number through a tightly controlled and precise mechanism that occurs in both acute as well as chronic wounds [18]. Fibroblast cells are vital in reinforcing the normal wound healing process, and are implicated in major processes including resolving the fibrin clot, and depositing and constructing new extracellular matrix (ECM) and collagen that support other cells associated with wound healing. Fibroblasts help in contracting the wound and respond to injury by proliferating and migrating to the injured sites [19]. Buranasin et al. [20] mentioned that hyperglycaemia impairs fibroblast cell proliferation and migration due to high glucose-stimulated oxidative stress. Chronic hyperglycaemia causes greater stiffness to the skin, such that it becomes less flexible, making it more prone to injury mainly due to differences in the synthesis of collagen and its degradation [20]. These suggestions give explanation to the delayed wound healing in patients with impaired glucose metabolism and alterations in micro- and macro-vascular circulation, advancing the risk of postponed wound healing [21].

Although PBM has demonstrated its capability to treat chronic wounds, the absence of distinct parameters and a complete understanding of its effect at both a cellular and molecular level hinders its adoption as a

treatment method in the management of chronic wounds. This study assessed the effect of PBM at a wavelength of 660 nm and a fluence of 5 J/cm^2 on proliferation, the release of bFGF and the activation of the GSK3β and β-catenin signalling pathway in diabetic wounded fibroblast cells *in vitro*. In this study, unirradiated diabetic wounded cells exhibited a significant decrease in cell proliferation as compared to unirradiated diabetic cells, indicating that wounding contributes to reduced cell proliferation. This study noted a significant increase in cell proliferation in irradiated diabetic wounded cells compared to their unirradiated controls, indicating the effect of PBM. In addition, irradiated diabetic wounded cells exhibited a significant increase in proliferation compared to irradiated diabetic cells. This shows that diabetic wounded cells respond more favourably to PBM than diabetic cells, possibly due to wounding as more stressed cells respond effectively to PBM [16]. Giannakopoulos et al. [22], demonstrated that PBM at 661 nm activates both cell migration and proliferation *in vitro*. A comparison study by Zhao et al. [23], suggested that LED-mediated PBM (630 nm and 810 nm) stimulates wound healing through the progression of fibroblast cell proliferation and release of growth factors. In agreement to these findings, this study observed a significant increase in the release of bFGF in irradiated cells as compared to their unirradiated controls, indicating that indeed PBM induces the release of growth factors, a critical aspect in wound healing as growth factors are essential for cell proliferation, migration, and vascularisation. In chronic wounds, growth factor levels are reduced due to both decreased production and extreme protease-mediated degradation [24]. bFGF promotes cell proliferation by phosphorylating and thereby inhibiting the activity of GSK3β [25]. This study observed a significant increase in p-GSK3β (inactive form of the protein which allows activation of downstream proteins), as well as its downstream substrate β-catenin in cells that were irradiated. These findings signify an effectual therapeutic approach and provides an experimental basis to support PBM in the visible red spectrum as a possible option to stimulate fibroblast cell proliferation in chronic diabetic wounds. Nevertheless, further studies including clinical, are needed to expose more about the effect initiated by PBM at 660 nm and a fluence of 5 J/cm² on cellular phenotypic variations at a molecular level.

REFERENCES

[1] Z. Wang, Regulation of Cell Cycle Progression by Growth Factor-Induced Cell Signaling. Cells. 3327, 2021. doi: 10.3390/cells10123327.

[2] N. Xu, Y. Lao, Y. Zhang, D.A. Gillespie. Akt: a double-edged sword in cell proliferation and genome stability. J Oncol. 951724, 2012. doi: 10.1155/2012/951724.

[3] Response to the Cellular Signal - Cell Signaling and Cell Growth. https://bio.libretexts.org/@go/page/13225. Accessed 26 April 2023.

[4] K. Chen, Y. Li, X. Zhang, R. Ullah et al., The role of the PI3K/AKT signalling pathway in the corneal epithelium: recent updates. Cell Death Dis. 513, 2022. https://doi.org/10.1038/s41419-022-04963-x.

[5] A.L. Carre, M.S. Hu, A.W. James, K. Kawai et al., β-Catenin-Dependent Wnt Signaling: A Pathway in Acute Cutaneous Wounding. Plast Reconstr Surg. 669-678, 2018.

[6] World Health Organisation (WHO). https://www.who.int/health-topics/diabetes#tab=tab_1. Accessed 08/05/2023.

[7] IDF Diabetes Atlas 2022 Reports. https://diabetesatlas.org/2022-reports/. Accessed 08/05/2023.

[8] J.L. Burgess, W.A. Wyant, B. Abdo Abujamra, R.S. Kirsner et al., Diabetic Wound-Healing Science. Medicina (Kaunas). 1072, 2021. doi: 10.3390/medicina57101072.

[9] N.K. Rajendran, N.N. Houreld, H. Abrahamse, Photobiomodulation reduces oxidative stress in diabetic wounded fibroblast cells by inhibiting the FOXO1 signaling pathway. J Cell Commun Signal. 195-206, 2021.

[10] S.F. Spampinato, G.I. Caruso, R. De Pasquale, M.A. Sortino et al., The Treatment of Impaired Wound Healing in Diabetes: Looking among Old Drugs. Pharmaceuticals (Basel). 60, 2020. doi: 10.3390/ph13040060.

[11] S. Passarella, T. Karu, Absorption of monochromatic and narrow band radiation in the visible and near IR by both mitochondrial and non-mitochondrial photoacceptors results in photobiomodulation. Journal of Photochemistry and Photobiology. B, Biology. 344-58, 2014.

[12] R.K. Chittoria, S.H. Kumar, 2018, In: Shiffman, M., Low, M. (eds) Chronic Wounds, Wound Dressings and Wound Healing. Recent Clinical Techniques, Results, and Research in Wounds 6. Springer, Cham. https://doi.org/10.1007/15695_2017_89.

[13] S.M. Ayuk, H. Abrahamse, N.N. Houreld, The Role of Matrix Metalloproteinases in Diabetic Wound Healing in relation to Photobiomodulation. J Diabetes Res. 2897656, 2016. doi: 10.1155/2016/2897656.
[14] S.M. Ayuk, N.N. Houreld, H. Abrahamse, Effect of 660 nm visible red light on cell proliferation and viability in diabetic models in vitro under stressed conditions. Lasers Med. Sci. 1085-1093, 2018.
[15] N.N. Houreld, T.M. Roland A. Heidi, Low-intensity laser irradiation at 660 nm stimulates cytochrome c oxidase in stressed fibroblast cells. Lasers Surg. Med. 429-434, 2012.
[16] S.M. Ayuk, N.N. Houreld, H. Abrahamse, Collagen production in diabetic wounded fibroblasts in response to low-intensity laser irradiation at 660 nm. Diabetes Technol. Ther. 1110-1117, 2012. doi:10.1089/dia.2012.0125.
[17] R.J. Duronio, Y. Xiong, Signaling pathways that control cell proliferation. Cold Spring Harb Perspect Biol. a008904. 2013. doi: 10.1101/cshperspect.a008904.
[18] I. Srdanovic, N. Yang, S. Ray, Cell proliferation, Reference Module in Biomedical Sciences, Elsevier, 2022, ISBN 9780128012383. https://doi.org/10.1016/B978-0-12-824315-2.00216-5.
[19] P. Bainbridge, Wound healing and the role of fibroblasts. J. Wound Care. 410-412, 2013.
[20] V. Goulding, The effects of diabetes on collagen within wound healing. Diabet. Foot. 75–80, 2015.
[21] P. Buranasin, K. Mizutani, K. Iwasaki, C.P. Mahasarakham et al., High glucose-induced oxidative stress impairs proliferation and migration of human gingival fibroblasts. PLoS One. e0201855, 2018. doi: 10.1371/journal.pone.0201855.
[22] E. Giannakopoulos, A. Katopodi, M. Rallis, K. Politopoulos et al., The effects of low power laser light at 661 nm on wound healing in a scratch assay fibroblast model. Lasers Med. Sci. 27, 2023. https://doi.org/10.1007/s10103-022-03670-5.
[23] H. Zhao, T. Ji, T. Sun, H. Liu et al., Comparative study on Photobiomodulation between 630 nm and 810 nm LED in diabetic wound healing both in vitro and in vivo. J. Innov. Opt. Health Sci. 2250010, 2022. doi: 10.1142/s1793545822500109.
[24] T.N. Demidova-Rice, M.R. Hamblin, I.M. Herman, Acute and impaired wound healing: pathophysiology and current methods for drug delivery, part 2: role of growth factors in normal and pathological wound healing: therapeutic potential and methods of delivery. Adv Skin Wound Care. 349-370, 2012.
[25] Z.C. Liu, H.S. Wang, G. Zhang, H. Liu et al., AKT/GSK-3β regulates stability and transcription of snail which is crucial for bFGF-induced epithelial-mesenchymal transition of prostate cancer cells. Biochimica et biophysica acta.3096-3105, 2014.

DOI 10.24412/cl-37136-2023-1-82-89

PHOTOBIOMODULATION IMPROVES WOUND HEALING THROUGH ACTIVATION OF THE RAS/MAPK AND PI3K/AKT PATHWAY

NICOLETTE HOURELD[1]

[1]*Laser Research Centre, University of Johannesburg, South Africa*

nhoureld@uj.ac.za

ABSTRACT

Diabetes mellitus (DM) is a metabolic non-communicable disease (NCD) that has been declared as a global burden, imposing a significant challenge to the health and well-being of individuals, families, and societies. According to the International Diabetes Federation (IDF), the global estimated prevalence of DM in 2021 stood at 537 million cases (adults aged 20-79; 1 in 10 of the world's population in this age group), with the largest increase seen in low- and middle-income countries [1]. The number of people with DM on the African continent in 2021 stood at 24 million (1 in 22 adults) and is thought to increase to 55 million by 2045 (an increase of 134%) [1]. The reality of these figures is probably much higher; over 1 in 2 people (54%) living with DM on the African continent are undiagnosed. South Africa is among the top 5 countries in the African region for age-adjusted prevalence of people with diabetes (20–79 years), with a prevalence of 10.8%, falling in 4th behind the Comoros (11.7%), Zambia (11.9%), and United Republic of Tanzania (12.3%) [1]. The proportion of deaths related to diabetes among people under the age of 60 in South Africa in 2021 stood between 9-12% [1]. DM is one of the fastest growing global health emergencies of the 21st century [2].

People living with DM are at risk of developing several life-threatening complications, leading to an increased need for medical care. Patients with DM repeatedly suffer from non-healing, chronic and frequently debilitating lower limb ulcers, which often necessitate amputation. Diabetic foot ulcers (DFUs) have a negative impact on patient quality of life and are a major source of preventable morbidity. The lifetime risk of developing a DFU stands at 19-34%, with recurrence rates as high as 65% at 3-5 years, a lifetime lower-extremity amputation incidence of 20%, and 5-year mortality of 50-70% [3]. Diabetic foot and lower limb complications, which affect 40 to 60 million people with diabetes globally, is the leading cause for non-traumatic lower limb amputations. It has been estimated that, globally, a lower limb (or part thereof), is lost to amputation every 30 seconds as a consequence of DM [2]. Several underlying pathologies contribute to the impaired wound healing seen in diabetes. These include, but not limited to, increased oxidative stress, inflammation and infection, and decreased immunity and angiogenesis. There is also decreased fibroblast migration and proliferation, often due to disturbances in essential growth factors and signal transduction pathways involved in the wound healing process. DFUs pose a major physical, social, and economic burden on patients and the public health sector and has caused an increase in the demand for effective and safe treatment modalities.

Current treatments for DFUs have not resulted in consistently lower amputation rates, and treatments are challenging, lengthy, costly, and associated with failure to heal and relapse and there is a demand for efficient wound healing interventions [3]. In recent years great emphasis has been directed at using photobiomodulation (PBM) to stimulate and accentuate cellular processes to contribute to more efficient resolution of wound healing, including DFUs. PBM, previously referred to as low-level laser therapy (LLLT), utilises non-thermal light at specific wavelengths (typically between 600 and 1,200 nm) to induce cellular photochemical and physiological changes and provide therapeutic benefits. PBM has been shown to stimulate cellular migration and proliferation, reduce inflammatory markers and increase the synthesis of various growth factors *in vitro*, and speed up the healing of wounds *in vivo*, including diabetic ulcers. Although PBM has been used with great success and no reported side-effects, and despite a significant focus on the photochemical mechanisms underlying PBM, its complex functions are yet to be fully elucidated [4].

PBM has been shown to have several positive effects on hyperglycaemic cells [5-8], stimulating cellular migration and proliferation [8], decreasing oxidative stress and inflammatory markers [7,9], and speeding up the

healing of DFUs [10,11]. Two recent reviews have highlighted the effects of PBM on signalling pathways [12,13]. Jere and colleagues [14] demonstrated that PBM at a wavelength of 660 nm and a fluence of 5 J/cm^2 was able to stimulate the release of epidermal growth factor (EGF) and activate the Janus kinase/Signal transducer and activators of transcription (JAK/STAT) signalling pathway. The same authors also showed the up-regulation of genes involved in this pathway [15]. Due to the multitude of transduction signals involved in the process of wound healing, more pathways may be activated in response to PBM.

This study aimed to investigate the effect of PBM at 660 nm on cellular migration, proliferation, and survival through activation of the PI3K/AKT and Ras/MAPK signalling pathway in a diabetic wounded fibroblast cell model. To achieve this, human skin fibroblast cells (WS1) were modeled into a wounded (W) and diabetic wounded (DW) *in vitro* cell model. A wound was simulated via the central scratch assay (Fig. 1), and a diabetic cell model was created by continuously growing the cells for several passages in high glucose media (22.6 mM glucose) [5-8,16,17]. For experiments (n=3), 6 X 10^5 cells were seeded into 3.4 cm diameter culture plates and incubated for 24 h. Thirty minutes prior to PBM, a 'wound' was created, and cells received PBM at a wavelength of 660 nm with a fluence of 5 J/cm^2 (power output density 11 mW/cm^2; energy 47.7 J; irradiation time 454 s). Unirradiated cells served as controls (0 J/cm^2). Cellular migration rate, proliferation, and survival (viability) was determined 24 and 48 h post-PBM. Proteins and receptors involved in the PI3K/AKT (PI3K, AKT1, mTOR1, and GSK3β) and Ras/MAPK (bFGFR,Ras, MEK1/2, MAPK) signalling pathway were evaluated, as were the growth factors vascular epithelial growth factor (VEGF) and basic fibroblast growth factor (bFGF) as activators of the pathways respectively.

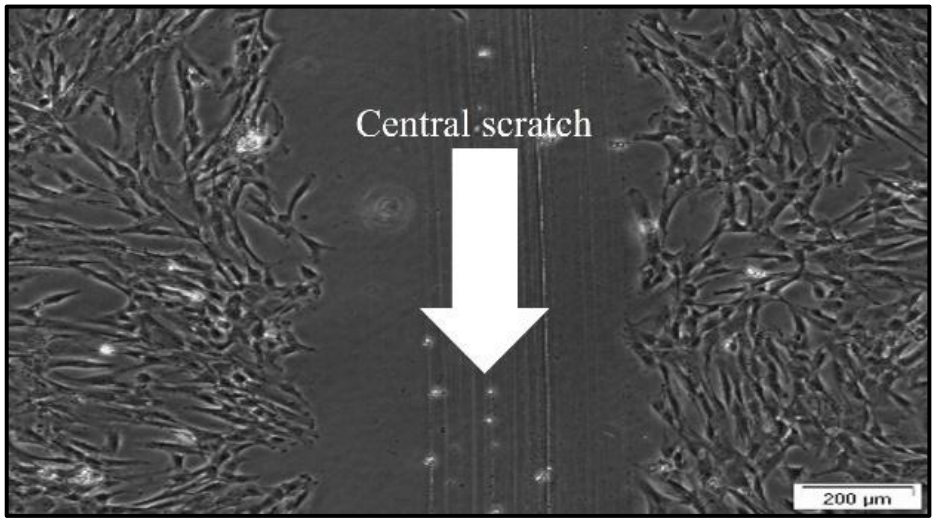

Figure 1: *Micrograph showing the 'wound' (central scratch). Magnification x200 [16].*

The distance between the wound margins were measured and used to calculate migration rate using the formula

$$(T_{0h} - T_{xh})/T_{0h} \times 100$$

where T_{0h} is the initial length connecting the borders edges of the 'wound' at 0 h, and T_{xh} is the succeeding measurement between the edges of the 'wound' at 24 or 48 h respectively. Post-PBM at 660 nm with 5 J/cm^2, wounded and diabetic wounded cells exhibited a significant increase in cellular migration rate (Table 1), and diabetic wounded cells showed complete 'wound closure' at 48 h, with no gaps visible in the central scratch.

Table 1: *Average rate for cellular motility in wounded and diabetic wounded cells. Significant probability as compared with respective control (0 J/cm^2) cells is shown *P ≤ 0.05, **P ≤ 0.01 and ***P ≤ 0.001 [5].*

	Wounded		Diabetic Wounded	
	0 J/cm^2	5 J/cm^2	0 J/cm^2	5 J/cm^2
24 h	50.50%	66.60%*	20.60%	79.70%***
48 h	83.10%	99.90%*	62%	100%**

Wounded and diabetic wounded cells exposed to PBM at 660 nm with 5 J/cm^2 showed a significant increase in actively proliferating cells (S phase) as determined by 5-bromo-2′-deoxyuridine (BrdU) and 7-aminoactinomycin D (7-AAD) staining as measured by flow cytometry 24 and 48 h post-PBM (Fig. 2).

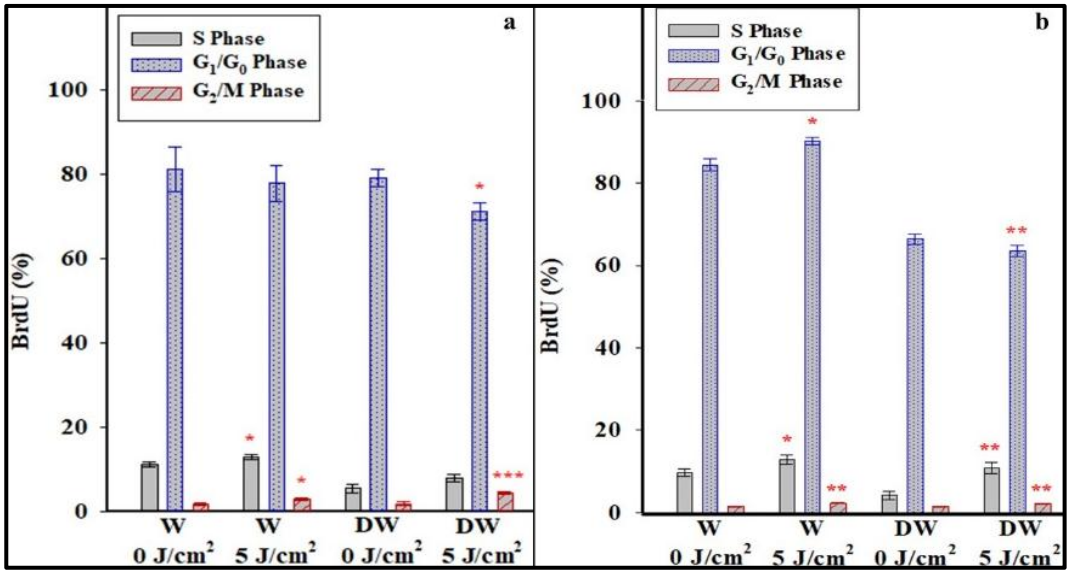

Figure 2: *Changes in percentage of cells in the proliferating (S), resting/preparing for DNA synthesis (G0/G1) and mitotic (G2/M) phases of the cell cycle at 24 h (a) and 48 h (b) following PBM at 660 nm with 5 J/cm^2 in wounded (W) and diabetic wounded (DW) cells. Significant probability as compared with respective control (0 J/cm^2) cells is shown as * P≤ 0.05 ** P ≤ 0.01 and *** P ≤ 0.001(SEM) [5].*

Cellular viability/survival was determined by the Trypan blue exclusion assay at 24 and 48 h post-PBM. Cell viability significantly increased in both the wounded and diabetic wounded models at 24 h, and in the diabetic wounded model at 48 h (Fig. 3).

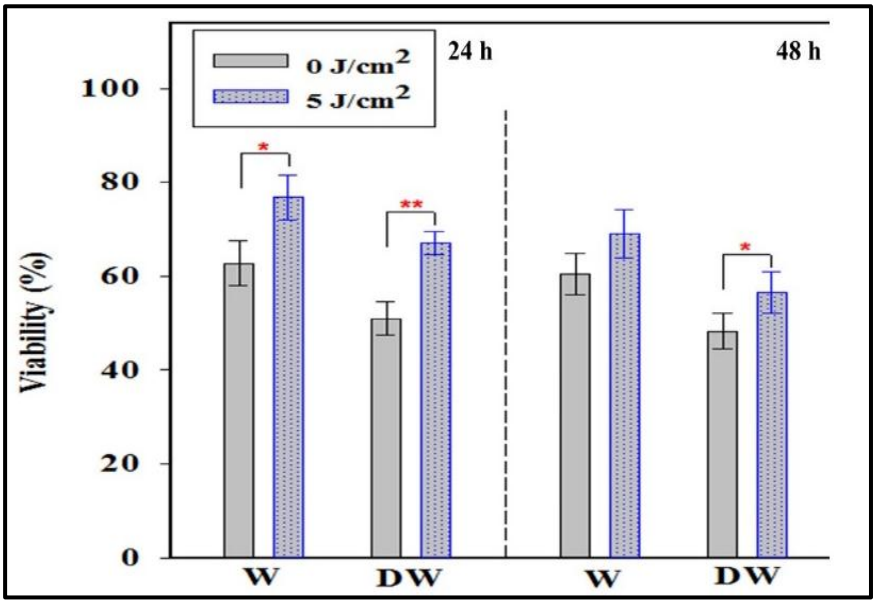

Figure 3: *Percentage cellular viability at 24 and 48 h post-PBM at 660 nm in wounded (W) and diabetic wounded (DW) cells. Significant probability as compared with respective control (0 J/cm^2) cells is shown as * P≤ 0.05 and ** P ≤ 0.01 (SEM) [5].*

The binding of ligands to their receptor stimulates downstream signalling pathways including the PI3K/AKT/mTOR pathway. Upon receptor binding, phosphorylation of phosphatidylinositol 3-kinase (PI3K)

activates the downstream serine/threonine protein kinase B (PKB; also known as AKT). Downstream targets of AKT includes the mammalian target of rapamycin complex (mTOR), forkhead box O1 (FOXO1), and glycogen synthase kinase-3 beta (GSK3β). GSK3β is active in its unphosphorylated form, thus the phosphorylation of GSK3β by AKT results in its inactivation, necessary for wound healing. mTOR controls the expression of cytokines, including VEGF [18]. Activation of the PI3K/AKT/mTOR pathway control different cellular functions such as cell proliferation, growth, metabolism, and survival [19]. Post-PBM at 660 nm, stimulation of the PI3K/AKT signalling pathway was determined by measuring the phosphorylation (activation) of AKT1, mTOR1 and PI3K by western blotting (Fig. 4). ELISA was used to measure total GSK3β and phosphorylated GSK3β (Ser9) (Fig. 5) and VEGF (Fig. 6). Wounded models showed a significant increase in PI3K at 24 and 48 h post-PBM, in p-AKT at 48 h, and a significant increase in total GSK3β at 24 h. PI3K and p-AKT was significantly increased in diabetic wounded models at both 24 and 48 h, while p-mTOR was significantly increased at 48 h. Diabetic wounded models showed no change in total GSK3β, but showed a significant increase in p-GSK3β at 24 and 48 h, as well as a significant increase in VEGF at both time points.

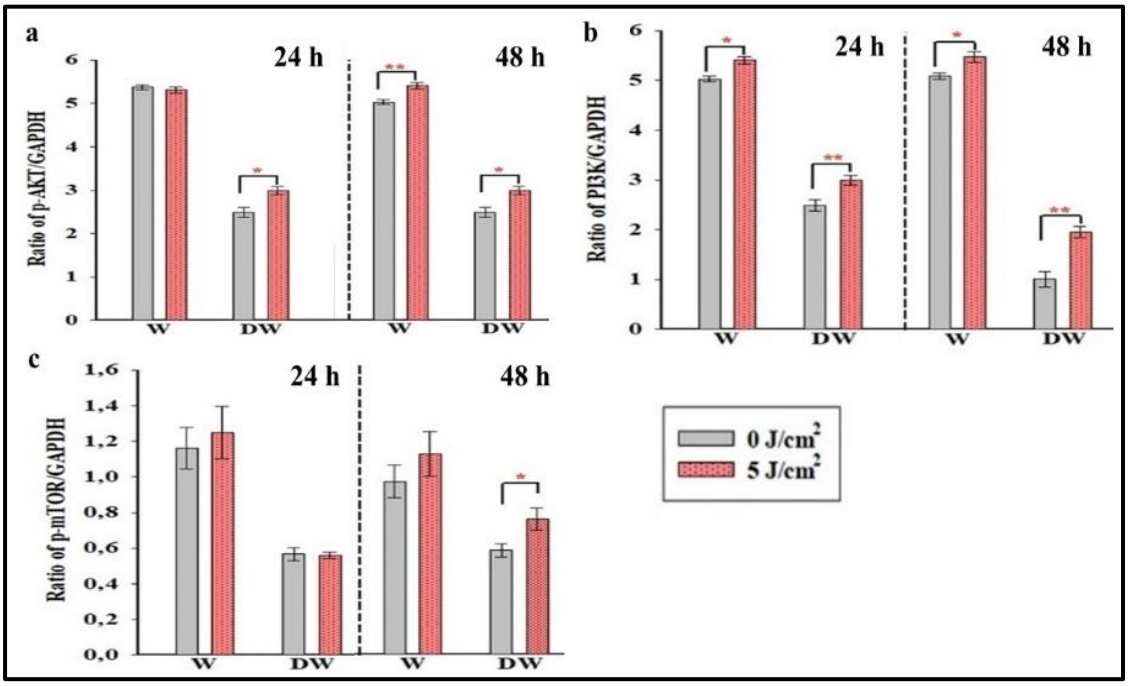

Figure 4: *Phosphorylated (p-) AKT (a), PI3K (b), and p-mTOR (c) was determined post-PBM at 660 nm in wounded (W) and diabetic wounded (DW) cells at 24 and 48 h. GAPDH was utilised as a loading control. Significant probability as compared with respective control (0 J/cm^2) cells is shown as *P ≤ 0.05, and **P ≤ 0.01 (SEM) [16].*

Binding of FGF to its receptor, FGFR results in the phosphorylation of FGFR and stimulation of downstream signalling pathways, including the Ras/MAPK pathway. Phosphorylation of FGFR activates Ras, which results in the phosphorylation of MEK1/2, that in turn phosphorylates and activates MAPK. MAPK is translocated to the nucleus where it activates genes involved in cellular proliferation, migration, differentiation, and angiogenesis. In this study, bFGF, p-Ras, p-MEK1/2 and p-MAPK was determined in wounded and diabetic wounded cell models by ELISA 24 and 48 h post-PBM at 660 nm. p-FGFR was measured by western blotting.

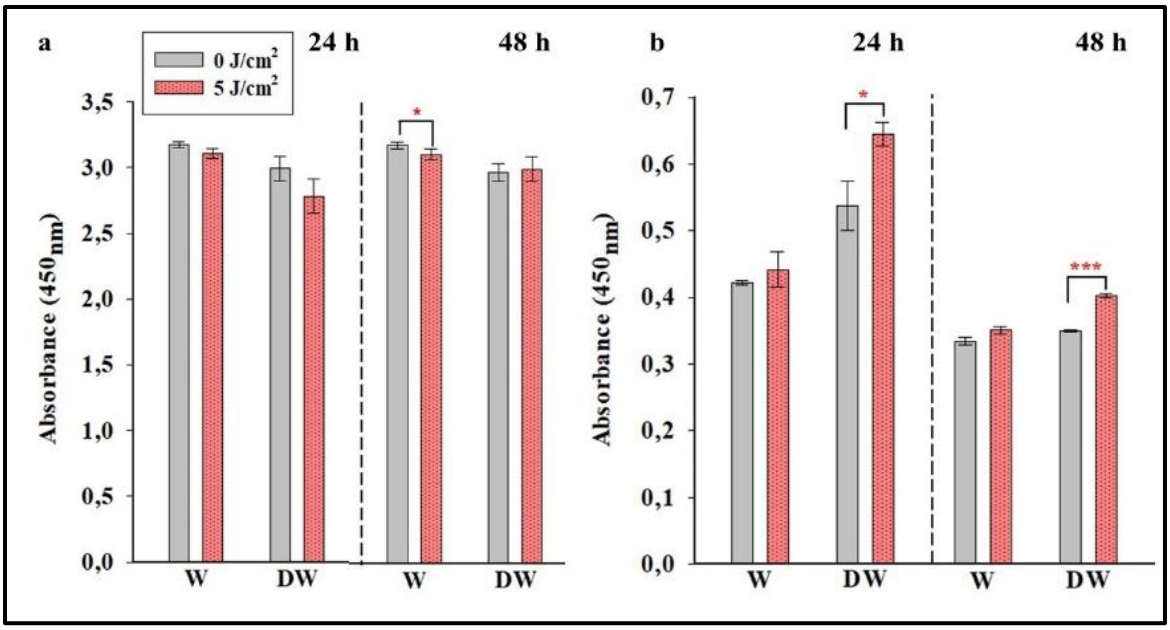

Figure 5: *Total GSK3β (a) and phosphorylated (p-) GSK3β (b) in wounded (W) and diabetic wounded (DW) cells at 24 and 48 h post-PBM at 660 nm. Significant probability as compared with respective control (0 J/cm^2) cells is shown as *P ≤ 0.05, and ***P ≤ 0.001 (SEM) [16].*

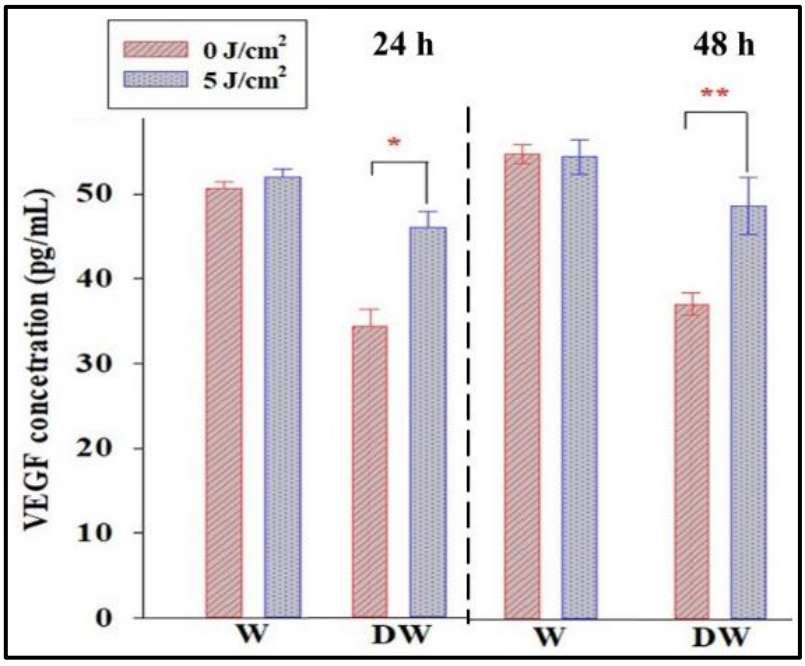

Figure 6: *Vascular endothelial growth factor (VEGF) as determined by ELISA in wounded (W) and diabetic wounded (DW) cells at 24 and 48 h post-PBM at 660 nm. Significant probability as compared with respective control (0 J/cm^2) cells is shown as *P ≤ 0.05, and **P ≤ 0.01 (SEM).*

Post-PBM at 660 nm, there was a significant increase in bFGF in diabetic wounded models at 24 h (Fig. 7a), with a corresponding increase in p-FGFR (Fig. 7b). However, at 48 h there was a significant decrease (Fig 7a) in bFGF released by the cells into the culture media. This decrease is likely due to the consumption of bFGF by the same cells in a paracrine fashion. At 24 h, there was a corresponding significant increase in p-Ras and p-MEK1/2 in the diabetic wounded models (Fig. 8a and 8b, respectively), while the increase observed in p-MAPK (Fig. 8c) at 48 h was insignificant (P=0.084), possibly due to the large error bar in the control cells. Wounded cells showed no change in bFGF and p-FGFR, a significant increase in p-Ras and p-MEK1/2 at 24 h, and no change in p-MAPK.

Currently, treatments for chronic wounds are limited and associated with repeated failure and relapse, and new therapies are required to treat DFUs. Numerous studies have pointed towards the positive effects of PBM,

however the cellular mechanisms after exposure to PBM are still not well understood and further research on the mechanisms of photon-tissue interaction and the specific parameters that establish the therapeutic results are required [4,20]. The multitude of positive effects seen in response to PBM through various studies appear to be dependent on cell type and PBM parameters used. This study unequivocally shows that PBM using visible red light at 660 nm with 5 J/cm^2 has a positive, stimulatory effect on diabetic wounded cells *in vitro*. A wound was simulated *in vitro* via the central scratch. Creating a scratch in a 2D cell model has limitations in that it lacks the complexity of the wound bed microenvironment, however the scratch assay is well established and provides a cost-effective assay used for measuring cell migration *in vitro* and allows for recolonisation and monitoring of the scratched region to quantify cell migration [21,22]. The scratch assay also assists in understanding the mechanisms that influence cellular migration in response to stimulus [23], and in this case PBM. Cellular migration rate was determined in wounded and diabetic wounded cell models in response to PBM at 660 nm. As expected, control diabetic wounded cells showed decreased migration rate, viability and proliferation as compared to the wounded cells grown under normoglycaemic conditions, however when exposed to PBM the migration rate of the diabetic wounded cells increased significantly, with complete 'wound closure' at 48 h. The same effect was evident in cell viability and proliferation post-PBM. It is well known that diabetic wounds exhibit decreased growth factors and have disrupted cell signalling pathways necessary for wound healing, and as expected the diabetic wounded control cells exhibited decreased VEGF and bFGF, as well as signalling proteins involved in both the PI3K/AKT and Ras/MAPK pathways as compared to the wounded control cells. Post-PBM at 660 nm, the levels of the measured growth factors released by diabetic wounded cells significantly increased, and there was activation of the PI3K/AKT/mTOR and Ras/MAPK pathways [16,17]. These results illustrate the effectiveness of PBM at 660 nm in activating cellular pathways in deficient diabetic wounded cells to speed up the healing process and has shown that PBM could be advantageous in the treatment of chronic DFUs. They also provide more insight into the cellular mechanisms involved when utilizing visible red light. There is a definite need to generate new treatment modalities to improve diabetic wound healing, and PBM has an unmistakable role to play.

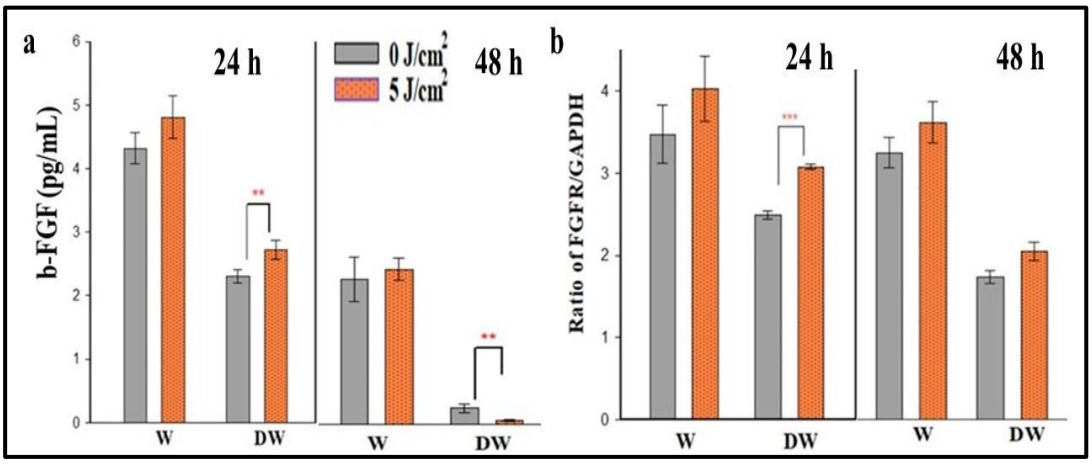

Figure 7: *Basic fibroblast growth factor (bFGF)(a) and phosphorylation (p-) of the receptor, FGFR (b) as determined in wounded (W) and diabetic wounded (DW) cells at 24 and 48 h post-PBM at 660 nm. Significant probability as compared with respective control (0 J/cm^2) cells is shown as **P ≤ 0.01, and ***P ≤ 0.001 (SEM) [17].*

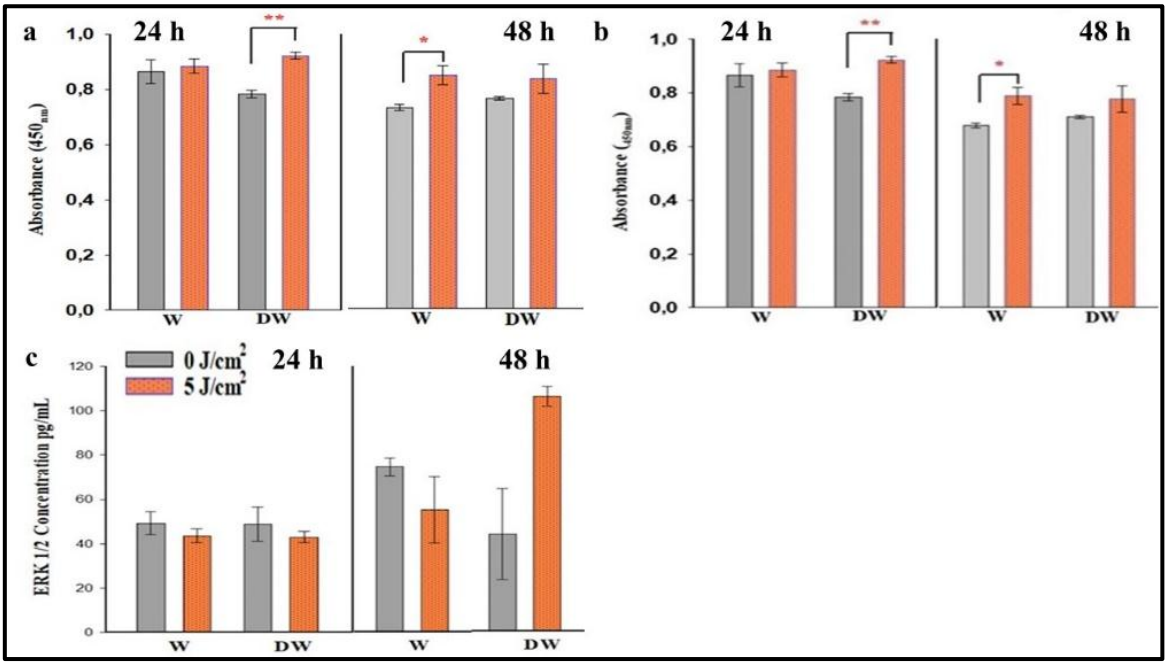

Figure 8: *Phosphorylation (p-)Ras (a) p-MEK1/2 (b) and p-MAPK (c)as determined in wounded (W) and diabetic wounded (DW) cells at 24 and 48 h post-PBM at 660 nm. Significant probability as compared with respective control (0 J/cm^2) cells is shown as *P ≤ 0.05, and **P ≤ 0.01 (SEM) [17].*

REFERENCES

[1] International Diabetes Federation, IDF Diabetes atlas, 10th ed. 2021. Available at: www.idf.org/diabetesatlas

[2] International Diabetes Federation, IDF Diabetes atlas, 9th ed. 2019. Available at: www.idf.org/diabetesatlas

[3] K. McDermott, M. Fang, A.J.M. Boulton, E. Selvin, C.W. Hicks, Etiology, Epidemiology, and Disparities in the Burden of Diabetic Foot Ulcers, Diabetes Care. 209-221, 2023.

[4] A. Liebert, W. Capon, V. Pang, D. Vila, B. Bicknell, C. McLachlan, H. Kiat, Photophysical Mechanisms of Photobiomodulation Therapy as Precision Medicine, Biomedicines. 237, 2023, doi: 10.3390/biomedicines11020237.

[5] S.W. Jere, N.N. Houreld, H. Abrahamse, Effect of photobiomodulation on cellular migration and survival in diabetic and hypoxic diabetic wounded fibroblast cells, Lasers Med Sci. 365–374, 2021.

[6] A. Shaikh-Kader, N.N. Houreld, N.K. Rajendran, H. Abrahamse, Levels of Cyclooxygenase 2, Interleukin-6, and Tumour Necrosis Factor-α in Fibroblast Cell Culture Models after Photobiomodulation at 660nm, Oxid Med Cell Longev. 6667812, 2021, doi: 10.1155/2021/6667812.

[7] N.K. Rajendran, N.N. Houreld, H. Abrahamse, Photobiomodulation reduces oxidative stress in diabetic wounded fibroblast cells by inhibiting the FOXO1 signaling pathway, J Cell Commun Signal. 195-206, 2021.

[8] S.M. Ayuk, H. Abrahamse, N.N. Houreld, Effect of 660 nm visible red light on cell proliferation and viability in diabetic models in vitro under stressed conditions. Lasers Med Sci. 1085–1093, 2018.

[9] K. Rupel, L. Zupin, A. Colliva, A. Kamada, A. Poropat, G. Ottaviani, M. Gobbo, L. Fanfoni, R. Gratton, M. Santoro, R. Di Lenarda, M. Biasotto, S. Zacchigna, Photobiomodulation at Multiple Wavelengths Differentially Modulates Oxidative Stress In Vitro and In Vivo, Oxid Med Cell Longev. 6510159, 2018, doi: 10.1155/2018/6510159.

[10] E. Sutton, S. Ganie, C. Chan, A. Kaur, E. Nussbaum, Photobiomodulation and diabetic foot and lower leg ulcer healing: A narrative synthesis, Foot (Edinb). 101847, 2021, doi: 10.1016/j.foot.2021.101847.

[11] A.G. Maiya, A.S. Kumar, A. Hazari, R. Jadhav, L. Ramachandra, H.M. Hande, S.K. Rajgopal, S.G. Maiya, P. Kalkura, L.G. Keni, Photobiomodulation therapy in neuroischaemic diabetic foot ulcers: a novel method of limb salvage, J Wound Care, 837-842, 2018.

[12] T.S. Leyane, S.W. Jere, N.N. Houreld, Cellular Signalling and Photobiomodulation in Chronic Wound Repair, Int. J. Mol. Sci. 11223, 2021, doi: 10.3390/ijms222011223.
[13] A.C. Barolet, A.M. Villarreal, A. Jfri, I.V. Litvinov, D. Barolet, Low-Intensity Visible and Near-Infrared Light-Induced Cell Signaling Pathways in the Skin: A Comprehensive Review, Photobiolmodul Photomed Laser Surg. 147-166, 2023.
[14] S.W. Jere, N.N. Houreld, H. Abrahamse, Photobiomodulation at 660 nm stimulates proliferation and migration of diabetic wounded cells via the expression of epidermal growth factor and the JAK/STAT pathway, J Photochem Photobiol B. 74-83, 2018.
[15] S.W. Jere, N.N. Houreld, H. Abrahamse, Photobiomodulation and the expression of genes related to the JAK/STAT signalling pathway in wounded and diabetic wounded cells, J Photochem Photobiol B. 111791, 2020, doi: 10.1016/j.jphotobiol.2020.111791.
[16] S.W. Jere, N.N. Houreld, H. Abrahamse, Photobiomodulation activates the PI3K/AKT pathway in diabetic fibroblast cells in vitro, J Photochem Photobiol B. 112590, 2022, doi: 10.1016/j.jphotobiol.2022.112590.
[17] P. Kasowanjete, H. Abrahamse, N.N. Houreld, Photobiomodulation at 660 nm Stimulates In Vitro Diabetic Wound Healing via the Ras/MAPK Pathway, Cells. 1080, 2023, doi: 10.3390/cells12071080.
[18] S. Wang, J. Lu, Q. You, H. Huang, Y. Chen, K. Liu The mTOR/AP-1/VEGF signaling pathway regulates vascular endothelial cell growth, Oncotarget. 53269–53276, 2016.
[19] Y. Tang, Z. Jiang, Y. Luo, X. Zhao, L. Wang, C. Norris, X.C. Tian, Differential effects of Akt isoforms on somatic cell reprogramming. J. Cell Sci. 3998–4008, 2014.
[20] T. Kushibiki, M. Ishihara, Biological Function of Low Reactive Level Laser Therapy (LLLT), In: Photomedicine - Advances in Clinical Practice, InTech, London, United Kingdom, 2017, Available from http://dx.doi.org/10.5772/65747
[21] Z.J. Chen, J.P. Yang, B.M. Wu, B. Tawil, A Novel Three-Dimensional Wound Healing Model, J Dev Biol, 198-209, 2014.
[22] S. Martinotti, E. Ranzato, Scratch wound healing assay. Methods Mol Biol. 225-229, 2020.
[23] A. Etemadi, S.T. Namin, M. Hodjat, E. Kosarieh, N. Hakimiha, Assessment of the Photobiomodulation Effect of a Blue Diode Laser on the Proliferation and Migration of Cultured Human Gingival Fibroblast Cells: A Preliminary In Vitro Study, Lasers Med. Sci. 491-496, 2020.

DOI 10.24412/cl-37136-2023-1-90-95

A STUDY ON THE FLOW OF CELLS THROUGH MICROFLUIDIC CHANNEL USING DIGITAL HOLOGRAPHIC MICROSCOPY

ASWATHY VIJAY[1], PAWAN KUMAR[1], NIJAS MOHAMED[1], AND RENU JOHN[1]

[1]*Biomedical Engineering department, Indian Institute of Technology Hyderabad, India*
bm18resch11018@iith.ac.in

ABSTRACT

Micro optofluidic platform is explored to image and track flow of objects through a microfluidic channel. Digital holographic microscopy is integrated with computer vision techniques for this technique. The method is noninvasive and label free. It can be used in biological platforms as most of them are relatively transparent. The surface profile of the objects flowing through a microfluidic channel are reconstructed numerically from the hologram recording. The phase images are tracked using blob analysis and optical flow methods to track the motion of the objects. This technique finds a wide range of applications in lab-on-a-chip platforms.

INTRODUCTION

Digital holographic microscopy (DHM) is a class of quantitative phase imaging techniques. It is used for the label free imaging of weakly scattering objects. It allows the quantitative estimation of parameters like refractive index, thickness etc. It has several applications in microfluidics, which is deals with the handling and manipulation of small volumes of samples in a system of micron sized channels and chambers. It can be used in inline, off axis and on axis geometries [1,2,3]. Computer vision (CV) techniques can be used in combination with DHM for tracking and analyzing the movement and behavior of particles flowing through the channels [4,5,6]. DHM is an ideal candidate to be coupled with a microfluidic device owing to the transparent nature of the device thus generating a opt microfluidic device [7,8,9]. Computer vision techniques are applied to the reconstructed wavefront from the hologram for 3-dimensional cell tracking. This method of optical tracking of cells using holography offers advantages such as non-invasive three-dimensional imaging, Quantitative analysis, and study dynamic processes, and quantitative phase information. It allows for the study of cell migration, interactions, and other complex phenomena with high spatiotemporal resolution, providing insights into cellular dynamics and biological processes. This method incorporates the following steps: A) image pre-processing to improve the signal to noise ratio, image quality and visibility. B) cell tracking from the extracted frames of a sequence of images or video and employing tracking algorithms like centroid tracking, particle filtering etc. C) feature extraction of the tracked cells, such cell position, velocity, shape, or optical properties, to characterize their behavior and properties over time. D)Data analysis and interpretation. The tracked cell data can be analyzed to extract meaningful information about cell dynamics, migration patterns, cell-cell interactions, or other parameters of interest. Statistical analysis, machine learning techniques, or other analytical methods can also be applied for interpretation and extraction of relevant insights. The current study deals with the phase reconstruction from holograms generated from an off-axis hologram, quantitative estimation and dynamic tracking of the particles flowing through the fabricated channel. We have used two computer vision-based methods of cell tracking – blob analysis and optical flow method [10,11,12]. The flow of polystyrene microbeads and human embryonic kidney (HEK) cells in a microfluidic channel are imaged and tracked using holography base 3d particle tracking method incorporating computer vison.

THEORY

An inhouse fabricated ‘S’ shaped microfluidic channel of depth 50µm and width 300µm is used. It is a PDMS based channel. The set up for holographic microscopy consists of a Mach–Zehnder arrangement (FIG 1). The source is a 532 nm laser (green light) (Verdi V2, power 10 mW, Coherent make) from which light spatially filtered and collimated using an arrangement of spatial filter and beam expander assembly. It is split into two paths via beam splitter. One arm act as the object beam path and the other acts as the reference beam path. The object beam after passing through the sample is collected by a microscope objective (63x, 0.9 NA). The light

from both the beams interferes and the pattern thus created is called a hologram which is recorded using a digital camera sensor (CMOS camera 1920 px x 1200 px. 2.3 MP, 164 fps).

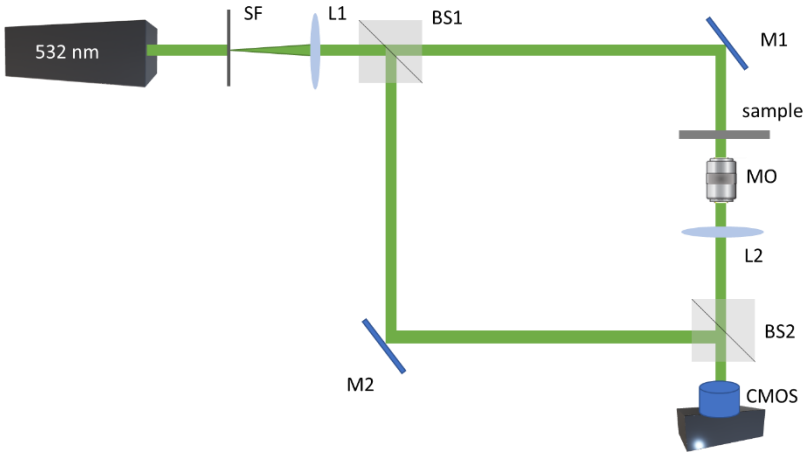

Figure 1: *set up for digital holographic microscopy. SF – spatial filter, L – lens, M – dichroic mirror, MO -microscope objective, CMOS - sensor*

The reconstructed complex wave front (ψ (ξ, η; z)) from a hologram after propagating a distance z using angular spectrum propagation method can be expressed as follows

$$\psi(\xi,\eta;\ z) = \int\int A(f_x, f_y;\ z) \exp[i(f_x x + f_y y)]\, df_x df_y \quad (1)$$

Angular spectrum at plane z is given as A (f_x, f_y; z): ξ, η are coordinates of image plane, f_x and f_y are the spatial frequencies. Amplitude contrast image ($A(x,y)$) and phase $\Phi(x,y)$ is obtained from the array of complex numbers, $\Gamma(x,y)$.

$$A(m,n) = Re[\Gamma(m,n)]^2 + Im[\Gamma(m,n)]^2 \quad (2)$$

$$\Phi(m,n) = arctan\left\{\frac{Im[\Gamma(m,n)]}{Re[\Gamma(m,n)]}\right\} \quad (3)$$

$\Phi(m,n)$ could be wrapped as it corresponds to modulo of 2π which can be corrected using phase unwrapping algorithms.

The sequence of phase reconstruction should be segmented by thresholding, (contrast-limited adaptive histogram equalization, binarization) and connected component analysis (perimeter overlay). Blob detection involves identifying and characterizing regions or objects of interest, often referred to as blobs or regions of interest (ROIs), within an image. It involves the steps of blob filtering, (where relevant blobs are retained based on their size, shape etc.) and blob characterization (where appropriate features or properties of the particles can be extracted and analyzed). The tracking of particles over time can also be done using optical flow algorithms. It is the estimation of apparent motion of the scene points from an image sequence. In Images we can measure the motion of brightness patterns or optical flow. It may or may not correspond to motion flow. It is difficult to measure the optical flow uniquely at each pixel solely based on the brightness variation of a particular pixel. The length of the vector gives an estimate of the speed of motion and the direction is indicated by the arrow in the vector. A method based on constraint equation can be used to constrain the optical flow at a pixel for constraining the problem and solving for the optical fluid at each pixel using a neighborhood of pixel. It is an under-constraint problem This is done using Lucas – Kanade method. It is based on the local derivatives of the image. To solve for the optical flow it uses the premise that optical flow in a very small neighborhood in the scene is same for all points within that neighborhood around that pixel. Consider an image I(x,y), where (x,y) indicate pixel positions. Consider a smaller motion where pixel displacement be (u,v). The new image be H(x,y). For (k,l) ϵ W: $I_x(k.l)u + I_y(k.l)u + I_t(k.l) = 0$. If we assume W has a size n × n. In matrix form

$$\begin{bmatrix} I_x(1,1) & I_x(1,1) \\ I_x(k,l) & I_x(k,l) \\ \vdots & \vdots \\ I_x(n,n) & I_x(n,n) \end{bmatrix} \begin{bmatrix} u \\ v \end{bmatrix} = \begin{bmatrix} I_t(1,1) \\ I_t(k,l) \\ \vdots \\ I_t(n.n) \end{bmatrix} \quad (4)$$

which can be expressed in the form of A u = B, which can be solved using least squares using pseudo – inverse method when A^TA is be invertible and well-conditioned.

METHODOLOGY

The suspension of microbeads and HEK cells in distilled water was kept in a syringe pump and was passed through the microfluidic channel at flow rate of 1300 nL/min. The hologram is recorded sequentially digitally. The frames are extracted and reconstructed numerically. The particle tracking is performed using the computer vision toolbox of MATLAB R2020a. The phase images are segmented, and objected perimeter is overlayed. Cells are detected as individual blobs based on their properties compared to the surrounding background. It focuses on identifying regions or objects with distinct characteristics, such as intensity, size, and centroid location. We have also employed optical flow method as mentioned above using Lucas – Kanade method to track the particles under observation to describe the image motion.

RESULTS

After numerical reconstruction the channel is amplitude and phase image of the channel is reconstructed. The thickness map is also plotted (Fig 3). The depth of the channel is 50 micron, and the obtained reconstruction agrees the actual value. The hologram vedio is recorded for microbeads and HEK cells flowing through the channel and reconstructed to obtain the phase images. Figure 4 shows the phase reconstruction at random time points of flow. The phase reconstruction of objects (microbeads and HEK cells) during the observation period are also shown.

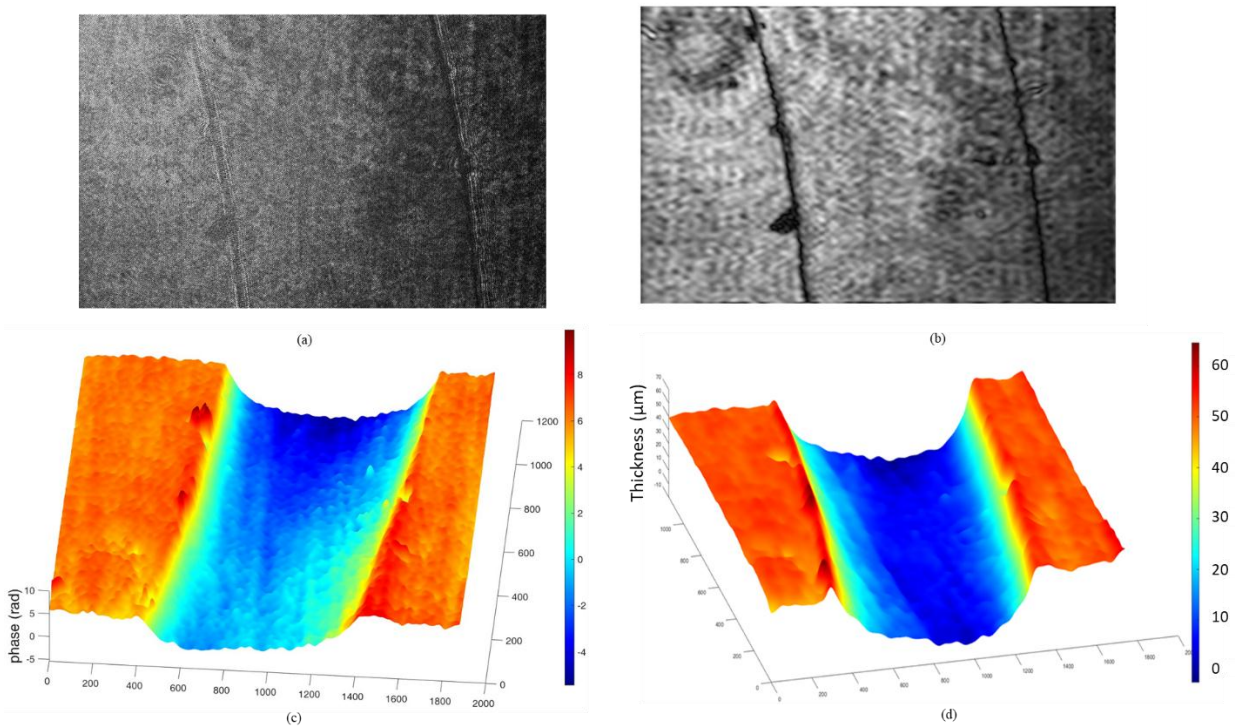

Figure 2: *(a) hologram of the microfluidic channel (b) amplitude image (c) phase image (d) thickness map*

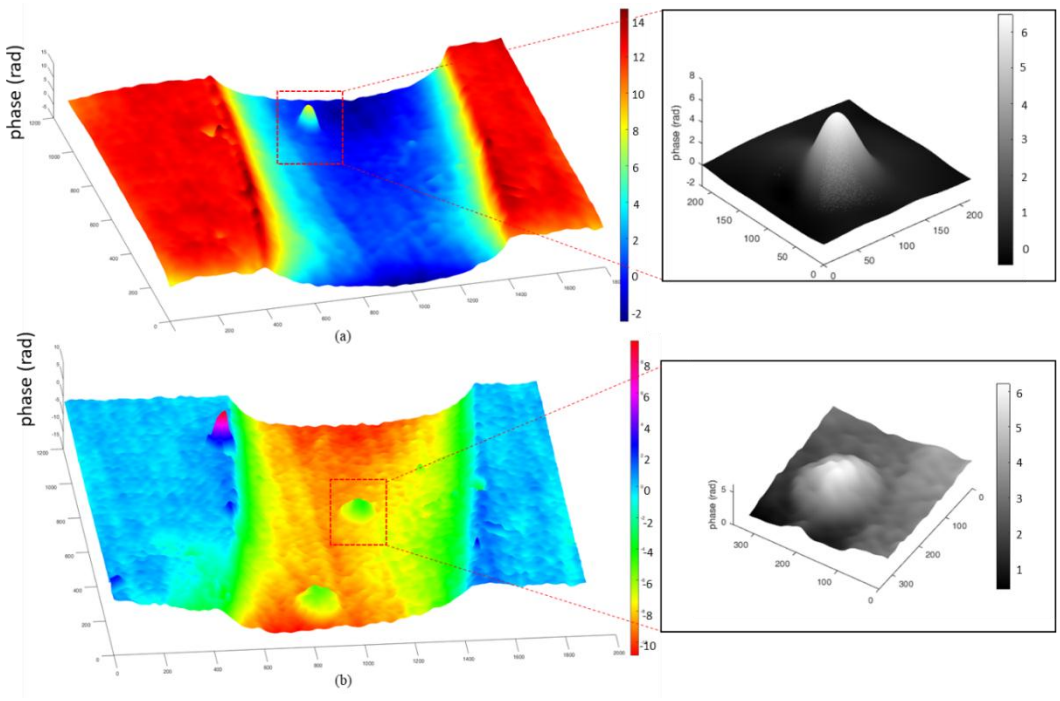

Figure 4: *(a) Phase reconstruction of polystyrene microbeads (b) HEK cells flowing through the channel*

Tracking of the cell using blob analysis method is performed by detection of the phase images and extraction of the features. The phase images are segmented by applying a threshold to binarize the image to separate out the individual blobs. and the blob filtering is performed based on the shape and size of the blobs to mark the cell boundaries. It is followed by the characterization of the individual blobs by extracting the features like area, diameter, centroid, orientation extra for the 8 -connected components in the image. This is done using the computer vision toolbox in MATLAB. In the current work centroid is used as the characterization property. The result from the tracking is depicted in Fig 5.

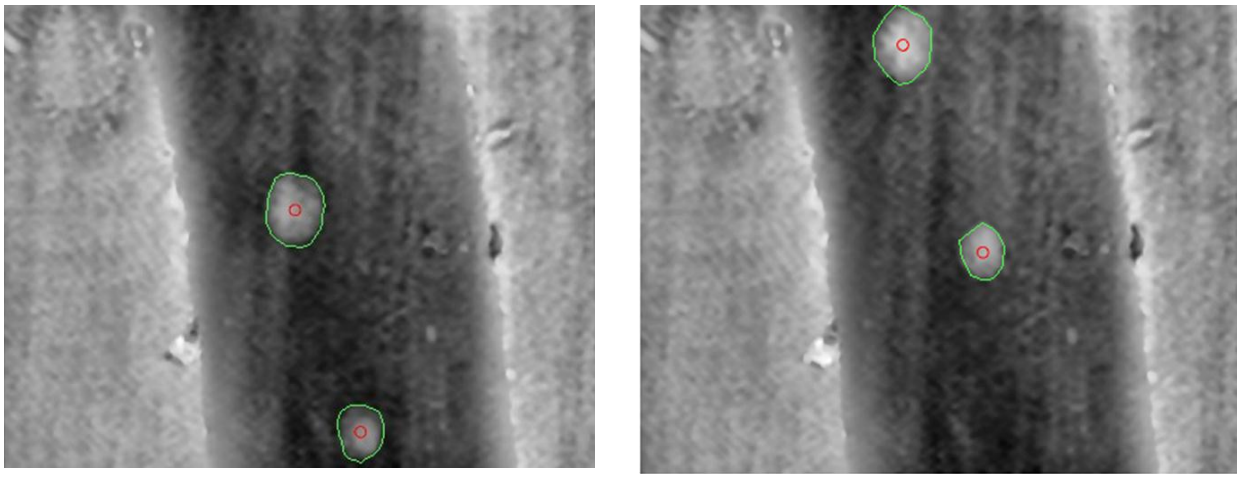

(a) (b)

Figure 5: *Tracking HEK cells using blob detection method at time points (a) t=24 ms (b) t= 54 ms . Red rcle indicates the detected centroid of the cell and the green outline is the detected perimeter of the cell.*

Optical flow method has also been employed for the tracking of the cells through the channels. Optical flow of the moving object is calculated from the solution of the optical flow constraint equation using Lucas-Kanade method. The determined flow vectors are overlayed on the corresponding points on the phase image (Fig 6) for tracking.

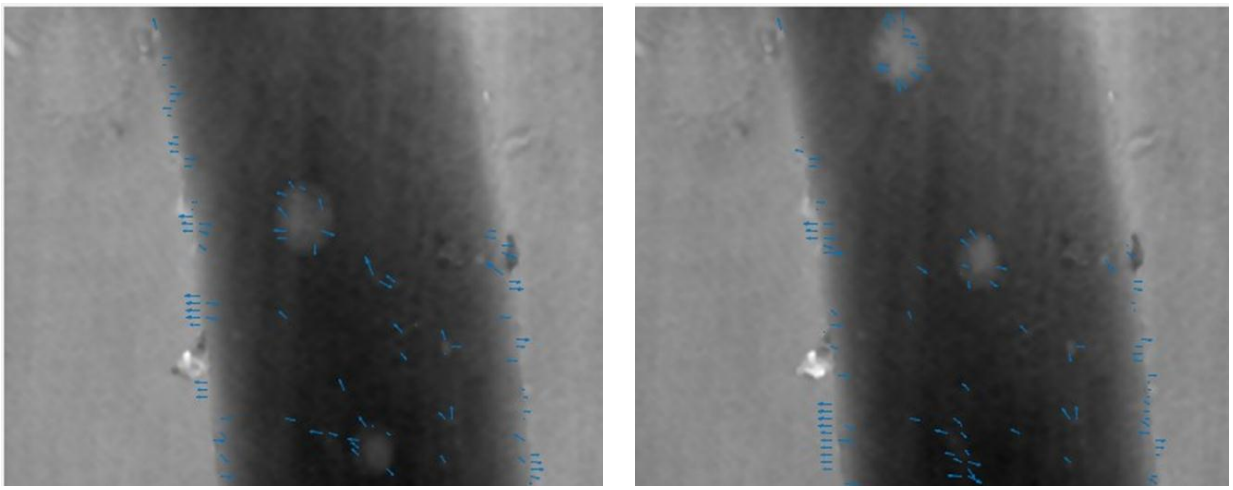

(a) (b)

Figure 6: *Tracking HEK cells using optical flow method at time points (a) t=24 ms (b) t= 54 ms . Blue arrow indicate the speed and direction of motion of dynamic objects in the image*

Blob detection primarily focuses on the identification of objects or region of interests based on distinct features that separates them from the surroundings. It can precisely localize particles like cells with from these features. It is based on simple processes like thresholding and connected component analysis methods which makes it faster compared to optical flow method. Each cell is considered as a separate entity in this method and the interactions or association of the objects are disregarded. It is not an effective method when cells are overlapping or closely packed together, and to distinguish between cells having similar characteristics. Optical flow method is used to track the apparent motion of the pixels between consecutive frames by capturing the motion of the objects in the image to generate dense motion vectors. The flow of individual cells can be tracked continuously while maintaining the cell identity. The challenge in this method arises in case of occlusions, appearance changes and complexities in motion patterns. It is a computationally intensive process.

CONCLUSION

A label free 3D tracking methodology for micro-optofluidic platforms has been developed using digital holography and compute vision. It is a fast and effective technique for imaging and tracking non-invasively. It is also possible to extract features of the object from the individual frames of the phase image. Two methods of tracking are applied in this study – blob analysis and optical flow method. It was possible to detect and track the cells under study accurately using both the methods.. The method of tracking of cells in a microfluidic platform depends on the cell characteristics, motion of the fluid and cells, computational efficiency, and accuracy requirements. An integrated approach promises an improved performance and robustness. Future directions in this study will be on tracking specific cells from a population of several objects in lab-on-a-chip applications for cell growth and disease screening

REFERENCES

[1] U. Schnars and W. Juptner. Digital Holography: Digital Hologram Recording, Numerical Reconstruction, and Related Techniques. Springer, 2005.

[2] M.K.Kim, Principles and techniques of digital holographic microscopy, *SPIE reviews*, *1*(1), 018005,(2010).

[3] L. Yaroslavsky, Digital holography and digital image processing: principles, methods, algorithms. Springer Science & Business Media, (2003).

[4] G. Danuser, Computer vision in cell biology. Cell, 147(5), 973-978, (2011).

[5] K. Li, E. D.Miller, M. Chen, T.Kanade, L. E. Weiss, & P. G. Campbell, Computer vision tracking of stemness. In 2008 5th IEEE international symposium on biomedical imaging: from nano to macro (pp. 847-850). IEEE. (2008, May).

[6] Galan, E. A., Zhao, H., Wang, X., Dai, Q., Huck, W. T., & Ma, S. (2020). Intelligent microfluidics: The convergence of machine learning and microfluidics in materials science and biomedicine. *Matter*, *3*(6), 1893-1922.

[7] V. P Pandiyan,.and R. John, Optofluidic bioimaging platform for quantitative phase imaging of lab on a chip devices using digital holographic microscopy. Appl. Opt., 55(3), A54-A59 (2016).
[8] D. Mark, S. Haeberle, G. Roth, F.Von Stetten, and Zengerle, R. Microfluidic lab-on-a-chip platforms: requirements, characteristics, and applications. Microfluidics based microsystems: fundamentals and applications, 305-376, (2010).
[9] S. Kumar, S. Kumar, M. A. Ali, P. Anand, V. V. Agrawal, R. John, and B. D. Malhotra, Microfluidic- integrated biosensors: Prospects for point- of- care diagnostics. Biotechnol. J., 8(11), 1267-1279, (2013).
[10] K. T. M. Han, and B. Uyyanonvara, A survey of blob detection algorithms for biomedical images, In 2016 7th International Conference of Information and Communication Technology for Embedded Systems (IC-ICTES) (pp. 57-60). IEEE, (2016, March).
[11] J. L. Barron, D. J. Fleet, S. S. Beauchemin, and T. A. Burkitt, Performance of optical flow techniques, In Proceedings of the IEEE Conference on Computer Vision and Pattern Recognition (CVPR),236-242. Champaign, IL: CVPR, (1992).
[12] I.,Kajo, A. S. Malik, and N. Kamel, Motion estimation of crowd flow using optical flow techniques: A review. In 2015 9th International Conference on Signal Processing and Communication Systems (ICSPCS) (pp. 1-9). IEEE, (2015, December).

DOI 10.24412/cl-37136-2023-1-96-101

BIO-IMAGING USING NOISE: APPLICATION OF LASER SPECKLES FOR DEEP TISSUE BLOOD FLOW IMAGING

MURALI K[1], RIA PAUL[1], SOUMYAJIT SARKAR[1] AND HARI M VARMA[1]

[1]*Department of Biosciences and Bioengineering, Indian Institute of Technology – Bombay, India*
harivarma@iitb.ac.in

ABSTRACT

We present a novel approach for deep tissue blood flow imaging using laser speckles. Our method utilizes a cost-effective system with low frame rate cameras for diffuse correlation spectroscopy (DCS) measurements. We demonstrate the effectiveness of our system through phantom and *in-vivo* studies, including stroke measurements in mice and number processing tasks in humans to measure the changes in cerebral blood flow. Additionally, we present our recent work on simulation of speckles using stochastic differential equation with desired statistical properties. Our studies contribute to the development of affordable solutions for high density deep tissue blood flow imaging.

INTRODUCTION

Blood flow is a fundamental physiological parameter that plays a vital role in maintaining the normal functioning of tissues and organs in the human body [1]. Accurate measurement and assessment of blood flow are crucial for understanding various physiological processes, diagnosing medical conditions, and guiding treatment strategies. Several optical imaging techniques have been developed to quantify blood flow non-invasively, including Laser Speckle Contrast Imaging (LSCI), Laser Doppler Flowmetry (LDF), Diffuse Correlation Spectroscopy (DCS), and Diffuse Correlation Tomography (DCT) [2,3].

These techniques exploit the unique properties of laser speckles, which arise from the interference and scattering of coherent light by tissues [4]. Laser speckles, appearing a randomly fluctuating intensity noise, carries valuable information about the underlying blood flow dynamics, which can be analyzed to extract meaningful flow-related parameters [5,6].

While LSCI and LDF have proven effective in assessing blood flow in superficial tissues, the measurement of deep tissue blood flow remains challenging [3]. DCS and DCT have emerged as promising approaches for non-invasively probing deep tissue blood flow by harnessing the speckle properties of scattered light. These techniques utilize the inherent noise present in laser speckles to derive quantitative information about blood flow dynamics and perfusion. DCS, in particular, utilizes intensity autocorrelation measurements at multiple distances from the source to quantify blood flow. However, it has limitations in terms of confined detection sites and the requirement for expensive multiple detectors [7].

To overcome these limitations, one alternative approach is to explore the use of array detectors in DCS. While array detectors are not commonly used in DCS, they offer potential solutions to the challenges associated with confined detection sites and the requirement for expensive multiple detectors. However, implementing array detectors for DCS requires high frame rate detectors with reasonable signal-to-noise ratio (SNR) at low exposure time, which are currently not readily available and tend to be more expensive [7,8]. Nevertheless, in light of these challenges, speckle contrast-based methods like SCOS [9], DSCA [10], SCOT, scDCT [11] and their variants [12] have been proposed as alternative techniques to enhance flow quantification in DCS. Speckle

contrast, which represents the ratio of the standard deviation to the mean intensity, serves as a key parameter that relates to the integrated intensity autocorrelation over the exposure time [2].

In this paper, we present an overview of our novel algorithm and a cost-effective system that utilizes low frame rate CCD \or CMOS cameras for DCS measurements. Our approach exploits the fact that multi-exposure speckle contrast data contains information on the intensity autocorrelation [13]. The algorithm employs a multi-step Volterra integral method (MVIM) to recover the full auto-correlation function from the multi-exposure speckle contrast data. We demonstrate the effectiveness of our system through experiments conducted on tissue-mimicking phantoms and human subjects, including hand-cuff occlusion and voluntary tasks such as apnea and number processing. Furthermore, we validate our system by measuring stroke in mice using a new small animal platform.

Additionally, we establish the equivalence between laser speckle contrast-based methods and DCS, supported by the Volterra integral equation theory [7, 13]. We emphasize the importance of regularized fitting in multi-exposure speckle contrast imaging to accurately recover the auto-correlation function. Moreover, we introduce M-DCT [14], a high-density DCT system that incorporates a spatially weighted filter to improve depth localization and eliminate unwanted surface artefacts. The iterative use of autocorrelation measurements at multiple delay times enhances the reconstruction results, which are validated through simulations, phantom experiments, and *in-vivo* human studies.

Lastly, we present our recently published novel approach to simulating laser speckles using a stochastic differential equation [15]. This method enables the generation of speckles with desired statistical properties, including different blood flow profiles and realistic noise models. The simulations encompass both superficial and diffuse speckles, making them applicable to deep tissue blood flow imaging. The validity of our simulation model is confirmed through comparisons with *in-vivo* studies conducted on mice and healthy human subjects.

METHODS

M-DCS algorithm:

The M-DCS algorithm utilizes the multi-step Volterra integral method (MVIM) to recover the field auto-correlation function. The relationship between speckle contrast (κ) and the normalized electric field auto-correlation function (g_1) is represented by the equation

$$\kappa^2\,(r,T) = \frac{2\beta}{T}\int_0^T \left(1-\frac{\tau}{T}\right)|g_1^2(r,\tau)|d\tau \qquad (1),$$

which is a Volterra integral equation of the first kind. To solve this equation, it is discretized using the trapezoidal rule and expressed in matrix form. The resulting matrix equation is then solved using Tikhonov regularized least square minimization, where the cost function is minimized to obtain the best estimate of $g1$. The algorithm incorporates the selection of important parameters such as correlation delay time (τ) and exposure time (T) to ensure accurate recovery. Furthermore, an iterative scheme is implemented to update the prior information (x_0) at each iteration, enhancing the accuracy of the recovered g_1. Detailed steps of the algorithm can be found in Algorithm (Fig 1(b)), and further information is available in reference [7].

(a)

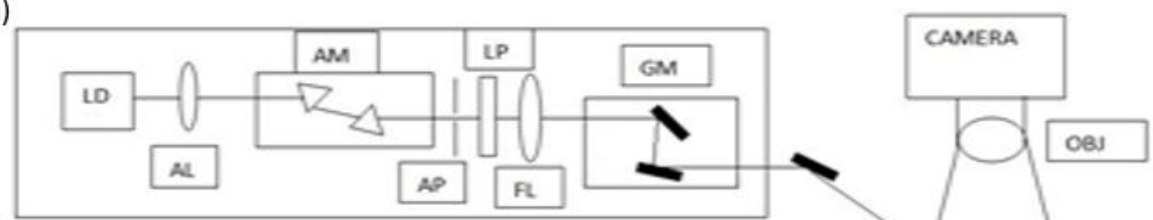

(b)

Algorithm 1 M-DCS Algorithm - Recovering Field Auto-Correlation Function

procedure $\mathbf{g_1}(r, tau)$(f)rom $\kappa(r, T)$
    Initialize parameters and variables
    Discretize the range of correlation time (τ_M) and exposure time (T_N)
    Set the correlation delay time step ($\Delta\tau$)
    Set the tolerance / error level for convergence
    Set the regularization parameter (λ)
    Set the maximum number of iterations
    Initialize prior information ($\mathbf{x}_0$) for $g_1(\tau)$ based on CDE
    Calculate the size of the kernel matrix $\mathbf{A}$ ($N \times N$)
    while not converged or maximum number of iterations reached **do**
        Update the field auto-correlation function using MVIM
        Discretize the integral using the trapezoidal rule
        Represent the integral equation in matrix form: $\mathbf{Ax} = \mathbf{b}$
        Solve the matrix equation using Tikhonov regularized least square minimization
        Update the prior information using an iterative scheme
    end while
    return Recovered field auto-correlation function ($\mathbf{g}_1$)
end procedure

(c)

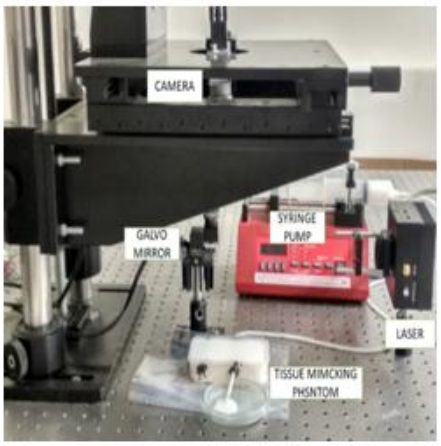

Figure 1: *(a) Schematic of the M-DCS / M-DCT system; The system consists of a focused laser source (LD- Laser diode; AL- Aspheric lens; AM- Anamorphic prism; AP- Aperture; FL- Focusing lens; GM – Galvo mirror) illuminated on the sample/ Phantom. The scattered light is captured to camera via objective lens (Obj). (b) A pseudocode of the M-DCS algorithm to recover g1. (c) Photograph of the system.*

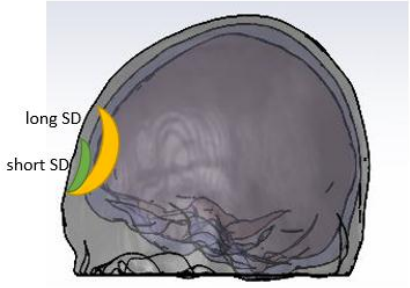

Figure 2: *Schematic of the human head for illustrating the M-DCT system; The idea is that short SDs that has information from extracerebral layers whereas the long SDs contain information from extracerebral as well as deep layers of brain. We design a filter based on short SD and use it to remove artefacts and extracerebral interferences from long SDs.*

M-DCS system:

The M-DCS system used in this study employs a low frame rate camera, specifically the Basler 640-120-um camera for phantom and small animal experiments, and the Photometrics Prime BSI camera for human studies. For deep tissue blood flow measurements, a pointed source illumination with a wavelength of 785 nm (Thorlabs L7850P90) laser is used, while uniform illumination is employed for surface blood flow measurements. The system configuration is illustrated in Figure 1(a) and includes the camera, laser source, and appropriate optical components. The system enables the measurement of multi-exposure speckle contrast at a specified source-detector separation.

High Density M-DCT system:

To overcome challenges associated with extracerebral interferences in diffuse correlation tomography (DCT) measurements, a high-density system is proposed. This system utilizes an array of sources and detectors, modeled as multi-speckle DCT (M-DCT), and incorporates multiple delay-times in an iterative reconstruction approach [14]. The goal is to improve depth localization and accurately measure blood flow in deep tissues. The modified Born approximation is utilized, where a filter design based on short source-detector separation is implemented to enhance discrimination between deep tissue blood flow signals and surface effects, as depicted in Fig (2).

The reconstructed filtered autocorrelation function, $g_1^{\delta,F}(r_s,r_d,\tau) = -\frac{2u_s'k_0^2}{G_1^0(r_s,r_d,0)}\int \tau G^F(r_d,r,\tau)G^F(r,r_s,\tau)W(r)D_B^\delta dr$, is computed using the proposed algorithm. Here $g_1^{\delta,F}$ is the filtered autocorrelation and W(r) is the weight function designed to address the biased sensitivity of the reconstruction towards shallower region. In addition, by implementing our previously proposed algorithm [16], which can eliminate the requirement for inverting the Jacobian matrix, and could reduce the computational time. All human and animal studies were approved by the Institute ethical committee at Indian Institute of Technology – Bombay and APT research center, Pune.

RESULTS AND DISCUSSION:

Phantom and *in-vivo* studies:

Here, we present two representative figures illustrating the capability of the M-DCS algorithm and system to recover the autocorrelation function using a low frame rate camera. Figure 3(a) displays the results of g1 obtained from multi-exposure speckle contrast at two different flow conditions. Figure 3(b) demonstrates the relative cerebral blood flow (rCBF) acquired during a number processing task performed by a given subject (n=3 trials). With an SD separation of 2 cm, it can be observed that blood flow increases during the task and decreases after completion, thereby validating the effectiveness of the M-DCS system and algorithm. Further details can be found in Ref [7,8,14].

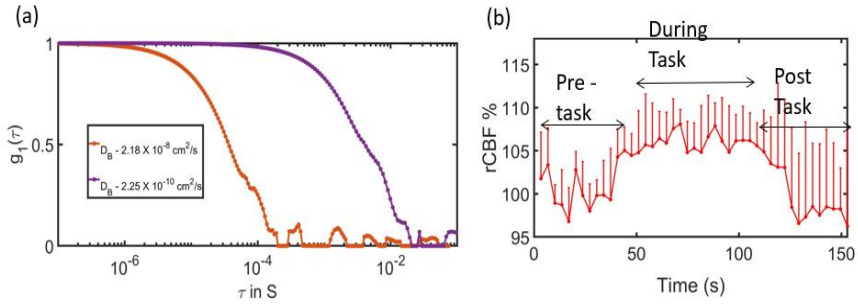

Figure 3: (a) g_1 recovered from multi exposure speckle contrast using M-DCS algorithm for two different flow. (b) in-vivo blood flow changes quantified as rCBF during a number processing task;

Animal studies:

To validate our algorithm in pre-clinical studies, we developed a portable modular small animal imaging platform (details in Ref [17]). Using this platform, we measured blood flow in different tissue types of the mouse brain, including arteries, veins, and parenchyma. Figure 4(c) illustrates the measurements obtained from our proposed M-DCS system in both the alive and post-sacrifice conditions. Furthermore, we present a 3D tomographic reconstruction of a blood flow changes associated with stroke in the left hemisphere of mice induced by photo-thrombosis in Figure 4(d).

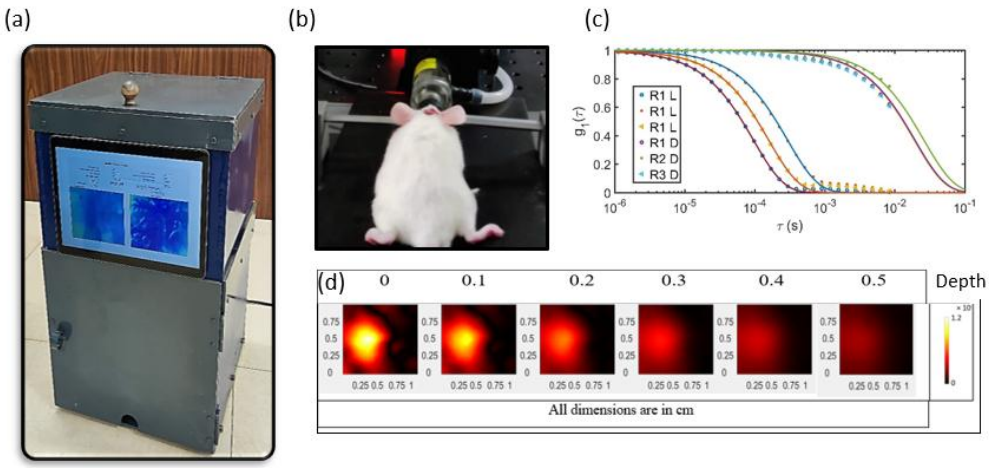

Figure 4: *A custom-built modular portable animal imaging platform is depicted. (b) An anesthetized animal placed in a stereotaxic frame is shown. (c) The results obtained from the M-DCS algorithm reveal distinct flow patterns in the artery (R1-L), vein (R2-L), and parenchyma (R3-L) regions, both when the animal was alive (indicated by suffix L) and after sacrifice (indicated by suffix D). (d) A tomographic reconstruction demonstrates blood flow during stroke in the left hemisphere induced by photo-thrombosis.*

Simulation of speckles using SDE:

All the above-mentioned speckle-based blood flow imaging methods requires testing with calibrating phantoms before translation. There are many different ways to simulate speckles in the literature most of which rely upon either the Fourier-based methods or statistical tools. We present a novel method for simulating laser speckles in blood flow imaging using stochastic differential equations (SDE) [15]. This method allows us to generate speckles with predefined probability density functions and temporal auto-correlation, enabling the modelling of different blood flow profiles and the simulation of both superficial and deep tissue speckles. We validated our simulation by comparing the results with *in-vivo* studies conducted on mice and healthy human subjects. Our method provides a valuable tool for the analysis and development of laser speckle-based imaging techniques. The algorithm, shown in Fig 5(a), utilizes the solution to the SDE based on the Milstein scheme,

$$I_{n+1} = I_n + a(I_n)\Delta t + b(I_n)\Delta W_n + 0.5b(I_n)b'(I_n)[(\Delta W_n)^2 - \Delta t] \quad (2),$$

where I(t) represent the intensity of the speckles. The parameters 'a' and 'b' are determined by the optical and dynamic properties of the tissue, and further details can be found in Ref [15]. The representative figure of the speckles generated using our proposed method is shown in Fig 5(b), along with their validation using autocorrelation and speckle contrast in Fig 5(c) and 5(d) respectively.

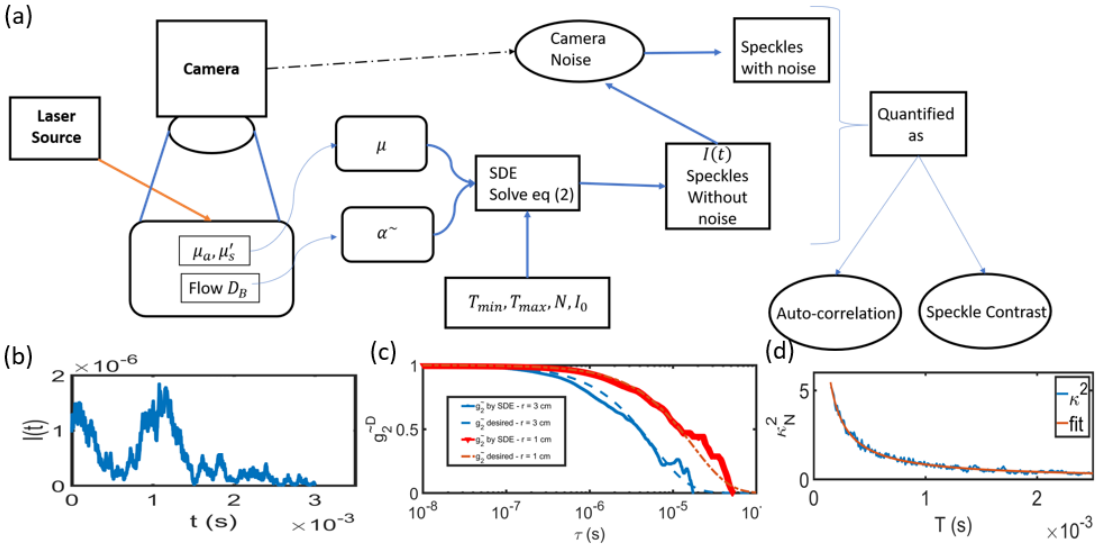

Figure 5: *Speckle simulation tool using SDE. (a) The algorithm used to simulate speckles for mimicking deep tissue blood flow is shown. The parameters μ and α˜ contain information on tissue optical and dynamic properties, which are fed into the SDE algorithm in equation (2). The intensity speckles (as shown in (b)) that*

follow an exponential probability density function and the autocorrelation based on the blood flow are generated. Speckle noise is added based on the detector. The algorithm is validated by quantifying either the autocorrelation (as shown in (c)) or the speckle contrast (as shown in (d)).

REFERENCES

[1] Zauner A, Daugherty WP, Bullock MR, Warner DS. Brain oxygenation and energy metabolism: part I - biological function and pathophysiology. Neurosurgery. 2002;51(2):289-302.

[2] Boas DA, Dunn AK. Laser speckle contrast imaging in biomedical optics. J Biomed Opt. 2010;15(1):011109

[3] Durduran T, Choe R, Baker W, Yodh AG. Diffuse optics for tissue monitoring and tomography. Rep Prog Phys. 2010;73(7):076701.

[4] Goodman JW. Speckle Phenomena in Optics: Theory and Applications. Roberts and Company Publishers; 2007.

[5] Dainty JC. Laser Speckle and Related Phenomena. Vol. 9. Springer Science & Business Media; 2013.

[6] Herranz Olazábal J, Wieringa F, Hermeling E, Van Hoof C. Camera-Derived Photoplethysmography (rPPG) and Speckle Plethysmography (rSPG): Comparing Reflective and Transmissive Mode at Various Integration Times Using LEDs and Lasers. Sensors. 2022 Aug 13;22(16):6059.

[7] Murali K, Nandakumaran AK, Durduran T, Varma HM. Recovery of the diffuse correlation spectroscopy data-type from speckle contrast measurements: towards low-cost, deep-tissue blood flow measurements. Biomed Opt Express. 2019;10(10):5395-5413.

[8] Murali K, Varma HM. Multi-speckle diffuse correlation spectroscopy to measure cerebral blood flow. Biomed Opt Express. 2020;11(11):6699-6709.

[9] Valdes CP, Varma HM, Kristoffersen AK, Dragojevic T, Culver JP, Durduran T. Speckle contrast optical spectroscopy, a non-invasive, diffuse optical method for measuring microvascular blood flow in tissue. Biomed Opt Express. 2014;5(8):2769-2784.

[10] Bi R, Dong J, Lee K. Deep tissue flowmetry based on diffuse speckle contrast analysis. Opt Lett. 2013;38(9):1401-1403.

[11] Huang C, Irwin D, Lin Y, Shang Y, He L, Kong W, Luo J, Yu G. Speckle contrast diffuse correlation tomography of complex turbid medium flow. Med Phys. 2015;42(7):4000-4006.

[12] Seong M, Oh Y, Lee K, Kim JG. Blood flow estimation via numerical integration of temporal autocorrelation function in diffuse correlation spectroscopy. Computer Methods and Programs in Biomedicine. 2022 Jul 1;222:106933.

[13] Murali K, Nandakumaran AK, Varma HM. On the equivalence of speckle contrast-based and diffuse correlation spectroscopy methods in measuring in vivo blood flow. Optics Letters. 2020 Jul 15;45(14):3993-6.

[14] Paul R, Murali K, Varma HM. High-density diffuse correlation tomography with enhanced depth localization and minimal surface artefacts. Biomed Opt Express. 2022;13(11):6081-6099.

[15] Murali K, Varma HM. Laser speckle simulation tool based on stochastic differential equations for bio imaging applications. Biomed Opt Express. 2022;13(12):6745-6762.

[16] Paul R, Murali K, Chetia S, Varma HM. A simple algorithm for diffuse optical tomography without Jacobian inversion. Biomed Phys Eng Express. 2022;8(4):045001.

[17] Paul R, Sarkar S, Marathe SD, Murali K, Das S, Abraham NM, Varma HM. Functional imaging of olfactory bulb and somatosensory cortex in mice using small-animal blood flow imaging platform. InDynamics and Fluctuations in Biomedical Photonics XX 2023 Mar 7 (Vol. 12378, pp. 45-48). SPIE.

[18] Murali K, Varma HM. Exploring different source configurations for laser speckle-based blood flow measurement system. InEuropean Conference on Biomedical Optics 2021 Jun 20 (pp. EM1A-23). Optica Publishing Group.

DOI 10.24412/cl-37136-2023-1-102-106

BIOPHOTONICS AND ARTIFICIAL INTELLIGENCE FOR IMPROVED DIAGNOSTICS: APPLICATIONS IN HEALTH, PHARMACEUTICALS AND AGRICULTURE

PATIENCE MTHUNZI-KUFA[1,2,3], NKAPHE TSEBESEBE[1,2], LEBOGANG THOBAKGALE[1], KELVIN MPOFU[1] AND SIPHUMELELE NDLOVU[1]

[1]Council for Scientific and Industrial Research, Photonics Centre, South Africa.
[2]Department of Human Biology, Division of Biomedical Engineering, University of Cape Town, South Africa.
[3]School of Chemistry and Physics, University of KwaZulu-Natal.

pmthunzikufa@csir.co.za

ABSTRACT

A lot of individuals residing in resource limited settings where timely access to medical care is a challenge and healthcare infrastructure is usually poor have no access to laboratory facilities. Disease diagnosis in such sites is dependent on the presence of point-of-care (POC) devices. These POC diagnostics play a key role in ensuring rapid patient care because they are simple to use, inexpensive, portable, instrument independent and do not require a trained technician to operate. To date, optical spectroscopy has become the most important and promising approach in every field of medical, analytical, life, food, and pharmaceutical sciences. However, most currently available spectrometers are bulky and cannot be easily integrated in miniaturized devices. In this work, different biophotonics techniques, artificial intelligence and machine learning models are used to expedite POC diagnostic apparatus for different pathogens, non-communicable diseases, substandard drugs and towards application in food safety as well as security.

INTRODUCTION

Lately, there has been a growing interest in incorporating artificial intelligence and machine learning techniques in biophotonics (1). Biophotonics is an interdisciplinary field that combines the principles of optics, photonics, and biology to study biological systems at the molecular, cellular, and tissue levels. It has a wide range of biomedical applications, including medical diagnostics, drug discovery, and tissue engineering (2). The use of light-based technologies in biophotonics allows for non-invasive, label-free, and high-resolution imaging of biological samples. One of the key advantages of biophotonics is its ability to provide label-free and high-resolution imaging of biological samples (3). This allows the study of biological structures and processes without the need for exogenous labels or dyes, which can alter the natural behavior of the sample. Additionally, the use of light-based technologies in biophotonics allows for non-invasive and real-time monitoring of biological systems (2).

On the other hand, machine learning is proving to have great potential as a tool for disease diagnostics (4). Classical machine learning (ML) has proven to be highly effective in various tasks, including classification, regression, and clustering (5). However, there are limitations to classical algorithms, particularly when handling large and complex datasets. This necessitates the development of quantum algorithms (6). Quantum-enhanced machine learning (QEML) can provide significant improvements in the speed and accuracy of ML algorithms for specific tasks. Quantum machine learning offers more efficient and faster computational capacity, making it advantageous when dealing with complex and high-dimensional data. Furthermore, quantum computers can encode complex feature representations that surpass the capabilities of classical computers. Quantum optimization algorithms also offer advantages over their classical counterparts in parameter optimization.

Separately, the growing prevalence of HIV around the globe has continued to promote the growth of the HIV diagnostic market. Sub-Saharan Africa remains the most severely affected region where 70% of HIV positive people in the world reside (7). The global HIV diagnostic market by region comprises of North America, Acia Pacific, Europe, South Africa, and the rest of the world. Tuberculosis (TB) an airborne infection caused by mycobacterium tuberculosis (MTB), until the coronavirus (COVID-19) pandemic, TB was the

leading cause of death from a single infectious agent, ranking above human immunodeficiency virus, an acquired immunodeficiency syndrome (HIV/AIDS) (8). In other reports, the production of substandard medication has become a growing concern in the pharmaceutical industry due its infiltration across all the continents, reaching a billion-dollar estimated value by the World Health Organization (WHO). They also report that the lack of knowledge pertaining to the formulation and distribution of these drugs, affects third world countries who are burdened with various health diseases (9). In general, the most basic way to probe pharmaceutical drugs is by focusing on their chemical behaviour in terms of reaction kinetics and molecular bonding (10-12). Many re-search methods have been proposed and applied for quality control of drugs and such include subdisciplines of chromatography, mass spectrometry and electrochemistry (13-15). Although these methods are successful in detecting and analysing pharmaceutical drugs, their application in large scale drug monitoring and quality control remains limited due to their inherent disadvantages such as complex preparation steps, expensive reagents, long processing times and sample destruction (16-17).

Amidst the modern and complex solutions discussed earlier, it often slipped our minds that optics and photonics can be readily integrated into the field of agriculture. The simplest examples would be the adjustment of plantation direction for optimum sunlight exposure, as well as the usage of incandescent light bulbs in egg incubation and hatching (18). Over recent decades, academics have been alerted to the potential of optics and photonics in the agricultural industry. This has led to progressive developments that utilize optics and photonic techniques in maximizing the quality and productivity of agricultural products.

METHODS

Different optical, photonics and spectroscopy methods are applied in these studies, detailed laboratory protocols can be found in our published literature. Figure 1 (adopted from (19)), below is an example of some of the custom-built optical setups applied in the diagnosis of different microorganisms, work that is intended for point of care diagnostics.

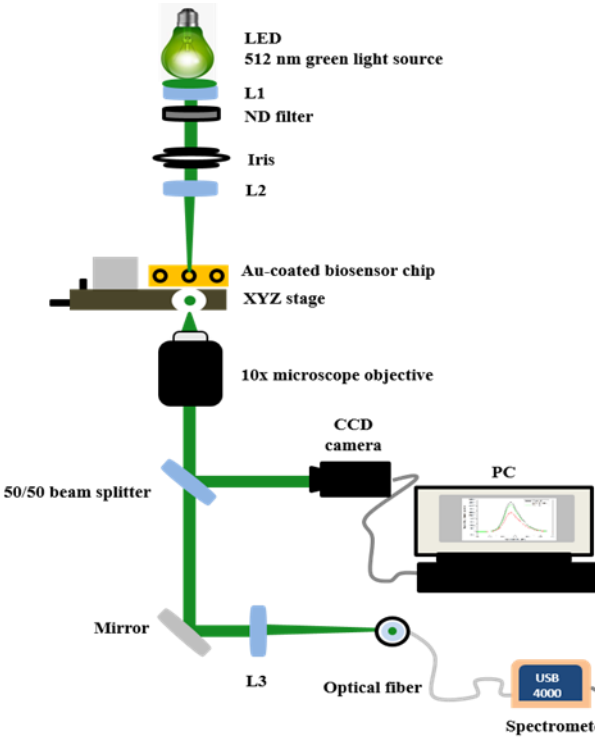

Figure 1: *The biosensing rig applied in measuring transmitted light. The system is based on a 512nm green light source with a power of 3.1 mW, collimating lenses (L1 and 2), XYZ stage, a 10x microscope objective, and an imaging system consisting of a CCD camera and computer, focussing lens (L3), an optical fiber, and a portable USB spectrometer connected to a computer (19).*

Whilst the current setup is a lab-based tool towards diagnosing communicable with potential applications in assessing markers for non-communicable diseases, the eventual aim is to miniaturize the setup for applications in POC settings.

The field of biophotonics has seen rapid advances in recent years, with new applications being developed all the time. Machine learning techniques have played a significant role in these advancements, as they have the potential to improve the performance and accuracy of biophotonics systems. As machine learning algorithms continue to evolve, the potential for further improvements in biophotonics is expected to continue to grow. Of note, ML algorithms, such as CNNs, have been used to automate the process of image segmentation, which involves separating the foreground of an image from the background. This is an important step in image analysis as it allows for the study of specific regions of interest within an image. In biophotonics, image segmentation has been used to identify and isolate individual cells or structures within a tissue sample. In object detection, ML algorithms have been used to automate the process of identifying and locating objects within an image. This is important in biophotonics as it allows for the identification and tracking of specific cells or structures within a tissue sample. Then in image classification, ML algorithms, such as CNNs and SVMs, have been used to classify images into different categories, such as normal vs. abnormal tissue.

This is important in biophotonics as it allows for the automated diagnosis of diseases such as cancer based on the analysis of microscopic images. Additionally in cell tracking, ML algorithms have been used to automate the process of tracking the movement of cells over time. This is important in biophotonics as it allows for the study of dynamic biological processes, such as cell migration, and can provide insight into the mechanisms of disease (20). Finally in spectral imaging, Machine learning algorithms have been used to process and analyze spectral images, which can contain large amounts of data. Spectral imaging can provide information about the molecular and cellular structure of a tissue sample, and machine learning can be used to extract this information and classify the tissue as normal or abnormal.

The work here follows supervised learning where the algorithms (a convolutional neural network, a support vector machine and a decision tree) are provided with labeled sample data for training to predict outputs. The algorithms are optimized by employing hyperparameter optimization techniques. The techniques were implemented using Python programming language on Google Colab (21-22). The aim of the work is to develop an optimized automatic TB detection system to classify chest X-ray images into healthy and TB infected. The research methodology follows these steps: dataset preparation, hyperparameter optimization, convenient model, comparison of the optimized models and comparisons of the models under study with different lightweight deep learning systems using different performance metrics. The process of classifying chest X-ray images is shown in Figure 2.

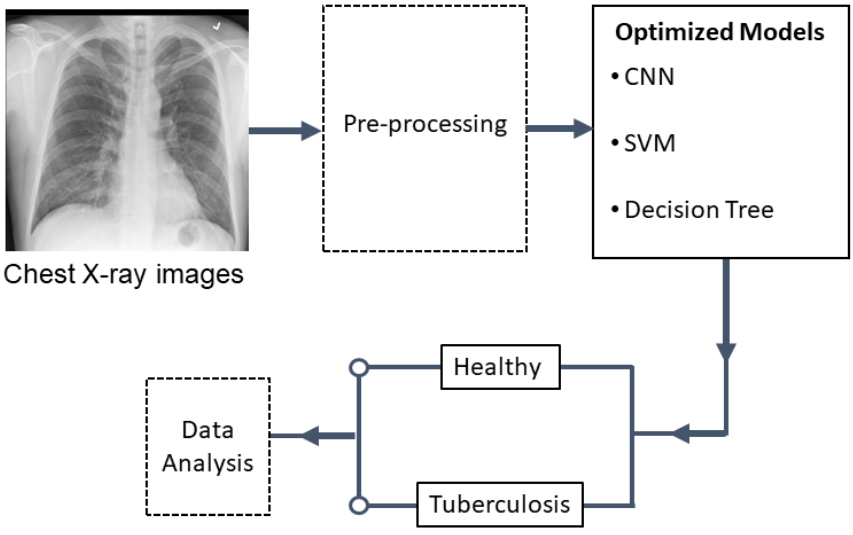

Figure 2: *An illustration of the approach followed in our research.*

The input chest X-ray images were adopted from publicly available Kaggle datasets (23-24). The input images are enhanced with image processing techniques (image reshaping, flattening and normalization) to

minimize error rates and improve detection performance. The output of the preprocessing stage are updated image inputs (25). Thereafter optimized models perform the classification of the images into healthy or tuberculosis, for which their accuracy is evaluated.

CONCLUSION

With the rapid advances in the field, new applications are being developed all the time, and the potential for machine learning to improve the performance and accuracy of biophotonics systems is expected to continue to grow. With the increasing demand for high-precision and real-time data analysis, the use of machine learning in biophotonics will become increasingly important. Continued research and development in this field, allows anticipation to new breakthroughs and advancements in biophotonics.

REFERENCES

[1] P. Pradhan, S. Guo, O. Ryabchykov, J. Popp, and T. W. Bocklitz, Deep learning a boon for biophotonics? Journal of Biophotonics, 13(6). https://doi.org/10.1002/jbio.201960186, 2020.

[2] E. Spyratou, M. Makropoulou, E. Mourelatou, and C. Demetzos, Biophotonic techniques for manipulation and characterization of drug delivery nanosystems in cancer therapy. Cancer Letters, 327(1–2), 111–122, https://doi.org/10.1016/j.canlet.2011.12.039, 2012.

[3] S. Melzer, R. Ankri, D. Fixler, and A. Tarnok, Nanoparticle uptake by macrophages in vulnerable plaques for atherosclerosis diagnosis. Journal of Biophotonics, 8 (11–12), 871–883. https://doi.org/10.1002/jbio.201500114, 2015.

[4] E. Valla, S. Nõmm, K. Medijainen, P. Taba, and A. Toomela, "Tremor-related feature engineering for machine learning based Parkinson's disease diagnostics," Biomed Signal Process Control, vol. 75, doi: 10.1016/j.bspc.2022.103551, 2022.

[5] L. Zhou, S. Pan, J. Wang, and A. V Vasilakos, "Machine learning on big data: Opportunities and challenges," Neurocomputing, vol. 237, pp. 350–361, 2017.

[6] N. G. Paterakis, "Hybrid quantum-classical multi-cut Benders approach with a power system application," Comput Chem Eng, vol. 172, 2023, doi: 10.1016/j.compchemeng, 108161, 2023.

[7] A. Buvé, K. Bishikwabo-Nsarhaza and G. Mutangadura, The spread and effect of HIV-1 infection in sub-Saharan Africa, The Lancet, 359, 2011–17, 2002.

[8] World Health Organisation, WHO Global Tuberculosis Report, 2022.

[9] https://www.who.int/news-room/fact-sheets/detail/substandard-and-falsified-medical-products

[10] A. Jouyban and E. Rahimpour, Sensors/nanosensors based on up conversion materials for the determination of pharmaceuticals and biomolecules, Talanta., 121383. https://doi.org/10.1016/j.talanta, 121383, 2020.

[11] J. Izo, S. Jesus, R. De, Löbenberg and NA, Bou-chacra, Raman Spectroscopy for Quantitative Analysis in the Pharmaceutical Industry. J Pharm.Sci., 24–46. DOI: 10.18433/jpps30649, 2022.

[12] S. Adomavičiūtė, M. Velička, V. Šablinskas, Detection of aspirin traces in blood by means of surface-enhanced Raman scattering spectroscopy. J Raman Spectrosc.; 51(6):919–31. https://doi.org/10.1002/jrs.5853, 2020.

[13] O. Heydari Shayesteh, R. Mahjub, A. Ranjbar, K Derakhshandeh and M. Jamshidi M, Nano optical and electrochemical sensors, and biosensors for detection of narrow therapeutic index drugs, Microchimica Acta 188(12):411 Available from: https://doi.org/10.1007/s00604-021-05003-, 2021.

[14] S. Er, U. Laraib, R. Arshad, S. Sargazi, A. Rahdar and S. Pandey, Amino Acids, Peptides, and Proteins: Implications for Nano-technological Applications in Biosensing and Drug / Gene Delivery, Nanomaterials (Basel); 1–36. doi: 10.3390/nano11113002, 2021.

[15] E.C. Le Ru and P.G. Etchegoin, Single-Molecule Surface-Enhanced Raman Spectroscopy, Annu Rev Phys Chem; 63(1):65–87. doi: 10.1146/annurev-physchem-032511-143757, 2012.

[16] I. Aretz and D. Meierhofer, Advantages and Pitfalls of Mass Spectrometry Based Metabolome Profiling in Systems Biology. Int J Mol Sci., 17(5):632. doi: 10.3390/ijms17050632, 2016.
[17] D. Sadutto and Y. Picó, Sample Preparation to Determine Pharmaceutical and Personal Care Products in an All-Water Matrix: Solid Phase Extraction. Molecules, 25(21):5204. doi: 10.3390/molecules25215204, 2020.
[18] S. Sumriddetchkajorn, How Optics and Photonics is Simply Applied in Agriculture? Proceedings of the International Conference on Photonics Solutions (ICPS), Pattaya City, Thailand, p. 888311, 2013.
[19] C. Maphanga, S. Manoto, S. Ombinda-lemboumba, Y. Ismail and P. Mthunzi-Kufa, Localized surface plasmon resonance biosensing of Mycobacterium tuberculosis biomarker for TB diagnosis, Sens. Bio-Sensing Res. 39, 2023.
[20] S. Corsetti and K. Dholakia, Optical manipulation: advances for biophotonics in the 21st century, Journal of Biomedical Optics, 26 (07). https://doi.org/10.1117/1.jbo.26.7.070602, 2021.
[21] E. Bisong and E. Bisong, Google colaboratory. Building machine learning and deep learning models on google cloud platform: a comprehensive guide for beginners, pp.59-64, 2019.
[22] T.B. Kimber, Y. Chen, and A. Volkamer, Deep learning in virtual screening: recent applications and developments. International Journal of Molecular Sciences, vol. 22, pp.4435, 2021.
[23] L. Quaranta, F. Calefato and F. Lanubile, KGTorrent: A dataset of python Jupyter notebooks from kaggle., IEEE/ACM 18th International Conference on Mining Software Repositories (MSR), pp.550-554, 2021.
[24] M.D. Kohli, R.M. Summers and J.R. Geis, 2017. Medical image data and datasets in the era of machine learning – whitepaper from the MIMI meeting dataset session, Journal of digital imaging, vol. 30, pp.392-399, 2016.
[25] S.I. Nafisah, and G. Muhammad, Tuberculosis detection in chest radiograph using convolutional neural network architecture and explainable artificial intelligence, Neural Computing and Applications, pp.1-21, 2022.

DOI 10.24412/cl-37136-2023-1-107-112

INVESTIGATION OF THE INFLUENCE OF THERMALLY-INDUCED METHEMOGLOBIN IN THE SKIN LAYERS ON THE EFFICIENCY OF LASER SCLEROSING OF TELANGIECTASIAS

ANDREY BELIKOV[1,2], VIKTOR CHUCHIN[1,3]

[1]Institute of Laser Technologies, ITMO University, Russia
[2]Research Institute of Dentistry and Maxillofacial Surgery, Pavlov First St. Petersburg State Medical University, Russia
[3]Sector of Medical Laser Technologies, "NPP VOLO" LLC, Russia

avbelikov@gmail.com

ABSTRACT

Lasers are widely used in dermatology for the treatment of telangiectasias, which are persistent dilation of the dermis blood vessels (venules, capillaries, arterioles) [1]. Blood absorbs electromagnetic radiation in the visible range effectively [2]. The small penetration depth of visible light into the skin is the problem of using visible lasers for sclerosis of the deep telangiectasias, which are not amenable to such treatment. Effective treatment of large telangiectasias requires a high energy density, which causes heating, undesirable damage to the surrounding tissues and increases the healing time [3]. Changing the skin optical properties is necessary to increase the sclerosis efficiency of deep and large telangiectasias with visible laser radiation. There is a known a method for increasing the optical transmission of human blood at certain wavelengths up to 50% by heating it up to 65 °C [4], which may be associated with the transformation of hemoglobin to methemoglobin [5]. We assume to heat the skin locally, achieve maximum increase of the optical transmission, and then perform sclerosis of the pathological vessel with a visible laser pulse.

First of all, it is necessary to develop an adequate skin optical model for a theoretical assessment of the effect of thermally induced methemoglobin on the optical properties of skin and on effectiveness of sclerosis. A seven-layer optical model of the skin is relevant today (Fig. 1): the stratum corneum, the layer of living cells of the epidermis, the papillary dermis, the superficial vascular plexus, the reticular dermis, the deep vascular plexus and the subcutaneous fat [6-10]. The thicknesses of the layers are presented in [6]. The refractive indexes of these layers are given in [11-13]. The stratum corneum and living epidermis absorption coefficients ware calculated using the equations from [8]. The absorption coefficients of other skin layers and whole blood were calculated using the equations from [14], the volume concentrations of chromophores are presented in [8, 15-30]. Then, the absorption coefficients were calculated for the case when all hemoglobin was replaced by methemoglobin [31, 32] in the skin layers and whole blood. Methods for calculating scattering coefficients and anisotropy factors are described in [7].

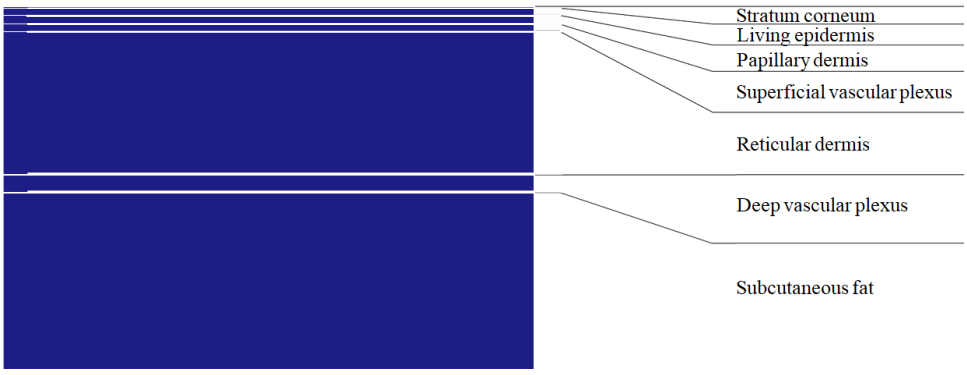

Figure 1: *Skin layers in the model*

The transport extinction coefficients (μ*tr*) for both cases (containing hemoglobin and methemoglobin) were calculated for whole blood [33]. The change in optical transmission of whole blood (*OT*) resulting from the replacement of hemoglobin with methemoglobin was estimated using the equation:

$$OT = \frac{\mu tr_{Hb}}{\mu tr_{MetHb}}$$

The wavelengths with the highest and lowest *OT* values of whole blood were selected for optical simulation. Optical simulation of skin was performed by the Monte Carlo method in the TracePro 7.0.1 (Lambda Research Corporation, USA). Laser exposure was carried out by a 4 mm diameter parallel beam (10,000 rays) perpendicular to the skin surface. The absorbed optical power distributions in skin at selected wavelengths were obtained for both cases for further thermophysical simulation as a volume heat source.

Thermophysical simulation was performed in COMSOL Multiphysics (COMSOL Inc., USA) and was performed by the method of radiative-conductive heat transfer. The values of the thermophysical properties of the skin layers are presented in Table 1. The maximum temperature of skin heating by laser radiation and depth which a temperature of 42 °C (start temperature of the coagulation process) was reached at have been estimated as a result of thermophysical simulation for both cases and compared with each other.

Table 1. Thermophysical properties of the skin layers [34]

Thermophysical property	Stratum corneum	Living epidermis	Papillary dermis	Superficial vascular plexus	Reticular dermis	Deep vascular plexus	Subcutaneous fat
Thermal conductivity, $c\left(\frac{J}{kg \times K}\right)$	3600		3800				2250
Density, $\rho\left(\frac{kg}{m^3}\right)$	1200		1200				850
Thermal conductivity, $k\left(\frac{W}{m \times K}\right)$	0.21		0.53				0.19

The results of *OT* calculations showed that the largest *OT* growth is observed at 441 nm (*OT*=1.96) and 574 nm (*OT*=2.50), and the largest *OT* reduce – at 629 nm (*OT*=0.37) and 1105 nm (*OT*=0.55). The distribution of absorbed optical power in the skin at these wavelengths was obtained as a result of optical simulation.

Heating of the skin with 100% concentration of hemoglobin in the blood by laser radiation at a wavelength of 441 nm with a power of 2 W for 1 s showed a maximum temperature of 113 °C (Fig. 2a). Heating of the skin with 100% concentration of methemoglobin in the blood by laser radiation at this wavelength with same parameters showed a maximum temperature of 103 °C (Fig. 2b) due to a decrease in absorption at this wavelength.

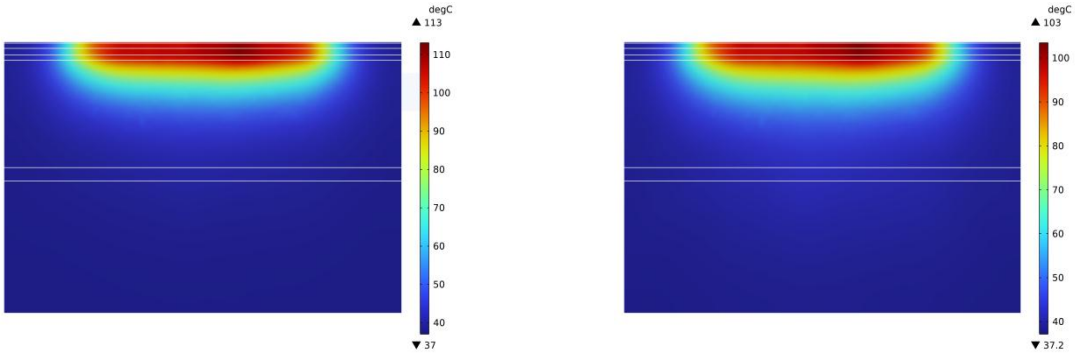

a b

Figure 2: *Heating of skin with 100% concentration of hemoglobin (a) and 100% concentration of methemoglobin (b) in the blood by 441 nm radiation*

Heating of the skin with 100% concentration of hemoglobin in the blood by laser radiation at a wavelength of 574 nm with a power of 2 W for 1 s showed a maximum temperature of 92 °C (Fig. 3a). Heating of the skin with 100% concentration of methemoglobin in the blood by laser radiation at this wavelength with same parameters showed a maximum temperature of 78.8 °C (Fig. 3b) due to a decrease in absorption at this wavelength.

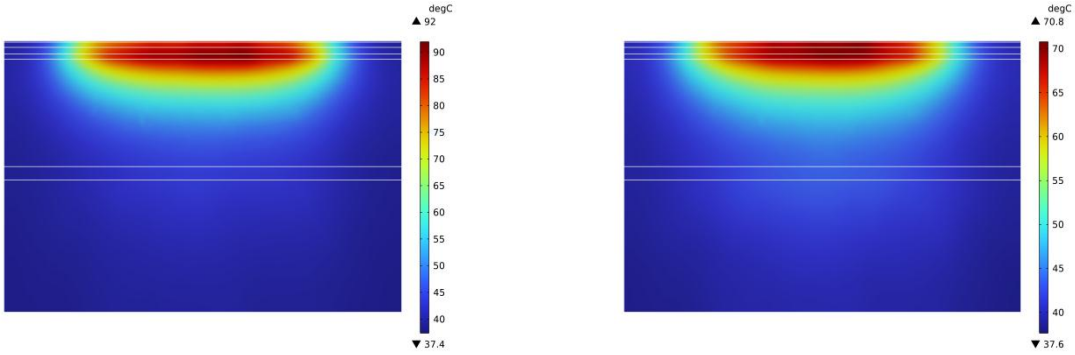

a b

Figure 3: *Heating of skin with 100% concentration of hemoglobin (a) and100% concentration of methemoglobin (b) in the blood by 574 nm radiation*

Heating of the skin with 100% concentration of hemoglobin in the blood by laser radiation at a wavelength of 629 nm with a power of 2 W for 1 s showed a maximum temperature of 53 °C (Fig. 4a). Heating of the skin with 100% concentration of methemoglobin in the blood by laser radiation at this wavelength with same parameters showed a maximum temperature of 70.4 °C (Fig. 4b) due to an increase in absorption at this wavelength.

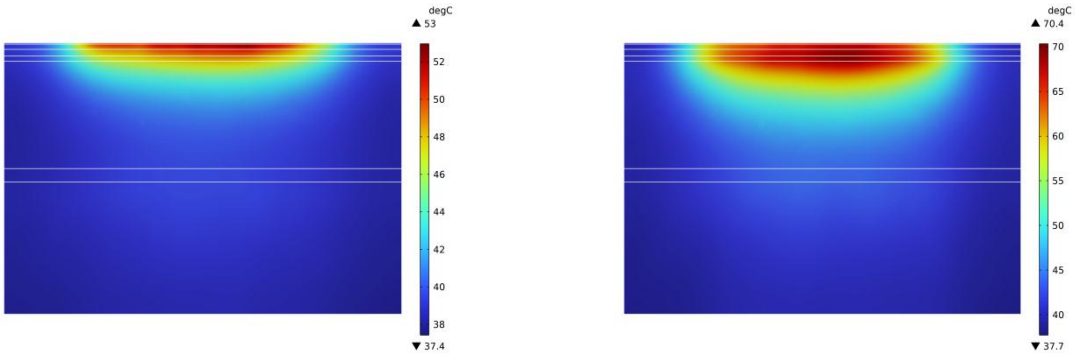

a b

Figure 4: *Heating of skin with 100% concentration of hemoglobin (a) and 100% concentration of methemoglobin (b) in the blood by 629 nm radiation*

Heating of the skin with 100% concentration of hemoglobin in the blood by laser radiation at a wavelength of 1105 nm with a power of 2 W for 1 s showed a maximum temperature of 44.5 °C, (Fig. 5a). Heating of the skin with 100% concentration of methemoglobin in the blood by laser radiation at this wavelength with same parameters showed a maximum temperature of 58.5 °C (Fig. 5b) due to an increase in absorption at this wavelength. There is a heating zone in the area of the deep vascular plexus.

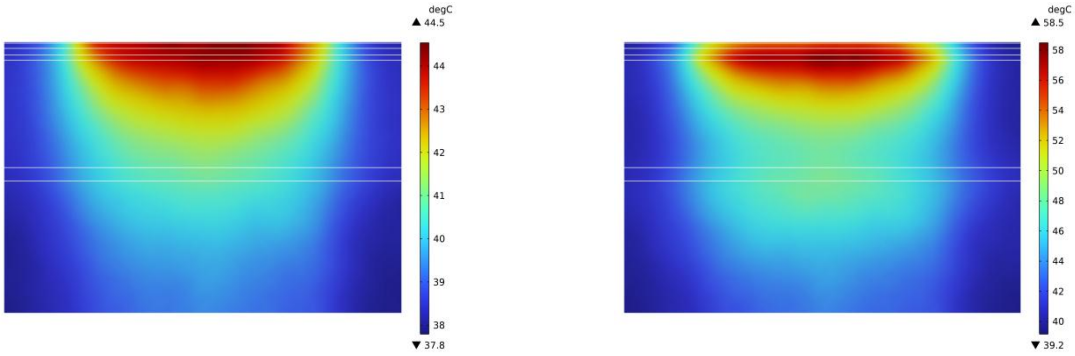

a b

Figure 5: *Heating of skin with 100% concentration of hemoglobin (a) and 100% concentration of methemoglobin (b) in the blood by 1105 nm radiation*

The results of assessing the heating depth to a temperature of 42 °C (h_{42}) are shown in Figure 6. It can be seen that when hemoglobin is replaced by methemoglobin this heating depth increases at all wavelengths.

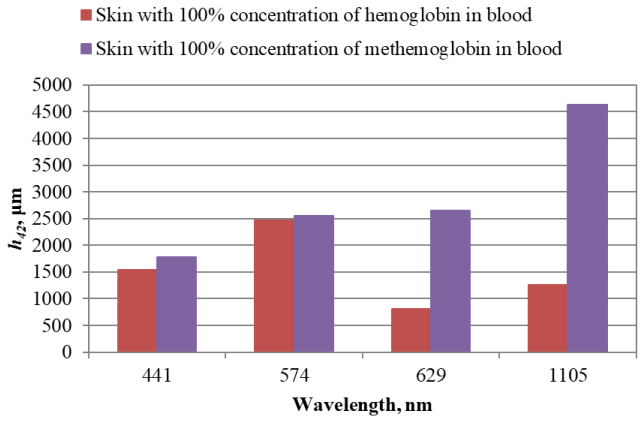

Figure 6: *Comparison of the heating depth to a temperature of 42 °C (h_{42}) at each wavelength*

For 441 nm and 574 nm, the depth h_{42} increases due to the decrease in absorption coefficients at these wavelengths in the skin layers. However, for 629 nm and 1104 nm, the depth also increases on the contrary due to an increase in absorption at these wavelengths in the skin layers, which does not allow laser energy to be dissipated over the entire volume of the skin.

The paper considers the possibility of using thermally induced methemoglobin to control the optical properties of a biological tissue. It has been established that methemoglobin in the composition of the skin leads to the greatest growth in its optical transmission at wavelengths near 441 nm and 578 nm and reduce optical transmission at wavelengths near 629 nm and 1105 nm. It has been demonstrated that the hemoglobin to methemoglobin transformation leads to a change in the absorbed optical power in the skin layers and affects the maximum temperature and depth of heating at selected wavelengths. Numerical methods have shown the possibility of using thermally induced methemoglobin to control the optical properties of the skin, which can be used to create laser systems and technologies for the treatment of skin diseases, including laser sclerosing of telangiectasias.

REFERENCES

[1] Goldman M.P., Weiss R.A. Sclerotherapy E-Book: Treatment of Varicose and Telangiectatic Leg Veins (Expert Consult). Elsevier Health Sciences, p. 455, 2016.

[2] Nachabé R., Evers D.J., Hendriks B.H.W., Lucassen G.W., Van der Voort M., Wesseling J., Ruers T.J.M. Effect of bile absorption coefficients on the estimation of liver tissue optical properties and related implications in discriminating healthy and tumorous samples, Biomedical optics express. 600–614, 2011.

[3] Barton J.K., Frangineas G., Pummer H., Black, J.F. Cooperative Phenomena in Two- pulse, Two- color Laser Photocoagulation of Cutaneous Blood Vessels, Photochemistry and Photobiology. 642–650, 2001.

[4] Baranov V.Y., Chekhov D.I., Leonov A.G., Leonov P.G., Ryaboshapka O.M., Semenov S.Y., Tatsis G.P. Heat-induced changes in optical properties of human whole blood in vitro, Optical diagnostics of biological fluids IV. 180–187, 1999.

[5] Seto Y., Kataoka M., Tsuge K. Stability of blood carbon monoxide and hemoglobins during heating, Forensic science international. 144–150, 2001.

[6] Dremin V., Zherebtsov E., Bykov A., Popov A., Doronin A., Meglinski I. Influence of blood pulsation on diagnostic volume in pulse oximetry and photoplethysmography measurements, Applied optics. 9398–9405, 2019.

[7] Bashkatov A.N., Genina E.A., Tuchin V.V., Altshuler G.B., Yaroslavsky I.V. Monte Carlo study of skin optical clearing to enhance light penetration in the tissue: implications for photodynamic therapy of acne vulgaris, Advanced Laser Technologies 2007. 80–91, 2008.

[8] Meglinski I.V., Matcher S.J. Quantitative assessment of skin layers absorption and skin reflectance spectra simulation in the visible and near-infrared spectral regions, Physiological measurement. 741–753, 2002.

[9] Kim O., McMurdy J., Lines C., Duffy S., Crawford G., Alber M. Reflectance spectrometry of normal and bruised human skins: experiments and modeling, Physiological measurement. 159–175, 2012.

[10] Meglinski I.V., Matcher S.J. Computer simulation of the skin reflectance spectra, Computer methods and programs in biomedicine. 179–186, 2003.

[11] Bashkatov A.N., Genina E.A., Tuchin V.V. Optical properties of skin, subcutaneous, and muscle tissues: a review, J. of Innovat Opt. Health Sci. 9–38, 2011.

[12] Ding H., Lu J.Q., Wooden W.A., Kragel P.J., Hu X.-H. Refractive indices of human skin tissues at eight wavelengths and estimated dispersion relations between 300 and 1600 nm, Physics in Medicine & Biology. 1479–1489, 2006.

[13] Müller G. J., Roggan A. Laser-induced interstitial thermotherapy. SPIE Press, p.549, 1995

[14] Calabro K. Modeling biological tissues in light tools. – Access link: https://www.synopsys.com/content/dam/synopsys/optical-solutions/documents/modeling-tissues-lighttools-paper.pdf (date of the application 23.06.2023)

[15] Lee S.H., Jeong S.K., Ahn S.K. An update of the defensive barrier function of skin, Yonsei medical journal. 293–306, 2006.

[16] Groen D., Gooris G.S., Barlow D.J., Lawrence M.J., Van Mechelen J.B., Demé B., Bouwstra J.A. Disposition of ceramide in model lipid membranes determined by neutron diffraction, Biophysical journal. 1481–1489, 2011.

[17] Seteykin A.Yu. Model for calculating temperature fields arising under the action of laser radiation on a multilayer biological tissue, Optical journal. 42–47, 2005. (in Russian)

[18] Labib R.S., Anhalt G.J., Patel H.P., Diaz L.A. Epidermal proteins. I. Differential extraction and quantitative polyacrylamide gel-electrophoretic analysis of basal spinous-cell proteins of neonatal mouse epidermis, Archives of dermatological research. 253–263, 1985.

[19] Chaudhary P., Kumar A., Saxena N., Biswal U.C. Hyperbilirubinemia as a predictor of gangrenous/perforated appendicitis: a prospective study, Annals of gastroenterology: quarterly publication of the Hellenic Society of Gastroenterology. 325–331, 2013.

[20] Malskies C.R., Eibenberger E., Angelopoulou E. The Recognition of Ethnic Groups based on Histological Skin Properties, Proc. of the Vision, Modeling, and Visualization Workshop. 353-360, 2011.

[21] Nicolaides N. Skin lipids. II. Lipid class composition of samples from various species and anatomical sites, Journal of the American Oil Chemists' Society. 691–702, 1965.
[22] Nachabé R., Evers D.J., Hendriks B.H.W., Lucassen G.W., Van der Voort M., Wesseling J., Ruers T.J.M. Effect of bile absorption coefficients on the estimation of liver tissue optical properties and related implications in discriminating healthy and tumorous samples, Biomedical optics express. 600–614, 2011.
[23] McMaster J.D., Jenkinson D.M., Noble R.C., Elder H.Y. The lipid composition of bovine sebum and dermis, British Veterinary Journal. 34–41, 1985.
[24] Waller J.M., Maibach H.I. Age and skin structure and function, a quantitative approach (II): protein, glycosaminoglycan, water, and lipid content and structure, Skin Research and Technology. 145–154, 2006.
[25] Yannas I.V., Burke J.F., Gordon P.L., Huang C., Rubenstein R.H. Design of an artificial skin. II. Control of chemical composition, Journal of biomedical materials research. 107–132, 1980.
[26] Bonnett R., Davies J.E., Hursthouse M.B. Structure of bilirubin, Nature. 326–328, 1976.
[27] Ermakov I.V., Gellermann W. Dermal carotenoid measurements via pressure mediated reflection spectroscopy Journal of biophotonics. 559–570, 2012.
[28] Haynes W.M. CRC handbook of chemistry and physics. CRC press, p. 2670, 2016.
[29] Thomas L.W. The chemical composition of adipose tissue of man and mice, Quarterly Journal of Experimental Physiology and Cognate Medical Sciences: Translation and Integration. 179–188, 1962.
[30] Mujkić R., Mujkić D.Š., Ilić I., Rođak E., Šumanovac A., Grgić A., Divković D., Selthofer-Relatić K. Early Childhood Fat Tissue Changes—Adipocyte Morphometry, Collagen Deposition, and Expression of CD163+ Cells in Subcutaneous and Visceral Adipose Tissue of Male Children, International Journal of Environmental Research and Public Health. 3627–3637, 2021.
[31] Khatun F., Aizu Y., Nishidate I. In Vivo Transcutaneous Monitoring of Hemoglobin Derivatives Using a Red-Green-Blue Camera-Based Spectral Imaging Technique, International Journal of Molecular Sciences. 1528–1545, 2021.
[32] Kuenstner J.T., Norris K.H. Spectrophotometry of human hemoglobin in the near infrared region from 1000 to 2500 nm, Journal of Near Infrared Spectroscopy. 59-65, 1994.
[33] Al'tshuler G.B., Smirnov M.Z., Pushkareva A.E. Modeling of the laser and lamp treatment of telangiectasia, Optics and spectroscopy. 141–144, 2004.
[34] Astafieva L.G., Zheltov G.I. Dynamics of the temperature field inside a blood vessel under the action of laser radiation, Optics and Spectroscopy. 689-694, 2005. (in Russian)

DOI 10.24412/cl-37136-2023-1-113-117

INVESTIGATION OF HAIR OPTICAL PROPERTIES FOR ITS LASER COLORING

VLADISLAV ERMOLAEV

Institute of laser technologies, ITMO University, Russia
v_m_ermolaev@mail.ru

ABSTRACT

In order to successfully solve optical problems related to the effect of light on hair, it is necessary to know their optical parameters, such as refractive index, absorption and scattering coefficients (extinction), as well as anisotropy factor [1]. Unfortunately, data on optical properties of hair, unlike other biotissues, are rather scarce and fragmentary [2]. Therefore, obtaining the most detailed spectra of optical parameters of hair is an actual task of biophotonics.

The information about the optical properties of hair can be used for the creation of cosmetological devices for laser hair coloring. Laser hair coloring is a new approach to hair coloring. The idea is that exposure to radiation under certain parameters is able to change the color of the hair without damaging its integrity. Earlier it was shown that broad-spectrum light sources can cause noticeable yellowing and discoloration of hair [3,4]. Research into the possibility of using monochromatic radiation for hair coloring is the next step towards the creation of a new laser hair coloring technology.

Melanin pigments are responsible for hair color. Melanins come in two varieties: brown and black eumelanins and yellowish and reddish pheomelanins. Combinations of these pigments in different concentrations produce all sorts of natural hair tones. It is the change in concentrations of melanins in the hair when exposed to radiation that contributes to the change in hair color [5]. It is important to keep in mind that the initial differences in chemical composition between hairs of different colors create differences in their interaction with radiation.

The aim of the study was to obtain continuous spectra of the extinction coefficient of human hair of different colors for their laser coloring. The goal was achieved in two ways: by means of computer simulation and by experimental measurements.

To calculate the extinction spectra of hair of different colors, an optical model of hair was created in TracePro program (Lambda Research Corporation, USA; version 7.0.1). The model consisted of a three-layer parallelepipedal structure with dimensions of 2000x2000x60 microns: the middle layer, the cortex, 50 microns thick was enclosed between identical 5 microns thick cuticle layers (Fig. 1). The number and thicknesses of the layers corresponded to those of the real hair, except for the medulla, the inner hair layer, which was not included in the model because of its negligible effect on hair properties [6]. In addition, the cylindrical shape of the hair was not considered in the model, because it would introduce noticeable losses due to reflection of radiation from the surface, which are not of interest for the measurement of the desired coefficient.

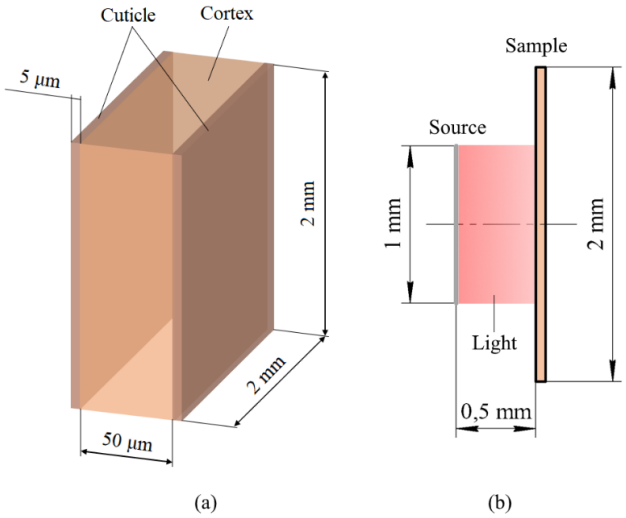

Figure 1: *(a) Hair model scheme (not in scale); (b) optical simulation scheme.*

In optical modeling it was assumed that the cuticle consists of pure keratin, and the cortex consists of keratin, water, eumelanin, and pheomelanin. Concentrations of cortex components were calculated according to literature data for five hair colors: dark, white, gray, brown, and chestnut [7]. The required optical coefficients of cortex components were taken from the literature [8-13]; the total cortex optical coefficients were estimated as the sums of the products of cortex component coefficients by the corresponding concentrations. In the TracePro program, the hair model was irradiated with a 1 W monochromatic circular radiation source with a diameter of 1 mm and zero divergence. The wavelength of the source was varied in the range from 330 to 2240 nm in increments of 20 nm. At each wavelength, 100,000 rays were calculated by the Monte Carlo method and the power of the transmitted radiation was recorded. The ratio of the incident radiation power to the transmitted radiation power gave the permittivity of the hair, which when divided by the total thickness of the model gave the extinction coefficient. Thus, the spectra of extinction of hair of five colors were obtained (Fig. 2).

Figure 2 shows that the character of hair spectra of different colors is similar, there are differences in the values of extinction coefficients. The maxima in the range from 330 to 400 nm and six peaks (1200, 1520, 1740, 1940, 2060 and 2180 nm) are clearly visible. The large values of the extinction coefficient in the ultraviolet (UV) range are associated with the absorption of melanins, the peaks at 1200 and 1740 nm give the stretching vibrations of CH molecules, the peak at 1520 nm gives the stretching vibrations of OH molecules, the peak at 1940 nm gives the stretching vibrations of OH molecules and the scissor vibrations of H_2O molecules, the peaks at 2060 and 2180 nm give amides [5,8,14]. Fluctuations of OH and H_2O molecules occur in water, and fluctuations of CH molecules and absorption by amides in keratin, which is part of the hair.

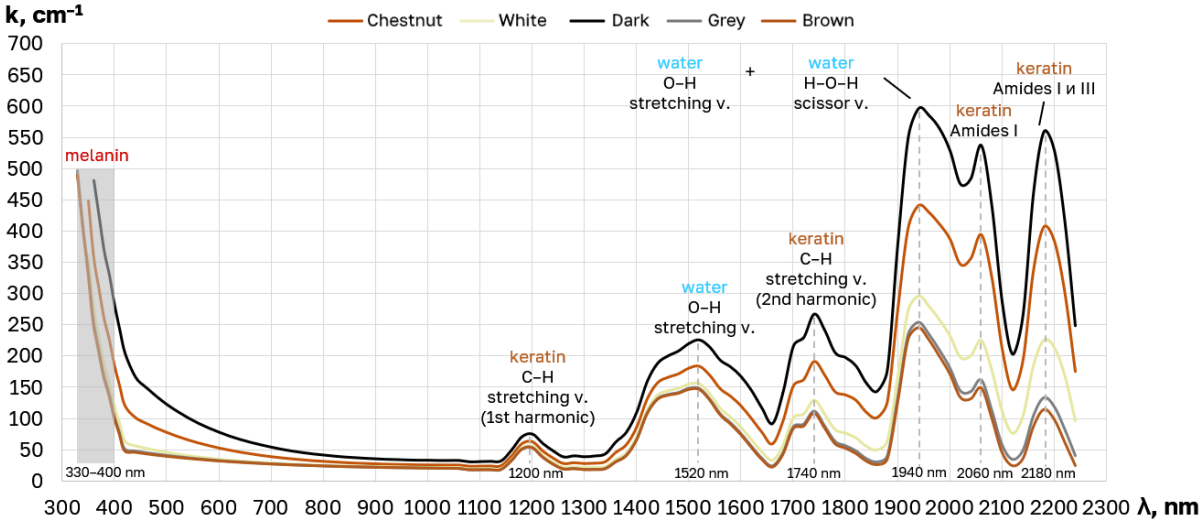

Figure 2: *Calculated extinction spectra of hair of five colors from 330 to 2240 nm.*

To apply the data obtained according to the purpose of the study, it is important to understand what effects occur in the hair under the action of radiation of different wavelengths, primarily in terms of changes in their color. A number of works are devoted to the study of photodegradation of hair under the influence of radiation of the optical spectrum: UV, visible and infrared (IR). Effects of UV and visible light are studied in more detail due to the fact that melanins, responsible for hair color, are well absorbed by this radiation [5]. We know that UV and visible light can cause yellowing of blond, red, dark and brown hair, as well as reducing the yellowness of gray hair [3]. Yellowing in this case refers to the positive color coordinate b in the CIELAB system. It was found that UV radiation is capable of destroying the structure of hair, including through the destruction of disulfide bonds. In general, it can be argued that UV and visible radiation, with the former to a greater extent, contribute to the photodegradation of melanin, i.e. change its reflection spectrum, which determines the coloration of the entire hair [15]. As for the effects of infrared radiation, it has been shown that it can cause yellowing of gray hair, as well as its bleaching, similar to what is achieved by washing hair with hydrogen peroxide. However, to change the coloration of hair, infrared light requires a higher power density and a longer exposure time than UV or visible light [4]. Thus, the most preferred sources for laser hair coloring appear to be low-power UV sources capable of changing hair color without causing significant damage.

The initial step in the experimental determination of hair extinction spectra was to evaluate the colors of four hair samples. For this purpose, the CIELAB color system is used, as it more accurately shows how the human eye perceives colors. In this system, color is given by three coordinates: *L* – the lightness, *a* – the coordinate between red and green, and *b* – the coordinate between yellow and blue. There are different ways of measuring color coordinates. In this work, the color assessment was carried out by means of a scanner and a computer. Using a scanner allows you to evenly illuminate the samples and ensure identical image registration conditions. High-resolution photos of four hair samples were fixed with a scanner and averaged color coordinates of each sample were obtained on the computer in Adobe Photoshop (Adobe Systems, USA; version number 24.0.1). According to these coordinates, the names of hair colors closest to the experimental data were selected according to the palettes of hair dyes of the largest manufacturers (Fig. 3)

Appearance				
Coordinates L, a, b	35, 17, 23	14, 2, –4	76, 6, 24	30, 7, 9
Hair color				
Hair color name	Light brown	Natural black	Light ash blond	Dark ash brown

Figure 3: *Results of hair samples color evaluation.*

A UV/VIS T90 spectrophotometer (PG Instruments, United Kingdom) was used to measure hair spectra. Samples were prepared from blond hair. Hair was cut with scissors into fragments no longer than 1 cm in length and ground using a mechanical mill (manufacturer, country) to obtain a fine powder. Next, a piece of transparent scotch tape with a width of at least 1 cm and a length of at least 2 cm was attached to the inside of the mill cover with an adhesive side inside the mill. The thickness of the adhesive tape was 20±5 μm. The mill was then run for about 10 seconds more, and the hair powder was deposited on the piece of scotch tape in the center of the inside of the lid. The piece of tape was then carefully removed from the cover and cleaned of excess powder and coarse hairs with a metal blade. Then, a piece of the same scotch without powder was placed on this piece of tape on the side containing particles of hair powder, and in this way a 90±5 microns thick sample for the experiments was obtained. Thus, in the sample, the hair powder was enclosed between the two pieces of scotch tape. Before the measurements of the hair spectrum, the baseline was measured: samples similar to those described earlier, but without hair powder, were placed in both channels of the instrument. Correction of the baseline made it possible to exclude the influence of light interaction with the tape on the

desired result. The measurements were performed in the fast mode with the spectral step equal to 1 nm. A total of 20 spectral measurements were made and the average extinction spectrum was calculated from them (Fig. 4).

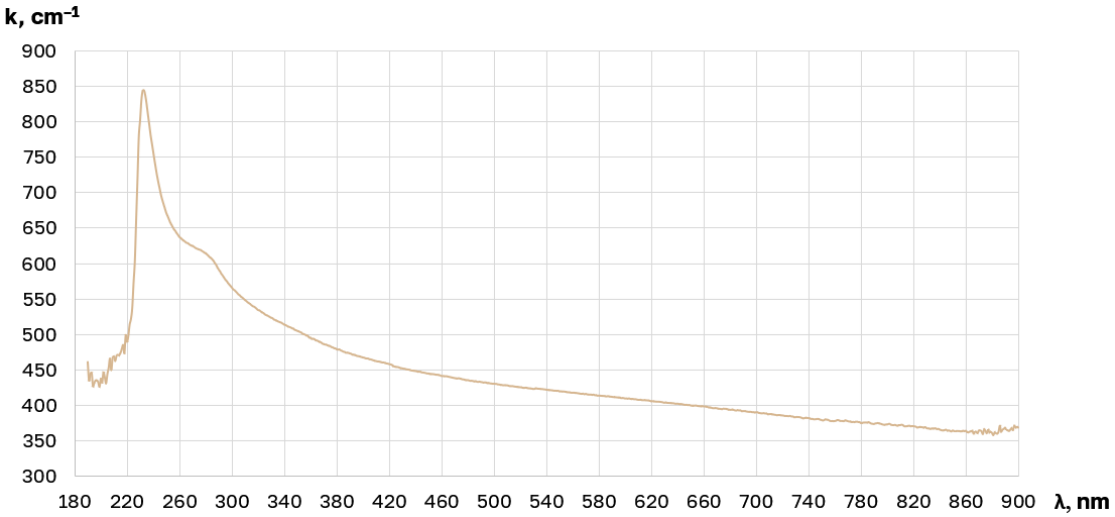

Figure 4: *Measured extinction spectrum of light ash blond hair from 190 to 900 nm.*

Thus, as a result of the study, the spectra of extinction of hair of five colors in the spectral range from 330 to 2240 nm have been obtained using computer optical modeling, and the characteristics of the extinction peaks have been given. Data on the effects occurring in the hair under the influence of radiation of different wavelengths were systematized. Using a scanner and a computer, the color of four real samples of human hair using the CIELAB system was evaluated. Using a spectrophotometer, experiments were carried out to measure the spectrum of light hair extinction. Comparison of the calculated and experimental data showed the similarity of the characters of the extinction spectra with differences in the values of the extinction coefficient. This could be due to the difference between the concentrations of melanin in the model and in the experimental samples, which influenced the results, especially in the UV range, where melanin strongly absorbs radiation. In addition, the shredded hair structure in the samples may have somewhat different scattering characteristics, which could also affect the final values of the extinction coefficient.

REFERENCES

[1] Tuchin V. V. Light interaction with biological tissues: overview: Static and Dynamic Light Scattering in Medicine and Biology; 1993 Jan 21-22; Los Angeles, USA.

[2] Huang X., Protheroe M.D., Al-Jumaily A.M., Paul S.P., Chalmers A.N. Review of human hair optical properties in possible relation to melanoma development. J. Biomed. Opt. 2018;23(5).

[3] Nogueira A. C. S., Richena M., Dicelio L. E., Joekes I. Photo yellowing of human hair. J. Photoch. Photobio. B. 2007;88(2):119-125.

[4] Richena M., Silveira M., Rezende C.A., Joekes I. Yellowing and bleaching of grey hair caused by photo and thermal degradation. J. Photoch. Photobio. B. 2014;138:172-181.

[5] Nogueira A. C. S., Joekes I., Dicelio L. About photo-damage of human hair. Photocem. Phtobio. S. 2006;5:165-169.

[6] Robbins C. R. Chemical and physical behavior of human hair. Berlin (Germany): Springer; 2012.

[7] Bashkatov A. N., Genina E. A., Kochubei V. I., Tuchin V. V. Estimate of the melanin content in human hairs by the inverse Monte-Carlo method using a system for digital image analysis. Quantum. Electron. 2006;36(12):1111-1118.

[8] Pande C. M., Yang B. Near-infrared spectroscopy: Applications in hair research. J. Cosmet. Sci. 2000;51(3):183-192.

[9] Pande C. M., Albrecht L., Yang B. Hair photoprotection by dyes. J. Cosmet. Sci. 2001;52(6):377-390.

[10] Baranoski G. V. G., Chen T. F. Optical properties of skin surface. In: Humber P., Fanian F., Maibach H. I., Agache P., editors. Agache's Measuring the Skin. Berlin: Springer; 2017. p. 1-14.

[11] Sardar D. K., Mayo M. L., Glickman R. D. Optical characterization of melanin. . J. Biomed. Opt. 2001;6(4):404-411.

[12] Jacques S. L. Optical properties of biological tissues: a review. Phys. Med. Biol. 2013;58(11).
[13] Segelstein D. J. The complex refractive index of water: diss. Kansas City: University of Missouri, 1981.
[14] Dufour E. Principles of infrared spectroscopy. In: Sun D.-W., editor. Infrared spectroscopy for food quality analysis and control. Boston: Academic Press, 2009. p. 1-27.
[15] Signori V. Review of the current understanding of the effect of ultraviolet and visible radiation on hair structure and options for photoprotection. Int. J. Cosmetic Sci. 2004;55(1):95-113.

DOI 10.24412/cl-37136-2023-1-118-128

ALUMINIUM PHTHALOCYANINE-GOLD NANOPARTICLE ENHANCE THE THERAPEUTIC EFFECT OF PDT IN OESOPHAGEAL CANCER.

ONYISI CHRISTIANA DIDAMSON[1], RAHUL CHANDRAN[1] AND HEIDI ABRAHAMSE [1]

1 Laser Research Centre, Faculty of Health Sciences, University of Johannesburg, South Africa

christydidamson@gmail.com

ABSTRACT

BACKGROUND

Gold nanoparticles mediated photodynamic therapy (PDT) has been reported to boost the efficiency and specificity of cancer treatment; however, their impact on oesophageal cancer is limited. In this study, we performed an *in vitro* assessment of aluminium phthalocyanine ($AlPcS_4Cl$)-gold nanoparticle (AuNPs) mediated PDT targeting oesophageal cancer cells. The $AlPcS_4Cl$-AuNPs conjugate was synthesized through a non-covalent method. The synthesized $AlPcS_4Cl$-AuNPs were confirmed by ultraviolet-visible (UV–vis) absorption spectral analysis and high-resolution transmission electron microscopy. *In vitro*, effects of AlPcS4Cl-AuNPs based PDT in an oesophageal cancer cell line (HKESC-1) was examined. Cellular parameters which include cell viability, cellular proliferation, and cytotoxicity, were assessed by MTT assay, ATP cell proliferation assay, and lactate dehydrogenase (LDH) assay respectively. Fluorescent microscopy was used to determine the internalisation of the conjugates in cellular organelles. Furthermore, Mitochondrial membrane potential (MMP) integrity and reactive oxygen species (ROS) generation indications of cell death were also examined. The findings showed that PDT with aluminium (III) phthalocyanine chloride tetra sulfonic acid ($AlPcS_4Cl$) conjugated gold nanoparticle (AuNPs)($AlPcS_4Cl$-AuNPs) significantly inhibit cell viability/cellular proliferation, increase cytotoxicity, and ROS generation. Fluorescent microscopy revealed that $AlPcS_4Cl$-AuNPs was localised in the mitochondria and Endoplasmic reticulum (ER), suggesting that the induction of biochemical cell death pathways could be mitochondria and ER-dependent. More importantly, $AlPcS_4Cl$-AuNPs significantly altered the mitochondrial membrane integrity in HKESC-1 cells. This further means the mitochondria-dependent cell death pathway may be involved. In conclusion, our findings demonstrated that $AlPcS_4Cl$-AuNPs conjugates improved the anti-cancer effects of PDT in oesophageal cancer cells, proposing a better measure to boost the therapeutic efficiency of PDT in oesophageal cancer.

INTRODUCTION

Oesophageal cancer is a lethal digestive tract tumour, representing the eighth cancer-associated illness and the sixth cancer-associated death worldwide [1]. Risk factors associated with the emergence of oesophageal cancer include tobacco intake, alcohol ingestion, poor oral health, ingestion of carcinogenic agents, gastroesophageal reflux disease (GORD), obesity, and genetic and epigenetic changes [2]. The conventional therapy for oesophageal cancer consists of surgery, chemotherapy, and radiotherapy or combinations of these therapies. These treatments have tremendously improved the treatment of oesophageal. However, conventional treatments are faced with unfavourable side effects, ineffective treatment outcomes, treatment resistance, tumour relapse, low survival rate [3]. Hence, the search for an effective treatment measure, efficient at eliminating tumour cells without relapse, improving prognosis and without adverse effects, is critical. Photodynamic therapy (PDT), an efficient, non-invasive modality, has emerged for the treatment of cancer and other neoplastic disorders. Concerning conventional treatments, PDT has minimal side effects, providing safe and efficient measures that preferentially eradicate cancer cells from non-cancerous cells. Photodynamic therapy consists of three vital parameters, a photoactive agent called a photosensitiser (PS), molecular oxygen and light of the correct wavelength. These three parameters work together to eliminate tumour cells [3, 4]. Various PSs have been employed for PDT of different tumours, including Aluminium (III) Phthalocyanine Chloride Tetra Sulfonic Acid ($AlPcS_4Cl$). The PS $AlPcS_4Cl$ has attracted much attention due to its high tissue penetration and increased reactive oxygen species (ROS) production. Studies have investigated the effects of $AlPcS_4Cl$-

mediated PDT in different cancers [5-7], including oesophageal cancer [8]. Nevertheless, cellular internalisation is slow due to the repulsion that is created between the negative charges of the sulfonated group on the PS and the cell membrane. Hence an efficient delivery of $AlPcS_4Cl$ into tumour cells is needed.

With the emergence of nanotechnology, the application of nanoparticles as carriers to deliver drugs has been investigated. Several nanoparticles have been used as carriers for drug delivery in PDT. Gold nanoparticle (AuNPs) has gained much interest among several nanoparticles as a nanocarrier due to their chemical uncreativeness, efficient optical features and biocompatibility [4]. The effects of AuNPs mediated PDT have been reported on different cancer types [9-12]; however, its impact on oesophageal cancer is limited. Therefore, in this study, we evaluated the effects of $AlPcS_4Cl$-AuNPs conjugates in enhancing the therapeutic efficiency of PDT in oesophageal cancer using *in vitro* assays.

MATERIALS AND METHODS

Reagent Preparation and Characterisation of $AlPcS_4Cl$-AuNPs

The $AlPcS_4Cl$ (Frontier Scientific, AlPcS-834) with a molecular weight of 895.21 g/mol was reconstituted to a concentration of 1.0 mM, covered with aluminium foil and kept in the dark at room temperature. AuNPs (Sigma Aldrich, 765457), with a diameter size of 10 nm, functionalised with PEGylated carboxylic acid end (AuNP-PEG3000-COOH) with a stock concentration of 3 mg/ml were used in this study. The $AlPcS_4Cl$ was adsorbed onto AuNPs as previously described [10]. Briefly, the $AlPcS_4Cl$ and AuNPs were first filtered using a filter of 0.22-mm. The conjugation was achieved by adding $AlPcS_4Cl$ and AuNPs in a 1:2 ratio and vortexed for five minutes without a wash step. This method was adopted to retain the concentration of the conjugates. The ultraviolet-visible (UV–vis) absorption spectral of $AlPcS_4Cl$, AuNPs, and $AlPcS_4Cl$-AuNPs conjugates were evaluated using a UV–vis spectrophotometer (Jenway, GENOVA NANO Spectrophotometer, 67912). A high-resolution transmission electron microscope (JEOL Ltd., Tokyo, Japan, HR-TEM; JEM-2100) was used to determine the size and shape of AuNPs, and $AlPcS_4Cl$-AuNPs using varying magnification using a method previously demonstrated [12].

Culture of oesophageal cancer cells, HKESC-1 and WS1 cells (control cells)

The human oesophageal cancer cell line (HKESC-1) (Cellonex, Johannesburg, South Africa) was propagated in T75 culture flasks in Dulbecco's modified Eagle's medium (DMEM) (Sigma-Aldrich, D5796) supplement with 10% Fetal Bovine Serum (FBS) (Biochrom, S0615), 1mM sodium pyruvate 1% antibiotic (Amphotericin B and Penicillin-streptomycin). The human skin fibroblast cell line (WS1) (ATCC®, CRL-1502™) was used as normal control cells. The cells were cultured in a complete growth medium composed of Minimum Essential Medium (MEM) from SAFC (51412C). The medium was supplemented with 0.1 mM MEM Non-essential Amino Acid Solution (NEAA) from Sigma-Aldrich (M7145), 2 mM L-Glutamine solution (L-Glut) from Sigma-Aldrich (G7513), 1 mM Sodium pyruvate solution, 10% fetal bovine serum (FBS), and 1% antibiotics. All cells were cultured under 5% CO_2, 37°C and 80% humidity. The culture medium was changed every two days intervals. Experimental cells were seeded at a density of 5×10^5 cells in 35mm diameter culture plates containing 2mL of pre-warmed DMEM.

Intracellular Localisation of $AlPcS_4Cl$-AuNPs conjugate

Fluorescent microscopy was used to determine the cellular localisation of $AlPcS_4Cl$-AuNPs in oesophageal cancer with the aid of organelle trackers labelled with fluorescence dyes. Oesophageal cancer cells (HKESC-1) were cultured at a seeding concentration of 5×10^5 cells in 35mm culture plates in pre-warmed growth media containing glass coverslips. Following the attachment, 20 μM of $AlPcS_4Cl$-AuNPs conjugate was added and incubated for four hours. After incubation, cells were washed with Hank's balanced salt solution (HBSS). Cellular organelles in the cytoplasm were immediately stained with Mito-Tracker (100 nM) (M7514, Invitrogen™),) Lyso-Tracker (65 nM) (L7526, Invitrogen™), and ER-Tracker (65 nM) (E12353, Invitrogen™). After staining, the cytoplasmic organelle cells were rinsed with HBSS, and the nuclei were stained using 40–6-Diamidino-2 phenylindole (DAPI) (ID1306, Invitrogen™) and then rinsed with HBSS. Coverslips were removed and mounted onto sterile glass microscope slides. The slides were observed, and images were taken with a live imaging microscope (Carl Zeiss Axio Z1, Göttingen, Germany).

In vitro Photodynamic treatment

HKESC-1 cells were cultured at a concentration of 5 x10^5 concentration in 35mm cell culture plates containing 2 mL of complete culture medium and were grouped into control and test groups. Cells were incubated with DMEM, $AlPcS_4Cl$, (1,25, 2.5, 5, 10, and 20 μM) and $AlPcS_4Cl$-AuNPs (1,25, 2.5, 5, 10, and 20 μM) for four hours in the dark. After incubation, the cells were irradiated at 673.2 nm with 5 J/cm^2 fluence using a continuous wave semiconductor diode laser (Oriel Corporation). The cells were further incubated for 24 hours post-irradiation, after which biochemical assays were performed.

MTT assay

Cellular proliferation was measured using the CyQUANT™ MTT Cell Proliferation Assay (V13154, Invitrogen™)). This assay relies on the ability of the mitochondria from live cells to hydrolyse MTT (dimethyl thiazolyl diphenyltetrazolium bromide) to an insoluble formazan resulting in yellow-to-purple colour formation. Briefly, twenty-four hours following treatment, 100 μL of cell suspension was added in a 96 microwell plate, and 10 μL of 12nM MTT solution was pipetted to each well, and the cells were then incubated at 37^{o}C for three hours. After incubation, 150 μL of DMSO (dimethyl sulfoxide) was added, mixed properly, and incubated for 10 minutes at 37^{o}C. Absorbance at 570 nm was read using a plate reader PerkinElmer, VICTOR NivoTM.

ATP proliferation assay

Adenosine Triphosphate (ATP) level, which is directly proportional to cellular proliferation and cell viability, was evaluated using the CellTiter-Glo® 3D luminescence (G968A, Promega) according to the manufactural instruction as previously described [8].

Cytotoxicity assay

A cytotoxicity assay was conducted to measure the lactate dehydrogenase (LDH) enzyme released by the damaged cell membrane. Following the manufacturer's instructions, the test was achieved using the Cyto Tox 96® Non-Radioactive Cytotoxicity assay (Promega, G179A).

Reactive oxygen species measurement

To determine the levels of reactive oxygen species (ROS) within the cells, the fluorescent probe 2',7'-dichlorofluorescein diacetate (DCFDA/H2DCFD) was utilised. The cellular ROS assay (ab113851, Abcam) was employed for this test. HKESC-1 cells were grown in 96-well tissue culture plates and treated with 5 μM $AlPcS_4Cl$ for 4 hours, followed by photodynamic therapy (PDT). After a 24-hour post-PDT incubation, the cells were incubated with DCFH-DA (5 μM) at 37 °C for 10 minutes. Subsequently, the cells were transferred to a 96-well black plate. The fluorescence intensity was measured using the PerkinElmer VICTOR Nivo™ plate reader with an excitation/emission filter set at 485 nm/538 nm. The amount of ROS produced in the treated cells was estimated as a ratio in relation to the control cells.

Mitochondrial membrane potential assay

The rhodamine-123 efflux fluorimetry assay (ab275545, Abcam) was employed to assess the mitochondrial membrane potential (MMP) on oesophageal cancer cells. Rhodamine-123, a fluorescent dye that localises in mitochondria, was used for this purpose. When the mitochondrial membrane potential is compromised, rhodamine leaks out of the mitochondria, resulting in reduced cell fluorescence intensity. After 24 hours of PDT treatment, the cells were detached, harvested, and washed twice with 1x PBS. The cells were then resuspended in 100 μL of 1x PBS and stained with a 25 μM solution of rhodamine-123 for 15 minutes at room temperature, protected from light. Following staining, the cells were washed twice with 1x PBS, and 400 μl of PBS was added, mixed, and transferred into a 96-well black plate. The cells were then incubated for 30 minutes at room temperature, protected from light. The fluorescence signal of rhodamine-123 was quantified using the PerkinElmer VICTOR Nivo™ plate reader with a filter of 485 nm excitation and 538 nm emission.

Results

Characterisation of $AlPcS_4Cl$-AuNP

$AlPcS_4Cl$-AuNPs were synthesised as previously described [10] and characterised using a UV–vis absorption spectroscopy and TEM. Following the successful adsorption of $AlPcS_4Cl$ to AuNPs, the absorption band of AuNPs was 520nm Figure 1(b) before adsorption was shifted to 540nm after adsorption, as demonstrated in Figure 1(c). The TEM analysis revealed that the AuNPs exhibited a uniform spherical shape with a smooth surface, and there was no evidence of agglomeration observed Figure 19(e). Both the $AlPcS_4Cl$-AuNPs and the AuNPs displayed similar surface characteristics. However, the $AlPcS_4Cl$-AuNP had a larger

diameter (33.20 ±1.93 nm) compared to the AuNPs (14.74±3.37 nm) Figure 1(f), indicating that the combination of $AlPcS_4Cl$ with the AuNPs was successful and stable.

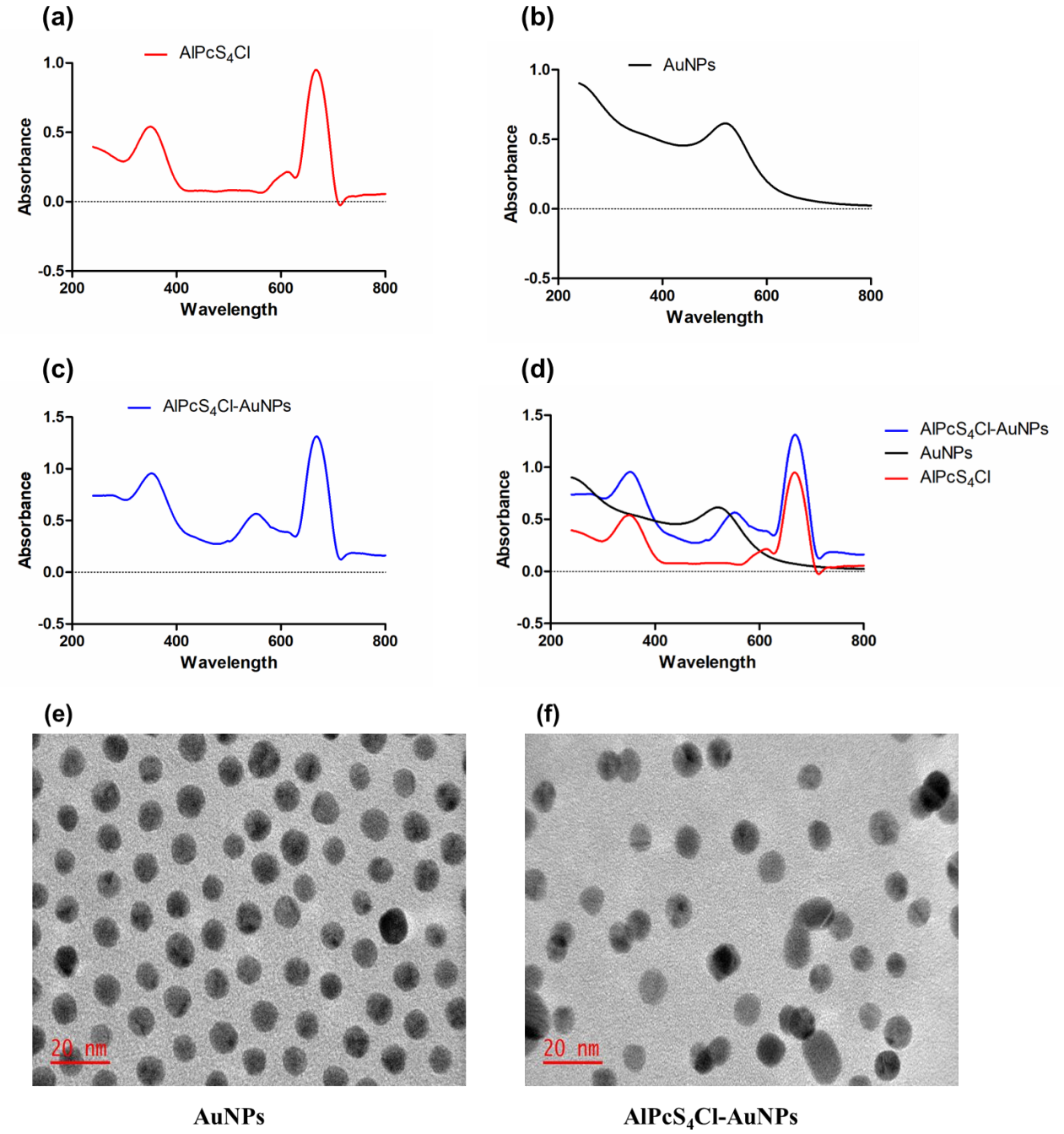

Figure 1. *UV-Vis spectral characterisation of (a) $AlPcS_4Cl$ (λmax 675nm), (b) AuNPs (λmax 520nm), (c) $AlPcS_4Cl$-AuNPs (λmax 672nm and 540nm) and (d) combinations of (a)-(c). Transmission electron microscopy images of (e) AuNP and (f)AlPcS4Cl-AuNPs. Scale bars, 20 nm.*

Subcellular Localisation of $AlPcS_4Cl$-AuNPs in oesophageal cancer

Localisation of the $AlPcS_4Cl$-AuNPs in HKESC-1 oesophageal cancer cells was examined using the Zen Pro (3.1) Carl Zeiss software on a Carl Zeiss fluorescent microscope. A remarkable accumulation of $AlPcS_4Cl$-AuNPs was observed in the nucleus, mitochondria, and the ER of HKESC-1 oesophageal cancer cells, as depicted in Figure 2. This was clearly demonstrated by the merging of the blue fluorescence from the nuclei, green fluorescence from the mito tracker and ER tracker and red fluorescence from the $AlPcS_4Cl$-AuNPs,

resulting in a yellow colour. The yellow colour showed that the $AlPcS_4Cl$-AuNPs were specifically accumulating in the nucleus, mitochondria, and ER. This

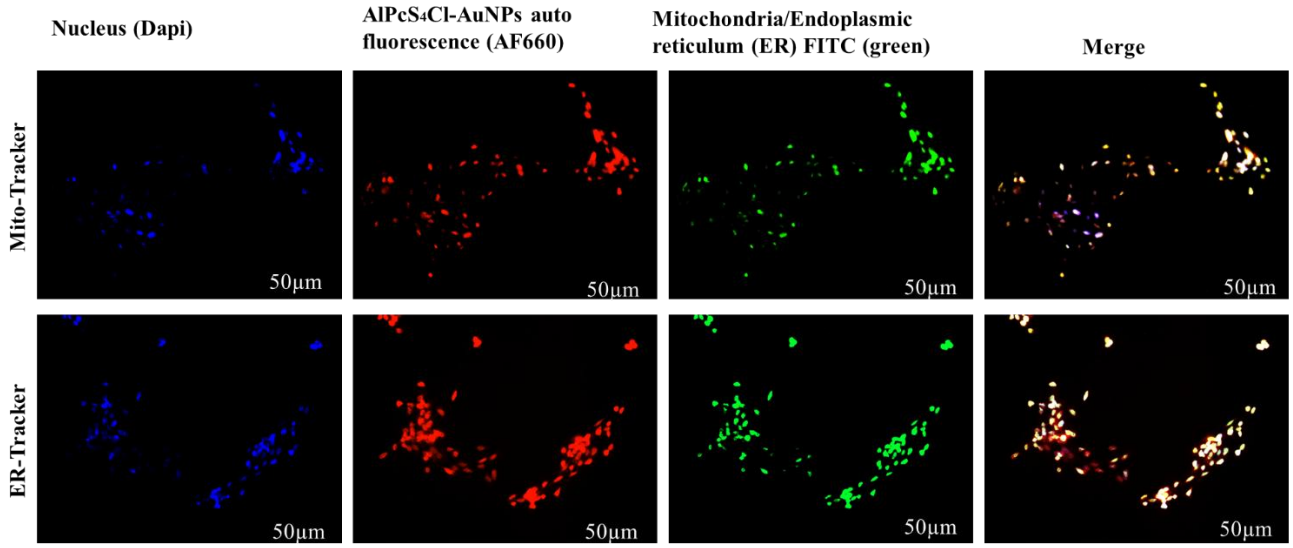

Figure 2. *$AlPcS_4Cl$-AuNPs localisation in HKESC-1 oesophageal cancer cells displaying intracellular organelle localisation. The nuclei are counterstained with DAPI (blue), mitochondria, ER stained with FITC (green), and $AlPcS_4Cl$-AuNPs auto fluoresces (red). The merged yellow/white colour showed an accumulation of $AlPcS_4Cl$-AuNPs in the mitochondria, ER and the nucleus. Scale bar:50µm*

In Vitro Effects of $AlPcS_4Cl$-AuNPs Conjugates Mediated PDT on Oesophageal Cancer

Dose-Response Evaluation of $AlPcS_4Cl$-AuNPs Conjugates

A dose-response was performed on HKESC-1 cells to obtain the appropriate concentration of $AlPcS_4Cl$, and the conjugates required for the downstream application of PDT on HKESC-1 cells. The IC_{50} values were evaluated by using MTT cell viability assay post 24 h treatment with increasing concentrations of $AlPcS_4Cl$ and of AlPcS4Cl-AuNPs (1.25, 2.5, 5, 10, and 20µM). The results showed that $AlPcS_4Cl$-AuNPs have a low IC_{50} of 2.88 µM ($p<0.001$) when compared to $AlPcS_4Cl$ with an IC_{50} of 5.21 µM as depicted in figure 3.

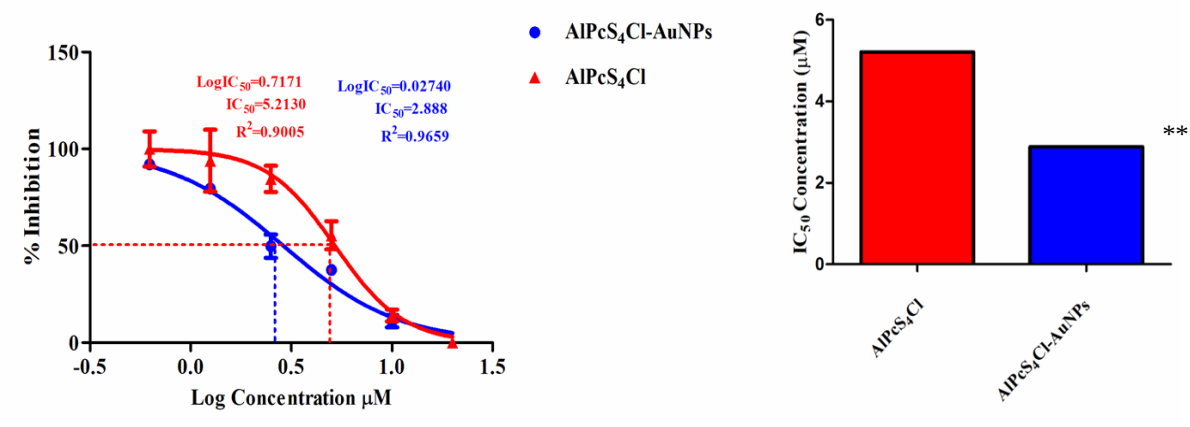

Figure 3. *Determination of 50% inhibitory concentration (IC_{50}) using MTT Cell Viability assay of $AlPcS_4Cl$-AuNPs and the free $AlPcS_4Cl$ in Oesophageal cancer. The results are depicted as ± SEM (n = 3); (***p <0.001).*

Cytotoxicity Evaluation

Cytotoxicity assay was performed by evaluating the quantity of lactate dehydrogenase (LDH) enzyme leakage in the cell culture media of HKESC-1 oesophageal cancer cells and normal cells (WS1, fibroblast cell). Cells that have damaged cell membrane integrity leak out LDH indicative of cytotoxicity. LDH release was measured following PDT at a light dose of 5 J/cm^2 at concentrations of 5 μM each for AlPcS$_4$Cl-AuNPs and AlPcS$_4$Cl. At 24 hours post-PDT, statistically significant results were observed for all PDT concentrations tested in the HKESC-1 oesophageal cancer cells (AlPcS$_4$Cl 5 μM at 5 J/cm^2, and AlPcS$_4$Cl-AuNPs 5 μM at 5 J/cm^2), as depicted in Figure 4(a). The significance levels were reported as ***$p < 0.001$, compared to the control group untreated. No statistical significance was found when comparing the AlPcS$_4$Cl-AuNPs dark cells and AlPcS$_4$Cl dark cells to the control dark cells. Conversely, no statistical significance was demonstrated in the normal control cells both between the treated and untreated group and within the treated and untreated cells (Figure 4(b)).

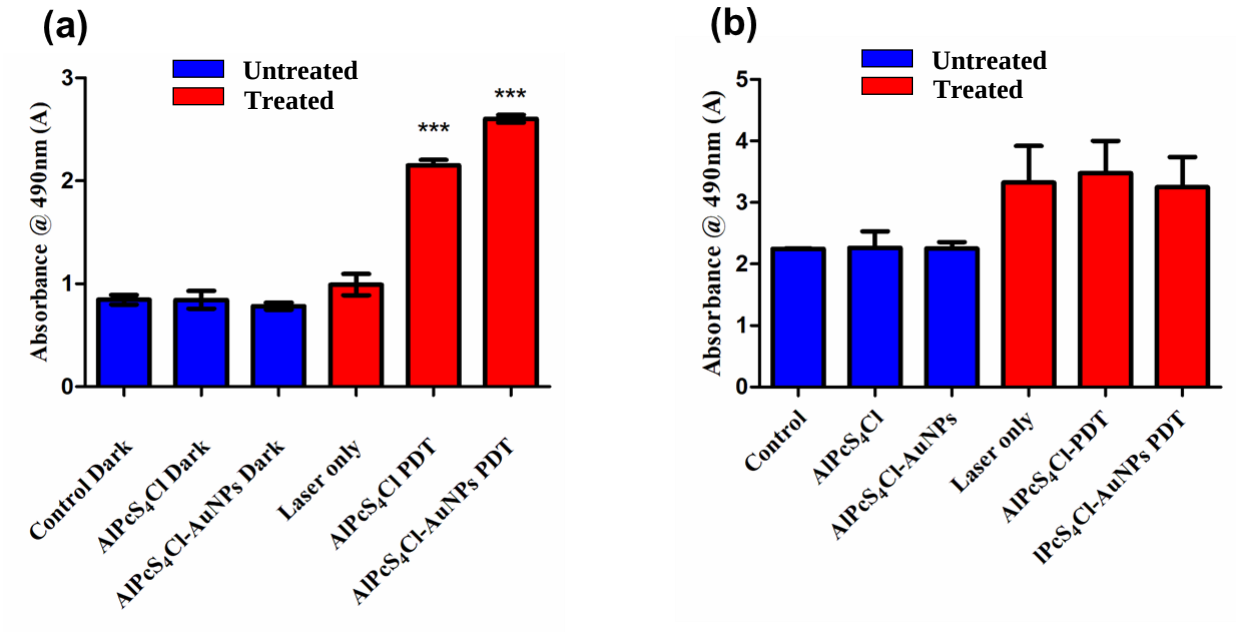

Figure 4. *The cytotoxic effects of AlPcS$_4$Cl-AuNPs and AlPcS$_4$Cl were determined by LDH release cytotoxicity assay. (a) The cytotoxic effects of AlPcS$_4$Cl-AuNPs and AlPcS4Cl on HKESC-1 oesophageal cancer cells. The amount of LDH release after AlPcS$_4$Cl-AuNPs and AlPcS$_4$Cl with 5 J/cm^2 irradiation, with AlPcS$_4$Cl-AuNPs conjugate showing increased LDH release compared to AlPcS$_4$Cl and the control. (b) The cytotoxic effects of AlPcS$_4$Cl-AuNPs and AlPcS$_4$Cl on normal cells (WS1 fibroblast cells). No statistical significance was observed in the. The results are depicted as ± SEM (n = 3); (**p < 0.01, ***p <0.001).*

ATP Cellular Proliferation Assessment

Oesophageal cancer cells were evaluated for cellular proliferation ability with and without photoactivation using ATP proliferation assay. Proliferation results showed that the non-irradiated cancer cells displayed high proliferation activity with increased ATP levels. While the irradiated cells at a concentration of 5 μM at 5 J/cm^2 showed a significant decrease of ATP activities in the cells administered with the AlPcS$_4$Cl-AuNPs conjugate (**p<0.01) and AlPcS$_4$Cl (*p<0.05), with the conjugate showing a more ATP inactivity (Figure 5).

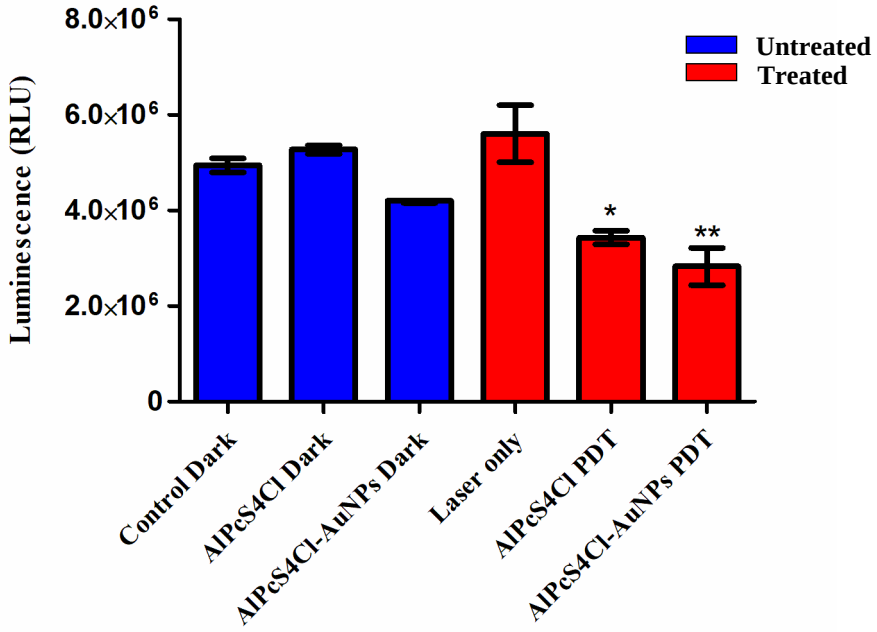

Figure 5*. The cellular proliferative effects of AlPcS$_4$Cl-AuNPs and AlPcS$_4$Cl on oesophageal cancer cells. Blue: the non-irradiated cells showed increased proliferative ATP activities with no significant difference between the control cells and cells administered with AlPcS$_4$Cl and the conjugate. Red: the irradiated cells at 5 J/cm2 demonstrated reduced proliferative actions with reduced ATP levels between the conjugate and the free PS (*p < 0.05 ***p < 0.001). The values shown are ± SEM (standard error of the mean) (n=3).*

Mitochondria membrane potential Assessment

Oesophageal cancer cells were evaluated for MMP function using the rhodamine-123 efflux fluorimetry assay. The MMP results revealed that the untreated cancer cells displayed high MMP integrity. While the treated irradiated cells at a concentration of 5 μM at 5 J/cm^2 showed a significant decrease of MMP integrity in the cells administered with the AlPcS$_4$Cl-AuNPs conjugate (***p<0.001) and AlPcS$_4$Cl (***p<0.001), with the conjugate showing a more MMP impairment (Figure 6).

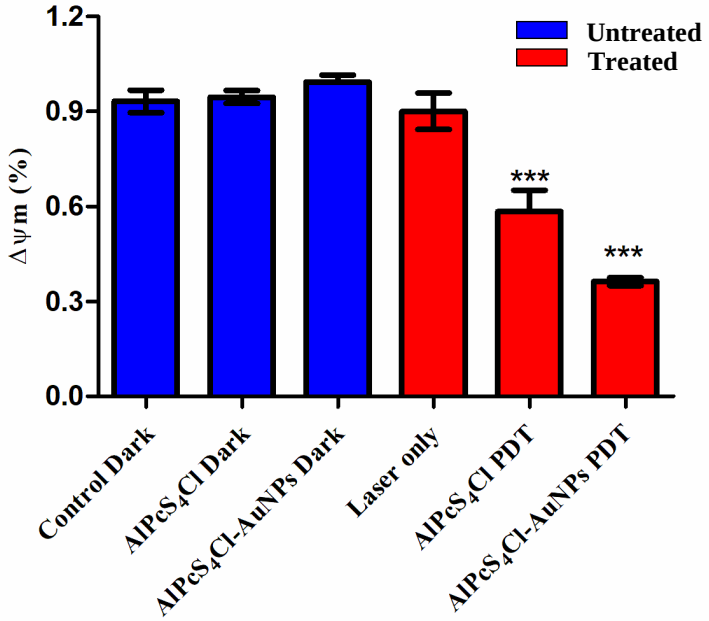

Figure 6*. AlPcS$_4$Cl-AuNPs conjugate and AlPcS$_4$Cl mediated PDT effects on Mitochondrial Membrane potential (MMP) Integrity of oesophageal cancer cells. Blue: the non-irradiated control cells showed decrease MMP impairment. Red: the irradiated cells treated with AlPcS$_4$Cl-AuNPs conjugate and AlPcS$_4$Cl at 5 J/cm^2*

*demonstrated significant MMP alterations (**p < 0.01 ***p < 0.001). The values shown are ± SEM (standard error of the mean) (n=3).*

Measurement of Reactive Oxygen Species (ROS)

Fluorescent probe 2′,7′-dichlorofluorescein diacetate (DCFDA/H2DCFD), cellular reactive oxygen species (ROS) probe was used to quantify intracellular ROS generation of $AlPcS_4Cl$-AuNPs conjugate and $AlPcS_4Cl$ based PDT in HKESC-1 cells. The ROS generated was measured post-PDT at a light dose of 5 J/cm^2 at concentrations of 5 μM for both $AlPcS_4Cl$-AuNPs and $AlPcS_4Cl$. The results showed a statistically significant increase in ROS production PDT treated group $AlPcS_4Cl$ (**p<0.01) and $AlPcS_4Cl$-AuNPs (***p<0.001) when compared with the untreated controls as seen in Figure 7.

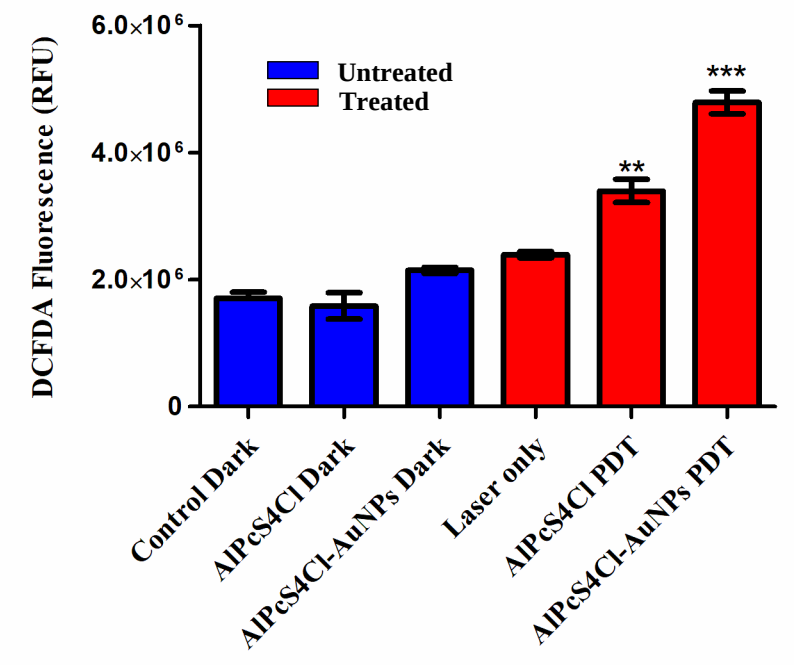

Figure 7. *Intracellular ROS production of $AlPcS_4Cl$-AuNPs conjugate and $AlPcS_4Cl$ mediated PDT in HKESC-1oesophageal cancer cells. Blue: the non-irradiated control cells showed decreased ROS generation. Red: the irradiated cells treated with $AlPcS_4Cl$-AuNPs conjugate and AlPcS4Cl at 5 J/cm^2 increase ROS generation (**p < 0.01 ***p < 0.001). The values shown are ± SEM (standard error of the mean) (n=3).*

DISCUSSION

In this study, we investigated the effects of $AlPcS_4Cl$-AuNPs conjugates in enhancing the therapeutic efficiency of photodynamic therapy (PDT) in oesophageal cancer. Nanoparticles, specifically gold nanoparticles (AuNPs), have garnered significant interest as potential nanocarriers for drug delivery due to their chemical inertness, efficient optical properties, and biocompatibility. While the use of AuNPs as carriers for drug delivery in PDT has been extensively studied in various cancer types, its impact on oesophageal cancer remains limited. Therefore, we evaluated the therapeutic efficiency of PDT using $AlPcS_4Cl$-AuNPs conjugates by assessing various parameters such as intracellular localisation, cell viability, LDH enzyme release, MMP integrity and ROS production.

The synthesised $AlPcS_4Cl$-AuNPs were confirmed by UV-Vis spectral absorption spectroscopy and TEM analysis. The results showed a red shift in the maximum absorption band of the AuNPs from 520nm before synthesis to 540nm after synthesis (Figure 1 (b) and (c). While the $AlPcS_4Cl$ showed a left shift from 675nm before synthesis to 672nm after synthesis (figure 1(a) and (c). The TEM analysis was performed to determine the morphological variation of the AuNPs before and after synthesis. The results showed a change in the diameter of AuNPs from 14.74 nm ± 3.37 before synthesis to 33.20 nm ±1.93 after synthesis. This result confirms the successful adsorption of $AlPcS_4Cl$-AuNPs (Figure 1(e)(f).

Intracellular localisation evaluation was performed to determine the preferential accumulation sites of the $AlPcS_4Cl$-AuNPs in oesophageal cancer cells. Understanding the impact of $AlPcS_4Cl$-AuNPs on organelle-specific responses to cell death machinery can be modulated to boost the therapeutic efficacy of PDT. For instance, targeting photosensitisers to specific organelles through nanoparticle conjugation or other delivery strategies can potentially enhance the selectivity and effectiveness of PDT. In this investigation, we discovered that $AlPcS_4Cl$-AuNPs selectively internalised in the mitochondria, ER, and nucleus (Figure 2). This suggests that these organelles may be necessary for the $AlPcS_4Cl$-AuNPs enhanced PDT action of cell damage. This is consistent with a study by Mkhobongo and colleagues that showed that $AlPcS_4Cl$-AuNPs are localised in the mitochondria and lysosomes of melanoma cells [11].

Findings from cell viability analysis using MTT assay revealed that $AlPcS_4Cl$-AuNPs and the free $AlPcS_4Cl$ mediated PDT significantly inhibited cell viability (Figure 3). However, the $AlPcS_4Cl$-AuNPs mediated PDT group had enhanced reduction in the cell viability when compared to the $AlPcS_4Cl$ group. The results also showed that $AlPcS_4Cl$-AuNPs mediated PDT has a statistically significant lower IC_{50} concentration of 2.88 μM when compared to the IC_{50} of $AlPcS_4Cl$-mediated PDT of 5.02 μM on HKESC-1 oesophageal cancer cells (Figure 3).

The cytotoxicity evaluation of $AlPcS_4Cl$-AuNPs and $AlPcS_4Cl$ mediated PDT on HKESC-1 oesophageal cancer cells and on normal control cells was conducted using the LDH release cytotoxicity assay. This assay evaluates the extent to which LDH enzymes leak out after cellular insult. We observed statistically significant high efflux of LDH enzyme in the $AlPcS_4Cl$-AuNPs and $AlPcS_4Cl$ mediated PDT group when compared with the control cells as shown in Figure 4(a). However, the $AlPcS_4Cl$-AuNPs PDT group has more enhanced cytotoxicity effects. This aligned with the finding by Mkhobongo and co-worker which showed that $AlPcS_4Cl$-AuNPs mediated PDT enhanced the cytotoxicity effects in Melanoma cells [11] and lung cancer cells and cancer stem cells [9, 13]. We further determine the effects of the conjugates and the free PS on normal non-cancerous cells using the concentration of 5uM, to ascertain if it is toxic to normal cells. Our finding showed that the $AlPcS_4Cl$-AuNPs and the free $AlPcS_4Cl$ do not induce any cytotoxic effects on normal cells. This implies that the conjugates and the free PS preferentially accumulation in tumour cells.

The effects of $AlPcS_4Cl$-AuNPs on ATP cellular production levels in oesophageal cancer cell which serves as an indicator of cellular metabolic activity was evaluated. ATP is an essential molecule that serves as a primary energy source for cellular processes. Tumour cells rely on aerobic glycolysis, a metabolic pathway known as the Warburg effect, to generate ATP. Mitochondria play a crucial role in producing ATP during cellular respiration[14]. The decrease in ATP production observed in oesophageal cancer cells following the photodynamic action of the $AlPcS_4Cl$-AuNPs conjugate and $AlPcS_4Cl$ photosensitiser suggests that the photosensitiser localised in specific subcellular organelles involved in maintaining cellular homeostasis. By targeting these organelles, the photosensitiser disrupts their normal functioning and leads to the inhibition of oesophageal cancer cells. This observation is similar to the finding of $AlPcS_4Cl$-AuNPs conjugates inhibiting the ATP cellular proliferation activity in lung cancer stem cells [13].

The mitochondrial is known to be the powerhouse of cellular ATP production and damage to this organelle can alter its function. In this study we investigated the effects of $AlPcS_4Cl$-AuNPs mediated PDT on the MMP activity of oesophageal cancer cells. The results demonstrated that $AlPcS_4Cl$-AuNPs and $AlPcS_4Cl$ mediated PDT significantly alter the MMP of the cell. The $AlPcS_4Cl$-AuNPs mediated PDT group has more MMP dysfunction. This finding agrees with the reduced ATP cellular production observed in this study. Finally, the effects of $AlPcS_4Cl$-AuNPs mediated PDT in promoting ROS generation was examined. Our results showed increased ROS production with the $AlPcS_4Cl$-AuNPs mediated PDT group than the free $AlPcS_4Cl$ mediated PDT. Suggesting the conjugate enhances the PDT effects in oesophageal cancer cells.

CONCLUSION

The findings showed that PDT with aluminium (III) phthalocyanine chloride tetra sulfonic acid ($AlPcS_4Cl$) conjugated gold nanoparticle (AuNPs)($AlPcS_4Cl$-AuNPs) significantly inhibit cell viability/cellular proliferation, increase cytotoxicity, and ROS generation. Fluorescent microscopy revealed that ($AlPcS_4Cl$-AuNPs) was localised in the nuclei, mitochondria and ER suggesting the biochemical cell death pathways induction could be mitochondria and ER dependent. More importantly, $AlPcS_4Cl$-AuNPs significantly altered

the mitochondrial membrane integrity in HKESC-1 cells. Further confirming the mitochondria dependent cell death pathway. In conclusion, our findings demonstrated that $AlPcS_4Cl$-AuNPs conjugates improved the anti-cancer effects of PDT in oesophageal cancer cells, proposing a better measure to boost the therapeutic efficiency of PDT in oesophageal cancer.

Author Contributions: Conceptualisation, OCD; methodology, OCD; validation, OCD, RC and HA; formal analysis, OCD; investigation, OCD; resources, RC and HA; writing—original draft preparation, OCD; writing—review and editing, OCD, RC and HA; supervision, RC and HA; project administration, OCD, RC and HA; funding acquisition, OCD, RC and HA. All authors have read and agreed to the published version of the manuscript.

Funding: The research was financially supported by various entities. These included the Department of Science and Innovation (DSI) funded African Laser Centre (grant number HLHA23X task ALC-R007), the University Research Council (grant number 2022URC00513), the Department of Science and Technology's South African Research Chairs Initiative (grant number 98337). Additionally, the Article Processing Charges (APC) were covered by the University of Johannesburg Faculty of Health Sciences. Furthermore, funding was contributed by the University of Johannesburg Global Excellence and Stature, Fourth Industrial Revolution (GES 4.0) Doctoral Scholarship.

Informed Consent Statement: Not applicable.

Data Availability Statement: The datasets generated during and/or analysed during the current study are available from the authors upon request.

Acknowledgments: The authors sincerely thank the University of Johannesburg and the Laser Research Centre for their facilities and equipment.

Conflicts of Interest: The authors declare no conflict of interest.

REFERENCES

[1] Ferlay, J., et al., *Cancer statistics for the year 2020: An overview.* International Journal of Cancer, 2021. 149(4): p. 778-789.

[2] Thrumurthy, S.G., et al., *Oesophageal cancer: risks, prevention, and diagnosis.* BMJ, 2019. 366: p. l4373.

[3] Didamson, O.C. and H. Abrahamse, *Targeted Photodynamic Diagnosis and Therapy for Esophageal Cancer: Potential Role of Functionalized Nanomedicine.* Pharmaceutics, 2021. 13(11): p. 1943.

[4] Didamson, O.C., R. Chandran, and H. Abrahamse, *A Gold Nanoparticle Bioconjugate Delivery System for Active Targeted Photodynamic Therapy of Cancer and Cancer Stem Cells.* Cancers, 2022. 14(19): p. 4558.

[5] Chizenga, E.P., R. Chandran, and H. Abrahamse, *Photodynamic therapy of cervical cancer by eradication of cervical cancer cells and cervical cancer stem cells.* Oncotarget, 2019. 10(43): p. 4380-4396.

[6] Crous, A., S.S. Dhilip Kumar, and H. Abrahamse, *Effect of dose responses of hydrophilic aluminium (III) phthalocyanine chloride tetrasulphonate based photosensitiser on lung cancer cells.* J Photochem Photobiol B, 2019. 194: p. 96-106.

[7] Ndhundhuma, I.M. and H. Abrahamse, *Susceptibility of In Vitro Melanoma Skin Cancer to Photoactivated Hypericin versus Aluminium(III) Phthalocyanine Chloride Tetrasulphonate.* Biomed Res Int, 2017. 2017: p. 5407012.

[8] Didamson, O.C., R. Chandran, and H. Abrahamse. *Invitro Effects of Aluminium (III) Phthalocyanine Chloride Tetra Sulphonic Acid Mediated Photodynamic Therapy on Oesophageal Cancer*. in *The Proceedings of SAIP2022, the 66th Annual Conference of the South African Institute of Physics*. 2022.

[9] Crous, A. and H. Abrahamse, *Photodynamic Therapy with an AlPcS4Cl Gold Nanoparticle Conjugate Decreases Lung Cancer's Metastatic Potential.* Coatings, 2022. 12(2): p. 199.

[10] Chi, Y.-f., et al., *Enhanced anti-tumor efficacy of 5-aminolevulinic acid-gold nanoparticles-mediated photodynamic therapy in cutaneous squamous cell carcinoma cells.* Brazilian Journal of Medical and Biological Research, 2020. 53.

[11] Mkhobongo, B., R. Chandran, and H. Abrahamse, *In Vitro Photodynamic Treatment Modality for A375 Melanoma Cell Line Using a Sulphonated Aluminum Phthalocyanine Chloride-Photosensitizer-Gold Nanoparticle Conjugate.* Pharmaceutics, 2022. 14(11).

[12] Mokoena, D., B.P. George, and H. Abrahamse, *Conjugation of Hypericin to Gold Nanoparticles for Enhancement of Photodynamic Therapy in MCF-7 Breast Cancer Cells.* Pharmaceutics, 2022. 14(10): p. 2212.
[13] Crous, A. and H. Abrahamse *Effective Gold Nanoparticle-Antibody-Mediated Drug Delivery for Photodynamic Therapy of Lung Cancer Stem Cells*. International Journal of Molecular Sciences, 2020. 21, DOI: 10.3390/ijms21113742.
[14] Özlem Sultan, A., *In Vitro Cytotoxicity and Cell Viability Assays: Principles, Advantages, and Disadvantages*, in *Genotoxicity*, L.L. Marcelo and S. Sonia, Editors. 2017, IntechOpen: Rijeka. p. Ch. 1.

DOI 10.24412/cl-37136-2023-1-129-130

PHOTOACOUSTIC MOLECULAR IMAGING TECHNOLOGY AND APPLICATIONS

CHENGBO LIU

Shenzhen Institute of Advanced Technology, Chinese Academy of Sciences, China

cb.liu@siat.ac.cn

ABSTRACT

Photoacoustic molecular imaging possesses the merits of both high optical contrast and large acoustic penetration. It is expected to play a more and more important role in both fundamental research and clinical applications, and has the potential to revolutionize the playground of tumor and cardiovascular disease management and treatment. In this talk, I will focus on how we improve the speed of photoacoustic molecular imaging. I will start with conventional photoacoustic microscopy using point-by-point mechanical scanning. Then I will move on to fast optical scanning based on MEMS and polygon mirror devices. After that, I will introduce single pixel imaging method without the need of scanning. Combined with sparse sampling, the imaging speed can be improved by 20 times. Besides photoacoustic microscopy, we also built photoacoustic computed tomography system which uses an array of ultrasound transducers to sense the signals. Due to simultaneous acquisition of photoacoustic signals, PACT can acquire 100 frames of two-dimensional images in one second. We applied our technology and instrumentation to study tumor microenvironment and evolution of tumor, as well as to investigate the mechanism of neurovascular coupling in the brain. We also intraoperatively guided a biopsy needle with photoacoustic imaging to extract tissue samples from sentinel lymph node to monitor tumor metastasis status. Our technology has also been successfully translated to human imaging to diagnose vascular plaques and image periphery blood vessels, aiming at better management of diseases such as diabetic foot or varicosity.

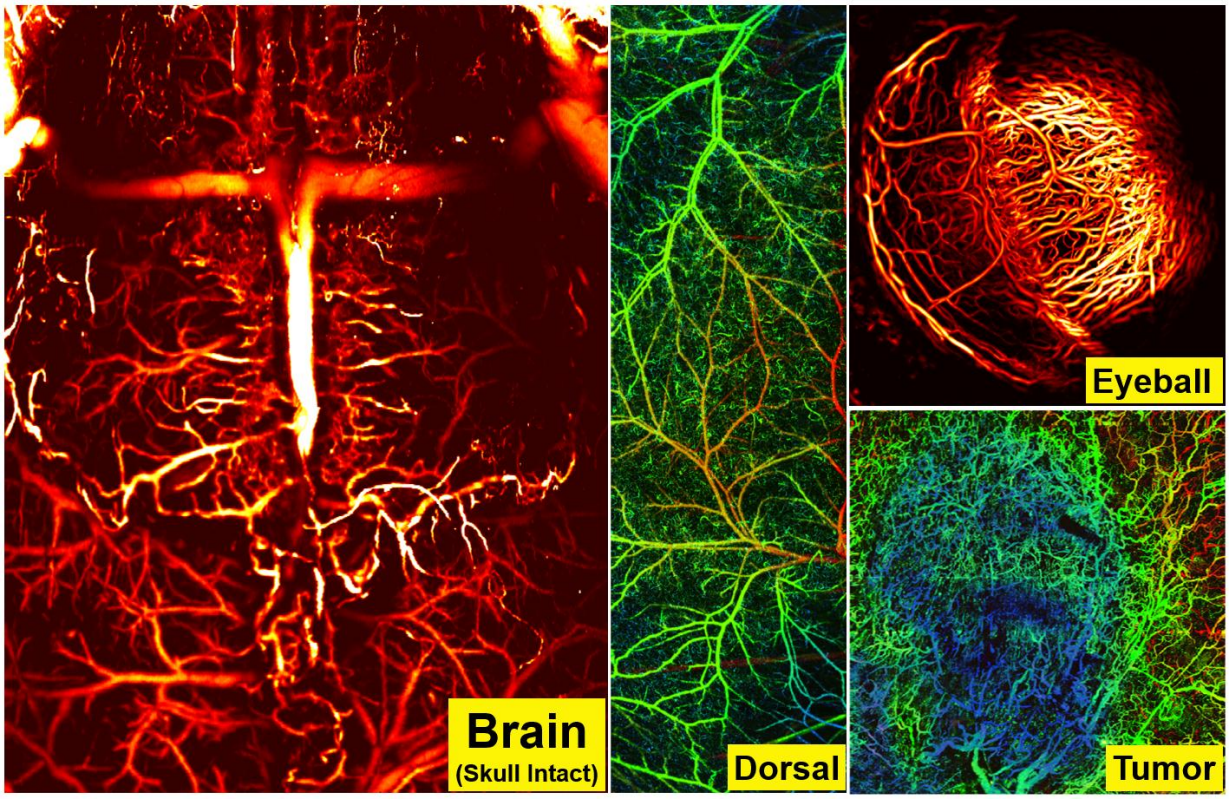

Figure 1: *Photoacoustic imaging of microvessels at different organ sites*

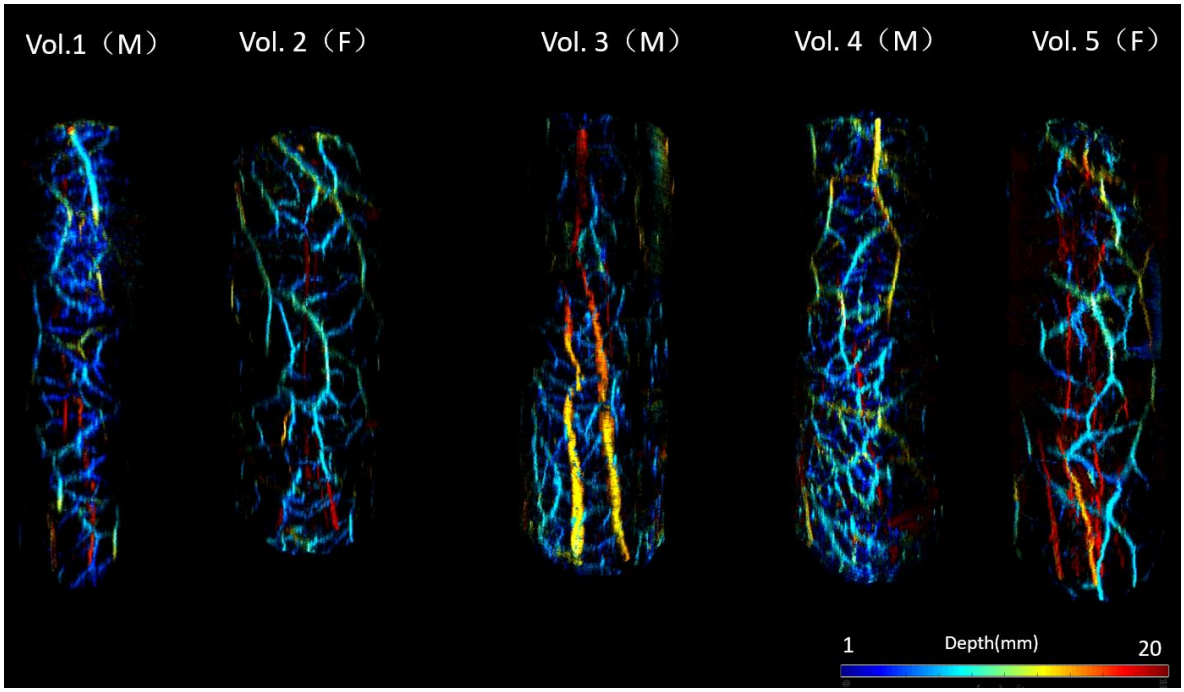

Figure 2: *Photoacoustic imaging of calf gastrocnemius region of five human volunteers, M: male, F: female*

REFERENCES

[1] Ningbo Chen, Jia Yu, Liangjian Liu, Zhiqiang Xu, Rongkang Gao, Tao Chen, Liang Song, Wei Zheng*, Chengbo Liu, "Video-rate high-resolution single-pixel nonscanning photoacoustic microscopy, Biomedical Optics Express. 3823-3835, 2022.

[2] Zhiqiang Xu, Yinhao Pan, Ningbo Chen, Silue Zeng, Liangjian Liu, Rongkang Gao, Jianhui Zhang, Chihua Fang, Liang Song, Chengbo Liu, "Visualizing tumor angiogenesis and boundary with polygon-scanning multiscale photoacoustic microscopy, Photoacoustics. 100342, 2022.

[3] Tao Chen, Liangjian Liu, Xiaohui Ma, Ying Zhang, Huadong Liu, Rongqin Zheng, Jie Ren, Huichao Zhou, Yaguang Ren, Rongkang Gao, Ningbo Chen, Hairong Zheng, Liang Song, Chengbo Liu, Dedicated photoacoustic imaging instrument for human periphery blood vessels: A new paradigm for understanding the vascular health, IEEE Transactions on Biomedical Engineering. 1093–1100, 2022.

[4] Huangxuan Zhao, Ziwen Ke, Fan Yang, Ke Li, Ningbo Chen, Liang Song, Chuansheng Zheng, Dong Liang, and Chengbo Liu, Deep Learning Enables Superior Photoacoustic Imaging at Ultralow Laser Dosages, Advanced Science. 2003097, 2021.

[5] Huangxuan Zhao, Ningbo Chen, Tan Li, Jianhui Zhang, Riqiang Lin, Xiaojing Gong, Liang Song, Kunya Zhang, Zhi Yang, Zhicheng Liu, Chengbo Liu, Motion Correction in Optical Resolution Photoacoustic Microscopy, IEEE Transactions on Medical Imaging. 2139–2150, 2019.

DOI 10.24412/cl-37136-2023-1-131-133

THROUGH-INTACT-SKULL WINDOW: A CHRONIC SKULL OPTICAL CLEARING WINDOW FOR LONG-TERM CORTICAL OBSERVATION

DONGYU LI[1,2], ZHENGWU HU[1], WANG XI[4], JUN QIAN[3], DAN ZHU[1,*]

[1] Britton Chance Center for Biomedical Photonics - MoE Key Laboratory for Biomedical Photonics, Wuhan National Laboratory for Optoelectronics, Huazhong University of Science and Technology, Wuhan, Hubei 430074, China.
[2] School of Optical Electronic Information, Huazhong University of Science and Technology, Wuhan, Hubei 430074, China.
[3] State Key Laboratory of Modern Optical Instrumentations, Centre for Optical and Electromagnetic Research, College of Optical Science and Engineering, International Research Center for Advanced Photonics, Zhejiang University, Hangzhou 310058, China.
[4] Interdisciplinary Institute of Neuroscience and Technology, Department of Anesthesiology, the Second Affiliated Hospital, School of Medicine, Zhejiang University, Kaixuan Road 258th, Hangzhou, 310020, PR China.

li_dongyu@hust.edu.cn

ABSTRACT

Modern optical imaging techniques provide powerful tools for observing cortical structure and functions at high resolutions. Various skull windows have been established for different applications of cortical imaging, and each has its advantages and limitations. Most critical of the limitations, none of the current skull windows is suitable for observing the responses to some acute craniocerebral injuries on a large scale and at high resolution.

In order to develop a skull window technique capable of simultaneously meeting requirements, including maintenance of the internal environment and provision of a wide field of view, high resolution, and durability, we developed a chronic optical clearing window skull, named “Through-Intact-Skull (TIS) window” by firstly removing the collagens and lipids in skull, and secondly stabilizing its transparent state using an ultraviolet curing adhesive. Fig.1 and 2 shows the performance of TIS window.

TIS window enables the observation of an immune response on a bilateral cortical scale and at single-cell resolution after traumatic brain injury without affecting the pathological environment of the brain. What we have observed in this research, including simultaneously discerning the movements of immune cells in different regions and perceiving random hemorrhages that occur in the bilateral cerebral cortex after acute traumatic brain injury (TBI), could not be achieved before now using previous skull window techniques. In addition, the TIS window also has the advantages of craniotomy-freeness, centimeter-field of view, synaptic resolution, large imaging depth, long-term observation capability, and suitability for awake mice.

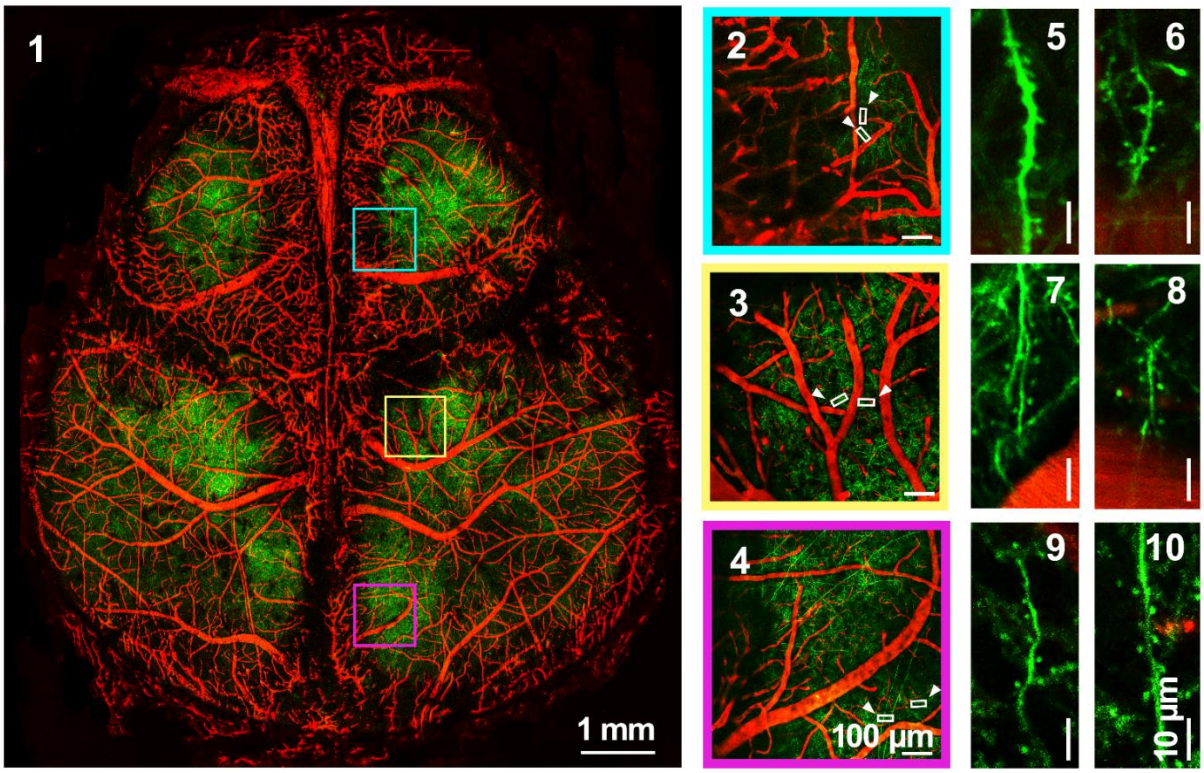

Figure 1: *Large-scale high-resolution cortical neurovascular imaging through TIS window.*

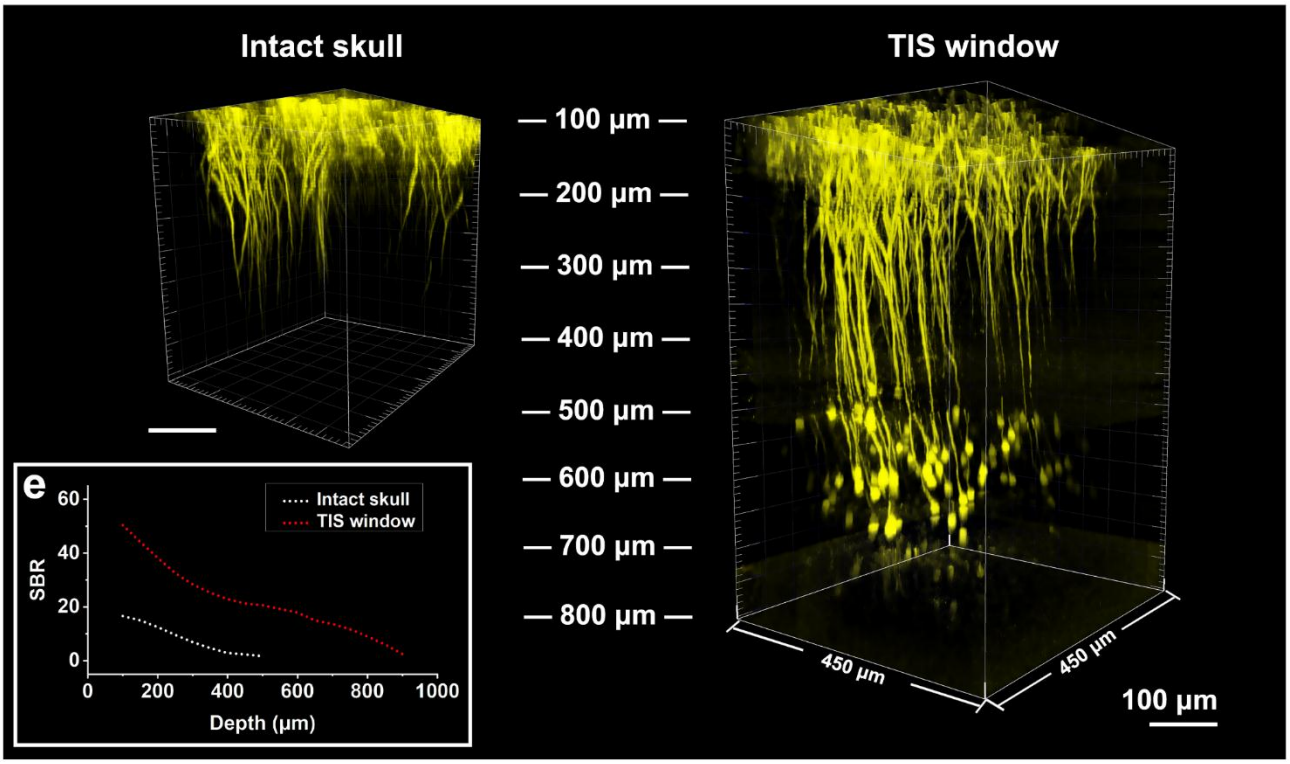

Figure 2: *Three-photon fluorescence imaging of deep=cortical neurons through TIS window.*

Therefore, the TIS window is a promising new approach for intravital cortical microscopy in basic research in neuroscience. The craniotomy-free TIS window with easy and quick steps, as a chronic skull optical clearing window, has advantages over the open-skull glass window, thinned skull window, "transparent skull" window, and skull optical clearing window, and is capable of continuous cortical monitoring at high resolution and on a centimeter-scale, with minimized influence on the brain environment. Therefore, the TIS window technique holds great potential for physiological and pathological research in brain science.

REFERENCES

[1] D. Li et al., "Visible-near infrared-II skull optical clearing window for in vivo cortical vasculature imaging and targeted manipulation," Journal of Biophotonics 13(10), e202000142 (2020).

[2] M. He et al., "Aggregation-induced emission nanoprobe assisted ultra-deep through-skull three-photon mouse brain imaging," Nano Today 45((2022).

[3] Z. Hu et al., "In vivo tissue optical clearing assisted through-skull targeted photothrombotic ischemic stroke model in mice," J Biomed Opt 27(6), 065001 (2022).

[4] D. Li et al., "Optical clearing imaging assisted evaluation of urokinase thrombolytic therapy on cerebral vessels with different sizes," Biomedical Optics Express 13(6), 3243-3258 (2022).

[5] Li et al., "A Through-Intact-Skull (TIS) chronic window technique for cortical structure and function observation in mice," eLight 2(1), (2022).

DOI 10.24412/cl-37136-2023-1-134-140

IMAGE-GUIDED NEAR INFRARED SPECTRAL TOMOGRAPHY FOR BREAST CANCER DIAGNOSIS

JINCHAO FENG[1], CHENGPU WEI[1], SHUMIN LIN, ZHE LI, KEBIN JIA AND SHUDONG JIANG[2]

[1]*Faculty of Information Technology, Beijing University of Technology, China*
[2]*Thayer School of Engineering, Dartmouth College, NH, USA*

fengjc@bjut.edu.cn

ABSTRACT

Breast cancer is the most common cancer diagnosed among women in the world [1-5], which accounts for 30% of all new cancer diagnosis in women. It is noticeable that breast cancer mortality rates improve dramatically when breast tumor can be detected with imaging tools at an earlier and more treatable stage[6].

Fig. 1 depicts current main imaging modalities for breast cancer screening, diagnosis, and treatment. Although conventional breast imaging modalities may be useful for breast cancer screening or diagnosis [7-9]; however, these approaches are largely dependent on tumor size or structural features of abnormalities and provide comparatively little functional information about molecular-level changes in breast tissue [10], which limits opportunities to detect smaller lesions at early stage before lesions spread regionally and symptoms develop.

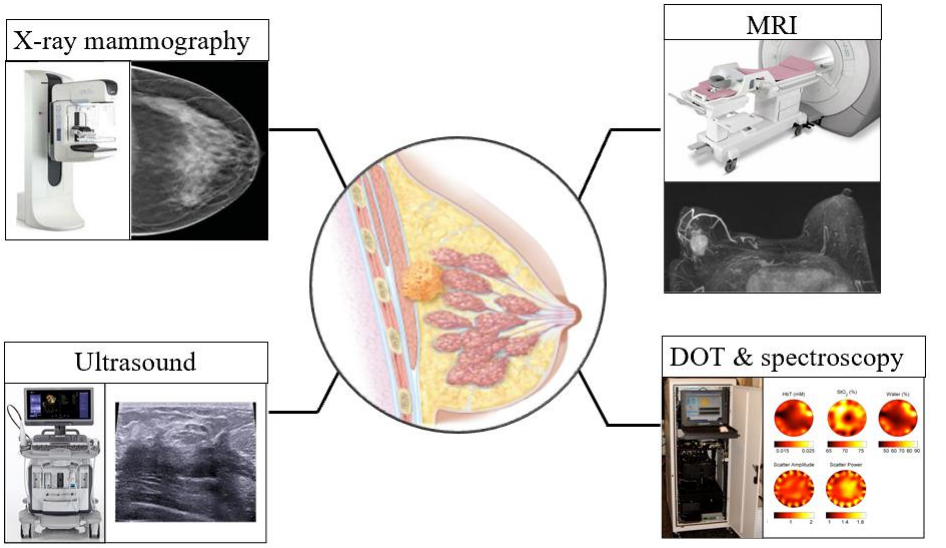

zzzz

Figure 1. *Clinical breast imaging modalities.*

As a non-invasive and low-cost imaging modality [11], near infrared spectral tomography (NIRST) has a great potential in breast cancer diagnosis and monitoring therapeutic response of neoadjuvant chemotherapy. The aim of NIRST is to use near infrared light to illuminate the breast, and to infer the internal distribution of chromophore concentrations from acquired signals. However, NIRST alone may not replace existing imaging modalities due to its poor spatial resolution (near 4-7 mm), which limits tumor size detection [12].

Since MRI has extremely high sensitivity and provides good structural a prior information about the breast, while NIRST provides functional information about the breast tissue, the integration of NIRST into MRI has attracted much attention in recent years. Fig. 2 shows an MRI-NIRST imaging system designed for breast imaging, and the details about the system can be found in Ref. [13]. To incorporate MRI images into NIRST, the widely used methods are hard [14] or soft [15] priors-based algorithms. However, the main shortcoming of the above two techniques is that both methods require manual segmentation to identify regions. This segmentation may lead to the objectivity in the process of combining images. Additionally, the segmentation step can be time-consuming, and requires sufficient segmentation experience to avoid segmentation bias or error.

To overcome the shortcoming of segmenting the MRI images, a direct regularization imaging (DRI) method has been developed for NIRST reconstruction [16]. However, T1-weighted (T1W), T2-weighted (T2W), T1-weighted dynamic contrast enhanced (DCE) and diffusion weighted (DW) images are often acquired in standard clinical breast MRI. Among the NIRST absorber concentrations, total hemoglobin (HbT) and water have shown the greatest potential to distinguish malignant from benign breast abnormalities [17]. Considering that total hemoglobin (HbT) values are highly related to DCE contrast, and water values are expected to be highly related to DW contrast, we presented a reconstruction algorithm to encode directly the spatial information derived from DCE and DW MRI into multiple regularization matrices for recovering NIRST HbT and water contents [16]. The motivation for pursuing this algorithm is to improve the accuracy of estimating HbT and water simultaneously. Simulation studies were used to test the approach, and the results are shown in Fig. 3. By combining prior information from dynamic contrast enhanced (DCE) and diffusion weighted (DW) MR images, the absolute bias errors of HbT and water were reduced by 35% and 34% compared to the no-prior case.

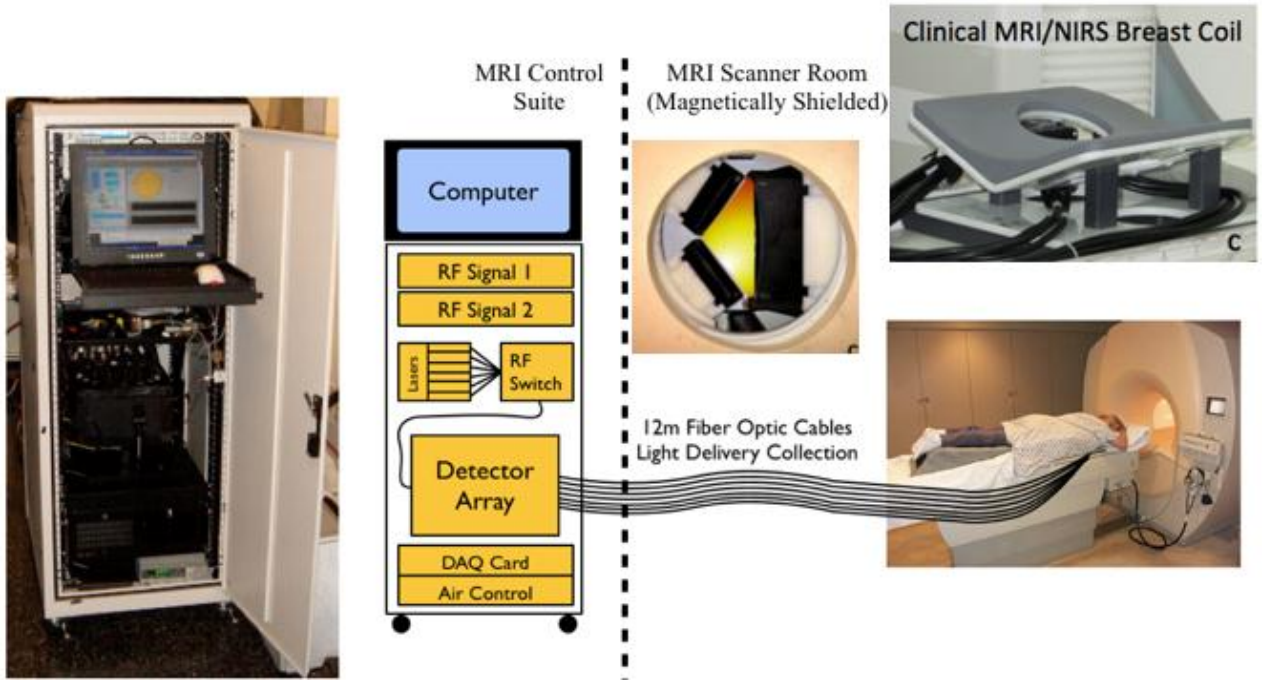

Figure 2*. The MRI-NIRST imaging system used in the following patient experiments. More details about the system can be found in Ref. [13].*

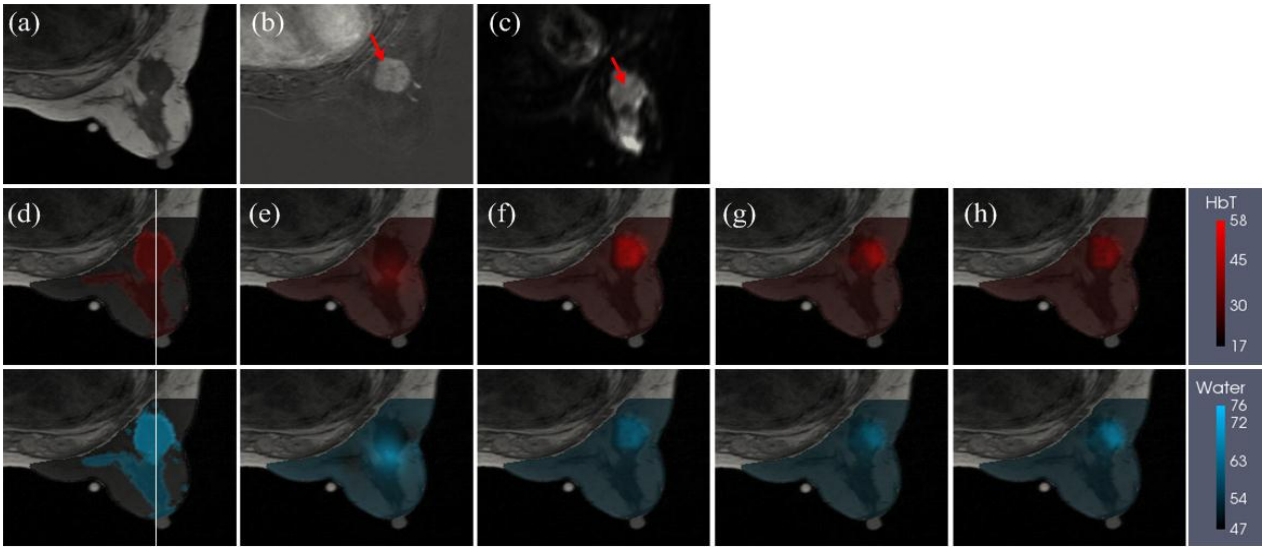

Figure 3. *Simulation breast study. (a) MRI T1 image; (b) DCE image; and (c) DW image in the plane z= -9.7 mm from a patient MRI exam. (d) Simulated true HbT (left) and water (right) images; (e-h) reconstructed HbT (μM) and water (%) images guided by no-prior information (e), DCE prior (f) DW prior (g) and both DCE and DW (DCE-DW) priors (h). Reconstructed images are overlaid on the MRI T1 images. Red arrows in (b) & (c) indicate the tumor. White lines in (d) denote cross sections, through the center of the tumor.*

Although DCE MRI is recognized as the most sensitive examination for breast cancer detection, it has a substantial false positive rate and gadolinium (Gd) contrast agents are not universally well tolerated. As a result, alternatives to diagnosing breast cancer based on endogenous contrast are of growing interest. Considering this, endogenous NIRST guided by T2 MRI was evaluated to explore whether the combined imaging modality, which does not require contrast injection or involve ionizing radiation, can achieve acceptable diagnostic performance [18]. Twenty-four subjects were simultaneously imaged with MRI and NIRST system shown in Fig. 2 prior to definitive pathological diagnosis. MRIs were evaluated independently by three breast radiologists blinded to the pathological results. Optical image reconstructions were constrained by grayscale values in the T2 MRI. MRI and NIRST images were used, alone and in combination, to estimate the diagnostic performance of the data. Outcomes were compared to DCE results. Sensitivity, specificity, accuracy, and area under the curve (AUC) of noncontrast MRI when combined with T2-guided NIRST were 94%, 100%, 96%, and 0.95, respectively, whereas these values were 94%, 63%, 88%, and 0.81 for DCE MRI alone, and 88%, 88%, 88%, and 0.94 when DCE-guided NIRST was added, as shown in Fig. 4.

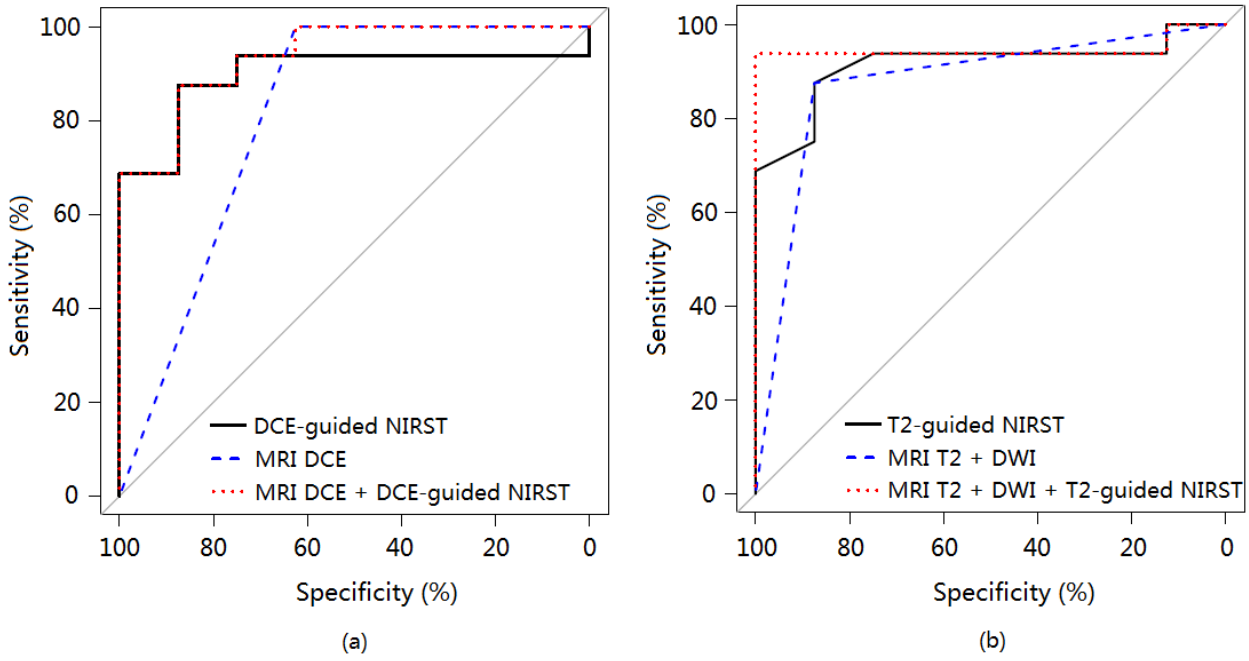

Figure 4. *ROC curves for a DCE-guided NIRST, DCE MRI, and combined DCE MRI and DCE-guided NIRST, and b T2-guided NIRST, T2 + DWI MRI, and combined T2 + DWI MRI and T2-guided NIRST. DCE dynamic contrast-enhanced, MRI magnetic resonance imaging, NIRST near-infrared spectral tomography.*

Note that DRI does not need to segment anatomical images; however, it still needs to model light propagation in tissue, and model errors due to mesh discretization, imperfect boundary conditions, and approximate governing equations, are inevitable in NIRST image reconstruction. Deep learning (DL) has been investigated and shown to improve certain image reconstruction problems [25-26]. Inspired by these developments and with the unique opportunity to incorporate anatomical images into these networks that can further improve NIRST image quality, we developed a DL based algorithm (Z-Net) for MRI guided NIRST image reconstruction [27]. In our approach, segmentation of MRI images and modeling of light propagation are avoided and the concentrations of chromophores of oxy-hemoglobin (HbO), deoxy-hemoglobin (Hb), and water are recovered from acquired NIRST signals guided by MRI images through end-to-end training with simulated datasets. Fig. 5 shows the Z-Net architecture for 2D experiments. Optical signals at 9 wavelengths (661, 735, 785, 808, 826, 852, 903, 912, and 948 nm) and MRI images provide the input to the network. Fig. 6 shows representative recovered images of HbO, Hb and water in the case of a phantom with three inclusions. Compared to reconstructed images by DRI, images recovered with Z-net have values much closer to their ground truths with fewer artifacts. the proposed Z-net method provided accurate recovery of HbO, Hb and water concentrations and errors in recovered values were less than 2% of known values. Compared with DRI, MSE obtained with Z-Net was 92.6%, 99.7% and 91.7% lower for HbO, Hb, and water, respectively. Finally, we applied the Z-net approach to image reconstruction of patient data, and the results are shown in Fig. 7.

In conclusion, MRI image-guided NIRST improves quantification of breast tissue chromophore and breast cancer diagnosis.

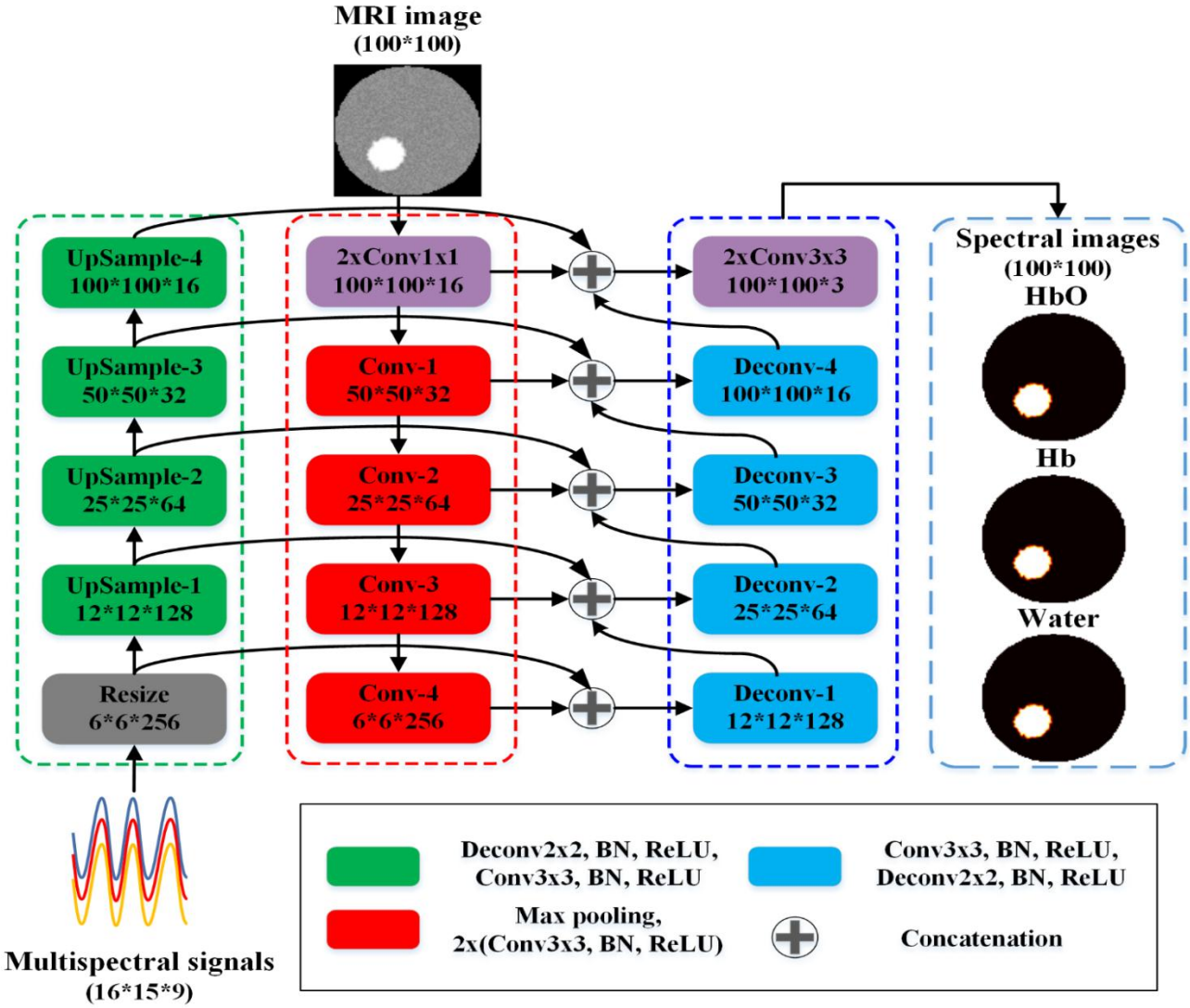

Figure 5. *The Z-Net architecture designed for MRI guided NIRST experiments.*

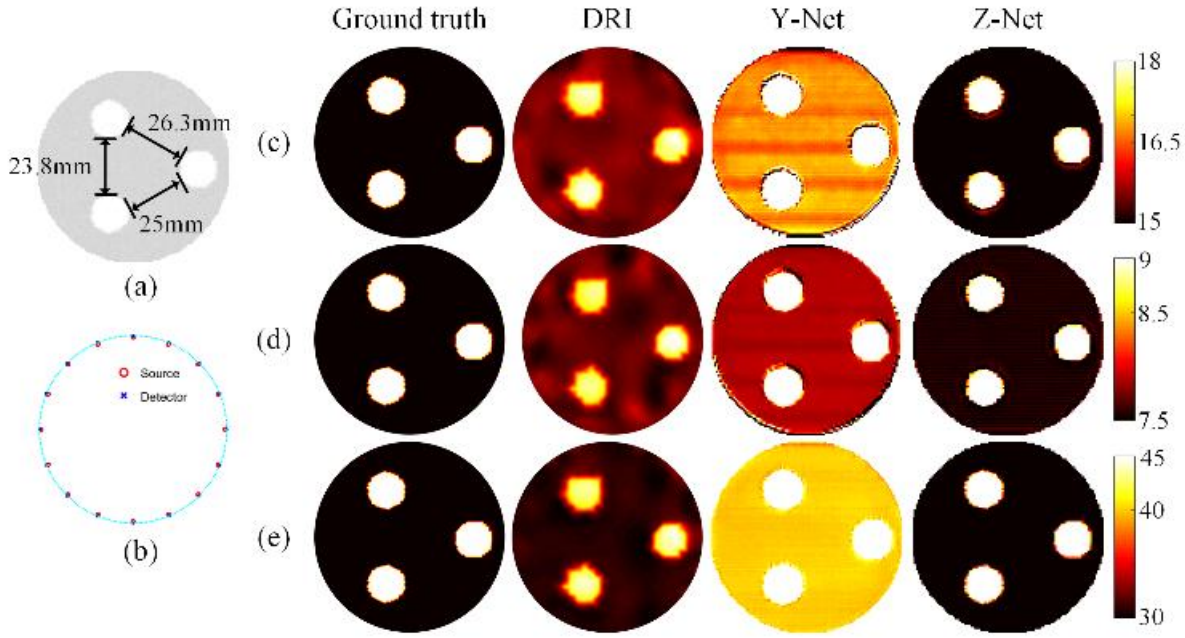

Figure 6. *Reconstructed images of HbO, Hb, and water in the case of three inclusions. (a) MRI images, (b) source/detector positions around the phantom, (c)-(e) true and reconstructed images of HbO, Hb, and water, respectively.*

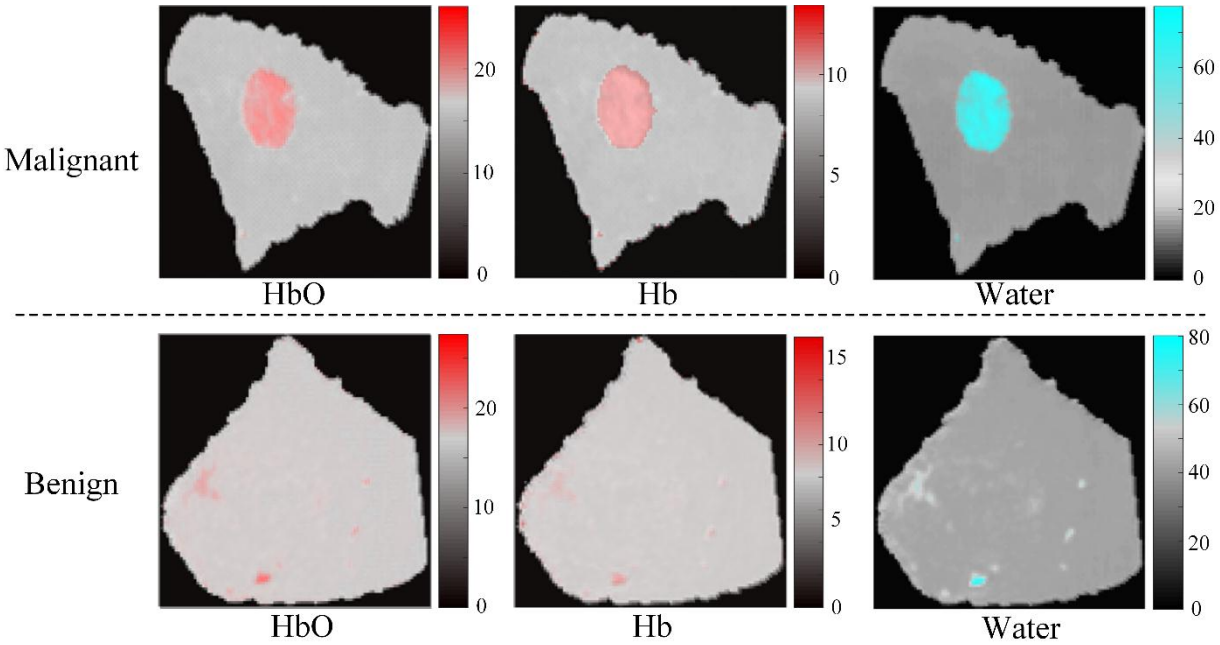

Figure 7. *The reconstructed HbO, Hb, and Water images for two patients with the Z-net. The first row shows the Z-net results from a breast cancer patient with a malignant lesion, and the second row is the results from a subject with a benign lesion. Reconstructed images are overlaid on the DCE-MRI.*

REFERENCES

[1] B. Chance, S. Nioka, J. Zhang, E. F. Conant, E. Hwang, S. Briest, S. G. Orel, M. D. Schnall, and B. J. Czerniecki, Breast cancer detection based on incremental biochemical and physiological properties of breast cancers: a six-year, two-site study, Acad. Radiol., 12(8), 925–933, 2005.

[2] S. Kukreti, A. E. Cerussi, W. Tanamai, D. Hsiang, B. J. Tromberg, and E. Gratton, Characterization of metabolic differences between benign and malignant tumors: high-spectral-resolution diffuse optical spectroscopy, Radiology, 254(1), 277–84, 2010.

[3] W. Chen, K. Sun, R. Zheng, H. Zeng, S. Zhang, C. Xia, Z. Yang, H. Li, X. Zou, and J. He, Cancer incidence and mortality in China, 2014, Chinese J. Cancer Res., 30(1), 1–12, 2018.

[4] C. E. DeSantis, J. Ma, A. Goding Sauer, L. A. Newman, and A. Jemal, Breast cancer statistics, 2017, racial disparity in mortality by state, CA. Cancer J. Clin., 67(6), 439–448, 2017.

[5] R. L. Siegel, K. D. Miller, and A. Jemal, Cancer statistics, 2019, CA. Cancer J. Clin., 69(1), 7–34, 2019.

[6] B. L. Yun, S. M. Kim, M. Jang, H. S. Ahn, C. Y. Lyou, M. S. Kim, S. A. Kim, T. Song, Y. Yoo, J. H. Chang, and Y. Kim, Does adding diffuse optical tomography to sonography improve differentiation between benign and malignant breast lesions?: observer performance study, J. Ultrasound Med., 34(5), 749–757, 2015.

[7] C. K. Kuhl, Current status of breast MR imaging part2. clinical applications, Radiology, 244(3), 672–691, 2007.

[8] C. K. Kuhl, K. Strobel, H. Bieling, C. Leutner, H. H. Schild, and S. Schrading, "Supplemental breast MR imaging screening of women with average risk of breast cancer, Radiology, 28(2), 361-370, 2017.

[9] S. C. Agner, M. A. Rosen, S. Englander, J. E. Tomaszewski, M. D. Feldman, P. Zhang, C. Mies, M. D. Schnall, and A. Madabhushi, Computerized image analysis for identifying triple-negative breast cancers and differentiating them from other molecular subtypes of breast cancer on dynamic contrast-enhanced MR images: a feasibility study, Radiology, 272(1), 91–99, 2014.

[10] B. W. Pogue, S. Jiang, H. Dehghani, C. Kogel, S. Soho, S. Srinivasan, X. Song, T. D. Tosteson, S. P. Poplack, and K. D. Paulsen, Characterization of hemoglobin, water, and NIR scattering in breast tissue: analysis of intersubject variability and menstrual cycle changes, J. Biomed. Opt., 9(3), 541–52, 2004.

[11] D. A. L. Ighter, J. A. H. Ughes, I. A. I. N. S. Tyles, A. Ndrew, F. Iler, and H. A. D. Ehghani, Multispectral, non-contact diffuse optical tomography of healthy human finger joints, Biomed. Opt. Express, 9(4), 1445–1460, 2018.

[12] P. K. Yalavarthy, B. W. Pogue, H. Dehghani, C. M. Carpenter, S. Jiang, and K. D. Paulsen, Structural information within regularization matrices improves near infrared diffuse optical tomography, Opt. Express, 15(13), 8043–8058, 2007.
[13] M. A. Mastanduno, J. Xu, F. El-Ghussein, S. Jiang, H. Yin, Y. Zhao, K. Wang, F. Ren, J. Gui, B. W. Pogue, and K. D. Paulsen, MR-Guided near-Infrared spectral tomography increases diagnostic performance of breast MRI, Clin. Cancer Res. 21(17), 3906-3912, 2015.
[14] V. Ntziachristos, A. G. Yodh, M. D. Schnall, and B. Chance, MRI-guided diffuse optical spectroscopy of malignant and benign breast lesions, Neoplasia 4(4), 347–354, 2002.
[15] P. K. Yalavarthy, B. W. Pogue, H. Dehghani, C. M. Carpenter, S. Jiang, and K. D. Paulsen, Structural information within regularization matrices improves near infrared diffuse optical tomography, Opt. Express 15(13), 8043–8058, 2007.
[16] J. Feng, S. Jiang, J. Xu, Y. Zhao, B. W. Pogue, and K. D. Paulsen, Multiobjective guided priors improve the accuracy of near-infrared spectral tomography for breast imaging, J. Biomed. Opt. 21(9), 090506, 2016.
[17] H. Soliman, A. Gunasekara, M. Rycroft, J. Zubovits, R. Dent, J. Spayne, M. J. Yaffe, and G. J. Czarnota, Functional imaging using diffuse optical spectroscopy of neoadjuvant chemotherapy response in women with locally advanced breast cancer, Clin. Cancer Res. 16, 2605-2614, 2010.
[18] J. Feng, J. Xu, S. Jiang, H. Yin, Y. Zhao, J. Gui, K. Wang, X. Lv, F. Ren, B. W. Pogue and K. D. Paulsen, Addition of T2-guided optical tomography improves noncontrast breast magnetic resonance imaging diagnosis, Breast Cancer Research 19:117, 2017.
[19] G. Yang, S. Yu, H. Dong, G. Slabaugh, P. L. Dragotti, X. Ye, F. Liu, S. Arridge, J. Keegan, Y. Guo, and D. Firmin, DAGAN: deep dealiasing generative adversarial networks for fast compressed sensing MRI reconstruction, IEEE Trans. Med. Imaging 37(6), 1310-1321, 2018.
[20] K. H. Jin, M. T. McCann, E. Froustey, and M. Unser, Deep convolutional neural network for inverse problems in imaging, IEEE Trans. Image Process. 26(9), 4509-4522, 2017.
[21] H. Lan, D. Jiang, C. Yang, F Gao, and F. Gao, Y-Net: hybrid deep learning image reconstruction for photoacoustic tomography in vivo, Photoacoustics, 20, 100197, 2020.
[22] Y. Gao, K. Wang, Y. An, S. Jiang, H. Meng, and J. Tian, Nonmodel-based bioluminescence tomography using a machine-learning reconstruction strategy, Optica 5(11), 1451-1454, 2018.
[23] S. Sabir, S. Cho, Y. Kim, R. Pua, D. Heo, K. H. Kim, Y. Choi, and S. Cho, Convolutional neural network-based approach to estimate bulk optical properties in diffuse optical tomography, Appl. Opt. 59(5), 1461-1670, 2020.
[24] H. Wang, N. Wu, Z. Zhao, G. Han, Jun Zhang, and J. Wang, Continuous monitoring method of cerebral subdural hematoma based on MRI guided DOT, Biomed. Opt. Express 11(6), 2964-2975, 2020.
[25] J. Yoo, S. Sabir, D. Heo, K. H. Kim, A. Wahab, Y. Choi, S. Lee, E. Y. Chae, H. H. Kim, Y. M. Bae, Y. Choi, S. Cho, and J. C. Ye, Deep learning diffuse optical tomography, IEEE Trans. Med. Imaging 39(4), 877-887, 2020.
[26] Y. Takamizu, M. Umemura, H. Yajima, M. Abe, and Y. Hoshi, Deep learning of diffuse optical tomography based on time-domain radiative transfer equation, arXiv:2011.12520, 2020.
[27] J. Feng, W. Zhang, Z. Li, K. Jia, S. Jiang, H. Dehghani, B. W. Pogue, and K. D. Paulsen, Deep-learning based image reconstruction for MRI-guided near-infrared spectral tomography, Optica, 9(3), 264-268, 2022.

DOI 10.24412/cl-37136-2023-1-140-142

ENHANCING STIMULATED EMISSION DEPLETION IMAGING THROUGH OPTICAL METHODS, PROBES AND DEEP-LEARNING

JUNLE QU, JIA LI, WEI YAN, LUWEI WANG, ZHIGANG YANG

College of Physics and Optoelectronic Engineering, Shenzhen University

jlqu@szu.edu.cn

ABSTRACT

Stimulated emission depletion (STED) microscopy is an advanced imaging technique that was first proposed in 1994 and later experimentally performed. This technique requires two laser beams to achieve super-resolution imaging. The first laser beam is pulsed and is used to transfer fluorescent dyes to excited states, generating a fluorescent spot due to optical diffraction. The second laser beam, called the STED laser, has a larger pulse width and produces a doughnut-shaped spot that selectively deactivates fluorescent dyes lying in the overlapping region of the excitation and STED laser spots. The doughnut-shaped STED beam suppresses fluorescence photon emission in the periphery of the excitation beam, ensuring almost zero intensity at the center, and thus determining the imaging resolution.

To achieve better spatial resolution in STED microscopy, it is important to select appropriate fluorescent dyes with excellent nonlinear response, especially for biological samples. All the fluorophores around the focal excitation spot need to be in their fluorescent "off" state to attain exceptionally high resolution since the stimulated emission rate has a nonlinear dependence on the intensity of the STED beam. The high-resolution images are obtained by scanning the focal spot across the object. Increasing the intensity of the STED pulses can theoretically compress the full-width-at-half maximum (FWHM) of the point spread function (PSF) at the excitation focal spot, as presented in equation (1).

$$\Delta r = \frac{\Delta}{\sqrt{1+I_{max}/I_S}} \text{Место для формулы.} \qquad (1)$$

Where, Δr is the lateral resolution, Δ represents the FWHM of the diffraction limited PSF, I_{max} is the peak intensity of the STED laser, and I_s stands for the threshold intensity needed in order to achieve saturated emission depletion.

Where, Δr is the lateral resolution, Δ represents the FWHM of the diffraction limited PSF, I_{max} is the peak intensity of the STED laser, and I_s stands for the threshold intensity needed in order to achieve saturated emission depletion.

STED microscopy is a powerful imaging technique that can achieve lateral resolutions of 10-80 nm and longitudinal resolutions of 30-600 nm with high imaging speed. These capabilities have led to its increasing use in visualizing and understanding complex biological structures and dynamic functions at the nanoscale level in a wide range of cell and tissue types. However, when used for live cell imaging, the intense laser required for STED microscopy can cause significant photodamage to cells, tissues, and fluorophores. Additionally, the use of an intense STED laser beam can accelerate the photobleaching process of fluorophores, which can impede long-term STED imaging. Therefore, optimizing the STED laser power is crucial to achieving high-quality STED images while minimizing photodamage and photobleaching.

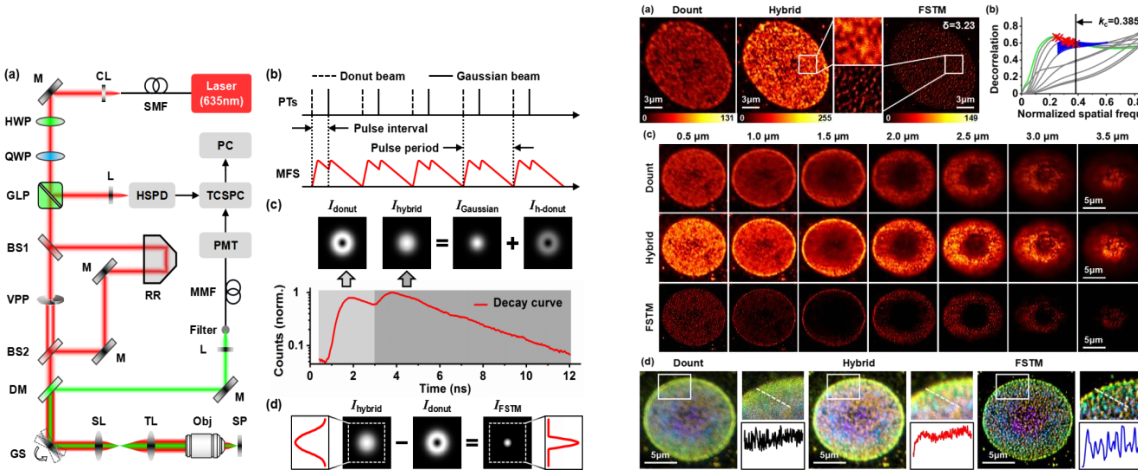

Figure: *(a) Scheme of fluorescence spatiotemporal modulation (FSTM) nanoscopy. (b) FSTM imaging of nuclear pore complex (NPC).*

In this presentation, I will discuss our recent advances in STED microscopy and related work. Our research has focused on two major strategies to achieve successful STED imaging with reduced STED laser power. The first approach involves the development of novel STED imaging techniques, such as adaptive optics STED, phasor analysis STED, and digitally enhanced STED. These techniques have been designed to lower the depletion power required during STED image acquisition.

The second significant method to minimize STED laser power involves the development of new dedicated STED probes and fluorophores with improved photostability and lower saturation intensity (IS). Our team has successfully developed several new fluorescent materials, including perovskite quantum dots, carbon dots, organosilicon nanohybrids, and enhanced squaraine variant probes. These materials enable STED imaging with very low STED laser power, exhibit superior photostability, and much lower saturation intensity compared to traditional STED probes.

Furthermore, we have developed a dual-color STED microscope with a single laser source, which has achieved spatial resolutions of 75 nm and 104 nm for mitochondria and tubulin in HeLa cells. These advancements in STED microscopy hold great promise for improving our understanding of complex biological structures and functions at the nanoscale level while minimizing the risk of photodamage and photobleaching.

In addition, we have made significant progress by developing a deep-learning-based algorithm for the generation of super-resolution images directly from diffraction-limited confocal images.

REFERENCES

[1] W. Yan, Z. Yang, Y. Tan, X. Chen, Y. Li, J. Qu, T. Ye, Coherent optical adaptive technique improves the spatial resolution of STED microscopy in thick samples, Photonics Res., 5:176-181(2017).

[2] L. Wang L., W. Yan, R. Li, X. Weng, J. Zhang, Z. Yang, L. Liu, J. Qu, Aberration correction for improving the image quality in STED microscopy using the genetic Algorithm, Nanophotonics, 7:1971-1980(2018).

[3] Y. Chen, L. Wang, W. Yan, X. Peng, J. Qu, J. Song, Elimination of Re-excitation in Stimulated Emission Depletion Nanoscopy Based on Photon Extraction in a Phasor Plot, Laser Photonics Rev., 14: 1900352(2020).

[4] S. Ye, W. Yan, M. Zhao, X. Peng, J. Song, J. Qu, Low-Saturation-Intensity, High-Photostability, and High-Resolution STED Nanoscopy Assisted by CsPbBr3 Quantum Dots, Adv. Mater., 30:201800167(2018).

[5] X. Yang, Z. Yang, Z. Wu, Y. He, C. Shan, P. Chai, C. Ma, M. Tian, J. Teng, D. Jin, W. Yan, P. Das, J. Qu, P. Xi, Mitochondrial dynamics quantitatively revealed by STED nanoscopy with an enhanced squaraine variant probe, Nature Communications, 11, 1:1-9(2020).

[6] J. Wang, J. Zhang, L. Wang, X. Gao, Y. Shao, L. Liu, Z. Yang, W. Yan, J. Qu, Dual-color STED super-resolution microscope using a single laser source, J. Biophotonics, 13: e202000057(2020).
[7] L. Wang, J. Li, Y. Chen, Y. Yong, Z. Yang, X. Weng, W. Yan, J. Qu, Implementation of a fluorescence spatiotemporal modulation super-resolution microscope, Optics Letters,47(3):581-584(2022).
[8] B. Huang, J. Li, B. Yao, Z. Yang, E. Y. Lam, J. Zhang, W. Yan, J. Qu, Enhancing image resolution of confocal fluorescence microscopy with deep learning, PhotoniX, 4:2: doi.org/10.1186/s43074-022-00077-x (2023).

DOI 10.24412/cl-37136-2023-1-143-146

SINGLE-MOLECULE LOCALIZATION SUPER-RESOLUTION MICROSCOPY AND ITS APPLICATIONS

FEN HU[1], MENGDI HOU[1], FULIN XING[1], JIANYU YANG[1], AND LEITING PAN[1,2]

[1]*The Key Laboratory of Weak-Light Nonlinear Photonics of Education Ministry, School of Physics and TEDA Institute of Applied Physics, Nankai University, China*
[2] *State Key Laboratory of Medicinal Chemical Biology, Frontiers Science Center for Cell Responses, College of Life Sciences, Nankai University, China*

plt@nankai.edu.cn

ABSTRACT

At the beginning of this century, super-resolution fluorescence microscopy techniques have been invented to break the diffraction limit of traditional optical microscopy, thereby provide unprecedented accesses to life science researches at the micrometer and nanometer scales. Nowadays, a variety of super-resolution techniques have been developed continually, which can be mainly divided into two classes: (1) Patterned illumination-based microscopy involving stimulated emission depletion microscopy (STED) [1] and structured illumination microscopy (SIM) [2]; (2) Single-molecule localization microscopy (SMLM) such as photoactivated localization microscopy (PALM) [3] and stochastic optical reconstruction microscopy (STORM) [4]. Owing to the straightforward principle, relatively easy implementation, and outstanding spatial resolution, SMLM has gain more and more attention from researchers.

Single fluorophore labels can be switched "on" and "off" in a controllable manner in SMLM [5]. Afterward, a series of diffraction-limited images featuring each subset of temporarily active and spatially distinct fluorophores can be acquired by repeated imaging sparse stochastic subsets of blinking fluorophores in a sample. Individual fluorophores are localized at sub-diffraction precision by finding the centers of their point spread functions. Finally, the superposition of the calculated particle positions will generate a super-resolution reconstruction image. Based on the sparse fluorophore detection, localization and superposition, SMLM can discern and pinpoint individual molecules even with dense labeling, thus allow molecular localization accuracies at the nanometer level. The spatial resolution of the reconstructed SMLM image is determined by the number of photons detected from individual molecules, as well as the labeling efficiency or density [6].

The application of SMLM offers new opportunities to resolve the three-dimensional ultrastructure, organization, and dynamics of subcellular nanostructures at the nanoscale [7]. For instance, dual-color STORM imaging unveils the fantastic periodic structure of membrane-associated skeleton in neuron synapses [8]. STORM clearly resolves the radial eight-fold symmetry structure of nuclear pore complex [9], the radial nine-fold symmetry structure of ciliary basal body [10], as well as the nanoscale architecture of necrosomes [11]. STORM also demonstrates the spatial colocalization and functional link of purinosomes with mitochondria [12]. At the meantime, PALM maps the nanoscale protein organization in subcellular molecular assemblies including focal adhesions [13] and podosomes [14]. On the other hand, SMLM have been widely used to measure the nanoscale clustering of membrane receptors such as T cell receptors (TCR), glucose transporter GLUT1 and glutamate receptors (GluR) [15-17]. Besides, SMLM can also be applied in visualizing the dynamic information of cellular organelles and proteins in live cells [18,19].

Utilizing three-dimensional (3D)-STORM super-resolution microscopy, we studied the ultrastructural spatiotemporal organization and regulation of podosome clusters formed in primary mouse peritoneal macrophages (Figure 1) [20]. Podosomes are actin-based protrusive devices critical for cell migration, invasion,

mechanosensing and extracellular matrix remodeling [21]. The unique “core-ring-cap” architecture and highly dynamic natures of podosomes have made them fascinating and attracted many scientists to develop new technologies for their analysis [22]. We first visualized the nanoscale 3D landscape of individual macrophage podosomes with ~20/50 nm (lateral/axial) spatial resolution (Figure 1*a*). We presented rich information on how podosomes are organized into cluster-like mesoscale superstructures in mouse peritoneal macrophages. 3D-STORM clearly delineates a snowman-like portrait of macrophage podosome core. Then, we performed dual-color 3D-STORM microscopy to reveal the nanoscale mutual localization of the F-actin core, paxillin ring, and myosin IIA ring in the macrophage podosomes. Through a particle superimposing method, we provide the precise mutual localization of podosome actin core and ring component proteins. We thus determined a ~90 nm difference in the axial localization between the paxillin ring and the myosin IIA ring in macrophage podosomes, which is indistinguishable from diffraction-limited microscopy (Figure 1*b*). Moreover, by dual-color 3D-STORM, we revealed a direct mechanical link between podosomes and microtubules cytoskeletons at the layer of myosin IIA in primary macrophages (Figure 1*b*). Combined with pharmacological approaches, we suggested that microtubules physically stabilize podosome clusters formed in macrophages in addition to regulate their assembly through the commonly assumed Rho/ROCK-myosin IIA signaling (Figure 1*c*). These results enriched the information of the nanoscale architecture of podosomes, as well as provide novel insights in the regulation mechanisms of podosomes.

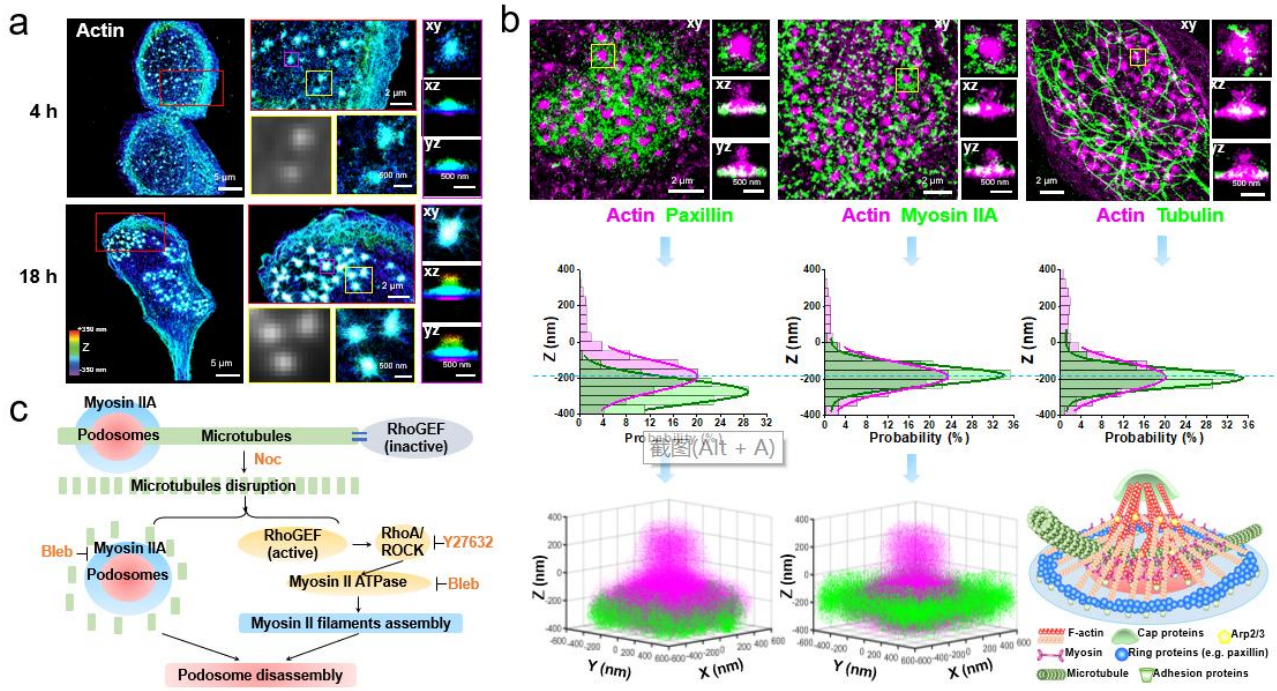

Figure 3 *3D-STORM reveals nanoscale architecture and regulation of podosome clusters in primary macrophages. a) The nanoscale 3D landscape of individual podosomes in mouse peritoneal macrophages with different culture time. b) The spatial relationship of podosome components and the crosslink between podosome and microtubules revealed by two-color 3D-STORM. c) Schematic diagram of the mechanisms on microtubules disruption-caused disassembly of podosomes in macrophages.*

Furthermore, by combination of ultrastructure expansion microscopy (U-ExM) with SMLM, we developed a method of U-ExSMLM to resolve the skeleton organization of erythrocytes, a textbook prototype for the submembrane cytoskeleton of metazoan cells [23]. Using poly-l-lysine to treat the glass slide substrate and fix the expanded gel, we realized resistance to shrinkage at the two-dimensional scale, successfully combining ExM and SMLM with a 4.3-fold physical expansion. It increases the 25 nm resolution of SMLM to a molecular resolution of about 6 nm (Figure 2*a*). We investigated the nanoscale spatial distribution of several skeleton proteins, including N/C-terms of β-spectrin, protein 4.1, as well as tropomodulin. Our results by U-ExSMLM were in good accordance with the acknowledged model of erythrocyte skeleton structure. Then, we created

weak adhesion conditions that can maintain the native biconcave shape of erythrocytes, and performed imaging with U-ExSMLM. It was found that spectrin skeleton in the erythrocyte dimple region is longer than that in the rim region, while the density of the spectrin skeleton in the dimple region is greater than that in the rim region (Figure 2*b*). These findings provide direct molecular resolution evidence for the asymmetry of the cytoskeleton in biconcave human erythrocytes. It also provides a novel super-resolution imaging method for studying the subcellular structure and functions near-cytoplasmic membrane.

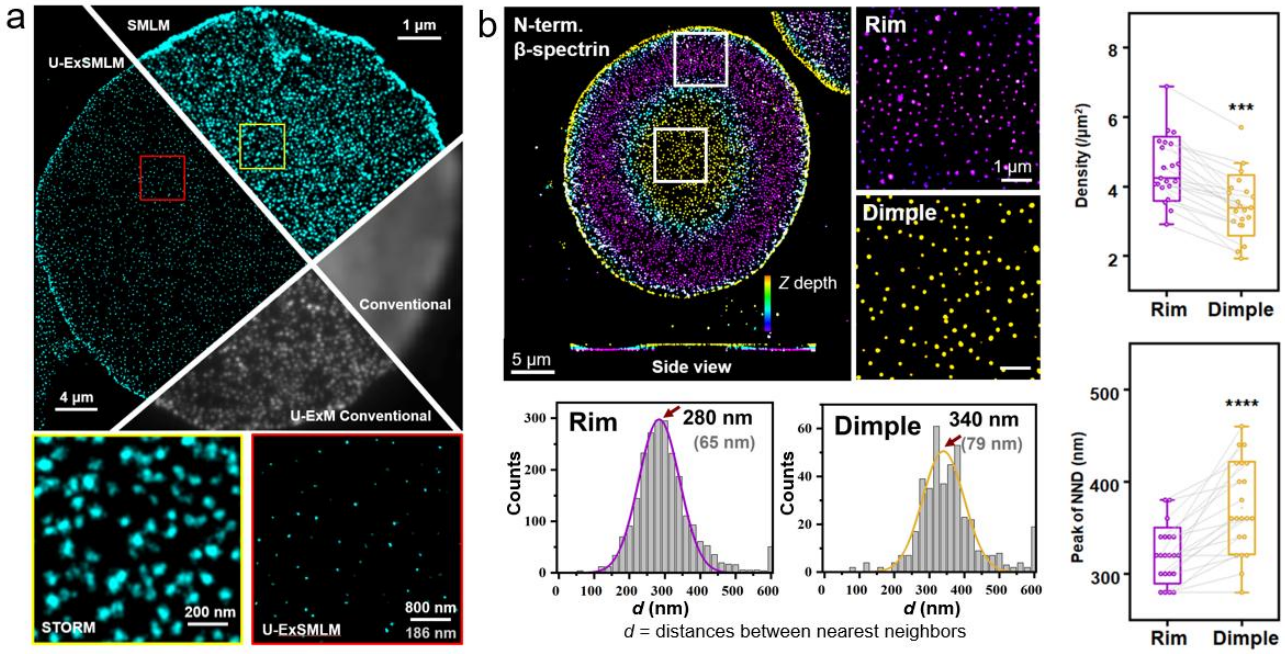

Figure 2 *U-ExSMLM achieves molecular resolution. a) Conventional, U-ExM, STORM, and U-ExSMLM images of N-termini of β-spectrin of representative erythrocytes. b) U-ExSMLM image of the rim region and dimple region of a biconcave-shaped erythrocyte with N-termini of β-spectrin labeled. Statistics of density and the peak of NND (nearest neighboring distance) of the dimple and the rim regions in biconcave erythrocytes.*

To sum up, based on SMLM super-resolution microscopy, we elucidate the nanoscale arrangement of podosome clusters in primary peritoneal macrophages with ~20/50 nm (lateral/axial) spatial resolution. Furthermore, we demonstrate that microtubules pass through podosomes at the layer of myosin IIA and physically stabilize podosome clusters in addition to regulate their assembly through the commonly assumed Rho/ROCK-myosin signaling. We also proposed a strategy for the combination of SMLM and ExM relied on poly-l-lysine adhering, reaching the molecular resolution of ~6 nm, and directly revealed the asymmetry of the erythrocyte cytoskeleton, providing a molecular explanation for understanding the unique biconcave morphology in human erythrocytes. These findings will provide new information and innovative methods for the exploration of the ultrastructure and function of subcellular nanostructures.

REFERENCES

[1] T. A. Klar, S. Jakobs, M. Dyba, A. Egner, S. W. Hell, Fluorescence microscopy with diffraction resolution barrier broken by stimulated emission. Proc. Natl. Acad. Sci. U. S. A. 8206–8210, 2000.
[2] M. G. Gustafsson, Nonlinear structured-illumination microscopy: wide-field fluorescence imaging with theoretically unlimited resolution. Proc. Natl. Acad. Sci. U. S. A. 13081–13086, 2005.
[3] E. Betzig, G. H. Patterson, R. Sougrat, O. W. Lindwasser, S. Olenych, J. S. Bonifacino, M. W. Davidson, J. Lippincott-Schwartz, H. F. Hess, Imaging intracellular fluorescent proteins at nanometer resolution. Science 1642–1645, 2006.
[4] M. J. Rust, M. Bates, X. Zhuang, Sub-diffraction-limit imaging by stochastic optical reconstruction microscopy (STORM). Nat. Methods 793–796, 2006.
[5] K. Finan, B. Flottmann, M. Heilemann, Photoswitchable fluorophores for single-molecule localization microscopy. Methods Mol. Biol. 131–151, 2013.
[6] R. Diekmann, M. Kahnwald, A. Schoenit, J. Deschamps, U. Matti, J. Ries, Optimizing imaging speed and

excitation intensity for single-molecule localization microscopy. Nat. Methods 909–912, 2020.
[7] Y. M. Sigal, R. Zhou, X. Zhuang, Visualizing and discovering cellular structures with super-resolution microscopy. Science 880–887, 2018.
[8] K. Xu, G. Zhong, X. Zhuang, Actin, spectrin, and associated proteins form a periodic cytoskeletal structure in axons. Science 452–456, 2013.
[9] A. Szymborska, A. de Marco, N. Daigle, V. C. Cordes, J. A. Briggs, J. Ellenberg, Nuclear pore scaffold structure analyzed by super-resolution microscopy and particle averaging. Science 655–658, 2013.
[10] X. Shi, G. Garcia 3rd, J. C. Van De Weghe, R. McGorty, G. J. Pazour, D. Doherty, B. Huang, J. F. Reiter, Super-resolution microscopy reveals that disruption of ciliary transition-zone architecture causes Joubert syndrome. Nat. Cell Biol. 1178–1188, 2017.
[11] X. Chen, R. Zhu, J. Zhong, Y. Ying, W. Wang, Y. Cao, H. Cai, X. Li, J. Shuai, J. Han, Mosaic composition of RIP1-RIP3 signalling hub and its role in regulating cell death. Nat. Cell Biol. 471-482, 2022.
[12] J. B. French, S. A. Jones, H. Deng, A. M. Pedley, D. Kim, C. Y. Chan, H. Hu, R. J. Pugh, H. Zhao, Y. Zhang, T. J. Huang, Y. Fang, X. Zhuang, S. J. Benkovic, Spatial colocalization and functional link of purinosomes with mitochondria. Science 733-737, 2016.
[13] P. Kanchanawong, G. Shtengel, A. M. Pasapera, E. B. Ramko, M. W. Davidson, H. F. Hess, C. M. Waterman, Nanoscale architecture of integrin-based cell adhesions. Nature 580–584, 2010.
[14] J. C. Herron, S. Hu, T. Watanabe, A. T. Nogueira, B. Liu, M. E. Kern, J. Aaron, A. Taylor, M. Pablo, T. L. Chew, T. C. Elston, K. M. Hahn, Actin nano-architecture of phagocytic podosomes. Nat. Commun. 4363, 2022.
[15] Y. S. Hu, H. Cang, B. F. Lillemeier, Superresolution imaging reveals nanometer- and micrometer-scale spatial distributions of T-cell receptors in lymph nodes. Proc. Natl. Acad. Sci. U. S. A. 7201-7206, 2018.
[16] Q. Yan, Y. Lu, L. Zhou, J. Chen, H. Xu, M. Cai, Y. Shi, J. Jiang, W. Xiong, J. Gao, H. Wang, Mechanistic insights into GLUT1 activation and clustering revealed by super-resolution imaging. Proc. Natl. Acad. Sci. U. S. A. 7033–7038, 2018.
[17] S. Siddig, S. Aufmkolk, S. Doose, M. L. Jobin, C. Werner, M. Sauer, D. Calebiro, Super-resolution imaging reveals the nanoscale organization of metabotropic glutamate receptors at presynaptic active zones. Sci. Adv. eaay7193, 2020.
[18] S. H. Shim, C. Xia, G. Zhong, H. P. Babcock, J. C. Vaughan, B. Huang, X. Wang, C. Xu, G. Q. Bi, X. Zhuang, Super-resolution fluorescence imaging of organelles in live cells with photoswitchable membrane probes. Proc. Natl. Acad. Sci. U. S. A. 13978–13983, 2012.
[19] L. Xiang, K. Chen, R. Yan, W. Li, K. Xu, Single-molecule displacement mapping unveils nanoscale heterogeneities in intracellular diffusivity. Nat. Methods 524–530, 2020.
[20] F. Hu, D. Zhu, H. Dong, P. Zhang, F. Xing, W. Li, R. Yan, J. Zhou, K. Xu, L. Pan, J. Xu, Super-resolution microscopy reveals nanoscale architecture and regulation of podosome clusters in primary macrophages. iScience 105514, 2022.
[21] Linder S, Cervero P, Eddy R, et al. Mechanisms and roles of podosomes and invadopodia. Nat Rev Mol Cell Biol 2023, 24: 86-106.
[22] K. van den Dries, S. Linder, I. Maridonneau-Parini, R. Poincloux, Probing the Mechanical Landscape-New Insights Into Podosome Architecture and Mechanics. J. Cell Sci. jcs236828, 2019.
[23] Mengdi Hou, Fulin Xing, Jianyu Yang, Fen Hu, Leiting Pan*, Jingjun Xu. Molecular Resolution Mapping of Erythrocyte Cytoskeleton by Ultrastructure Expansion Single-Molecule Localization Microscopy (U-ExSMLM). Small Methods, 2023, 7: 2201243.

DOI 10.24412/cl-37136-2023-1-147-147

PROBING THE INTERACTIONS BETWEEN NANOPARTICLES AND CELLS THROUGH DARKFIELD IMAGING AND RAMAN SPECTROSCOPY

RUI HU, ZHENHAO MO AND YANHUA ZOU

Center for Biomedical Photonics & College of Physics and Optoelectronic Engineering, Key Laboratory of Optoelectronic Devices and Systems, Shenzhen University, Shenzhen 518060, P. R. China

rhu@szu.edu.cn

ABSTRACT

In the past decades, functionalized nanomaterials have well been developed and attracted increasing attentions in biomedical research. They have found wide applications in bioimaging, biosensing and disease diagnosis and therapy. However, up to date, there has been very few formulations adopted in clinical practices. Among all nanomaterials, inorganic nanoparticles, such as semiconductor quantum dots, carbon nanomaterials, up-conversion nanoparticles, various 2-D nanomaterials, and metallic nanoparticles, have demonstrated outstanding physicochemical properties in biomedical applications. Recent reports have shown their great potential in targeted imaging, tracking, drug delivery and therapy. However, almost none of these inorganic nanoparticles have been approved by the FDA for clinical settings. One of the most discussed hurdles is their potential risk when introduced in vivo. No matter how many advantages they share, their accumulation in the major organs and the unclear long-term route in the biological system have greatly discouraged the clinicians. To sort out this problem, one should thoroughly and carefully examine the interactions between the nanoparticles and the biological system in details. In this contribution, we would like to introduce the recent developments in nanoparticle design and the efforts made in understanding the interactions between them and the biological system, down to the subcellular level. Due to their inert chemical properties, noble metal nanoparticles were regarded as chemically stable in biological system, and over previous study have shown that the gold nanoparticles would be intact and last over three months in mice, yet did not cause any adverse influence to the animal. In this work, gold nanoparticles have been adopted as a model nanoparticle to probe the interactions between the nanoparticles and the cells. Due to the localized surface plasmon resonance, the gold nanoparticles could be easily tracked through dark-field imaging and colocalized with subcellular organelles through fluorescent imaging. Through tracking and imaging, we found that the functionalized gold nanoparticles were transferred from endosomes to lysosomes and excreted through exocytosis. Also, the cell cycle of the macrophage was arrested at different stages for nanoparticle with different surface modifications. Further investigation has shown that the surface modification of the nanorods could alter the interactions between the nanoparticles and the proteins and lead to different results. The nanoparticles were further labelled with Raman reporters and the interactions between them and the subcellular structures were probed with Raman spectroscopy. These findings would provide some details on the nanoparticle–cell interactions and help us to get a better understanding on this issue.

REFERENCES

[1] Li Q, Huang C, Liu L, Hu R, Qu J. Effect of Surface Coating of Gold Nanoparticles on Cytotoxicity and Cell Cycle Progression. Nanomaterials, 8(12): 1063, (2018).

DOI 10.24412/cl-37136-2023-1-148-149

HIGH THROUGHPUT 3D IMAGING AND ITS APPLICATION IN NEUROSCIENCE

WEI GONG[1], XIAO XIAO[2], JIAJIA CHEN[1] AND KE SI[1,2]

[1]MOE Frontier Science Center for Brain Science & Brain-Machine Integration, NHC and CAMS Key Laboratory of Medical Neurobiology, School of Brain Science and Brain Medicine, Zhejiang University, Hangzhou, China
[2]College of Optical Science and Engineering, State Key Laboratory of Modern Optical Instrumentation, Zhejiang University, Hangzhou, China

weigong@zju.edu.cn

ABSTRACT

High-speed and high-resolution imaging for large volume biological samples is always an aspirational goal of microscopists. The unprecedented developments in optical imaging tools and fluorescence probes have provided numerous visual access to biological structure and function at cellular resolution, such as confocal laser scanning microscopy (CLSM), two photon–excited fluorescence laser-scanning microscopy (2PLSM), light field microscopy (LFM) and so on. Beyond these advanced techniques, however, perfect optical imaging complex larger volume samples also demands fast acquisition, wide field of view (FOV), protection against photobleaching and photoxicity and so on. One of promising approaches is light-sheet fluorescence microscopy (LSFM) combined with the optical clearing methods, which has been proved a powerful choice for large volumetric imaging in recent years.

Here, we provide two fast optical clearing methods for mouse and human brains, respectively. FOCM is a nontoxic ultrafast optical clearing method, which could clarify 300-μm-thick mouse brain slices within 2 min without morphology distortion [1]. The cheap reagents and easy operation make FOCM have great potential in the exploration of neuroscience. On this basis, we developed a multiscale aqueous method of rapid clearing and staining for human brain, which achieving high quality transparency of 1mm-thick human brain tissue within 1 day while maintaining deformation (Fig. 1a). Besides, this method can greatly increase the depth of staining and achieve exploration of the three-dimensional structure of the human brain (Fig. 1b). Overall, our method will provide great assistance to chart the cellular and molecular architecture of human brain and exploring the ultimate territory of humanity. In addition, we have developed imaging systems and image processing algorithms that are suitable for these two transparent methods [2-3], and established a high-throughput 3D imaging platform.

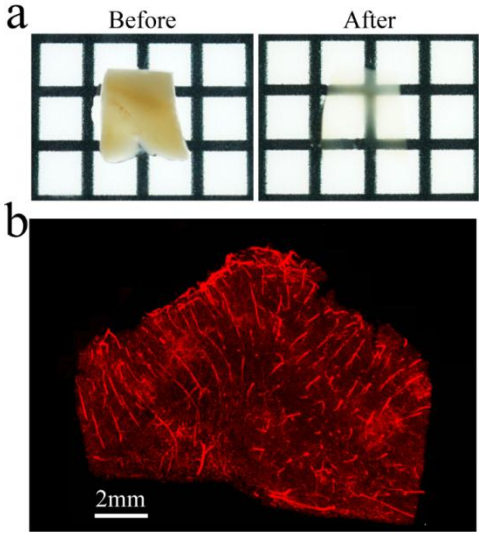

Figure: *(a) Transparency of 1mm-thick human brain cleared by our method. (b) 3D imaging of 1mm-thick human brain with blood vessels labelled.*

REFERENCES

[1] Zhu X, Huang L, Zheng Y, et al. Ultrafast optical clearing method for three-dimensional imaging with cellular resolution. Proc Natl Acad Sci U S A. 2019.

[2] Chen J, Du Z, Xu C, Xiao X, Gong W, Si K. Ultrafast 3D histological imaging based on a minutes-time scale tissue clearing and multidirectional selective plane illumination microscopy. Opt Lett. 2022.

[3] Hu L, Hu S, Gong W, Si K. Image enhancement for fluorescence microscopy based on deep learning with prior knowledge of aberration. Opt Lett. 2021.

DOI 10.24412/cl-37136-2023-1-39-46

RESEARCH ON SYNERGISTIC IMMUNOTHERAPY TRIGGERED BY PHOTOTHERAPY

WEN SONG, FEIFAN ZHOU

School of Biomedical Engineering, Hainan University

songwen@hainanu.edu.cn

ABSTRACT

In recent years, an increasing number of patients with advanced cancer have benefited from immunotherapy (1). However, attributing to the heterogeneity of tumors and the limited efficacy of these therapeutic modalities in eliminating solid tumors, the proportion of benefited cancer patients is less than 15%. Moreover, some modalities of immunotherapy could also cause side effects mainly due to insufficient targeting, which could sometimes be even fatal to patients. Therefore, finding efficient modalities of immunotherapy is of great importance.

Phototherapy, including photodynamic therapy and photothermal therapy, have gained great popularity among researchers (2). In particularly, phototherapy has a very high precision therapeutic effect on tumor regions due to its high spatio-temporal selectivity (3), while the toxic side effects on normal tissues are extremely limited. Therefore, is it possible to develop a synergistic immunotherapy triggered by phototherapy to achieve precise immunotherapy on tumors?

In this presentation, I will give an introduction to our recent works, which are focused on the development of strategies on synergistic immunotherapy triggered by phototherapy for tumor therapy.

In the first part (4), we designed and synthesized an amphiphilic chimeric peptide P-1MT to construct a strategy of immunotherapy triggered by photodynamic therapy. By designing the certain amino acid sequence, we combined 1-methyltryptophan (1-MT), a small molecule inhibitor of IDO pathway, with Asp-Glu-Val-Asp (DEVD), a caspase-responsive peptide sequence. Photodynamic therapy by protoporphyrin (PpIX) could induce tumor cell apoptosis and activate the expression of Caspases-3 to achieve precise release of 1-MT in tumor area, thereby inhibiting the IDO downstream pathway and ultimately achieving eradication of both primary and lung metastasis tumor.

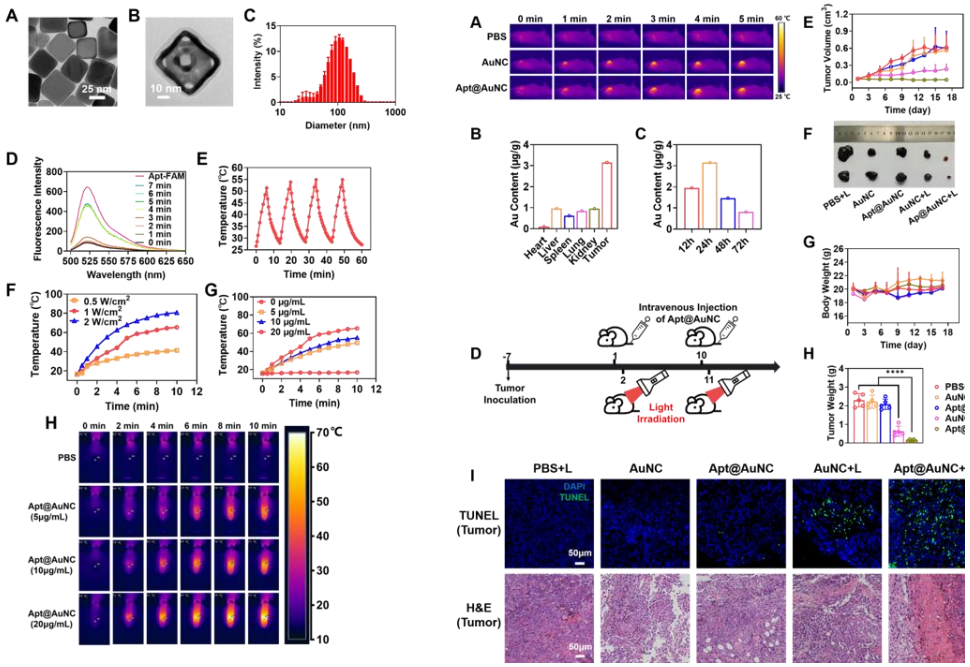

Figure: *Phototherapy-triggered immunotherapy for the application in cancer treatment*

In the second part (5), we designed and developed a photoactivated immunotherapy nanoplatform (Apt@AuNC) to construct a strategy of immunotherapy triggered by photothermal therapy. Gold nanocage (AuNC) was chosen as the photothermal material of the nanoplatform. A single-stranded DNA with a thiol modification at the 5'-terminus, 5'-SH-T-TTT-TTT-TTT-T-GTA-GTG-CAG-GGA-3', was attached to the surface of AuNC through gold-sulfur bonds. The aptamer Apt that could target PD-1 protein, 5'-FAM-GTA-CAG-TTC-CCG-TCC-CTG-CAC-TAC-A-3', is connected to the outermost layer of AuNC through the principle of complementary base pairing. At the same time, the Apt was modified with a fluorescent molecular FAM at the 5'-terminus. The fluorescence of FAM was quenched initially due to the localized surface plasmon resonance (LSPR) of AuNC. When illuminated, the thermal unwinding reaction of DNA double strands was activated via the heat generated by AuNC. Simultaneously, the aptamer Apt was released from the surface of Apt@AuNC and the fluorescence of FAM was recovered. Then, Apt combined with PD-1 protein on the surface of T lymphocytes to activate the immune system in tumor area, while the AuNC continued to kill tumor cells through photothermal effect.

In the third part (6), we constructed a nanoplatform (M@P@HA) to develop a strategy with amplification of the activation of STING pathway via photodynamic therapy to achieve activation of the innate immune system. Under light irradiation, the generated reactive oxygen species (ROS) disrupt the cellular redox homeostasis to lead cytoplasm leakage of damaged mitochondrial dsDNA which is the initiator of STING signal. Simultaneously, the decomposition of hollow mesoporous manganese dioxide could significantly increase the activity of related protein of STING signal to further amplify STING signal of tumor cells. Subsequently, the STING signal of tumor associated macrophages (TAM) is also activated by capturing dsDNA and Mn^{2+} escaped from tumor cells, so as to enhance innate immunity and ultimately strengthen the efficacy of anti-tumor therapy.

In summary, phototherapy-triggered synergistic immunotherapy strategy will provide new ideas for the clinical application for antitumor precision immunotherapy.

REFERENCES

[1] Kalbasi, A.; Ribas, A. Tumour-Intrinsic Resistance to Immune Checkpoint Blockade. Nat. Rev. Immunol. 2020, 20, 25−39.

[2] Xiong, J.; Chu, J. C. H.; Fong, W. P.; Wong, C. T. T.; Ng, D. K. P. Specific Activation of Photosensitizer with Extrinsic Enzyme for Precisive Photodynamic Therapy. J. Am. Chem. Soc. 2022, 144, 10647−10658.

[3] Chen, A.; Yang, F.; Kuang, J.; Xiong, Y.; Mi, B. B.; Zhou, Y.; Hu, J. J.; Song, S. J.; Wan, T.; Wan, Z. Z.; Huang, H. Y.; Li, X. R.; Song, W.; Qiu, W. X. A Versatile Nanoplatform for Broad-Spectrum Immunotherapy by Reversing the Tumor Microenvironment. ACS Appl. Mater. Interfaces 2021, 13, 45335−45345.

[4] Song, W.; Kuang, J.; Li, C. X.; Zhang, M.; Zheng, D.; Zeng, X.; Liu, C.; Zhang, X. Z., Enhanced Immunotherapy Based on Photodynamic Therapy for Both Primary and Lung Metastasis Tumor Eradication. ACS Nano 2018, 12, 1978-1989.

[5] Song, W.; Hu, J.-J.; Song, S.-J.; Xu, Y.; Yang, H.; Yang, F.; Zhou, Y.; Yu, T.; Qiu, W.-X., Aptamer-Gold Nanocage Composite for Photoactivated Immunotherapy. ACS Appl. Mater. Interfaces 2022. 14, 42931-42939.

[6] Song, W.; Song, S. J.; kuang, j.; Yang, H.; Yu, T.; Yang, F.; Wan, T.; Xu, Y.; Wei, S. T.; Li, M. X.; Xiong, Y.; Zhou, Y.; Qiu, W. X.. Activating Innate Immunity by a STING Signal Amplifier for Local and Systemic Immunotherapy. ACS Nano 2022. 16, 15977-15993.

DOI 10.24412/cl-37136-2023-1-153-153

INSTRUMENT DEVELOPMENT AND APPLICATIONS OF LASER SPECTROSCOPY/MASS SPECTROMETRY

YIXIANG DUAN[1], QINGYU LIN[1], WENWEN LI[1] AND ZHONGJUN ZHAO[1]

[1]*School of Mechanical Engineering, Sichuan University, China*
yduan@scu.edu.cn

ABSTRACT

At present, cancer seriously hampering the increasing life expectancy, developing an instant instrument and method has become an urgent objective. We developed a series of analytical instruments and further use them to recognition of tumor cells or early diagnosis of lunger cancer. We further focused on the analysis of tumor cells and tissue with Laser-induced breakdown spectroscopy. LIBS instrument and method can be used as the diagnostic analysis of clinical lung cancer tissues based on label-free imaging. The tumor cell can be also recognized by the corresponding aptamer sequence and can be detected by this SERS method. We proposed a novel PTR-TOF-MS instrument and developed a novel diagnostic method based on the detection of expired gas.

Figure: *Diagnostic lung cancer with the PTR-TOFMS instrument.*

DOI 10.24412/cl-37136-2023-1-154-154

THE SENSITIVE CYTOSENSOR BASED ON FIBER OPTIC LOCAL SURFACE PLASMONIC RESONANCE

ZEWEI LUO*, YIXIANG DUAN*

Research Center of Analytical Instrumentation, School of Mechanical Engineering, Sichuan University, Chengdu, Sichuan, PR China;
*Corresponding authors: zwluo@scu.edu.cn, yudn@scu.edu.cn

ABSTRACT

Fiber-optic-based localized surface plasmon resonance (FO-based LSPR) is a label-free analytical technique for directly analyzing cancer cells. FOs with different geometries have been reported to improve the sensitivity, including U-shaped[1, 2] and Ω-shaped fiber optic[3-5]. The Con A-modified U-shaped fiber optic enables a sensitive cytosensor for breast cancer cells. The limit of detectionof U-shaped fiber optic is 29-fold higher than that of the traditional straight one[2]. Further, an original Ω-shaped FO (Ω-FO) with high refractive index sensitivity was fabricated[3]. It was demonstrated that the enhanced binding area in Ω-FO improves sensitivity for cancer cell detection[4]. Due to the advantages of simple operation, compactness, and ease in fabrication, Ω-FO-based LSPR shows a promising application for cytosensor. Further, the induction of gold nanoparticles into gold nanorods for hybridized nanolayers enhances the electronic field and plasmonic photothermal effect[6]. Therefore, the Ω-FO-based LSPR shows great potential for a new platform for diagnosis and treatment of cancer.

REFERENCES

[1] **Z. Luo**, J. Zhang, Y. Wang, J. Chen, Y. Li, Y. Duan, An aptamer based method for small molecules detection through monitoring salt-induced AuNPs aggregation and surface plasmon resonance (SPR) detection, Sens. Actuat. B-Chem., 474-479, 2016.

[2] **Z. Luo**, Y. Wang, Y. Xu, X. Wang, Z. Huang, J. Chen, Y. Li, Y. Duan, Ultrasensitive U-shaped fiber optic LSPR cytosensing for label-free and in situ evaluation of cell surface N-glycan expression, Sens. Actuat. B-Chem., 582-588, 2019.

[3] Y. Xu, **Z. Luo**, J. Chen, Z. Huang, X. Wang, H. An, Y. Duan, Omega-Shaped Fiber-Optic Probe-Based Localized Surface Plasmon Resonance Biosensor for Real-Time Detection of Salmonella Typhimurium, Analytical Chemistry, Anal. Chem., 13640-13646, 2018.

[4] **Z. Luo**, Y. Cheng, L. He, Y. Feng, Y. Tian, Z. Chen, Y. Feng, Y. Li, W. Xie, W. Huang, J. Meng, Y. Li, F. He, X. Wang, Y. Duan, A T-shaped aptamer-based LSPR biosensor using Ω-shaped fiber optic for rapid detection of SARS-CoV-2, Anal. Chem., 2023, 1599-1607, 2023.

[5] **Z. Luo**, Y. Xu, L. He, F. He, J. Wu, Z. Huang, Y. Tian, Y. Li, Y. Duan, Development of a rapid and ultra-sensitive cytosensor: Ω-shaped fiber optic LSPR integrated with suitable AuNPs coverage, Sens. Actuat. B-Chem., 129706, 2021.

[6] L. He, F. He, L. He, Y. Feng, X. Wang, Y. Li, Y. Tian, A. Gao, P. Zhang, X. Qi, **Z. Luo**, Y. Duan, Hybridized nanolayer modified Ω-shaped fiber-optic synergistically enhances localized surface plasma resonance for ultrasensitive cytosensor and efficient photothermal therapy, Biosens. Bioelectron., 113599, 2021.

DOI 10.24412/cl-37136-2023-1-155-155

PHASE II CLINICAL TRIALS IN PHOTODYNAMIC THERAPY OF PHARYNGOTONSILLITIS

KATE BLANCO[1*], SIGRID SANTOS[2], AND VANDERLEI BAGNATO[1,3]

1 São Carlos Institute of Physics, University of São Paulo, São Carlos, Brazil.
2 Department of Medicine – UFSCar, Brazil
3 Biomedical Engineering, Texas A&M University, College Station, TX - USA.
kateblanco@ifsc.usp.br

ABSTRACT

Acute pharyngotonsillitis (PT) is a common clinical condition found in medical emergency outpatient clinics[1]. It can be broadly categorized as infectious (usually viral or bacterial) and non-infectious diseases. However, the symptoms of viral pharyngitis largely overlap with pharyngitis caused by treatable pathogens such as group A beta-hemolytic Streptococcus (SBHA)[2]. These clinical conditions present symptomatic pictures of serious conditions such as acute HIV infection and highly contagious infections such as coronavirus disease 2019. Although SBHA are always susceptible to penicillin, treatment failure occurs in up to 20% of treated patients[3]. Interruption of antibiotic therapy, the patient's immune status, internalization of SBHA, and penicillin tolerance may be the cause of the standard treatment failures. SBHA recovered from tonsils of patients, even those with tonsillectomy, can produce beta-lactamase that protect SBHA by inactivating penicillin in recurrent infections. Antimicrobial Photodynamic Therapy (aPDT) is a multistage process that includes topical photosensitizer (PS) administration, light irradiation, and interaction of the excited state with ambient oxygen, which has demonstrated antimicrobial activity in vitro and in vivo. The reactive oxygen species produced by photoactivation have non-specific targets of action including proteins, lipids and nucleic acids present in microbial cells. An clinical research was composed by PT treatment using PDT in adults with the objective of evaluating the therapeutic efficacy as a adjuvant. The participants underwent a rapid test for the detection of SBHA. Participants with streptococcal PT were divided into two groups: Group A1 = Antibiotic therapy + PDT; Group A2 = Antibiotic therapy + PDT placebo. Participants with non-streptococcal PT were divided into two groups: Group B1 = PDT; Group B2 = PDT Placebo.It was possible to observe in addition to PDT being safe in the treatment of PF presented a gain in the therapeutic effect with the association with the conventional treatment of acute PT caused by Streptocuccus sp. PDT acting locally to fight the infection caused the death of pathogenic bacteria and may aid in the repopulation of bacteria in the normal flora of the oropharynx that may have helped to fight the infection. The results showed that PDT can be indicated to avoid antibiotic failures in the treatment of PTs, as these cases are increasing by 10% every 10 years in some countries, which underlines the importance of the study. The cases of non-GABHS PT, caused by Fusobacterium necrophorum, Staphylococcus aureus, Group B Beta-hemolytic Streptococcus and virus, showed a reduction in symptoms in PDT referring to the same time of symptomatic treatment. PDT may be a treatment option for these cases, considering that we have observed a reduction in some symptoms characteristic of the infection.

REFERENCES

[1] G. J. Moran, “Diagnosis and management of urinary tract infection in the emergency department and outpatient settings,” Infect. Dis. Clin., vol. 28, no. 1, pp. 33–48, 2014.

[2] T. N. Thai, A. P. Dale, and M. H. Ebell, “Signs and symptoms of group A versus non-group A strep throat: a metaanalysis,” Fam. Pract., vol. 35, no. 3, pp. 231–238, 2018.

[3] I. Brook, “Failure of penicillin to eradicate group A beta-hemolytic streptococci tonsillitis: Causes and management,” J. Otolaryngol., vol. 30, no. 6, 2001, doi: 10.2310/7070.2001.19359

DOI 10.24412/cl-37136-2023-1-156-159

ASSOCIATION OF PHOTOTHERMAL THERAPY WITH OPTICAL CLEARING AGENTS FOR THE TREATMENT OF CUTANEOUS MELANOMA, USING AN INDOCYANINE GREEN NANOEMULTION

LETÍCIA MARTINELLI1 , GABRIEL JASINEVICIUS1 , LILIAN MORIYAMA1 , HILDE BUZZÁ2 , JUAN CHEN3 , GANG ZHENG3 AND CRISTINA KURACHI1

1São Carlos Institute of Physics, University of São Paulo, Brazil 2 Institute of Physics, Pontíficia Universidad Católica de Chile, Chile 3Department of Medical Biophysics, University of Toronto, Canada
cristina@ifsc.usp.br

ABSTRACT

Melanoma is a pigmented tumor that originates from melanin-producing cells called melanocytes. According to the National Cancer Data Base (NCDB-US), approximately 91.2% of melanomas originate in the skin [1]. Its main cause is prolonged exposure to the sun, especially in childhood and adolescence, due to ultraviolet rays (UV) [2]. Even representing only 5% of skin cancers, it is the most aggressive and invasive type, due to its high possibility of causing metastasis, being responsible for the highest rate of deaths from skin cancer, with approximately 80% to 85% [3]. First-line diagnostic procedures include clinical analysis of the lesions, mainly their ABCDEs macroscopic characteristics, which are evaluated in terms of asymmetry, borders, diameter, color and evolving [4]. Dermoscopy is also performed, which is a noninvasive means of evaluating suspicious lesions using magnification and light to visualize structures in the epidermis and superficial dermis that are not visible in routine exams with the naked eye [5]. When malignancy is suspected, an excisional biopsy is performed, where the melanoma is confirmed by histopathological examination. In the initial stages, the most used treatment today is surgery [6,7]. In more advanced cases, palliative treatments such as radio, chemo and immunotherapy are used. The difficulty in finding an effective treatment is mainly due to the presence of melanin: a highly absorbing and light-scattering agent, in addition to having an antioxidant and photoprotective action [8–10]. Knowing the limitations of melanoma treatment, new therapies such as photothermal therapy have been studied. It needs a molecule that is sensitive to light (photosensitizer) and to light in the NIR region (700–2000nm). By absorbing the energy from light, the photosensitizer goes to an excited state of higher energy level and undergoes a process called vibrational relaxation, where it returns to its fundamental state of energy, releasing heat [11,12]. This increase in temperature causes protein aggregation and denaturation, cytosol evaporation and cell lysis, leading to cell and tissue death. In biological systems, the range of 42 to 60ºC is known as hyperthermia, and this is where conformational changes occur in molecules, accompanied by destruction of bonds and membrane changes and cell immobility. At 60ºC, protein and collagen denaturation occurs, which leads to tissue coagulation and cell necrosis [13]. The photosensitizers with the best response to photothermal therapy are nanomolecules with strong absorbance in the infrared region [14]. Indocyanine green, used as a fluorescence imaging probe, is an FDA-approved photothermal agent with low dark toxicity and rapid clearance by the liver [15,16]. Because it has these characteristics, it has been studied encapsulated in nanoparticles or associated with drugs [17,18], for example. However, no study showed melanoma eradication in vivo. Therefore, we have been investigating the use of an ICG nanoemulsion (NanoICG) developed by Prof. Gang Zheng (University Health Network, Toronto, Canada), differing from other photothermal nanoparticles, since the ICG is not located inside the nanoparticle, but outside, and its interior is composed of glycerol trioctanoate (Figure 1). Its physical-chemical characterization demonstrated the stable formation of dimers and, therefore, greater applicability for photothermal and photoacoustic applications.

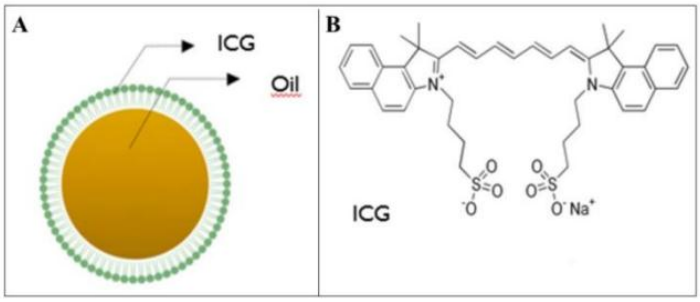

Figure 1: *(A) Estructure of NanoICG; (B) Molecule ICG.*

The animals used are immunosuppressants, balbC/nude and B16F10 melanoma cells injected intradermally. Treatment was performed when the tumor reached 3mm in thickness. Two concentrations of NanoICG (100 and 200μM) and two irradiances (1 and 0.5W/cm2) were tested in an in vivo model for intratumoral administration. The nanoemulsions were also administered intraperitoneally and its kinetics and treatment responses were measured by intradermal needle and thermographic camera. This group received 9.6 mg/kg of NanoICG and were irradiated with 0.5 W/cm2 for 10 minutes. So far, the group that presented the best results was with 200 μM of NanoICG intratumorally. The control group had a temperature increase of 12ºC, which is expected since melanin is a highly light absorbing component and the treatment one of 33ºC. With the thermographic camera, it was possible to visualize a localized temperature increase, meaning that the molecule did not spread to other tissues (Figure 2).

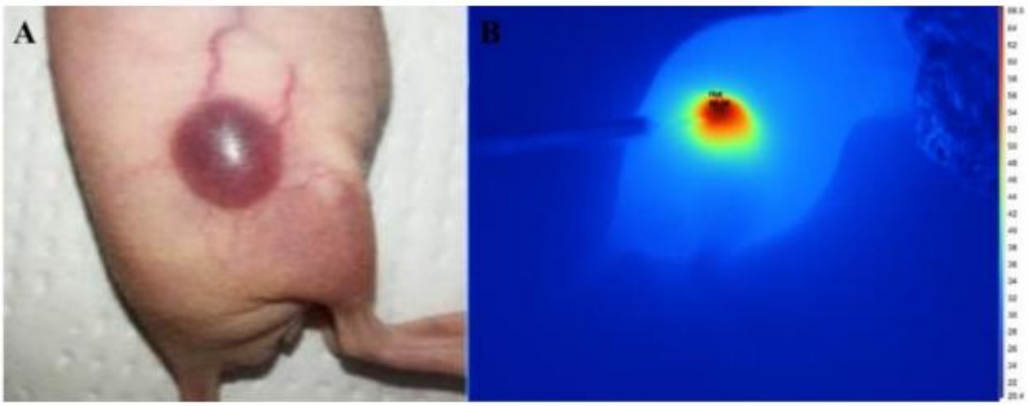

Figure 2: *(A) Cinical image of melanoma; (B) Thermographic image while the tumor was being irradiated.*

The Kepler-Meier curve was performed for the best experimental group, where within 25 days there was no tumor regrowth (Figure 3-A). Qualitatively, the tumors right after irradiation showed a whitish aspect due to the damage caused by the treatment and there was growth of a scab, showing a therapy-induced tumor necrosis (Figure 3-C). On the fourteenth day of treatment, there was skin regeneration in 67% of the animals and the absence of melanoma cells Immunohistochemical analyzes are being carried out to confirm with certainty that there were no remnants of tumor cells, and studies are also being carried out to determine whether there was any type of metastasis. Intravenous administration will also be performed and finally associate photothermal therapy with optical clearing agents (OCAs).

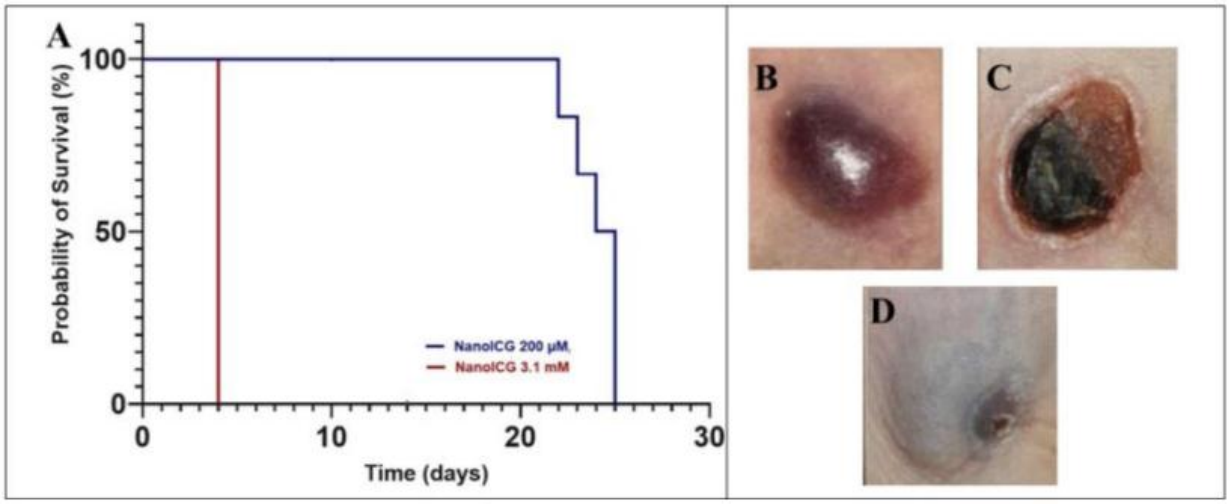

Figure 3: *(A) Kepler-Meier curve for intratumoral administration of 200 µM and systemic administration of 3.1mM; (B) Cinical image of melanoma before treatment; (C) Melanoma 3 days after treatment; (D) Melanoma after 14 days of treatment with regrowth.*

OCAs are non-toxic hyperosmic compounds with a refractive index ~ 1.4. They promote local osmotic dehydration, and tissue refractive index matching, reducing light scattering and improving the light penetration into the tumor [19–22]. Our group has previously demonstrated its potential to enhance light-based therapies in cutaneous pigmented melanoma, enabling the eradication of lesions with up to 1mm in thickness, using photodynamic therapy [23,24]. When the treatment is associated with clearings, it has already been verified that the light reaches deeper into the melanoma, making it more optically homogeneous [25]. Therefore, associating photothermia with OCAs leads us to believe that the response to treatment will be even more effective and the best protocol tested so far.

REFERENCES

[1] Chang AE, Karnell LH, Menck HR. The National Cancer Data Base Report on Cutaneous and Noncutaneous Melanoma. Cancer. 1998;83(8):1664–78.
[2] Gandini S, Sera F, Cattaruzza MS, Pasquini P, Zanetti R, Masini C, et al. Meta-analysis of risk factors for cutaneous melanoma: III. Family history, actinic damage and phenotypic factors. Eur J Cancer. 2005 Sep;41(14):2040–59.
[3] Aladowicz E, Ferro L, Vitali GC, Venditti E, Fornasari L, Lanfrancone L. Molecular networks in melanoma invasion and metastasis. Vol. 9, Future Oncology. 2013. p. 713–26.
[4] Tsao H, Olazagasti JM, Cordoro KM, Brewer JD, Taylor SC, Bordeaux JS, et al. Early detection of melanoma: Reviewing the ABCDEs American Academy of Dermatology Ad Hoc Task Force for the ABCDEs of Melanoma. J Am Acad Dermatol. 2015 Apr 1;72(4):717–23.
[5] Zager JS, Sondak VK, Kudchadkar R. Melanoma. 2016.
[6] Zalaudek I, Ferrara G, Argenziano G, Ruocco V, Soyer HP. Diagnosis and treatment of cutaneous melanoma: a practical guide. Vol. 2, Skinmed. 2003.
[7] Eggermont AMM, Spatz A, Robert C. Cutaneous melanoma. In: The Lancet. Lancet Publishing Group; 2014. p. 816–27.
[8] Mroz P, Huang YY, Szokalska A, Zhiyentayev T, Janjua S, Nifli AP, et al. Stable synthetic bacteriochlorins overcome the resistance of melanoma to photodynamic therapy. FASEB J. 2010 Sep;24(9):3160–70.
[9] Huang Y-Y, Vecchio D, Avci P, Yin R, Garcia-Diaz M, Hamblin MR. Melanoma resistance to photodynamic therapy: new insights. Biol Chem [Internet]. 2013 Feb 1;394(2):239–50. Available from: http://www.degruyter.com/view/j/bchm.2013.394.issue-2/hsz-2012-0228/hsz-2012-0228.xml
[10] Wang Z, Dillon J, Gaillard ER. Antioxidant Properties of Melanin in Retinal Pigment Epithelial Cells. Photochem Photobiol. 2006;82(2):474.
[11] Cortezon-Tamarit F, Ge H, Mirabello V, Theobald MBM, Calatayud DG, Pascu SI. Carbon Nanotubes and Related Nanohybrids Incorporating Inorganic Transition Metal Compounds and Radioactive Species as Synthetic Scaffolds for Nanomedicine Design. In: Inorganic and Organometallic Transition Metal Complexes with Biological Molecules and Living Cells. Elsevier Inc.; 2017. p. 245–327.

[12] Eskiizmir G, Baskın Y, Yapıcı K. Graphene-based nanomaterials in cancer treatment and diagnosis. In: Fullerens, Graphenes and Nanotubes [Internet]. Elsevier; 2018. p. 331–74. Available from: https://linkinghub.elsevier.com/retrieve/pii/B9780128136911000099
[13] Niemz MH. Laser-Tissue Interactions [Internet]. Third. Elias Greenbaum, editor. Berlin, Heidelberg: Springer Berlin Heidelberg; 2002. Available from: http://link.springer.com/10.1007/978-3-662-04717-0
[14] Doughty ACV, Hoover AR, Layton E, Murray CK, Howard EW, Chen WR. Nanomaterial applications in photothermal therapy for cancer. Materials (Basel). 2019;12(5).
[15] Shirata C, Kaneko J, Inagaki Y, Kokudo T, Sato M, Kiritani S, et al. Near-infrared photothermal/photodynamic therapy with indocyanine green induces apoptosis of hepatocellular carcinoma cells through oxidative stress. Sci Rep. 2017 Dec 1;7(1).
[16] Boni L, David G, Mangano A, Dionigi G, Rausei S, Spampatti S, et al. Clinical applications of indocyanine green (ICG) enhanced fluorescence in laparoscopic surgery. Surg Endosc. 2015 Jul 19;29(7):2046–55.
[17] Hwang J, Jin J-O. Attachable Hydrogel Containing Indocyanine Green for Selective Photothermal Therapy against Melanoma. Biomolecules [Internet]. 2020 Jul 29;10(8):1124. Available from: https://www.mdpi.com/2218-273X/10/8/1124
[18] Ledezma DK, Balakrishnan PB, Cano-Mejia J, Sweeney EE, Hadley M, Bollard CM, et al. Indocyanine Green-Nexturastat A-PLGA Nanoparticles Combine Photothermal and Epigenetic Therapy for Melanoma. Nanomaterials [Internet]. 2020 Jan 17;10(1):161. Available from: https://www.mdpi.com/2079-4991/10/1/161
[19] Millon SR, Roldan-Perez KM, Riching KM, Palmer GM, Ramanujam N. Effect of optical clearing agents on the in vivo optical properties of squamous epithelial tissue. Lasers Surg Med. 2006 Dec;38(10):920–7.
[20] Zhu D, Larin K V., Luo Q, Tuchin V V. Recent progress in tissue optical clearing. Laser Photonics Rev. 2013 Sep;7(5):732–57.
[21] Sdobnov AY, Darvin ME, Genina EA, Bashkatov AN, Lademann J, Tuchin V V. Recent progress in tissue optical clearing for spectroscopic application. Spectrochim Acta - Part A Mol Biomol Spectrosc. 2018 May 15;197:216–29.
[22] Sdobnov AY, Darvin ME, Schleusener J, Lademann J, Tuchin V V. Hydrogen bound water profiles in the skin influenced by optical clearing molecular agents—Quantitative analysis using confocal Raman microscopy. J Biophotonics [Internet]. 2019 May 4;12(5). Available from: https://onlinelibrary.wiley.com/doi/abs/10.1002/jbio.201800283
[23] Pires L, Demidov V, Vitkin IA, Bagnato V, Kurachi C, Wilson BC. Optical clearing of melanoma in vivo: characterization by diffuse reflectance spectroscopy and optical coherence tomography "Optical clearing of melanoma in vivo: characterization by diffuse reflectance spectroscopy and optical coherence tomography Optical clearing of melanoma in vivo: characterization by diffuse reflectance spectroscopy and optical coherence tomography. J Biomed Opt [Internet]. 2016;21(8):81210. Available from: https://www.spiedigitallibrary.org/terms-of-use
[24] Pires L, Demidov V, Wilson BC, Salvio AG, Moriyama L, Bagnato VS, et al. Dual-agent photodynamic therapy with optical clearing eradicates pigmented melanoma in preclinical tumor models. Cancers (Basel). 2020 Jul 1;12(7):1–17.
[25] Martinelli LP, Iermak I, Moriyama LT, Requena MB, Pires L, Kurachi C. Optical clearing agent increases effectiveness of photodynamic therapy in a mouse model of cutaneous melanoma: an analysis by Raman microspectroscopy. Biomed Opt Express [Internet]. 2020 Nov 1;11(11):6516. Available from: https://www.osapublishing.org/abstract.cfm?URI=boe-11-11-6516

DOI 10.24412/cl-37136-2023-1-160-165

ANTIMICROBIAL PHOTODYNAMIC THERAPY IN THE TREATMENT OF ORAL CANDIDIASIS

EWERTON MIMA[1] AND ANA PAVARINA[2]

1Department of Dental Materials and Prosthodontics, School of Dentistry, Araraquara, São Paulo State University (Unesp), Brazil ewerton.mima@unesp.br

ABSTRACT

The ageing of the global population is one of the most important medical and social demographic problem worldwide. According to World Health Organization, in 2020 there was 1 billion people aged 60 years and over and this population will double by 2050 [1]. In Brazil, elderly population corresponds to 14.7% in 2021 and they increased 39.8% in the last nine years [2]. In this scenario, illness and the well-being of elderly population became a global public health challenge. Especially in this population, edentulism (or teeth lost) is a healthcare problem associated with education and income status [3], leading to masticatory dificulties, speech alteration, impairment of systemic health, self-steem, and social life (4). Although the complete edentulism has decreased, partial edentualism has increased [5] and dental prostheses are required to restore the functions of the oral cavity. In addition to edentulism, elders may suffer from chronic diseases and debilitating conditions, such as Alzheimer, Parkinson, cancer, immunosuppression, etc., which affect their ability to selfcare, including oral hygiene [6]. Thus, elderly people may be more prone to oral diseases, such as caries, periodontal diseases, and also oppotunistic infections caused by fungi. Oral candidiasis is the most common oral fungal infection caused by species of Candida and associated with systemic and local predisposing factors, such as diabetes, antibiotic therapy, reduced salivary flow (xerostomia), poor hygiene, and, especially, immunosuppresion [7]. As opportunistic infections, yeasts thrive when the host's immune defences are debilitated. Among the manifestations of oral candidiasis, denture stomatitis is a chronic infection of oral mucosa beneath the denture characterized by mucosa inflammation ranging from to red dots to hyperplasia, usually without symptons, and with high prevalence in women [8]. An in vivo study with rats demonstrated that dentures with Candida albicans induce a shift in the oral microbiome from aerobic, health-associated species to anaerobic, inflammatory species [46]. Oral candidiasis may spread to oropharynge, causing oropharingeal candidiasis [9], and in immunosupprised patients the infection may reach the blood stream and cause candidemia, which have high mortality rates and it is a relevant nosocomial infection [10]. The genus Candida encompasses more than 150 species, but only a few are responsible by infections: C. albicans, C. glabrata, C. tropicalis, C. krusei, C. parapsilosis, C. guilliermondii, C. dubliniensis, and C. lusitaneae [11]. C. albicans is the most prevalent and virulent species found as commensal in the human body, such as skin, oral and genital mucosae. Among the virulence factors shown by C. albicans, polymorphism is the most striking feature and corresponds to the ability of reversebly changing its round shape cell morphology of yeast to elongated filamentous form of hyphae (parallel sides without consticton) and pseudo-hyphae (eliptical cells with constrictions) (Figure 1) [12]. The filamentous form is pathogenic, able to invade the host's epithelium and promote infection [13]. Other species, despite less virulent, are isolated from infections alone or with C. albicans, they show intrinsic resistance to antifungal agents, such as C. glabrata and C. krusei [14], and C. tropicalis is the most virulent non-albicans species commonly verified in Latin America and Asia [15]. The treatment of ora candidiasis involves the use of antifungal agents, which may be topical or systemic. Different from the wide range of antibiotics, there are only three classes of antifungal agents available commercially: polyenes, azoles, and echinocandins [16]. Different from bacteria, fungal cells are eukariotic cells, similar to mammalian cells, and hence they share similar features, which hinder the development of antifungal agents against specific fungal targets without cytotoxicity to the host. Polyenes (nystatin and amphotericin B) were the first antifungal agents discovered in 1949 and clinically used [16,17], they bind to the ergosterol and disrupt the fungal cell membrane. Therefore, they are fungicides, but nystatin is only topical and amphotericin B, despite systemic, has nefrotoxic side effect. In the

1960s, the first azoles (imidazoles) were introduced in the market, such as ketoconazole, miconazole, clotrimazole; they inhibit an enzyme responsible for the synthesis of ergosterol, thus they are fungistatic and, most of them, topical [16,18]. In the 1980s, in parallel to the HIV pandemic and other immunosuppression conditions caused by the development of medicine, such as organ transplantations, opportunistic fungal infections rose and the triazole drugs (fluconazole, itraconazole, voriconazole) emerged and revolutionized the antifungal treatments of systemic fungemia due to their efficacy and safety [16,19]. However, the widespread and the miuse of azoles brought up the problem of antifungal resistance, which is currently a big challenge of public health and involves all classes of antifungal drugs [20]. In 2020s, a new class of antifungal drugs, echinocandins (caspofungin, micafungin, and anidulafungin), was introduced in the market, they inhibit the β-glucan of the fungal cell wall, they are fungicide against some specias and fungistatic against other yeasts and they are systemic only administered by intravenous route [16,21]. Although these antifungal agents have demonstrated efficacy against superficial and systemic fungal infections, some species has developed resistance against one or more classes of antifungal agents and new species has emerged with multidrug resistance, such as Candida auris [22]. Therefore, this current scenario has imposed the search of new therapeutic modalities. Antimicrobial Photodynamic Therapy (aPDT) has been empolyed as an alternative or adjuvant method against Candida spp. and candidiasis in in vitro and in vivo studies, including animal models and clinical trials [23-26]. Several photosensitizers (PS) have been used, from first to third generation, such as porphyrins, clorins, phthalocyanines, curcumin, etc. But studies have shown that planktonic (free-floating cells) are more susceptible to aPDT than biofilms [23,24], which are complex communities of microrganisms attached on a biotic or abiotic surface and encased in a selfproduced polymeric matrix [27]. The matrix acts as a barrier that protect microbial cells against external antimicrobial agents and the host's immunity cells. Therefore, cells in biofilms are tolerant to antimicrobial approaches and infections caused by them are difficult to treat. This is the reason why several studies have been shown that, although planktonic cultures have been suscessfully inactivated by aPDT, biofilms have shown only reduction in their viability. When Photodithazine (PDZ) was used as a PS in aPDT against strains of C. albicans, C. glabrata, and C. tropicalis, their planktonic cultures showed complete inactivation or reduction raging from 4 to 5 log10, while their biofilm cultures have their viability reduced by 60% to 70% [28]. However, clinical infections, including oral diseases, are not caused by monospecies biofilms, but instead they are characterized by multispecies biofilms, where the pathogens share a consortium of mutual benefits. When a multispecies biofilm formed by C. albicans, C. glabrata, and Streptococcus mutans (the main bacterium involved in dental caries) was submitted to PDZ-mediated aPDT, significant reduction in their viability was observed, but the biofilm biomass was not reduced, suggesting that aPDT inactivated the microbial cells, but was not effective in disrupting the biofilm structure [29]. Therefore, an effective therapy may require several applications of aPDT instead of a single one. Using the same multispecies biofilm, three applications of PDZ-mediated aPDT resulted in higher inactivation than a single application, reducing the biofilm viability and also its total biomass [30]. aPDT mediated by PDZ was also used in vivo for the treatment of oral candidiasis in mice. It reduced the fungal load on the tongue of mice without harm the tissue [31] and demonstrated similar results to nystatin [25]. Similar efficacy was observed in vivo against fluconazole-resistant strains of C. albicans [32]. The biofilm maturation also influences its susceptibility to photoinactivation. Thus, the multispecies biofilm grown at 24 and 48 hours was submitted to aPDT mediated by curcumin (CUR), and 24-h biofilm showed higher reduction of viability and total biomass than 48-h biofilm [33]. aPDT mediated by CUR also inhibited biofilms of C. dubliniensis [34], a species genetically similar to C. albicans discovered in oral candidiasis of a HIV patient. CUR is an interesting PS because it is a natural compound with several therapeutic properties, such as antioxidant, anti-inflammatory, anticancer, and antimicrobial activities. However, CUR is not soluble in water (lipophilic) and unstable in solution, requiring toxic solvents, which hinder using CUR in vivo. Therefore, drug delivery systems have been employed to carry and solubilize CUR [35]. When CUR was encapsulated in polymeric nanoparticles and used as a PS against single and multispecies biofilms of C. albicans, S. mutans and methicillin-resistant Staphylococcus aureus (MRSA), the nanoparticles showed suitable chemico-physical properties and photoinactivation. Although cationic (positive charge) nanoparticles were more effective than anonic (negative charge) ones on biofilm photoinactivation, cationic nanoparticles were cytotoxic [36]. These nanoparticles were also used as PS in vivo in a murine model of oral candidiasis and significant

reduction of C. albicans from the tonghe of mice was verified without toxic effect on tissue, although the application of nystatin resulted in higher fungal inactivation [37]. However, in these studies the efficacy of CUR-loaded nanoparticles was lower than free CUR, which could be attributed to slow release of CUR from nanoparticles, which may be a shortcoming for topical use. Therefore, recently a smart nanosystem, a photoresponsive micelle was developed to load CUR and to be used as PS in aPDT. The photo-responsive micelle showed nano features similar to convencional micelles, improved the CUR release, and demonstrated photoinactivation of biofilms of C. albicans, MRSA, and Pseudomonas aeruginosa similar to CUR loaded in conventional micelles [38]. When nanotechnology is employed against microbial cells and biofilms, ideally the nanosystem should be cationic, i.e., it should have positive superficial charge. The superficial charge of microbial cell wall and of biofilm matrix is negative (anionic) due to their composition of polyssaccharide and also extracellular DNA in the matrix. Thus, the attraction between the different charges improves the antimicrobial activity [39]. Another PS, a phthalocyanine loaded in cationic nanoemulsion, demonstrated photoinactivation of a multispecies biofilm of C. albicans, C. glabrata, and S. mutans, although the total biomass was not reduced [40]. When used in vivo, aPDT mediated by phthalocyanine in cationic nanoemulsion also reduced the viability of C. albicans recovered from oral candidiasis in mice without adverse effect on the tongue's tissue [41] and reduced the virulence factors of adhesion and biofilm formation of C. albicans [42]. Other strategies have been also used to improve the photoinactivation of biofilms. The combination of aPDT with nystatin in a in vivo model of oral candidiasis resulted in reduction of C. albicans resistant to fluconazole and remission of the lesions on the mice's tongue [43]. The association of aPDT with Sonodynamic Therapy (SDT) demonstrated increased efficacy against biofilms of C. albicans compared with each therapy used alone, reducing both the fungal viability and the biofilm biomass [44]. Some drugs are able to reverse antimicrobial resistance by inhibiting the efflux pumps, which are transporters on microbial membrane that carry antimicrobial agents out of the cell. CUR acted as a efflux pump inhibitor of C. albicans, increasing its susceptibility to fluconazole and showing synergism with this antifungal agent. Although CUR-mediated aPDT reduced the viability fluconazole-resistant C. albicans in vitro, in vivo model using systemic infection of the larvae Galleria mellonella demonstrated that aPDT mediated by CUR did not increase the larvae survival neither reduced the recovery of C. albicans from larvae. Moreover, verapamil, a calcium blocker, was more effective as efflux pump inhibitor, incresing the survival of larvae infected with C. albicans resistant to fluconazole [45]. A clinical trial demonstrated that aPDT mediated by PDZ was effective as nystatin in the treatment of denture stomatitis, despite recurrent of lesions after both treatments [26]. All these studies have demonstrated that biofilms are still a challenge to be combated, despite all the technologies and recent advanced of aPDT. The combination of therapies aimed to target the biofilm matrix and also (but not only) the microbial cells demands further investigations.

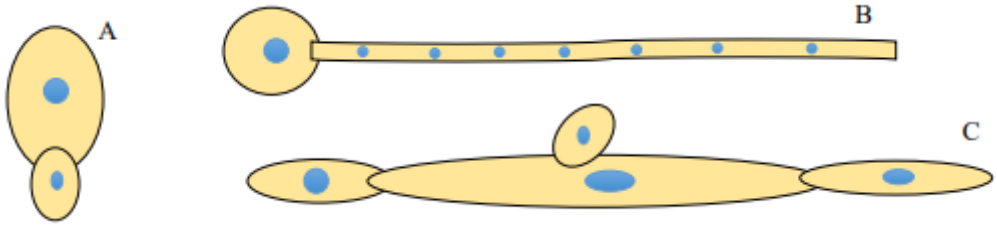

Figure 1: *Morphological forms of Candida albicans: yeast (A), hyphae (B), and pseudo-hyphae (C)*

REFERENCES

[1]ttps://www.who.int/news-room/fact-sheets/detail/ageing andhealth#:~:text=At%20this%20time%20the%20share,2050%20to%20reach%20426%20million (accessed on May 5, 2023).

[2] https://agenciabrasil.ebc.com.br/geral/noticia/2022-07/contingente-de-idosos-residentes-no-brasil-aumenta-398-em-9-anos#:~:text=Um%20novo%20levantamento%20realizado%20pela,31%2C23%20milh%C3%B5es%20de%20pessoas (accessed on May 5, 2023).

[3] M.A. Al-Rafee, The epidemiology of edentulism and the associated factors: A literature Review, J Family Med Prim Care. 30;9(4):1841-1843. 2020. doi: 10.4103/jfmpc.jfmpc_1181_19.
[4] E. Emami, R.F. de Souza, M. Kabawat, J.S. Feine, The impact of edentulism on oral and general health, Int J Dent. 2013:498305, 2013. doi: 10.1155/2013/498305.
[5] F. Memon, D. R. Khatri, D. Mirza, S. Memon, Prevalence Of Partial Edentulism, Complete Edentulism And Single Complete Opposing Partial Edentulism In Relation To The Age Groups And Gender In The Local Population Of Hyderabad,Journal of Bahria University Medical and Dental College, 8(1), 26–30, 2018. https://doi.org/10.51985/JBUMDC2018007
[6] T.F. Wang, C.M. Huang, C. Chou, S. Yu, Effect of oral health education programs for caregivers on oral hygiene of the elderly: A systemic review and meta-analysis, Int J Nurs Stud. 52(6):1090-6, 2015. doi: 10.1016/j.ijnurstu.2015.01.015.
[7] T. Vila, A.S. Sultan, D. Montelongo-Jauregui, M.A. Jabra-Rizk, Oral Candidiasis: A Disease of Opportunity, J Fungi (Basel). 2020 Jan 16;6(1):15. doi: 10.3390/jof6010015.
[8] L. Gendreau, Z.G.Loewy, Epidemiology and etiology of denture stomatitis, J Prosthodont. 20(4):251-60, 2011. doi: 10.1111/j.1532-849X.2011.00698.x.
[9] M. Swidergall, S.G. Filler, Oropharyngeal Candidiasis: Fungal Invasion and Epithelial Cell Responses, PLoS Pathog. 12;13(1):e1006056, 2017. doi: 10.1371/journal.ppat.1006056.
[10] J. Guinea, Global trends in the distribution of Candida species causing candidemia, Clin Microbiol Infect. 20 Suppl 6:5-10, 2014. doi: 10.1111/1469-0691.12539.
[11] S.R. Sá, A.G. Silva Junior, R.G. Lima-Neto, C.A.S. Andrade, M.D.L. Oliveira, Lectin-based impedimetric biosensor for differentiation of pathogenic candida species, Talanta. 1;220:121375, 2020. doi: 10.1016/j.talanta.2020.121375.
[12] P.E.Sudbery, Growth of Candida albicans hyphae, Nat Rev Microbiol. 16;9(10):737-48, 2011. doi: 10.1038/nrmicro2636.
[13] Moyes DL, Richardson JP, Naglik JR. Candida albicans-epithelial interactions and pathogenicity mechanisms: scratching the surface. Virulence. 2015;6(4):338-46. doi: 10.1080/21505594.2015.1012981.
[14] M.C. Arendrup, T.F. Patterson, Multidrug-Resistant Candida: Epidemiology, Molecular Mechanisms, and Treatment, J Infect Dis. 15;216(suppl_3):S445-S451, 2017. doi: 10.1093/infdis/jix131.
[15] D.L. Zuza-Alves, W.P. Silva-Rocha, G.M. Chaves, An Update on Candida tropicalis Based on Basic and Clinical Approaches, Front Microbiol. 13;8:1927, 2017. doi: 10.3389/fmicb.2017.01927.
[16] C.E. Vergani, P.V. Sanita, E.G. Mima, A.C. Pavarina, A.L. Machado, Oral candidiasis: Conventional and alternative treatment options. In: F. Contreras, P. Fuentes. Candidiasis. Nova Science Publishers Inc, 2013
[17] H. Carolus, S. Pierson, K. Lagrou, P. Van Dijck, Amphotericin B and Other Polyenes-Discovery, Clinical Use, Mode of Action and Drug Resistance, J Fungi (Basel). 27;6(4):321, 2020 Nov. doi: 10.3390/jof6040321.
[18] A.C. Souza, A.C. Amaral, Antifungal Therapy for Systemic Mycosis and the Nanobiotechnology Era: Improving Efficacy, Biodistribution and Toxicity, Front Microbiol. 7;8:336, 2017. doi: 10.3389/fmicb.2017.00336.
[19] H.Z. Zhang, L.L. Gan, H. Wang, C.H. Zhou, New Progress in Azole Compounds as Antimicrobial Agents, Mini Rev Med Chem. 17(2):122-166, 2017. doi: 10.2174/1389557516666160630120725.
[20] D.S. Perlin, R. Rautemaa-Richardson, A. Alastruey-Izquierdo, The global problem of antifungal resistance: prevalence, mechanisms, and management, Lancet Infect Dis. 17(12):e383-e392, 2017. doi: 10.1016/S1473-3099(17)30316-X.
[21] N.D. Grover, Echinocandins: A ray of hope in antifungal drug therapy, Indian J Pharmacol. 42(1):9-11, 2010. doi: 10.4103/0253-7613.62396.
[22] K. Saris, J.F. Meis, A. Voss, Candida auris, Curr Opin Infect Dis. 31(4):334-340, 2018. doi: 10.1097/QCO.0000000000000469.
[23] L.N. Dovigo, A.C. Pavarina, A.P. Ribeiro, I.L. Brunetti, C.A. Costa, D.P. Jacomassi, V.S. Bagnato, C. Kurachi,
Investigation of the photodynamic effects of curcumin against Candida albicans, Photochem Photobiol. 87(4):895-903, 2011. doi: 10.1111/j.1751-1097.2011.00937.x.
[24] L.N. Dovigo, A.C. Pavarina, J.C. Carmello, A.L. Machado, I.L. Brunetti, V.S. Bagnato, Susceptibility of clinical isolates of Candida to photodynamic effects of curcumin, Lasers Surg Med. 43(9):927-34, 2011. doi: 10.1002/lsm.21110.
[25] J.C. Carmello, F. Alves, F.G. Basso, C.A. de Souza Costa, V.S. Bagnato, E.G. Mima EG, A.C. Pavarina, Treatment of Oral Candidiasis Using Photodithazine®- Mediated Photodynamic Therapy In Vivo, PLoS One. 2;11(6):e0156947, 2016. doi: 10.1371/journal.pone.0156947.

[26] F. Alves, J.C. Carmello, G.C. Alonso, E.G.O. Mima, V.S. Bagnato, A.C. Pavarina, A randomized clinical trial evaluating Photodithazine-mediated Antimicrobial Photodynamic Therapy as a treatment for Denture stomatitis, Photodiagnosis Photodyn Ther. 32:102041, 2020. doi: 10.1016/j.pdpdt.2020.102041.
[27] J.S. Finkel, A.P. Mitchell, Genetic control of Candida albicans biofilm development, Nat Rev Microbiol. 9(2):109-18, 2011. doi: 10.1038/nrmicro2475.
[28] L.N. Dovigo, J.C. Carmello, M.T. Carvalho, E.G. Mima, C.E. Vergani, V.S. Bagnato, A.C. Pavarina, Photodynamic inactivation of clinical isolates of Candida using Photodithazine®, Biofouling. 29(9):1057-67, 2013. doi:
10.1080/08927014.2013.827668.
[29] C.C. Quishida, J.C. Carmello, E.G. Mima, V.S. Bagnato, A.L. Machado, A.C. Pavarina AC, Susceptibility of multispecies biofilm to photodynamic therapy using Photodithazine®, Lasers Med Sci. 30(2):685-94, 2015. doi: 10.1007/s10103-013-1397-z.
[30] C.C. Quishida, E.G. Mima, L.N. Dovigo, J.H. Jorge, V.S. Bagnato, A.C. Pavarina, Photodynamic inactivation of a multispecies biofilm using Photodithazine(®) and LED light after one and three successive applications, Lasers Med Sci. 30(9):2303-12, 2015. doi: 10.1007/s10103-015-1811-9.
[31] J.C. Carmello, L.N. Dovigo, E.G. Mima, J.H. Jorge, C.A. de Souza Costa, V.S. Bagnato, A.C. Pavarina, In vivo evaluation of photodynamic inactivation using Photodithazine® against Candida albicans, Photochem Photobiol Sci. 14(7):1319-28, 2015. doi: 10.1039/c4pp00368c. Erratum in: Photochem Photobiol Sci. 9;16(8):1336-1337, 2017.
[32] F. Alves, J.C. Carmello, E.G.O. Mima, C.A.S. Costa, V.S. Bagnato, A.C. Pavarina, Photodithazine-mediated antimicrobial photodynamic therapy against fluconazole-resistant Candida albicans in vivo, Med Mycol. 18, 2018. doi: 10.1093/mmy/myy083.
[33] C.C. Quishida, E.G. De Oliveira Mima, J.H. Jorge, C.E. Vergani, V.S. Bagnato, A.C. Pavarina, Photodynamic inactivation of a multispecies biofilm using curcumin and LED light, Lasers Med Sci. 31(5):997-1009, 2016. doi: 10.1007/s10103-016-1942-7.
[34] P.V. Sanitá, A.C. Pavarina, L.N. Dovigo, A.P.D. Ribeiro, M.C. Andrade, E.G.O. Mima, Curcumin-mediated anti-microbial photodynamic therapy against Candida dubliniensis biofilms, Lasers Med Sci. 33(4):709-717, 2018. doi: 10.1007/s10103-017-2382-8.
[35] J.K. Trigo-Gutierrez, Y. Vega-Chacón, A.B. Soares, E.G.O. Mima, Antimicrobial Activity of Curcumin in Nanoformulations: A Comprehensive Review, Int J Mol Sci. 22(13):7130, 2021. doi: 10.3390/ijms22137130.
[36] J.K. Trigo Gutierrez, G.C. Zanatta, A.L.M. Ortega, M.I.C. Balastegui, P.V. Sanitá, A.C. Pavarina, P.A. Barbugli, E.G.O. Mima, Encapsulation of curcumin in polymeric nanoparticles for antimicrobial Photodynamic Therapy, PLoS One. 12(11):e0187418, 2017. doi: 10.1371/journal.pone.0187418.
[37] V.T. Sakima, P.A. Barbugli, P.S. Cerri, M. Chorilli, J.C. Carmello, A.C. Pavarina, E.G.O. Mima, Antimicrobial
Photodynamic Therapy Mediated by Curcumin-Loaded Polymeric Nanoparticles in a Murine Model of Oral Candidiasis, Molecules. 23(8):2075, 2018. doi: 10.3390/molecules23082075.
[38] J.K. Trigo-Gutierrez, I.R. Calori, G.D.O. Bárbara, A.C. Pavarina, R.S. Gonçalves, W. Caetano, A.C. Tedesco, E.G.O. Mima, Photo-Responsive Polymeric Micelles for the Light-Triggered Release of Curcumin Targeting Antimicrobial Photodynamic Therapy, Front. Microbiol. 14, 1247, 2023. https://doi.org/10.3389/fmicb.2023.1132781
[39] S. Fulaz, S. Vitale, L. Quinn, E. Casey, Nanoparticle-Biofilm Interactions: The Role of the EPS Matrix, Trends Microbiol. 27(11):915-926, 2019. doi: 10.1016/j.tim.2019.07.004.
[40] J.K. Trigo-Gutierrez, P.V. Sanitá, A.C. Tedesco, A.C. Pavarina, E.G.O. Mima, Effect of Chloroaluminium phthalocyanine in cationic nanoemulsion on photoinactivation of multispecies biofilm, Photodiagnosis Photodyn Ther. 24:212-219, 2018. doi: 10.1016/j.pdpdt.2018.10.005.
[41] J.C. Carmello, F. Alves, A. Ribeiro, F.G. Basso, C.A. de Souza Costa, A.C. Tedesco, F.L. Primo, E.G. Mima, A.C. Pavarina, In vivo photodynamic inactivation of Candida albicans using chloro-aluminum phthalocyanine, Oral Dis. 22(5):415-22, 2016. doi: 10.1111/odi.12466.
[42] J.C. Carmello, F. Alves, F.G, Basso, C.A. de Souza Costa, A.C. Tedesco, F. Lucas Primo, E.G.O. Mima, A.C. Pavarina AC, Antimicrobial photodynamic therapy reduces adhesion capacity and biofilm formation of Candida albicans from induced oral candidiasis in mice, Photodiagnosis Photodyn Ther. 27:402-407, 2019. doi: 10.1016/j.pdpdt.2019.06.010.
[43] K. Janeth Rimachi Hidalgo, J.C. Carmello, C. Carolina Jordão, P. Aboud Barbugli, C.A. de Sousa Costa, E.G.O. Mima, A.C. Pavarina AC, Antimicrobial Photodynamic Therapy in Combination with Nystatin in the Treatment of Experimental Oral Candidiasis Induced by Candida albicans Resistant to Fluconazole, Pharmaceuticals (Basel). 18;12(3):140, 2019 Sep. doi: 10.3390/ph12030140.

[44] F. Alves, A.C. Pavarina, E.G.O. Mima, A.P. McHale, J.F. Callan. Antimicrobial sonodynamic and photodynamic therapies against Candida albicans. Biofouling. 34(4):357-367, 2018. doi: 10.1080/08927014.2018.1439935.
[45] Y. Vega-Chacón, M.C. de Albuquerque, A.C. Pavarina, G.H. Goldman, E.G.O. Mima. Verapamil inhibits efflux pumps in Candida albicans, exhibits synergism with fluconazole, and increases survival of Galleria mellonella. Virulence. 12(1):231-243, 2021. doi: 10.1080/21505594.2020.1868814.
[46] V.T. Sakima, Y. Vega-Chacón, P.S. Cerri, B. Shokeen, R. Lux, E.G.O. Mima. A Denture Use Model Associated with Candida spp. in Immunocompetent Male and Female Rats. J Fungi (Basel). 30;8(5):466, 2022. doi: 10.3390/jof8050466. PMID: 35628722; PMCID: PMC9147495

DOI 10.24412/cl-37136-2023-1-166-167

FORMULATION, CHARACTERIZATION, AND OPTIMIZATION OF LAURIC ACID AND TEA TREE OIL-LOADED SOLID LIPID NANOPARTICLES

FEZILE MOTSOENE, HEIDI ABRAHAMSE, SATHISH SUNDAR DHILIP KUMAR*

*Laser Research Centre, Faculty of Health Sciences, University of Johannesburg, P.O. Box: 17011, Johannesburg 2028, South Africa. *E-mail: sathishd@uj.ac.za*

ABSTRACT

Background. Over the past few decades, Solid Lipid Nanoparticles (SLNs) have demonstrated their potential as an alternative drug delivery system by overcoming the limitations of polymeric micro and nanoparticles, liposomes, and emulsions [1]. Solid lipid nanoparticles are site-specific and sub-colloidal lipid-based nanoparticles composed solid lipid core (within which the drug is located depending on its hydrophobicity or hydrophilicity) surrounded by a surfactant, which increases the drug stability, the stability and entrapment efficacy of the drug-loaded system. These particles have numerous benefits, including safeguarding sensitive compounds from harmful environmental factors like moisture, light, and pH [2,3]. Biological activity would be greatly diminished if this protection were not provided for the compounds [4]. In addition, SLNs have also enhanced the biocompatibility and delivery of lipophilic and hydrophobic drug molecules with natural active ingredients such as Tea tree oil and lauric acid in various medical applications. Therefore, the present study aimed to formulate, characterise, and determine the antibacterial effect of the Lauric acid (LA) and Tea Tree oil (TTO)-loaded Solid Lipid Nanoparticles (LT-SLNs). Lauric acid and TTO are hydrophobic drug molecules that have difficulty penetrating the skin's epithelial tissue. Lauric acid is a carbon-12 saturated fatty acid commonly found in palm kernel and coconut oil [5]. Lauric acid possesses good thermal, antibacterial and anti-inflammatory properties that effectively combat both Gramnegative and Gram-positive bacteria. Additionally, it facilitates cell migration and preserves the sterility of the wound bed. On the other hand, TTO contains several compounds, including p-cymene, 1,8-cineole, terpinen-4- ol, and γ-terpinene. These compounds are known to possess antiseptic, antibacterial, and anti-inflammatory properties that work against both gram-negative and gram-positive bacteria [6,7]. Therefore, using Stearic acid Solid Lipid Nanoparticles to deliver these drugs to the site of the wound is advantageous. This is because SLNs containing stearic acid have a high entrapment efficiency and are uniform in size , making them a potentially effective targeted preparation for epidermal delivery [8]. Furthermore, the usage of Tween 80 to stabilize SASLN results in a reduction of surface energy and prevents crystal growth. This ultimately leads to the production of smaller nanoparticles [9].

Methodology. The LT-SLNs were prepared by homogenization method at 17,500 rpm for 30 minutes. The prepared LT-SLNs were then cooled at room temperature to allow the SLN formation. Following this, the LT-SLNs were then filtered using a 200 nm sterile syringe and stored at 2°C. The LT-SLNs formulation surface charge, composition, and appearance were analyzed using techniques such as Zeta potential and size, HR-TEM, XRD, and FTIR. To determine its efficacy against bacterial cells, Pseudomonas aeruginosa was used. Evaluation methods included bacterial Growth Kinetics, Kirby-Bauer Disk Diffusion, Live/dead cell analysis using flow cytometry, and bacterial membrane damage study.

Results. Stearic acid, lauric acid and Tea tree oil were dissolved in 99% ethanol and the LT-SLNs were prepared by homogenization at 17,500 rpm for 30 minutes. Table 1 represents the polydisperse index (PDI), average particle size, and surface charge (Zp) of the SLN and LT-SLN formulations. In addition, an XRD experiment was also performed to demonstrate the crystallographic structure and chemical composition for all SLN and LT-SLN formulations compared to the standard lauric acid and stearic acid standard XRD readings. In addition, the minimum inhibition concentration results are shown in Figure 1.

Table 1: Surface charge (Zeta potential) Particle size distribution of SLN and LT-SL.

Formulation	Average Particle size Distribution (PSD) (d.nm)	Zeta Potential (mV)	Particle density Index
F1	239.58 ± 7.96	-9.36 ± 3.89	1.000
F2	284.7± 17.74	-13.2 ± 5.30	1.000
F3	212.4 ± 13.20	-12.1 ± 4.53	1.000
F4	344.7 ± 16.13	-9.05 ± 5.20	1.000
F5	270.1 ± 0.931	-12.3 ± 3.78	1.000

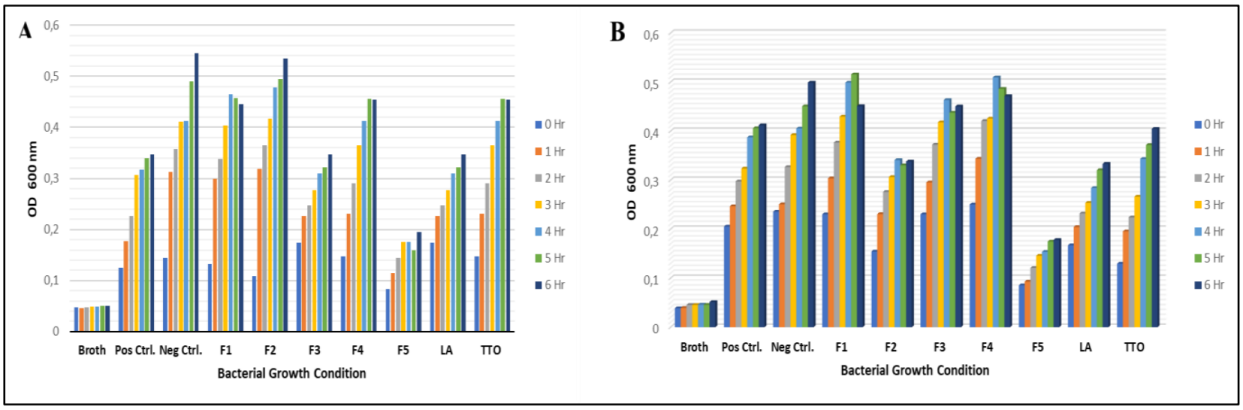

Figure 1: *Growth Kinetic study for the formulated SLN and LT-SLNs using P aeruginosa A) MIC 12,5 Trial 1 and B) 12,5mg/ml Trial 2 for P aeruginosa bacterial study.*

Conclusion. This study discussed the potential process of preparing, characterisation, and antibacterial effect of SLNs and LTSLNs and it may be useful for the treatment of pathogen-infected wounds. The SLNs and LT-SLNs were welldesigned with good physicochemical properties and biocompatibility,which allowed them to penetrate deep into the bacterial membrane of P. aeruginosa displaying their antibacterial effect. This makes them suitable for the treatment of pathogen-infected wounds.

REFERENCES.

[1] K.H. Ramteke, S.A. Joshi, S.N. Dhole, Solid Lipid Nanoparticle: A Review Ramteke K.H, IOSR Journal of Pharmacy. 6, 34–44. 2012

[2] P. Ekambaram, A. Abdul hasansathali, K. Priyanka, Solid Lipid Nanoparticles: A Review, Scientific Reviews & Chemical Communications. 2 (2011) 80–102.

[3] N.K. Rajendran, S.S.D. Kumar, N.N. Houreld, H. Abrahamse, A review on nanoparticle-based treatment for wound healing, J. Drug Deliv. Sci. Technol. 44, 421–430, 2018 https://doi.org/10.1016/j.jddst.2018.01.009.

[4] Y. Duan, A. Dhar, C. Patel, M. Khimani, S. Neogi, P. Sharma, N. Siva Kumar, R.L. Vekariya, A brief review on solid lipid nanoparticles: part and parcel of contemporary drug delivery systems, RSC Adv. 10, 26777–26791, 2020 https://doi.org/10.1039/d0ra03491f.

[5] M.S. Lerata, S. D'Souza, N.R.S. Sibuyi, A. Dube, M. Meyer, T. Samaai, E.M. Antunes, D.R. Beukes, Encapsulation of variabilin in stearic acid solid lipid nanoparticles enhances its anticancer activity in vitro, Molecules. 25, 830, 2020 https://doi.org/10.3390/molecules25040830.

[6] F.O. Nitbani, Jumina, D. Siswanta, E.N. Solikhah, Isolation and antibacterial activity test of lauric acid from crude coconut oil (cocos nucifera L.), Procedia Chem. 18,132–140,2016 https://doi.org/10.1016/j.proche.2016.01.021.

[7] R.C.V. Santos, L.Q.S. Lopes, C.F. dos S. Alves, V.P. Fausto, K. Pizzutti, V. Barboza, M.E. de Souza, R.P. Raffin, P. Gomes, D. Takamatsu, Y. Morinaga, A.A. Boligon, M.L. Athayde, C.C. Felippi, R. de Almeida Vaucher, Antimicrobial activity of tea tree oil nanoparticles against American and European foulbrood diseases agents, J. Asia. Pac. Entomol. 17, 343–347, 2014 https://doi.org/10.1016/j.aspen.2014.02.003.

[8] Xie F.-M., Zeng K., Li G.-F., Lin Z.-F., Sun L.-D., Preparation of stearic acid solid lipid nanoparticles containing podophyllotoxin, Di Yi Jun Yi Da Xue Xue Bao. 25, 99–101, 2005

[9] A. Sukmawati, W. Utami, R. Yuliani, M. Da'i, A. Nafarin, Effect of tween 80 on nanoparticle preparation of modified chitosan for targeted delivery of combination doxorubicin and curcumin analogue, IOP Conf. Ser. Mater. Sci. Eng. 311, 012024., 2011 https://doi.org/10.1088/1757-899x/311/1/012024.

DOI 10.24412/cl-37136-2023-1-168-174

EFFECTS OF NEAR-INFRARED PHOTOBIOMODULATION AT 830 NM IN A DIABETIC WOUNDED CELL MODEL

LINDOKUHLE HADEBE AND NICOLETTE HOURELD

1Laser Research Centre, Faculty of Health Sciences, South Africa University of Johannesburg
Hadebelindokuhle184@gmail.co

ABSTRACT

Diabetic wounds present a significant healthcare burden due to their failure to progress through the usual phases of healing within the expected time, leading to decreased cellular migration, skin ulceration, and impaired wound healing. Complications arising from these wounds, such as lower extremity amputation, can decrease patient quality of life and result in premature death. Photobiomodulation (PBM), previously known as low-level light therapy (LLLT) or cold laser therapy, is a non-invasive medical treatment that uses low-intensity light sources to stimulate cellular activity and aid healing in various tissues. This therapy has been researched for its ability to aid wound healing, decrease pain and inflammation, and increase tissue repair. However, the mechanisms that aid the induction of cell migration and survival using an 830 nm laser are poorly understood. Therefore, the present study was designed to evaluate the therapeutic efficacy of near-infrared (NIR) PBM at 830 nm in wounded and unwounded human skin fibroblast (WS1) cell models. Models were exposed to an 830 nm diode laser at a fluence of 5 J/cm2 , unirradiated models (0 J/cm2) were used as controls. Post-PBM, the Trypan blue exclusion assay and CellTiter-Glo® 3D Cell Viability Assay (measures adenosine triphosphate (ATP) luminescence) were used to determine the population of viable cells at 24 and 48 h. Morphological changes and migration rate in wounded models was also evaluated at 0 h and 24 h. PBM significantly increased cellular migration and enhanced cell viability, thus improving wound healing in diabetic conditions in vitro at 830 nm.

BACKGROUND

Diabetes mellitus (DM) refers to a group of chronic metabolic disorders that are characterized by increased blood sugar levels over an extended period. It is worth mentioning that this medical disorder can occur when the normal physiology of the pancreas is dysfunctional (i.e., Type I DM) or cells are unable to use the insulin produced by the body (i.e., Type II DM). The role of insulin is to regulate the body's uptake and assimilation of blood glucose [1]. Patients with DM are likely to develop major complications, such as stroke, cardiovascular diseases, retinopathy, angiopathy, neuropathy, and chronic non-healing ulcers, often on the lower limbs. The projected prevalence of DM in individuals aged 20 to 79 is anticipated to rise to 643 million by the year 2030, with a further increase to 783 million by 2045 [2]. Current treatment options have shown to be largely ineffective, highlighting the need for developing innovative strategies to enhance diabetic wounds. PBM is the non-invasive application of predominantly red and NIR light to stimulate and accelerate cellular processes to promote tissue repair and regeneration, wound healing, and reduce inflammation [3]. PBM is useful in the treatment of various disorders and chronic non-healing wounds, including diabetic wounds [1]. Therefore, this study was designed to investigate the effects of NIR PBM at 830 nm in a wounded and diabetic wounded cell model.

METHODOLOGY

Cell culture and experimental models This study used commercially available human skin fibroblasts, WS1 (ATCC®, CRL 1502TM), to create four models, namely, normal (N), normal wounded (NW), diabetic (D), and diabetic wounded (DW). A wounded cell model was created by performing a central scratch on the monolayer of WS1 cells seeded in 3.5 cm diameter tissue culture plates using a 1 mL sterile pipette [4]. The cells were incubated for 30 min post-wounding and before irradiation to allow the cells to acclimatize. A diabetic model was made by continuously culturing the cells in Minimum Essential Medium (MEM) containing

an additional 17 mM D-glucose. The diabetic cells were grown in a final glucose concentration of 22.6 mM since the media already contains 5.6 mM glucose [5]. Experimental cells were irradiated with a fluence of 5 J/cm2 at a wavelength of 830 nm and incubated for 24 and 48 h post-PBM. Non-irradiated cells (0 J/cm2) served as controls. Schematic representation is shown in Figure 1.

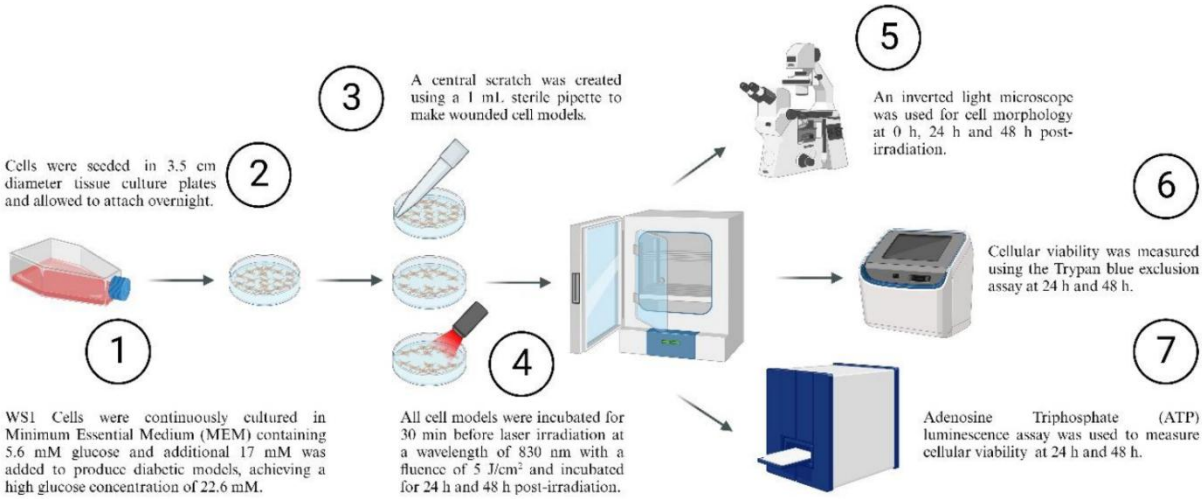

Figure 1: General overview of the study methodology.

Morphological analysis and cell migration

Cellular morphology and migration were determined by inverted light microscopy. Three images per cell culture plate were captured; images along the central scratch in wounded models (NW and DW) were taken in the same place. The wound distance (in µm) between the wound margins was measured using the microscope software (cellSens) at different time intervals over a period of 48 h (0, 24, and 48 h) to capture cell migration. The measured wound distances were used to calculate the migration rate using the following formula: At_{0h} - At_{time}/At_{0h} x 100, where At_{0h} is the scratch area at 0 h and At_{time} is the correspondent scratch area at different time points [6].

Cellular viability

The Trypan blue exclusion assay and CellTiter-Glo® 3D Cell Viability Assay (Promega, G9681) were used to determine cell viability. Trypan blue is a dye that is used to determine the number of viable cells, and its principle is based on dye exclusion; dead cells take up the dye due to their permeable cell membrane, while live (viable) cells do not take up the dye as their cell membranes are impermeable. Equal volumes (10 µL) of dye and cells were mixed and 10 µL loaded into a counting chamber. Viable (unstained) and non-viable (stained) cells was counted and reported in percentage using the automated cell counter (Invitrogen Countess II FL). The CellTiter-Glo® 3D Cell Viability Assay determines cell viability measuring the amount of ATP produced by metabolically acive cells. Briefly, equal amounts of Cell Tilter-Glo Reagent and cells (50 uL) were added and mixed on an orbital shaker for 2 min to induce cell lysis, followed by a 10 min incubation in the dark to stabilize the luminescent signal. Luminescence was read in Relative Light Unit (RLU) on a multilabel counter (Perkin Elmer, VICTOR3^{TM}, 1420). *Statistical analysis*

All experiments were repeated three times (n=3). SigmaPlot version 14 (Systat Software, Inc.) was used for statistical analysis. Statistical differences between groups were determined by the Student t test. Results are shown as standard error of the mean (SEM), and statistical significance compared to the controls in the graphs are shown as *p

RESULTS AND DISCUSSION

Morphological analysis and cell migration rate

Morphological changes were observed using an inverted light microscope across all cell models, namely, N, NW, D, and DW at 0 h, 24 h, and 48 h post-PBM. In both non-irradiated (0 J/cm2) and irradiated (5 J/cm2) cell models, high glucose concentrations had no effect on cellular shape. The cells kept their flat, elongated spindle form (Fig. 2). However, irradiated wounded cells demonstrated an accelerated cell migration from the

wound margins into the wound site (central scratch) compared to the non-irradiated cells (Fig. 3), where the wounds were partially or entirely closed at 48 h. The results of the present study are similar to those reported by Kasowanjete et al., [7] and Mokoena et al., [8]. This is in agreement with the results for migration rate, where a significant increase was observed in both NW (P=0.03) and DW (P=0.005) at 24 h (Fig. 4). This suggests that PBM at 830 nm with a fluence of 5 J/cm2 stimulates cellular migration and promotes wound closure.

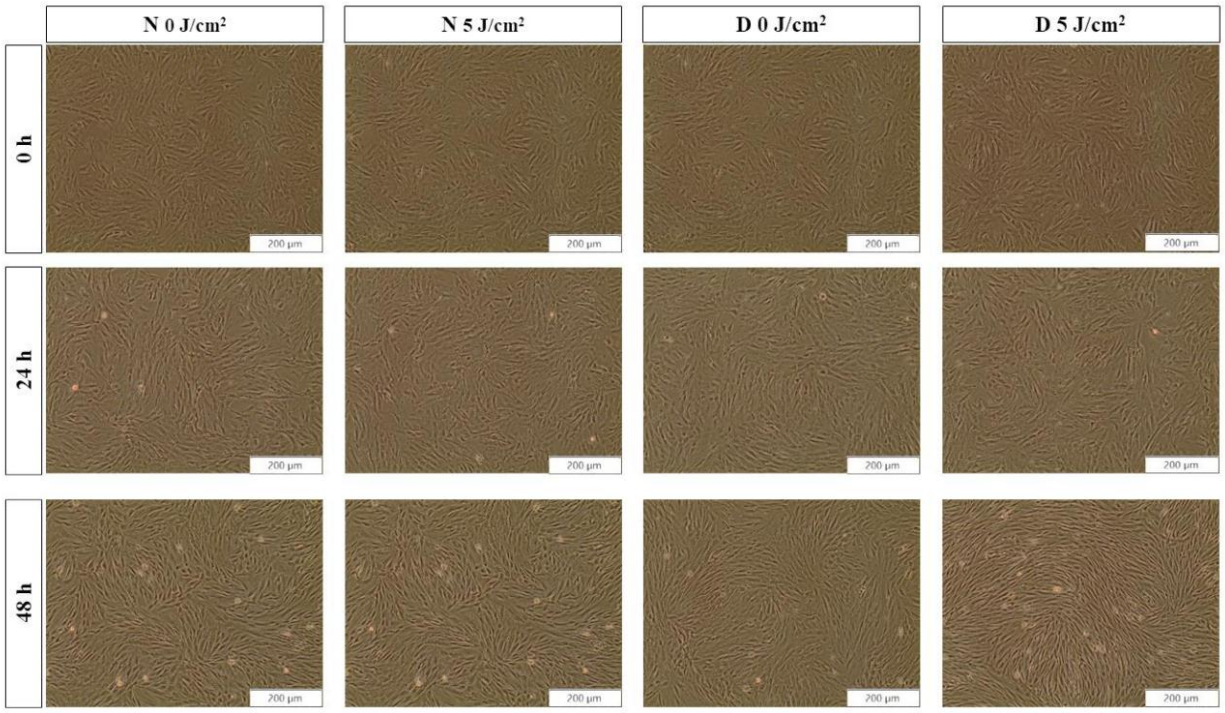

Figure 2: *Micrography showing the morphology of non-irradiated (0 J/cm2) and irradiated (5 J/cm2) normal (N) and diabetic (D) WS1 cell models at 0 h, 24 h and 48 h post-PBM using an 830 nm laser diode. No cellular morphological differences were observed across all models as they retained their basic morphology post-PBM.*

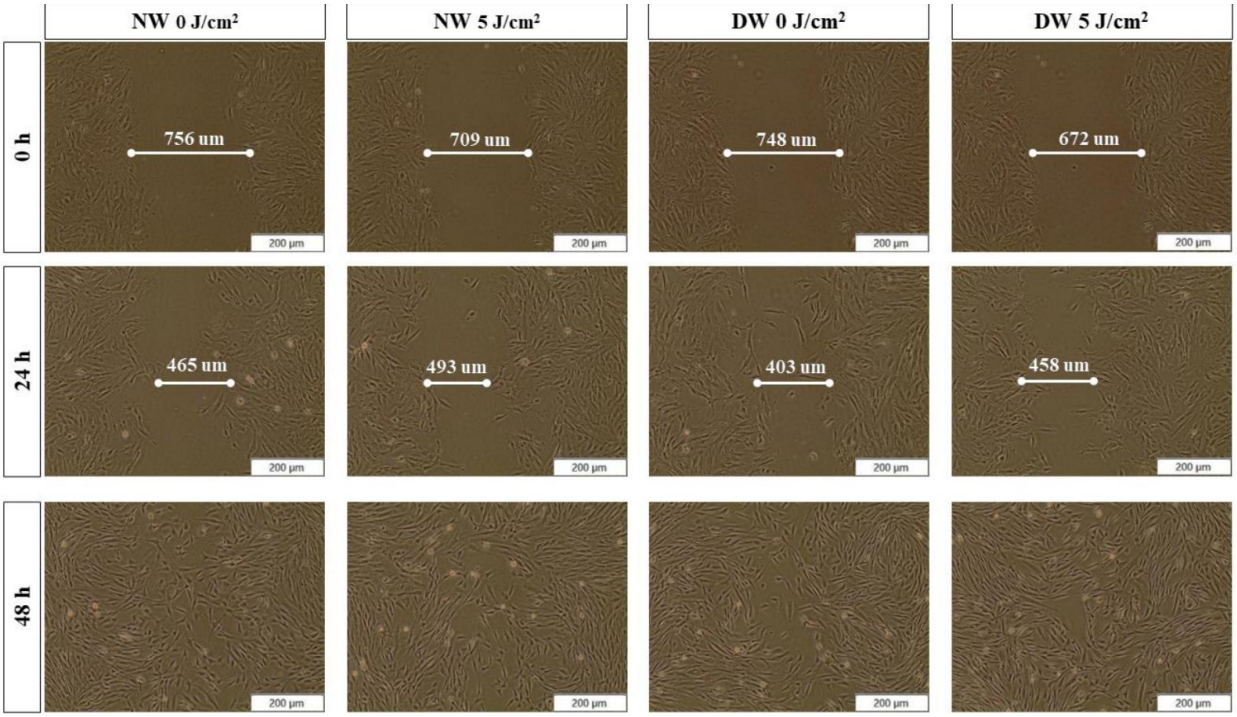

Figure 3: *Representative micrographs showing the morphology and migration of non-irradiated (0 J/cm2) and irradiated (5 J/cm2) normal wounded (NW) and diabetic wounded (DW) WS1 cells at 0 h, 24 h, and 48 h*

post-PBM using an 830 nm laser diode. Irradiated cells displayed accelerated cell migration into the central scratch to establish wound closure.

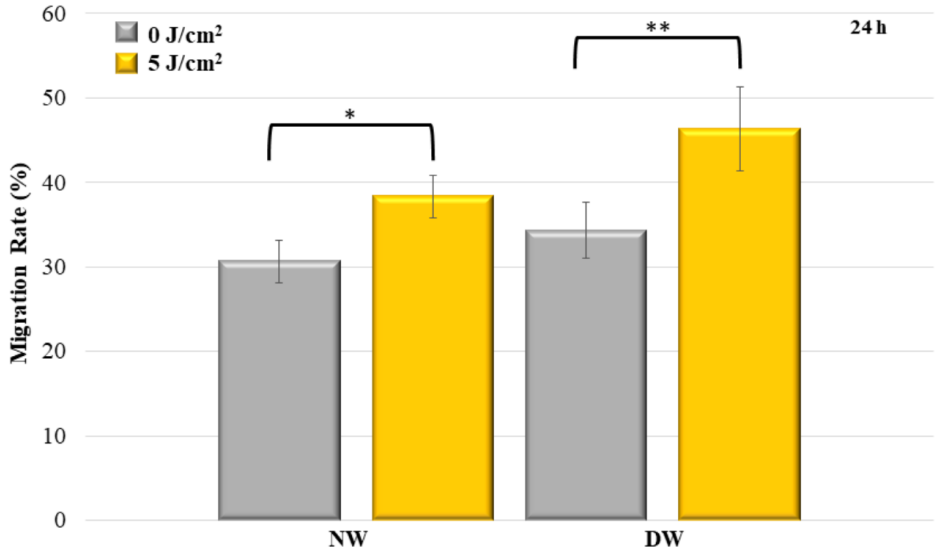

Figure 4: *Migration rate (%) in non-irradiated (0 J/cm2) and irradiated (5 J/cm2) normal wounded (NW) and diabetic wounded (DW) WS1 cells 24 h post-PBM using an 830 nm laser diode. Significant probability is shown as * p<0.05 and **p<0.01 (±SEM)*

Cellular viability

Cellular viability was assessed using the Trypan blue exclusion assay, which measures the number of viable and healthy cells in irradiated and non-irradiated cell models at 24 and 48 h (Fig. 5 and 6). At 24 h, the variation between the controls and PBM-treated N, NW, D, and DW cell models was not statistically significant (P=0.06, P=0.08, P=0.06, and P=0.07, respectively). However, all cell models (N, NW, D, and DW) showed a significant increase in cell viability (P=0.02, P=0.008, P=0.005, and P=0.03, respectively) at 48 h. This indicates the necessity of more extended incubation periods post-PBM to fully observe photobiomodulative effects in vitro. It also demonstrates that PBM at 830 nm is able to increase cellular viability under normoglycemic and hyperglycemic conditions. Irradiated cell models displayed higher (insignificant) ATP luminescence at 24 and 48 h (Fig. 7 and 8, respectively). Moreover, diabetic models have shown higher ATP production than the normal cell models at 24 and 48 h. However, there was no statistical significance observed.

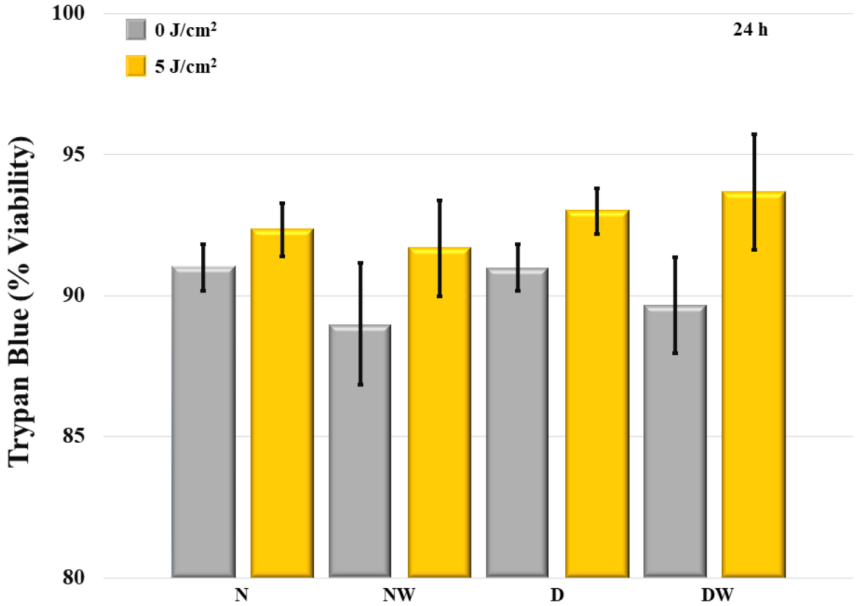

Figure 5: *Cellular viability (%) of normal (N), normal wounded (NW), diabetic (D), and diabetic wounded (DW) cell models was determined by the Trypan blue exclusion assay 24 h post-PBM at 830 nm (±SEM).*

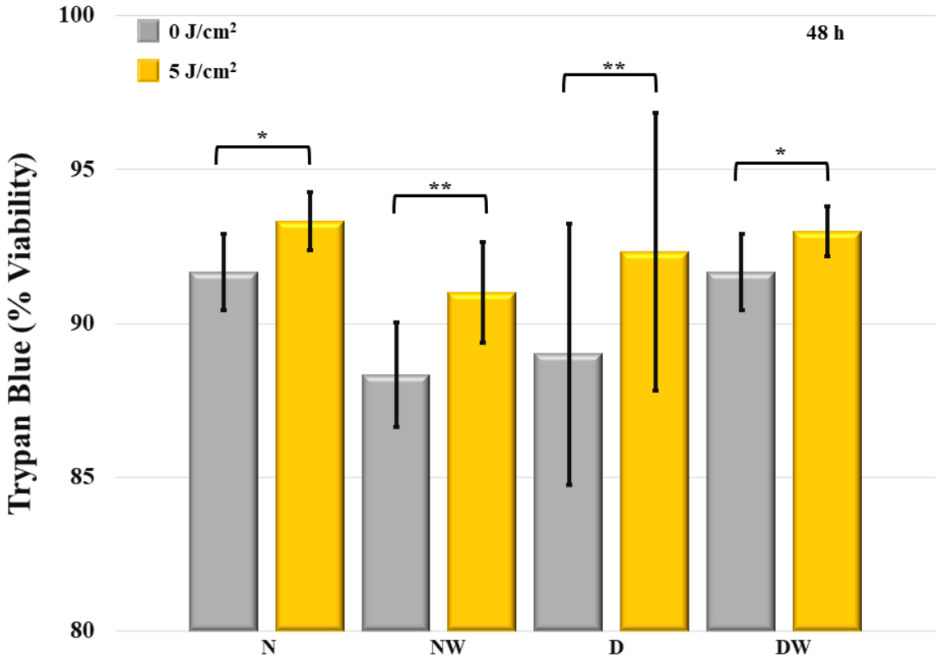

Figure 6: *Cellular viability (%) of normal (N), normal wounded (NW), diabetic (D), and diabetic wounded (DW) cell models was determined by the Trypan blue exclusion assay 48 h post-PBM at 830 nm. Significant probability is shown as *p<0.05 and **p<0.01(±SEM).*

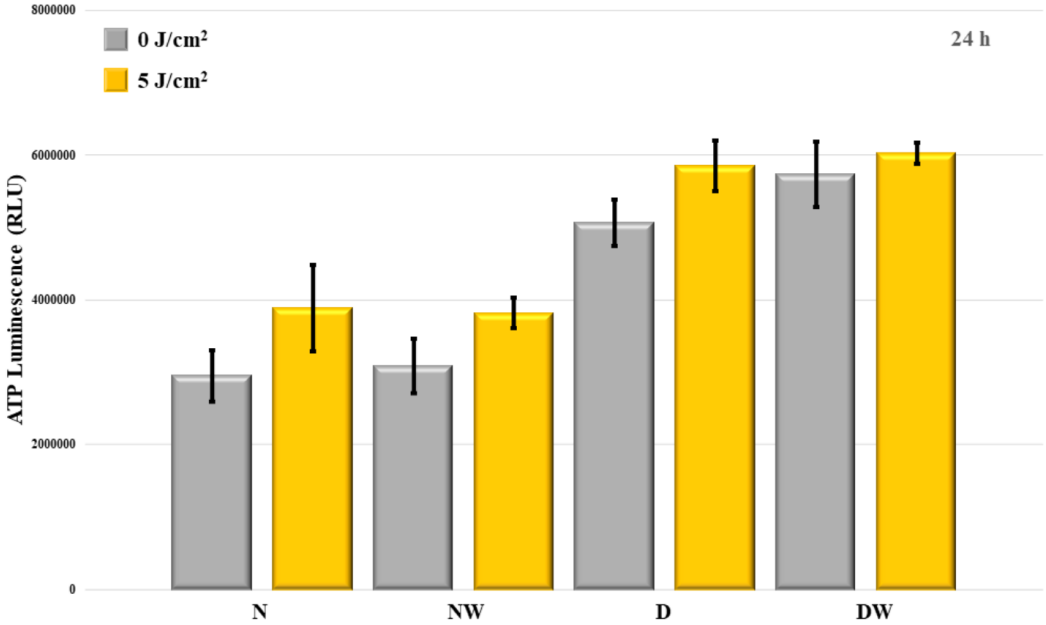

Figure 7: *Adenosine Triphosphate (ATP) luminescenc (relative light units, RLU) as a function of cellular viability was determined in normal (N), normal wounded (NW), diabetic (D), and diabetic wounded (DW) cell models 24 h post-PBM at 830 nm (±SEM).*

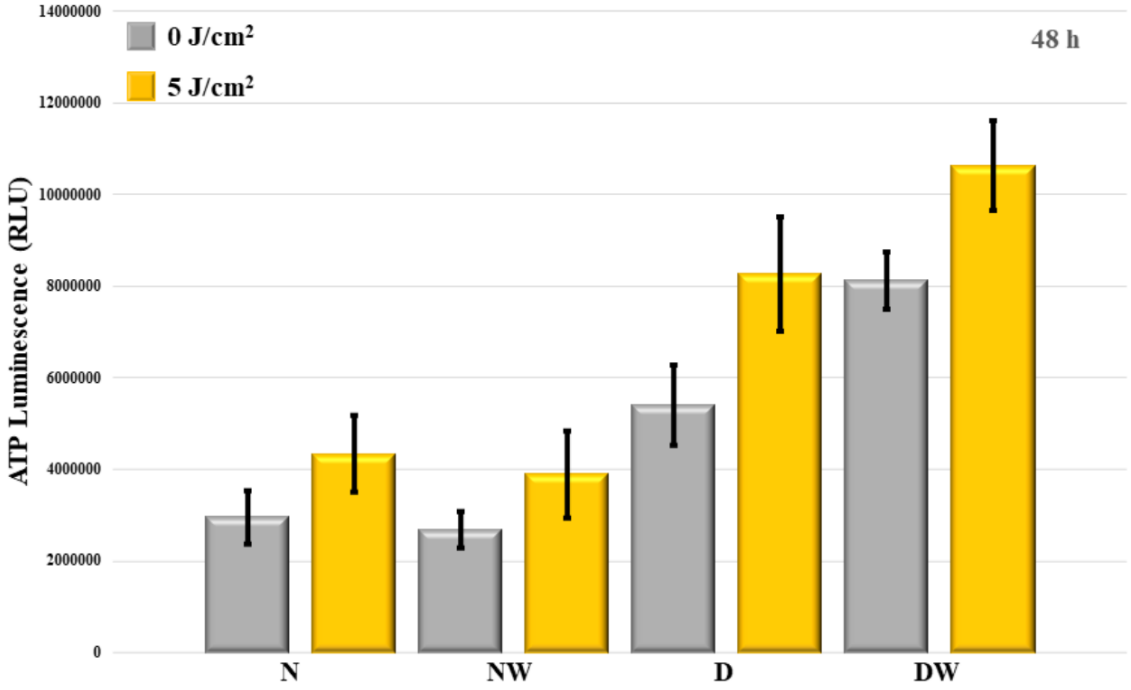

Figure 8: *Adenosine Triphosphate (ATP) luminescenc (relative light units, RLU) as a function of cellular viability was determined in normal (N), normal wounded (NW), diabetic (D), and diabetic wounded (DW) cell models 48 h post-PBM at 830 nm (±SEM).*

CONCLUSION

In conclusion, this study revealed that high glucose concentrations did not affect cellular morphology in non-irradiated (0 J/cm2) and irradiated (5 J/cm2) cell models. The cells maintained their elongated flat spindle shape. The study also revealed that PBM at 830 nm with a fluence of 5 J/cm2 enhances cellular migration rate, increases cellular viability, and promotes wound closure, even under hyperglycemic conditions. PBM at 830 nm could be used to stimulate the healing of slow, non-healing wounds.

ACKNOWLEDGMENTS AND FUNDING SOURCES

This work was funded by the South African Research Chairs Initiative of the Department of Science and Technology (DST) and National Research Foundation (NRF) of South Africa (Grant No 98337), the University of Johannesburg (URC), the NRF Competitive Programme for Rated Researchers (Grant No 1293270) and Council for Scientific and Industrial Research (CSIR) - National Laser Centre (NLC), Laser Rental Pool Programme. All lasers were supplied and set up by the NLC.

CONFLICT OF INTEREST Authors declare no conflict of interest.

REFERENCES

[1] S. Ponnusamy, R. Mosca, K. Desai, P. Arany, Photobiomodulation therapy in diabetic wound healing. In: Wound Healing, Tissue Repair, and Regeneration in Diabetes, D. Bagchi, A. Das, S. Roy, Eds.; Academic Press: San Diego, CA, USA, p. 305– 321, 2020.

[2] International Diabetes Federation, IDF Diabetes Atlas. 10th edition. Brussels, 2021.

[3] M. R. Hamblin, Photobiomodulation or low-level laser therapy. J Biophotonics. 1122–4, 2016.

[4] N. N. Houreld, H. Abrahamse, Low-Intensity laser irradiation stimulates wound healing in diabetic wounded fibroblast cells (WS1). Diabetes Technology & Therapeutics. 971-978, 2010.

[5] N. N. Houreld, H. Abrahamse, In vitro exposure of wounded diabetic fibroblast cells to a helium-neon laser at 5 and 16 J/cm2 . Photomedicine and Laser Surgery. 78-84, 2007.

[6] F. Felice, et al., Effect of different chitosan derivatives on in vitro scratch wound assay: a comparative study. Int J Biol Macromol. 236-241, 2015.

[7] P. Kasowanjete, H. Abrahamse, N. N. Houreld, Photobiomodulation at 660 nm stimulates in vitro diabetic wound healing via the Ras/MAPK pathway. Cells. 1080, 2023.
[8] D. R. Mokoena, N. N. Houreld, S. S. Dhilip Kumar, H. Abrahamse, Photobiomodulation at 660 nm stimulates fibroblast differentiation. Lasers Surg. Med. 671-681, 2020.

DOI 10.24412/cl-37136-2023-1-175-175

STRATEGIES FOR AN INDIVIDUALIZED LIGHT DOSIMETRY

THEREZA CURY FORTUNATO[1] , VICTOR PORTO GONTIJO DE LIMA[2] AND LILIAN TAN MORIYAMA[2]

1 Bright Photomedicine Ltda., Brazil 2 Sao Carlos Institute of Physics, University of Sao Paulo, Brazil
lili@ifsc.usp.br

ABSTRACT

In Biomedical Optics applications, either for therapy or diagnostics, it is important to establish the best strategy for tissue irradiation. The main difficulties rely on the fact that there are several types of equipment and several types of target tissues. It is noticeable that the best strategy of irradiation is not very simple to determine, and up to our knowledge, the influence of all these different parameters (technological and biological) has not been deeply explored yet. It is not clear, for instance, how light dosimetry for a certain phototherapy can be affected by tissue surface roughness, by the application of a cream or oil during the irradiation, or by the light delivery device. One of the biggest obstacles for establishment of individualized light dosimetry is that experimental measurements of all the features of a targe tissue would require an invasive procedure, like the insertion of an optical fiber, and it is infeasible and impractical. Monte Carlo simulations have been proven to be a powerful toll to assess light propagation through biological tissues. In this presentation we will address strategies our group is exploring to achieve an individualized light dosimetry.

REFERENCES

Fortunato TC. Monte Carlo simulations to investigate light coupling with optical skin phantom [Internet]. 2021 ;[citado 2023 abr. 12] Available from: https://www.teses.usp.br/teses/disponiveis/76/76132/tde02092021-160416/

DOI 10.24412/cl-37136-2023-1-176-180

STRATEGIES TO IMPROVE TOPICAL PHOTODYNAMIC THERAPY EFFICACY USING ANIMAL MODELS

MIRIAN DENISE STRINGASCI1 AND VANDERLEI SALVADOR BAGNATO1,2

1Sao Carlos Institute of Physics, University of Sao Paulo, Brazil 2Department of Biomedical Engineering, Texas A&M University, USA

miranstringasci@ifsc.usp.br

ABSTRACT

Photodynamic Therapy (PDT) is a therapeutic option for the treatment of malignant and potentially malignant lesions. This technique is based on a photosensitizer (PS) excited with light at a suitable wavelength for absorption. The interaction of excited PS with molecular oxygen generates reactive oxygen species that lead to cell death. [1] One of the limiting factors of topical PDT is the cutaneous permeation of the PS or precursor, as in the case of aminolevulinic acid (ALA) and methyl aminolevulinate (Methyl-ALA). There are reports that there is a strong relationship between temperature and the synthesis of porphyrin IX (PpIX) in biological tissue. This suggests that increasing skin temperature during ALA or Methyl-ALA incubation may increase tissue accumulation of PpIX, improving the effectiveness of PDT, especially in areas that naturally experience lower temperatures, such as the extremities. [2, 3] In a skin model, Wistar rats were used with the administration of cream containing ALA or Methyl-ALA, both at a concentration of 20%, for 15 minutes. The animals were divided into 5 groups: tissue cooling to 20 °C or tissue heating to 40 °C (before or after cream incubation) and the control group (unchanged temperature). In each animal, two regions of the back were shaved and each group was composed of 4 treatment regions. From collections of fluorescence spectra, using a laser for excitation at 408 nm, it was possible to evaluate the PpIX emission signal at 630 nm, which is directly related to the accumulation of the molecule in the tissue. [4] It was found that both ALA and Methyl-ALA showed increased PpIX production when tissue was heated before cream incubation, showing better penetration (Fig. 1). When the temperature was changed after incubation of the cream, PpIX production decreased by both heating and cooling, probably because the enzymes that make up biological tissue were no longer at their optimal functioning, which occurs at normal tissue temperature (around of 37°C), Fig. 2.

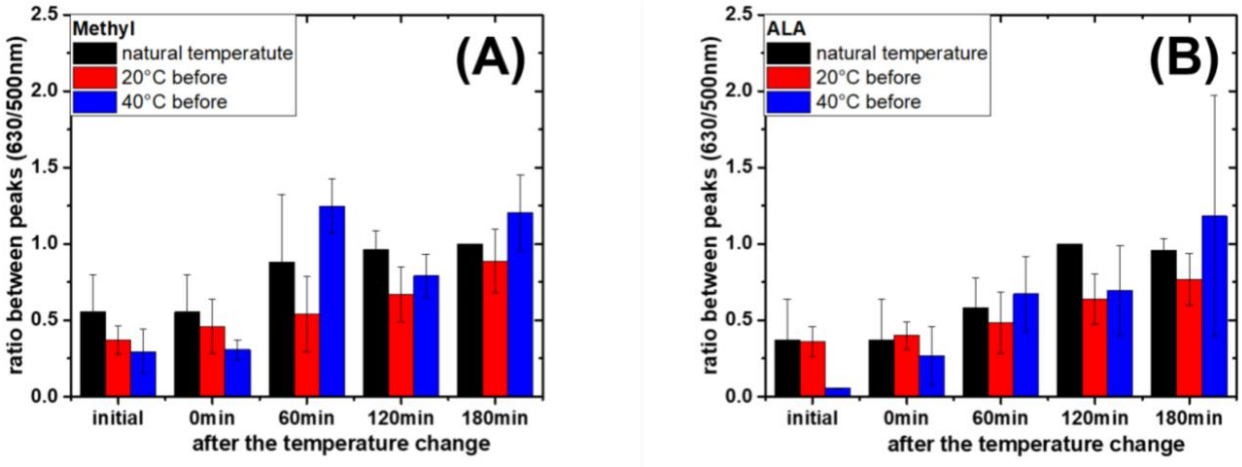

Figure 1: *Variation of PpIX production due to skin temperature change for 15 minutes before cream application (A) comparing the regions with methyl application; (B) ALA application; (C) comparing ALA and methyl without temperature change; (D) comparing ALA and methyl in tissue previously cooled to 20 ° C and (E) comparing ALA and methyl in previously heated tissue at 40 ° C*

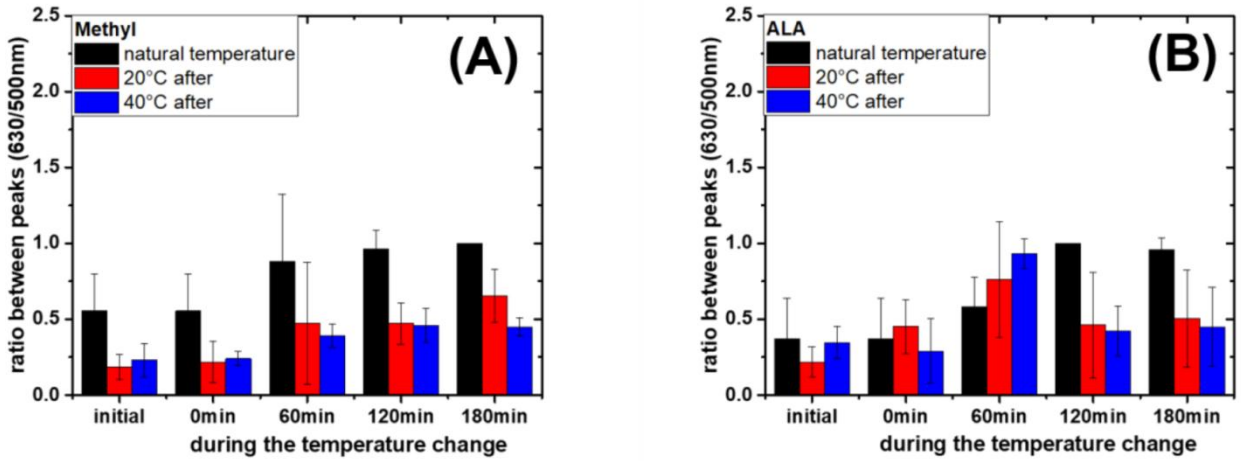

Figure 2: *Variation of PpIX production due to skin temperature change for 180 minutes after cream application (A) comparing the regions with methyl application; (B) ALA application; (C) comparing ALA and methyl without temperature change; (D) comparing ALA and methyl in tissue subsequently cooled to 20 ° C and (E) comparing ALA and methyl in subsequently heated tissue at 40 ° C.*

Another study aimed to test thermogenic/vasodilating agents incorporated into the precursor creams ALA and MethylALA to assess a possible improvement in the production of PpIX, in which menthol, methyl nicotinate (MN), and the extract of ginger. Again, healthy skins of Wistar rats were used, with 4 regions treated in each group, in the control group ALA or Methyl-ALA creams were used without the addition of agents. In each animal, two regions of the back were shaved, the cream containing 20% ALA was applied to one region, and the cream containing 20% Methyl-ALA was applied to the other. The creams were maintained with an occlusive dressing for 3 hours. Fluorescence spectroscopy measurements were used to assess PpIX formation, the results are presented in Fig. 3. [5]

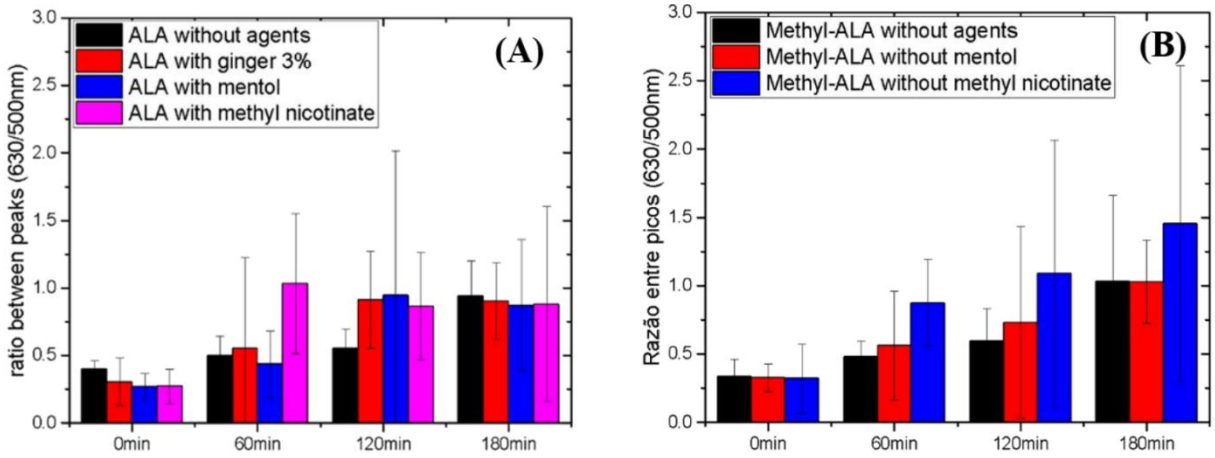

Figure 3: *(A) Comparison of the PpIX production of PpIX from the different agents incorporated into the cream containing ALA and (B) and methyl-ALA.*

It is possible to observe in Fig. 3 (B) that MN associated with Methyl-ALA showed the highest production of PpIX, at the end of 180 minutes this production is about 50% greater than that observed by Methyl-ALA without an added agent. The use of this agent may present a possible strategy to reduce the incubation time and/or increase PpIX production in more keratinized lesions. A new study was carried out to evaluate this better formulation (0.5% MN incorporated into 20% Methyl-ALA), in cell culture, non-cytotoxicity and increased cell metabolism were observed using confocal microscopy to calculate the redox rate. It was also possible to note the vasodilator effect of MN in a chorioallantoic membrane model (Fig. 4), in which after incubation with a 1% MN solution, the vessels dilated enough to rupture the smaller vessels and cause a small hemorrhage. in the demarcated region.

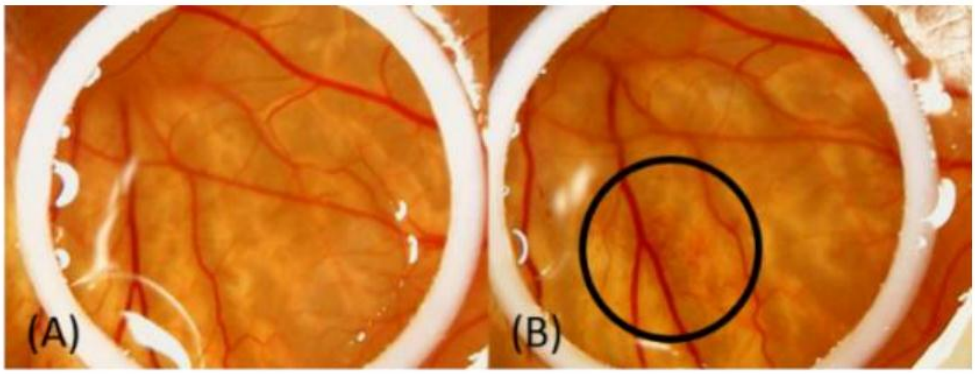

Figure 4: *Images of vessels in the chorioallantoic membrane model (A)before and (B) after sixty minutes of incubation with 1% MN.*

To evaluate the damage caused by the accumulation of PpIX in each situation, we performed PDT with the illumination using the LINCE® equipment (LINCE, MMOptics, Brazil) at the wavelength of 630 nm, with an intensity of 125 mW/cm2 for 20 min, totaling a dose of 150 J/cm2 . In Fig. 5 the necrosis generated in the tissues three days after the treatments using different incubation times of the cream Methyl-ALA with incorporated MN can be observed.

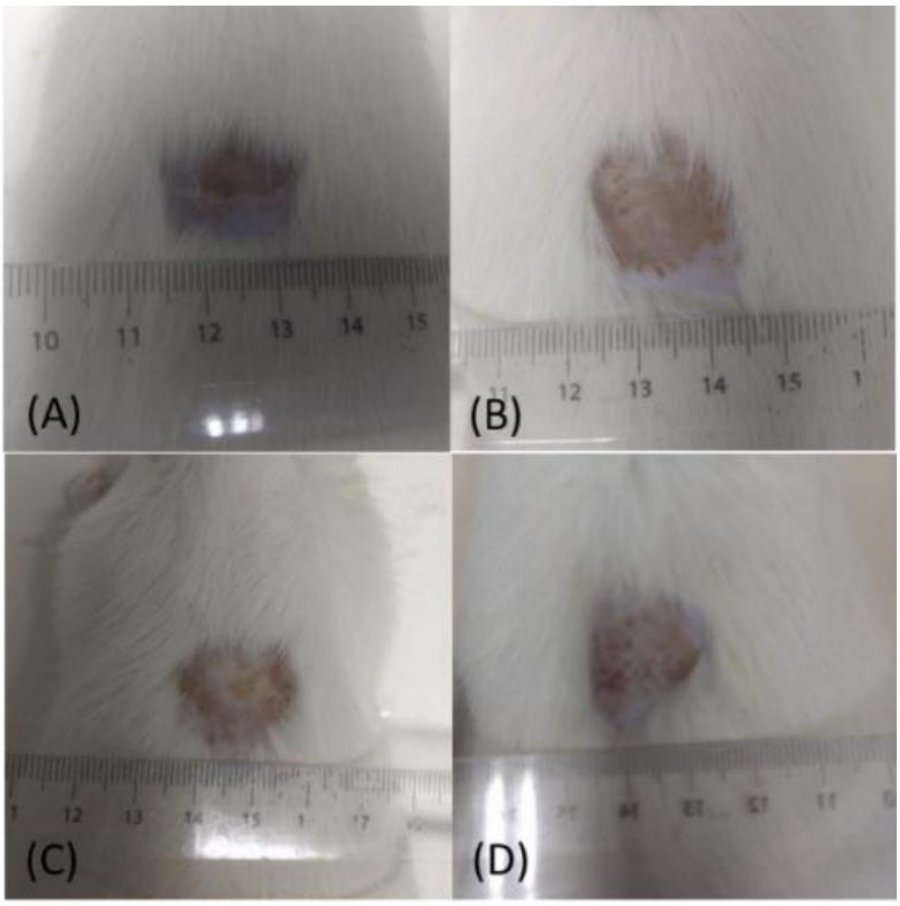

Figure 5: *Necrosis by PDT using (A) Methyl-ALA and MN for 1 hour; (B) Methyl-ALA and MN for 2 hours; (C) Methyl-ALA and MN for 3 hours and (D) pure Methyl-ALA for 3 hours.*

The analysis of the photographic images of damages and the histological slides showed that the incorporation of MN with Methyl-ALA increased the damage induced in the epidermis after PDT. Another important factor to ensure the effectiveness of PDT is the adequate presence of O2 molecules in the tissue. The PDT procedure is highly O2 dependent and its effectiveness is affected when there is a dramatic consumption of O2. Thus, to define the best protocol, the irradiance must consider the tissue oxygenation rate via blood flow to

ensure greater efficiency in the production of reactive oxygen species (ROS). [6–8] In a new study, vascular and tissue damages were evaluated for different PDT protocols applied in squamous cell carcinoma implanted in balb/c nude mice. The administration of PS occurred topically or systemically. For topical applications, about 30 μL of cream containing 20% MAL (PDT Pharma®, Cravinhos, Brazil) was positioned over the tumor, and incubated for one hour to accumulate PpIX. For systemic application, Photogem (Photogem®, Moscow, Russia) solution was prepared at 1.5 mg/kg of the animal's body mass concentration, diluted in saline, and injected intraperitoneally with an incubation time of 6 hours. All animals were irradiated using LINCE® equipment (MMOptics, São Carlos, Brazil) that is composed of LEDs emitting at 630 nm. The fluence deposited was 60 J/cm2 , varying in sort irradiation (100 mW/cm2 for 10 min) or long irradiation (50 mW/cm2 for 20 min). Angiographic images in and around the tumor region were recorded by optical coherence tomography (OCT) using the Telesto 320C model (ThorLab®, USA). Vessel density in the images was evaluated using ImageJ Software for the different protocols. It is possible to observe greater vascular destruction (lower vessel density) in tumors treated with topical photosensitization and short irradiation (Fig. 6a).

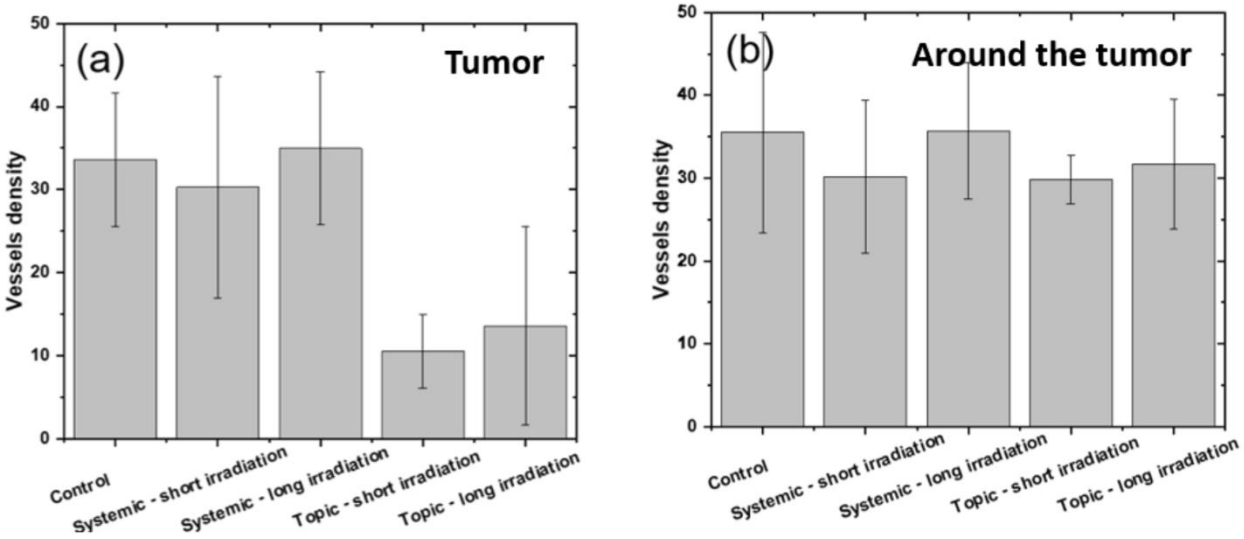

Figure 6: *Post PDT vessel density for different protocols assessed (a) in the tumor and (b) around the tumor.*

It is also possible to observe that both in the tumor and around it (Fig. 6a and b, respectively), the treatments with shorter irradiation periods and higher irradiance (all the protocols were set with the same fluence) presented a greater capacity to eliminate vessels, probably by causing higher temperature rise and shorter time for cell repair. Understanding tissue vascularization after treatment is essential for planning new protocols, especially in cases of treatments that require more than one session. The results of these studies are promising for the development of more effective topical PDT protocols for the treatment of non-melanoma skin lesions.

REFERENCES

[1] Wilson BC, Patterson MS. The physics, biophysics and technology of photodynamic therapy. Phys Med Biol 2008; 53: R61–R109.

[2] Willey A, Anderson RR, Sakamoto FH. Therapy for the Treatment of Actinic Keratosis Temperature-Modulated Photodynamic Therapy for the Treatment of Actinic Keratosis on the Extremities : Am Soc Dermatologic Surg 2014; 40: 1094–1102.

[3] Ishida N, Watanabe D, Mizutani K, et al. Heating increases protoporphyrin IX production in normal skin after delivery of 5-aminolevulinic acid by iontophoresis. Photodermatol Photoimmunol Photomed 25, 2009; 25: 333– 334.

[4] Stringasci MD, Moriyama LT, Vollet-Filho JD, et al. Temperature effect on the PpIX production during the use of topical precursors. Photodiagnosis Photodyn Ther 2020; 30: 101786.

[5] Stringasci MD, Vollet-Filho JD, Moriyama LT, et al. Investigation of protoporphyrin IX production induced by aminolevulinic acid combined with thermogenic and/or vasodilator substances. In: Hasan T (ed) 17th International Photodynamic Association World Congress. SPIE, p. 216.
[6] Li X, Kwon N, Guo T, et al. Innovative Strategies for Hypoxic- Tumor Photodynamic Therapy. Angew Chemie Int Ed 2018; 57: 11522–11531.
[7] Henderson BW, Busch TM, Snyder JW. Fluence rate as a modulator of PDT mechanisms. Lasers Surg Med 2006; 38: 489–493. [8] Wang W, Moriyama LT, Bagnato VS. Photodynamic therapy induced vascular damage: an overview of experimental PDT. Laser Phys Lett 2013; 10: 023001

DOI 10.24412/cl-37136-2023-1-181-185

NEUROMORPHIC LOCALIZATION MICROSCOPY FOR CELL BIOLOGY

ROHIT MANGALWEDHEKAR[1,2] AND DEEPAK NAIR[1]

1Centre for Neuroscience, Indian Institute of Science, India 2Department of Atomic and Molecular Physics, Manipal Academy of Higher Education, India

rohit.m3@learner.manipal.edu

rohitrm1998@gmail.com

ABSTRACT

Neuromorphic cameras have emerged as a novel sensor technology inspired by dynamic vision that work on the principle of detecting intensity changes as discrete events. These events are sampled asynchronously, independent of each pixel, resulting in sparse measurements. This inherent feature makes neuromorphic cameras ideal for imaging dynamic processes. By leveraging the unique properties of event-based sensors, we reconstruct event streams into images with temporal scales as low as 100 microseconds. We capitalize on the asynchronous recording of ON and OFF polarities, corresponding to increasing and decreasing intensity changes, respectively. This allows us to study the temporal variations of fluorescence emissions from single fluorescent particles, capturing their response to changes in excitation intensities. Moreover, we exploit the distinct characteristics of event-based sensors for precise localization of individual particles. By analyzing the ON and OFF processes independently, we achieve localization precision within the range of 10 nm. Additionally, through mathematical combinations of these independent processes from the same object, we surpass the diffraction limit and achieve sub-10 nm precision, pushing the boundaries of resolution. The white paper demonstrates the power of neuromorphic cameras in capturing dynamic processes and advancing the field of nanoscale imaging.

MAIN

In addition to its indispensable role in biological research, optical microscopy remains invaluable in the realms of materials science and nanotechnology. By enabling detailed observations and analyses, this technique contributes to advancements in various fields and continues to shape our understanding of the microscopic world. However, the resolution of the images is limited by the diffraction criterion as given by Abbe to be around 200nm. While this resolution is sufficient for many applications at the cellular level, there are several applications with regard to biomolecular interactions and organization that require higher resolutions in the order of a few nanometers. Super resolution microscopy encompasses a diverse range of advanced optical imaging techniques that surpass the diffraction limit of light, enabling the visualization and analysis of nanoscale structures and processes. The key principle underlying these techniques involves acquiring sparse data, either spatially or temporally, from fluorescently labelled samples thus allowing for imaging resolution limited molecules. By circumventing the limitations imposed by diffraction, super resolution microscopy opens up new avenues for investigating the intricate details of biological samples and other materials at unprecedented levels of spatial resolution [1]. While most microscopy techniques have been aided by state of the art detectors and cameras such as Electron multiplying Charge coupled devices(EMCCD) and scientific Complementary Metal oxide semiconductor(sCMOS), the detectors do not actively create sparsity in data [2]. Neuromorphic cameras, also known as event cameras or silicon retinas, revolutionize the field of light sensing by drawing inspiration from dynamic vision principles [3,4]. Unlike their counterparts, neuromorphic cameras asynchronously record these intensity changes as spikes, independent of other pixels in the visual field. Each pixel autonomously samples and detects events, resulting in two types of events: ON events (positive polarity) representing increases in light intensity, and OFF events (negative polarity) indicating decreases in intensity. Notably, pixels that perceive no change in intensity do not generate any data, minimizing the camera's digital footprint [3, 4]. The sparse nature of measurements obtained from neuromorphic cameras makes them

particularly well-suited for imaging dynamic processes characterized by sporadic events, such as the stochastic emission of individual molecules [2]. The unique detection paradigm of event cameras sets them apart from conventional cameras, such as EMCCDs, in terms of data output. Instead of capturing a stream of images at a fixed frame rate, event cameras provide data in the form of arrays or tuples containing timestamps, pixel coordinates, and polarity information. These sparse and asynchronous events represent changes in intensity, with ON events denoted by 1 and OFF events by 0. To reconstruct frames from the event data, a Computer Vision-based algorithm is employed on the Python platform. The algorithm accumulates events of different polarities into separate channel frames within user-defined temporal windows. One notable advantage of this post-acquisition image reconstruction approach is its flexibility in analyzing phenomena at different time scales. By reconstructing frames at varying time windows, researchers can gain insights into the dynamics of the phenomenon under investigation. Furthermore, the frame reconstruction process allows for flexibility in defining unequal time windows or even operating in the event regime, where each frame represents an arbitrary number of events and may not align in the time domain. This versatility enables researchers to explore and analyze the event data from different perspectives, enhancing our understanding of dynamic processes captured by neuromorphic cameras [2, 4]. Immobilized 100nm single fluorescent beads were illuminated by a 647 nm laser coupled with an acousto-optic tunable filter from Roper Scientific. The imaging process was controlled using MetaMorph software in streaming mode, with exposure times of 25 ms, 50 ms, 100 ms, and 200 ms. Fluorescence signals were captured using a highly sensitive EMCCD camera and a neuromorphic camera (DAVIS346, Inivation) using the DVS software. Freely diffusing beads in aqueous solution were also imaged using the same setup [2]. These cameras save continuously acquired data in the form of asynchronous event streams, typically in *.aedat4 or *.raw file formats depending on the camera model. To visualize and analyze the events, image reconstruction is performed. In this study, we developed a Python 3.7 code using the Computer Vision library (commonly known as OpenCV or cv2) to reconstruct the event stream data. The reconstruction of events into images is achieved by accumulating the events within a specified time or event window [2]. The accumulation or integration of polarities occurs by visualizing the ON events in the green channel and the OFF events in the red channel. It is important to note that when there are no intensity fluctuations, no measurements are recorded. Unlike standard cameras where the frame rate is predetermined, neuromorphic cameras allow the user to choose the frame rate post-acquisition. This flexibility enables the study of ensemble or single-particle fluorescence with a wide range of temporal resolutions [2].

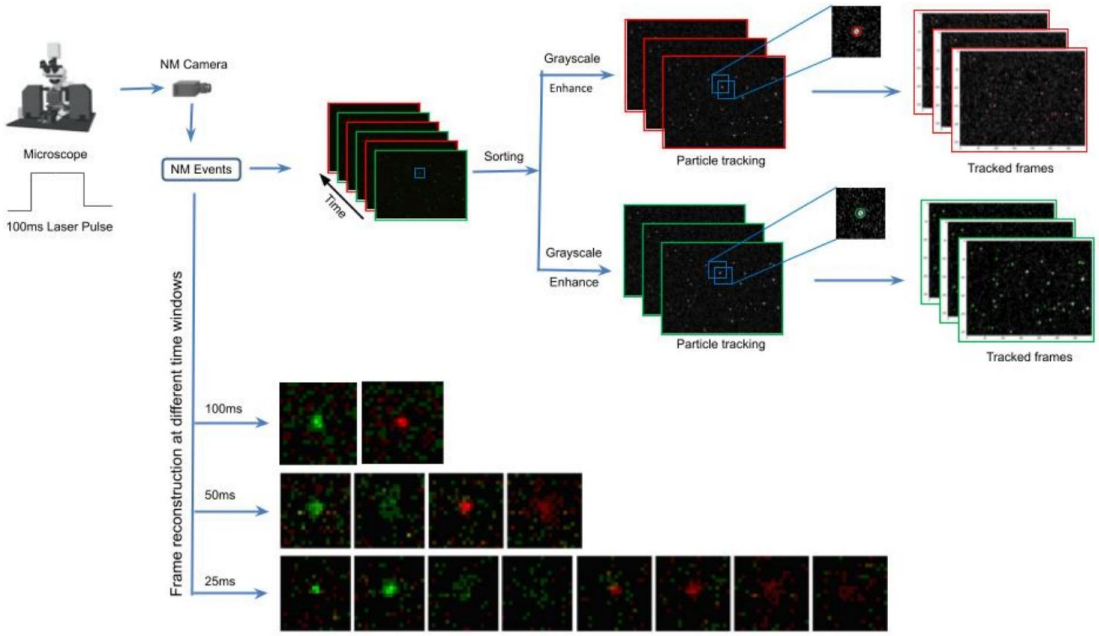

Figure 1: *Schematic of the workflow showing spatial(above) and temporal analysis.*

The image reconstruction process involved converting the recorded neuromorphic events into image frames at a rate of 5 ms per frame. The resulting time series clearly reveals the periodic nature of both the ON and OFF events, exhibiting a phase difference that accurately represents the true nature of the events. The

minimal overlap observed between the two sets of events highlights the low latency capabilities of neuromorphic cameras, further confirming their suitability for highspeed dynamic imaging applications [2].

To visualize the net polarity change occurring within a single particle over a specific time frame, the ON and OFF channels were summed together. This representation effectively demonstrates the overall polarity change exhibited by a single particle within the given time interval. Furthermore, the net polarities were cumulatively summed up in order to gain insight into the nature of integrated intensity of the fluorescence. In all three cases, the Fast Fourier Transform confirmed that the fluctuations in fluorescence was synchronous with the laser intensity [2].

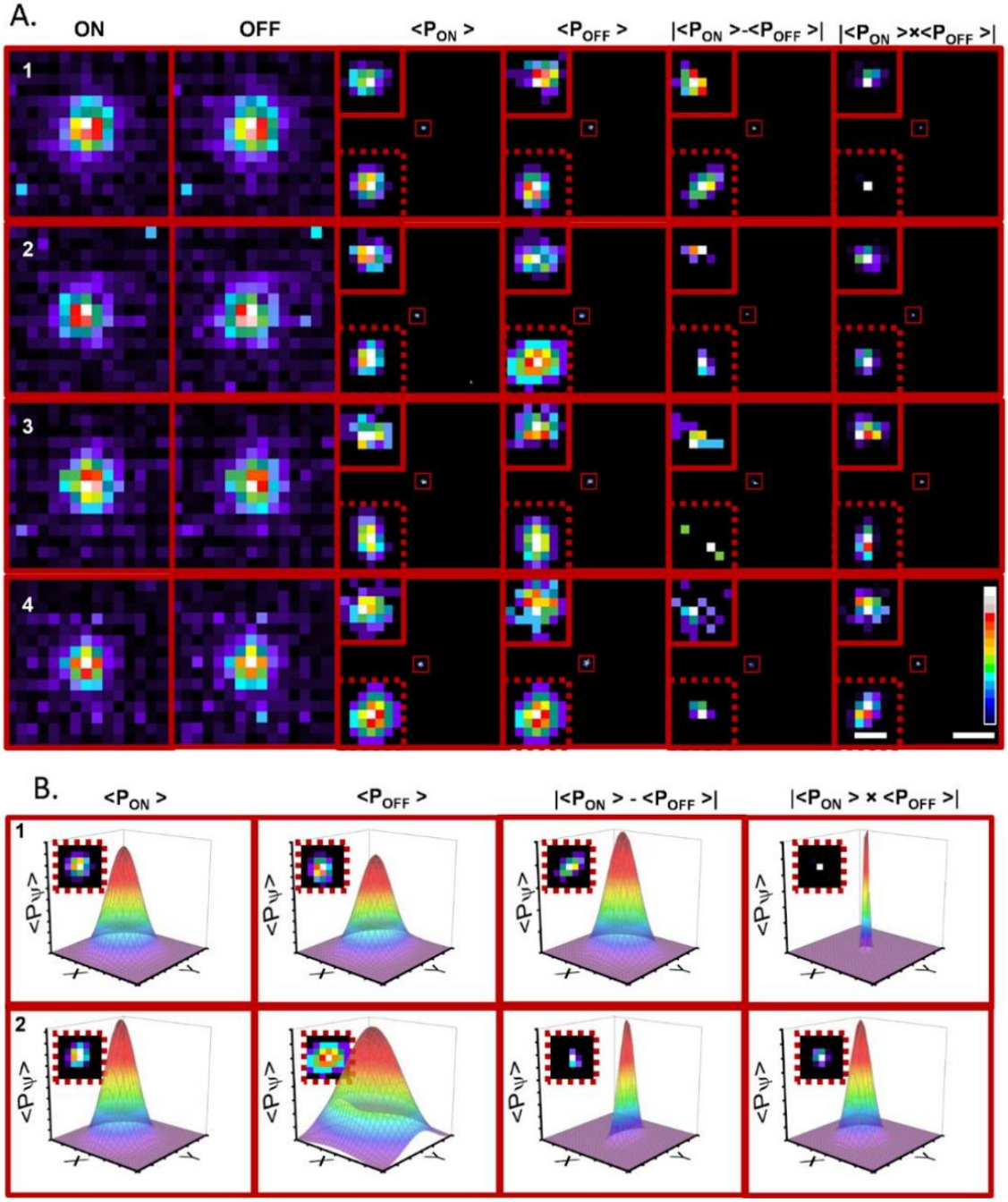

Figure 2: *Distributions of ON and OFF localizations and their combinations by subtraction and multiplication(from [2])*

By reconstructing images from the neuromorphic events and analyzing the resulting time series, we gain valuable insights into the dynamic behavior of the captured phenomena. This approach not only showcases the power of neuromorphic cameras in high-speed imaging but also allows for a more comprehensive understanding of the underlying processes taking place at a microscopic level [2].

The localization precisions of the immobilized single fluorescent particles were calculated by localizing the particles using DeepTrack, a deep learning based centroid tracking algorithm, and using a wavelet algorithm. The localization was performed on ON and OFF events independently. Furthermore, we were also able to show that the mathematical combination of the distributions of ON and OFF localizations could lead to further improving the localization precision. The localization precisions achieved are given in Table 1 [2].

Table 1: Localization precisions [2]

Localisation precision	ON	OFF	ON-OFF	ONxOFF
X(nm)	18.63	21.57	8.69	13.2
Y(nm)	17.8	21.65	22.54	11.47

On confirming the fidelity of the camera in the temporal and spatial regimes were confirmed, diffusing single particles were tracked thereby allowing us to study phenomena varying in the spatiotemporal paradigm. The event data was accumulated into various time windows and the single particles were tracked across this range of time periods. A panel of 5 single particles representing various amount of fractalization depending on the accumulation time is shown in Figure 3 [2].

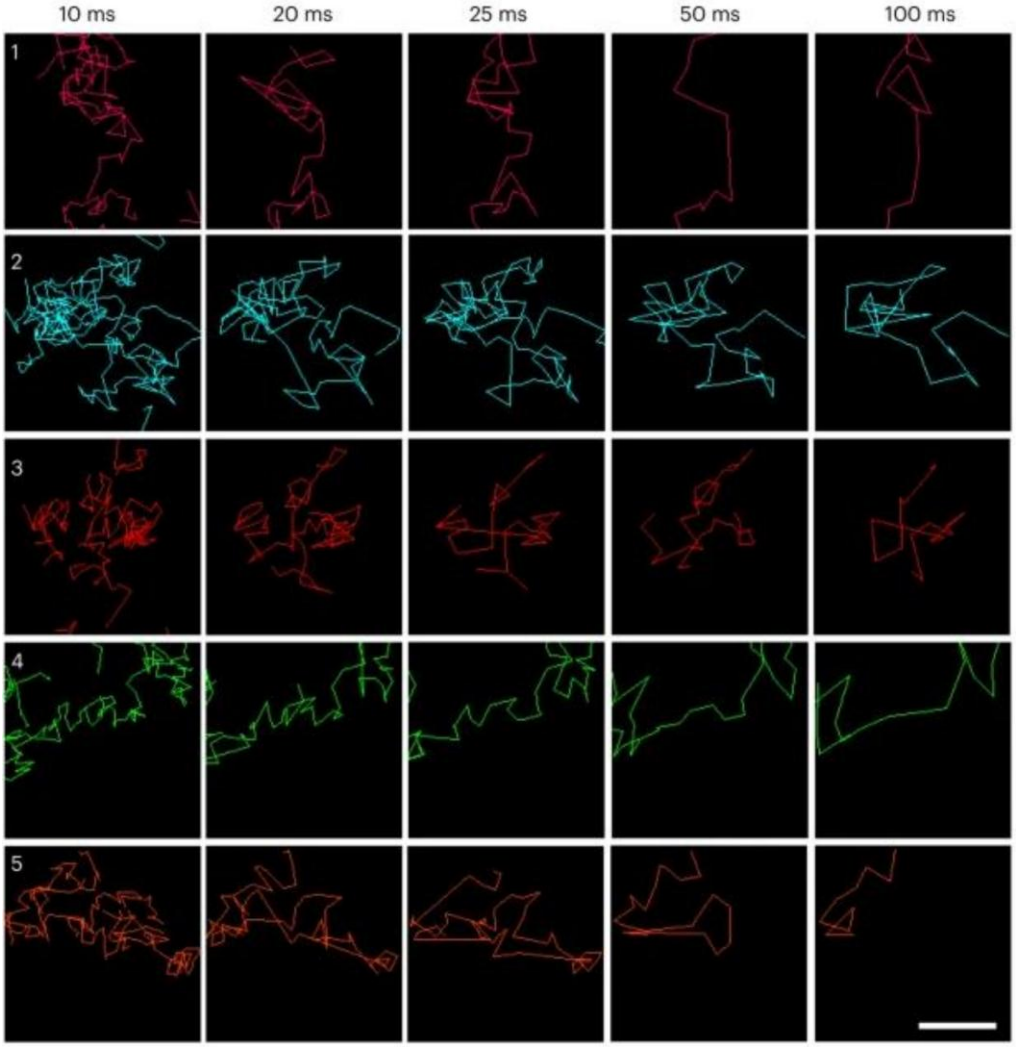

Figure 3: *A panel of 5 particles representing increasing fractalization with decreasing accumulation time[2]*

The unique capabilities of neuromorphic cameras enable them to effectively capture transient events, including the disappearance of fluorescence, making them a powerful tool for surpassing the diffraction limit. In our study, we have demonstrated that by combining the occurrence of ON/OFF events rather than analyzing them separately, we can achieve localization precision below the diffraction limit [2]. The localization precision

of diffraction limited single fluorescent paritcles relies on the number of photons (N) emitted per unit time ($\sigma \propto N^{-(1/2)}$). Nonlinear detection methods such as neuromorphic cameras, allow the localization of independent ON and OFF events at a higher precision, allowing these measurements to achieve the super Heisenberg limit ($\sigma \propto N^{-(\Delta/2)}$, where $\Delta \geq 2$) [2].

REFERENCES

[1] Hell SW, Sahl SJ, Bates M, Zhuang X, Heintzmann R, Booth MJ, Bewersdorf J, Shtengel G, Hess H, Tinnefeld P, Honigmann A. The 2015 super-resolution microscopy roadmap. Journal of Physics D: Applied Physics. 2015 Oct 14;48(44):443001.

[2] Mangalwedhekar R, Singh N, Thakur CS, Seelamantula CS, Jose M, Nair D. Achieving nanoscale precision using neuromorphic localization microscopy. Nature Nanotechnology. 2023 Jan 23:1-0.

[3] Gallego G, Delbrück T, Orchard G, Bartolozzi C, Taba B, Censi A, Leutenegger S, Davison AJ, Conradt J, Daniilidis K, Scaramuzza D. Event-based vision: A survey. IEEE transactions on pattern analysis and machine intelligence. 2020 Jul 10;44(1):154-80.

[4] Lakshmi A, Chakraborty A, Thakur CS. Neuromorphic vision: From sensors to event- based algorithms. Wiley Interdisciplinary Reviews: Data Mining and Knowledge Discovery. 2019 Jul;9(4):e1310.

DOI 10.24412/cl-37136-2023-1-186-188

HIGH-GRADE CERVICAL INTRAEPITHELIAL NEOPLASIA TREATMENT COMPARING PHOTODYNAMIC THERAPY PROTOCOLS

NATALIA INADA[1], CYNTHIA DE CASTRO[2], CAROLINA DA SILVA[3], LAURA MARCHETTI[3], WELINGTON LOMBARDI[3] AND VANDERLEI BAGNATO[1,4]

[1]São Carlos Institute of Physics, University of São Paulo, Brazil
[2]Federal University of São Carlos, Department of Morphology and Pathology, Brazil
[3]Woman Health Ambulatory, University of Araraquara, Brazil
[4]Hagler Institute for Advanced Studies, Texas A&M University, United States of America

nataliainada@ifsc.usp.br

ABSTRACT

Photodynamic therapy (PDT) is a therapeutical modality which offers a minimally invasive alternative for high-grade cervical intraepithelial neoplasia (CIN) treatment. This prospective randomized controlled clinical trial aims to compare two PDT protocols for histopathologically similar high-grade CIN treatment. In protocol 1, only ectocervix is illuminated; in protocol 2, the patients had both the ectocervix and endocervix illuminated simultaneously with LED plus LASER (a cylindrical diffuser fiber was coupled inside the squamocolumnar junction). In both groups was applied 20% MAL overnight (approximately 10 hours) and the irradiance delivered was 120 mW/cm^2, for 21 minutes, in a fluency rate of 150J/cm^2. Two years of follow-up showed 96% cure for group 1 and 87% for patients treated by protocol 2. No significant difference was observed between the two protocols. However, the number of patients who completed the two-year follow-up is still low and we expect better conclusions with more patients followed.

INTRODUCTION

Cervical cancer is squamous cell carcinoma often caused by Human papillomavirus (HPV) infection and has been the fourth-most common type of cancer and cause of death in women (1). The high-grade intraepithelial neoplasia (CIN) precedes cervical carcinoma and its major cause has been the persistent infection by HPV, and the vast majority of cervical cancer cases are caused by persistent or chronic HPV infection (2). Aminolevulinc acid (ALA) and methyl aminolevulinate (MAL) mediated photodynamic therapy (PDT) has showed be promising treatments for HPV-related diseases, such as condyloma acuminate and high grade CIN (3) (4) (5).

AIMS

We conducted a clinical trial designed to evaluate the efficacy and safety of photodynamic therapy (PDT) using a CerCa 150 System® available for the application of intra-canal fiber or no in patients with high grade cervical intraepithelial neoplasia.

METHODS

Patient Enrollment

The present study was approved by the Ethics Human Medical Ethics Committee (CEP 827.010, April 2013 CAAE: 90629218.8.0000.5383) and all patients provided informed written consent to participate. Patients with confirmed diagnosis of cervical intraepithelial neoplasia (CIN) grades 2/3 by histopathology were selected and invited to participate in this study. Thirty-seven patients were treated between April 2016 and October 2018 and monitored for two years. The patient inclusion was random and decided by the clinicians involved in the research, depending on the type of the transformation area and the lesion site: PDT LED ectocervix (1 or 2 session); PDT LED + LASER endocervix group (1 or2 sessions).

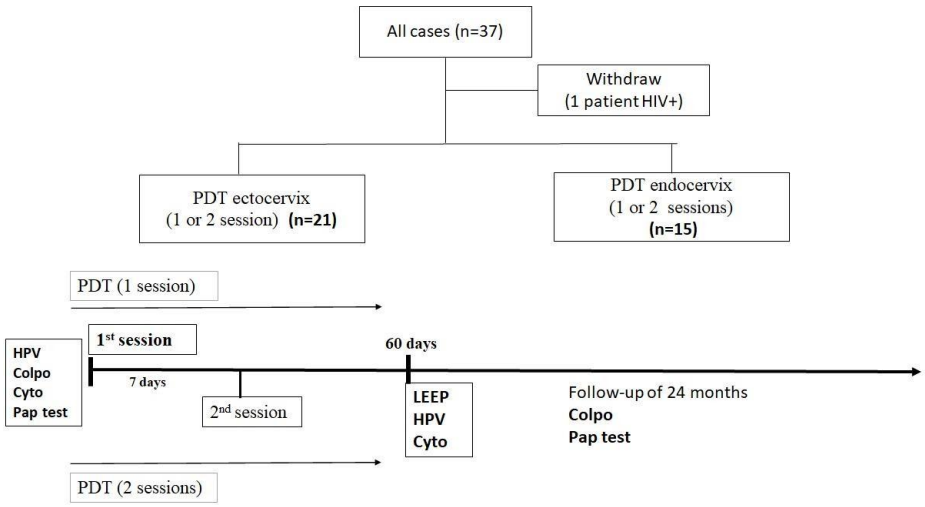

(a)

Figure *(a) Patient selection and study design. PDT: Photodynamic therapy; Cito: oncotic cervical cytology; Colpo: colposcopy;LEEP: loop electrosurgical excision procedure, Pap test: Papanicolau test.*

Photodynamic Therapy

When patients were treated two times, the interval between sessions was a week. The methyl aminolaevulinic acid (MAL) 20% cream (PDTPharma, Cravinhos, Sao Paulo, Brazil) was administered by the patient in the cervix by 10 hours (overnight). For illumination, the patient in the gynecological position was treated by the equipment CerCa 150 System® (MMOptics, São Carlos, São Paulo, Brazil). This device has LEDs (light-emitting diodes) emitting at 630 nm and can be anatomically positioned to illumine the entire ectocervix and also a cylindrical light diffuser (MedLight S.A., model RD30) for homogenous light distribution to the endocervical canal. The illumination was performed by delivering 120 mW/cm^2 for 21 minutes and fluency rate of 150 J/cm^2. Two months after one or two procedures, a conservative Excision of Transformation Zone (ETZ) is performed for histopathological analysis. The viral load test (digene® HC2 HPV DNA, Qiagen) was carried out in two moments: a) before the treatment and b) 60 days after LEEP.

RESULTS

The average age was 38,52±9,79 years to women treated with LED and 33,06±8,84 years to women treated with LED+LASER. LED was applied to 21 women (11 women received one session and 10 women received two sessions) and LED+LASER was applied to 15 women (5 women received one session and 10 women received two sessions).

60 days after treatment, the PDT performed on the ectocervix, LED, showed 52% of positive results in the cytological exams and 19% in the LEEP product. On the other hand, women treated intracanal, LED+LASER, had a 40% positive overall response in cytological exams and 13% in histopathological analysis.

The decrease in viral load, analyzed 60 days after one or two sessions of PDT, showed exactly the same percentage of decrease, comparing the two protocols. No protocol showed complete elimination of the viral load. This result generates an important discussion because this test, despite being recommended and the gold standard, may present flaws that dependon factors such as sample collection and storage.

Table 1*: Summary of results from patients treated with photodynamic therapy (PDT) for cervical intraepithelial neoplasia(CIN) 2/3.*

LED

Results		**General Response of PDT (%)**		**Total**
		Positive	Negative	
60 days follow up	**Cytology**	52	48	100
	Pathology of LEEP	19	71	100

2 years follow up		**96**	**4 (recurrence)**	100

LED+LASER

Results		**General Response of PDT (%)**		**Total**
		Positive	Negative	
60 days follow up	**Cytology**	40	60	100
	Pathology of LEEP	13	87	100
2 years follow up		**86.66**	**13.33 (recurrence)**	100

Considering all lesions with positive responses to PDT with follow-up of two years, there were 96% positive responses (n=20) with PDT in patients treated for LED and 4% recurrences (n=1). The intracanal LED+LASER treatments showed 86.66% (n=13) of positive response and 13.33% of lesion recurrence (n=2).

CONCLUSION

This retrospective study was postponed due to the coronavirus (Covid-19) pandemic. We concluded that just illuminating the cervix from the outside (ectocervix) with LEDs promoted a higher cure rate than the protocol that associates LED lighting with LASER (ecto + endocervix). We also concluded that the follow-up of this type of treatment should always belong-term (two years at least).

DISCLOSURES IF REQUIRED:

The authors declare no conflict of interest.

Acknowledgments

This research was funded by Fundação de Amparo à Pesquisa do Estado de São Paulo (FAPESP 2013/07276-1 and 2014/50857-8), Financiadora de Estudos e Projetos/Ministério da Saúde (FINEP/MS 01.130430.00) and Conselho Nacional de Desenvolvimento Científico e Tecnológico (CNPq 465360/2014-9).

REFERENCES

[1] Bray F, Ferlay J, Soerjomataram I, Siegel RL, Torre LA, Jemal A. Global cancer statistics 2018: GLOBOCAN estimates of incidence and mortality worldwide for 36 cancers in 185 countries. CA Cancer J Clin. Nov;68(6):394–424, 2018. http://doi.wiley.com/10.3322/caac.21492.

[2] Hillemanns P, Petry K-U, Soergel P, Collinet P, Ardaens K, Gallwas J, et al. Efficacy and safety of hexaminolevulinate photodynamic therapy in patients with low-grade cervical intraepithelial neoplasia. Lasers Surg Med. 46(6):456–61, 2014. http://www.ncbi.nlm.nih.gov/pubmed/24799181.

[3] Xie J, Wang S, Li Z, Ao C, Wang J, Wang L, et al. 5-aminolevulinic acid photodynamic therapy reduces HPV viral load via autophagy and apoptosis by modulating Ras/Raf/MEK/ERK and PI3K/AKT pathways in HeLa cells. J Photochem Photobiol B Biol. 194:46–55, 2019. https://doi.org/10.1016/j.jphotobiol.2019.03.012.

[4] Wang J, Li S, Li Z, Li J, Peng X, Li S, et al. Human papillomavirus DNA detection-guided ALA-photodynamic therapy for anogenital condyloma acuminata: A report of two cases. Photodiagnosis Photodyn Therapy. 25:460–2, 2019. https://doi.org/10.1016/j.pdpdt.2019.02.003.

[5] Inada, N.M.; Buzzá, H.H.; Leite, M.F.M.; Kurachi, C.; Trujillo, J.R.; de Castro, C.A.; Carbinatto, F.M.; Lombardi, W.; Bagnato,
V.S. Long Term Effectiveness of Photodynamic Therapy for CIN Treatment. Pharmaceuticals 12, 107, 2019. https://doi.org/10.3390/ph12030107.

DOI 10.24412/cl-37136-2023-1-189-192

DEVELOPMENT OF COMBINED PHOTOTHERMAL/PHOTODYNAMIC THERAPY USING A MODEL TUMOR: PILOT STUDY

VADIM D. GENIN[1,2]*, ALLA B. BUCHARSKAYA[1,2,3], NIKITA A. NAVOLOKIN[1,3], GEORGY S. TERENTYUK[3], BORIS N. KHLEBTSOV[4], NIKOLAI G. KHLEBTSOV[1,4], VALERY V. TUCHIN[1,2,5], ELINA A. GENINA[1,2]

1 – Saratov State University, st. Astrakhanskaya, 83, 410012, Saratov, Russia
2 – Tomsk State University, 36 Lenin Ave., 634050, Tomsk, Russia
3 – Saratov State Medical University, st. Bolshaya Kazachya, 112, 410012, Saratov, Russia
4 – Institute of Biochemistry and Physiology of Plants and Microorganisms, Federal Research Center "Saratov Scientific Center of the RAS", Entuziastov Ave., 13, Saratov, 410049 Russia
5 – Institute of Precision Mechanics and Control Problems of the Russian Academy of Sciences, Federal Research Center "Saratov Scientific Center of the RAS", st. Rabochaya, 24, Saratov, 410028 Russia
*e-mail: versetty2005@yandex.ru

The growth of a number of oncological diseases stimulates extensive development of both early tumor diagnostics and therapy methods. A promising area of research is using a combination of several methods, for example, photodynamic therapy (PDT) and plasmonic photothermal therapy (PPT) [1, 2]. Many research groups have proposed new treatment models that are based on the combination of PDT and PPT, using various types of nanoparticles and photosensitizers [3-6].

The purpose of the study was to develop a combined technology of PPT and PDT in rats with model tumors.

As a material of the study 4 outbreed albino male rats with a subcutaneously grafted experimental model tumors of liver bile ducts cancer (cholangiocarcinoma of the PC-1 line) were used. All rats were injected with a photosensitizer solution and a suspension of gold nanorods (GNRs) intratumorally at three points each. The points were equidistant from the center of the tumor to ensure a more uniform distribution of both nanoparticles and dyes inside the tumor. GNRs were functionalized with PEG-300. For PDT two rats were injected by Photosens (Niopik, Russia) solution (PS) and two ones were injected by indocyanine green (Sigma-Aldrich Cheme Gmbh, Germany) solution (ICG). The maximum absorption of the PS solution was at a wavelength of 680 nm, and the maximum absorption of the ICG solution was at a wavelength of 795 nm. The details of intratumoral injections design are presented in Table 1.

An hour after the injections, the tumors of rats 1 and 2 were irradiated percutaneously with a 660 nm laser Latus-T (Atkus, Ltd, Russia) at a power density of 0.5 W/cm^2 for 15 min (for PDT) and then with an 808 nm infrared laser (LS-2-N-808-10000, Russia) at a power density of 2.3 W/cm^2 for 15 min (for PPT). The tumors of rats 3 and 4 were irradiated percutaneously only with an 808 nm infrared laser at a power density of 2.3 W/cm^2 for 15 min (for PDT and PPT simultaneously). Figure 1 is shows the design of the experiment. The diffuse reflectance spectra before laser irradiation, after PDT and after PPT in range 450-2100 nm were taken from all tumors using commercial available spectrometers USB4000-Vis-NIR (Ocean Optics, USA) and NIRQuest (Ocean Optics, USA).

The withdrawal of animals and sampling of tumor tissues for histological examination was performed 72 hours and 21 days after the therapy. Morphological studies of tumor tissue were performed on tumor sections stained by standard methods and with immunohistochemical staining for the proliferation marker Ki-67 and the apoptosis marker Bax.

Table 1. Design of intratumoral injections of photosensitizer solutions and GNRs suspension.

Rat No.	Tumor me, cm^3	Photosensitizer	Solvent	Volume of photosensitizer solution	Photosensitizer centration in the solution	Volume of R suspension	GNR ntration in the uspension
Rat 1	~3.8	Photosens	Saline solution	0.30 ml	2 mg/ml	1.25 ml	400 mg/ml
Rat 2	~8.2			0.45 ml	2 mg/ml	2 ml	400 mg/ml
Rat 3	~2.5	Indocyanine green	PEG-300	0.18 ml	10 mg/ml	0.8 ml	400 mg/ml
Rat 4	~4.7			0.20 ml	10 mg/ml	1.57 ml	400 mg/ml

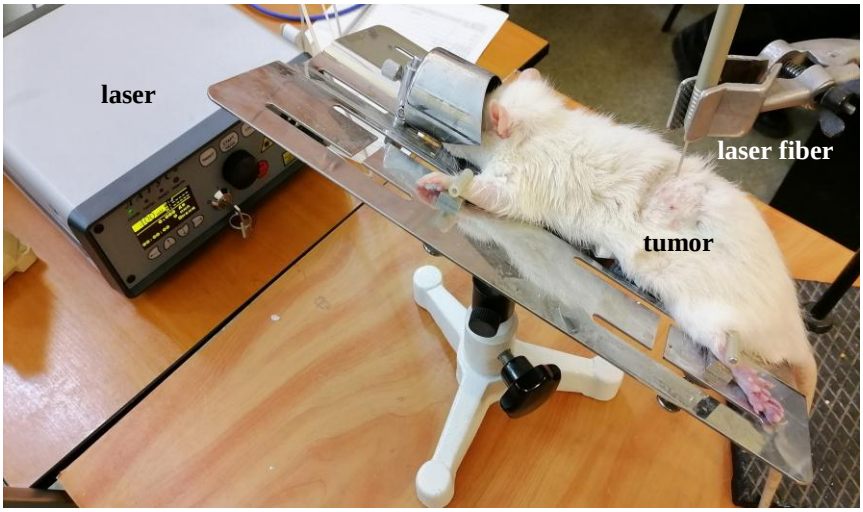

Figure 1. *The design of the experiment*

The local heating temperature of the skin above the tumor was measured with an IRI4010 thermal imager (IRYSYS, UK). The kinetics of skin surface heating over tumors is presented in Figure 2.

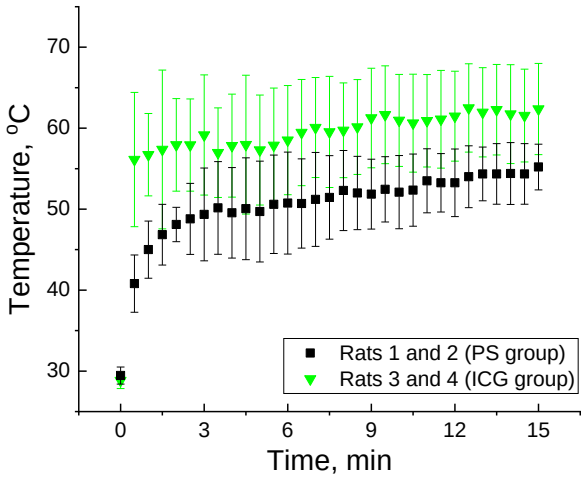

Figure 2. *Kinetics of skin surface over the tumor heating averaged by groups of rats*

During the combined therapy in PS and ICG groups, there was a pronounced rise in the temperature of local heating of the tumor up to 55.2±2.8 and 62.4±5.6 ºC, respectively. Necrosis of up to 95% of the tumor was observed in the PS group after 72 hours. In rat 4 (ICG group) after 72 hours, pronounced necrotic changes were observed in the tumor tissue, necrosis fields occupied up to 80% of the area. Preserved tumor cells were found only on the periphery of the tumor; they showed a decrease in the expression of the proliferation marker and an increase in the expression of the apoptosis marker. In rat 3 (ICG group) after 21 days, there was a complete destruction of the tumor.

Diffuse reflectance spectra of rat tumors at different stages of the experiment are presented in the Figure 3.

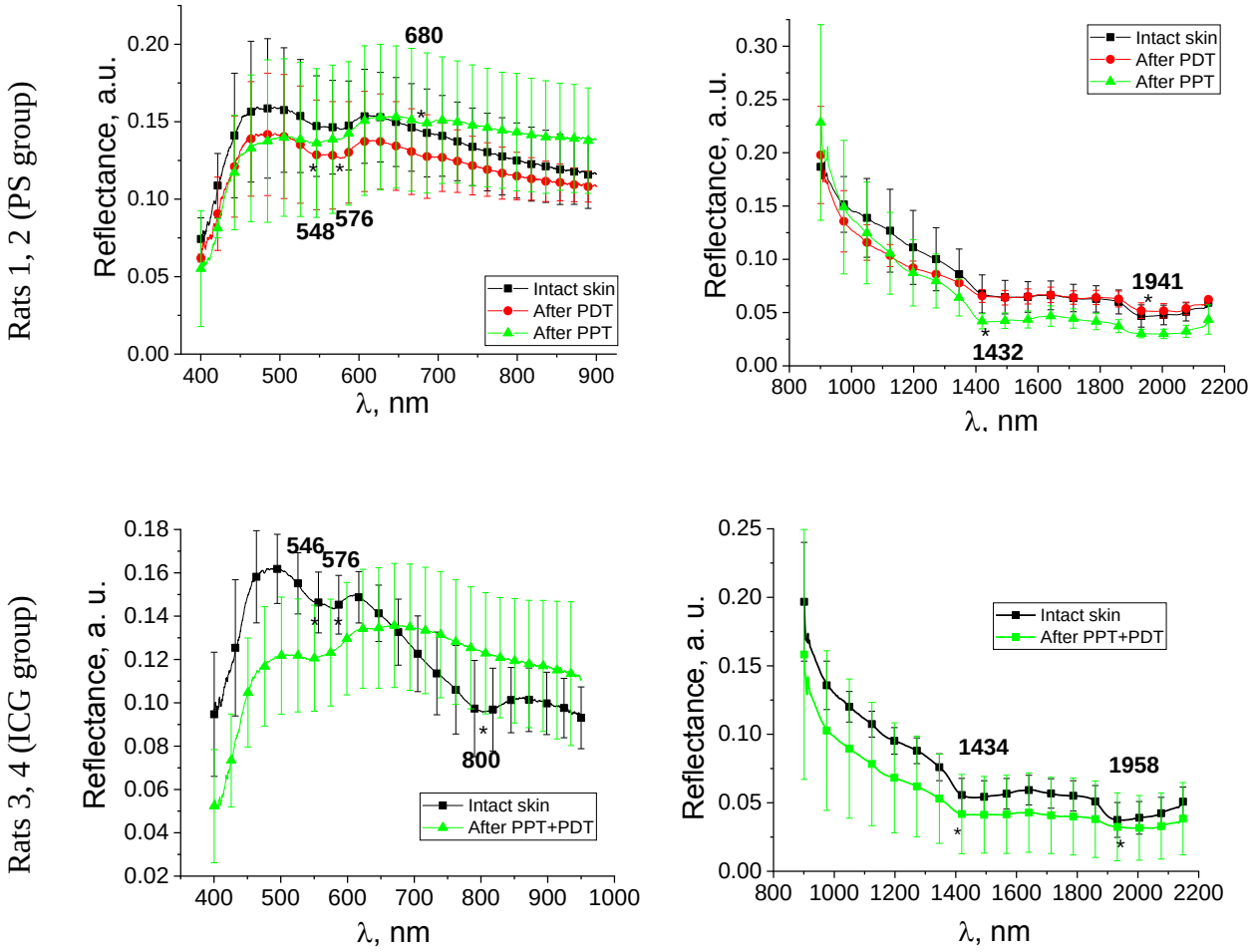

Figure 3. *Diffuse reflectance spectra of rat skin surface over the tumor at different stages of the experiment averaged by groups*

The diffuse reflectance spectra of all tumors demonstrate the presence of hemoglobin in the oxygenated form in the tumor (Q-bands at 546-548 and 576 nm). It can be seen that in all rats after the PPT the bands corresponded to the hemoglobin absorption peaks is smoothed out, which may be due to the transition of hemoglobin to a deoxygenated form. Also visible are dips due to the presence of PS (680 nm in rats 1 and 2) or ICG (800 nm in rats 3 and 4) in the tumors. In rats 3 and 4, the absorption band at 800 nm disappears after laser irradiation, which may be due to the photobleaching effect. Absorption bands of water are observed at 1432-1434 and 1941-1958 nm. The change in the NIR absorption bands of water is associated with dehydration due to high temperature during PPT.

The proposed combination PPT/PDT therapy technology caused pronounced damage to tumor tissue in rats with transplanted cholangiocarcinoma. Our results are in a good agreement with the result of other authors [1-6]. For example, Yan et al, which used ICG liposomes for PTT/PDT treatment of mice breast tumors [3]. The tumors were irradiated by the 808 nm laser at a power density of 1.0 W/cm^2 for 10 min. Almost complete regression of the tumor was achieved.

The work was supported by the RSF grant no. 23-14-00287.

REFERENCES

[1] Yang, Z.; Sun, Z.; Ren, Y.; Chen, X.; Zhang, W.; Zhu, X.; Mao, Z.; Shen, J.; Nie, S. Advances in Nanomaterials for Use in Photothermal and Photodynamic Therapeutics (Review). Mol Med Rep 20, 5-15 (2019).

[2] Bucharskaya A., Khlebtsov N., Khlebtsov B., Maslyakova G., Navolokin N., Genin V., Genina E., Tuchin V. Photothermal and photodynamic therapy of tumors with plasmonic nanoparticles: challenges and prospects. Materials 15, 1606 (2022).
[3] Yan, F.; Wu, H.; Liu, H.; Deng, Z.; Liu, H.; Duan, W.; Liu, X.; Zheng, H. Molecular Imaging-Guided Photothermal/Photodynamic Therapy against Tumor by iRGD-Modified Indocyanine Green Nanoparticles. J Control Release 224, 217-228 (2015).
[4] Choi, J.; Lee, S.-E.; Park, J.-S.; Kim, S.Y. Gold Nanorod-Photosensitizer Conjugates with Glutathione-Sensitive Linkages for Synergistic Cancer Photodynamic/Photothermal Therapy. Biotechnol Bioeng 115, 1340-1354 (2018).
[5] Ashkbar, A.; Rezaei, F.; Attari, F.; Ashkevarian, S. Treatment of breast cancer in vivo by dual photodynamic and photothermal approaches with the aid of curcumin photosensitizer and magnetic nanoparticles. Sci Rep 10, 21206 (2020).
[6] Yang, J.; Hou, M.; Sun, W.; Wu, Q.; Xu, J.; Xiong, L.; Chai, Y.; Liu, Y.; Yu, M.; Wang, H.; Xu, Z.P.; Liang, X.; Zhang, C. Sequential PDT and PTT Using Dual-Modal Single-Walled Carbon Nanohorns Synergistically Promote Systemic Immune Responses against Tumor Metastasis and Relapse. Adv Sci 7, 2001088 (2020).

DOI 10.24412/cl-37136-2023-1-193-200

HOW IS PHOTONICS POTENTIATING COMBINATIONS OF PHOTODYNAMIC THERAPY WITH OTHER NON-INVASIVE THERAPEUTIC TECHNOLOGIES FOR ENHANCED EFFICACY AND SELECTIVITY?

SANDILE SONGCA[1] AND OLUWATOBI OLUWAFEMI[2]

[1]School of Chemistry and Physics, Pietermaritzburg, University of KwaZulu-Natal, South Africa
[2]Department of Chemical Sciences, University of Johannesburg, Doornfontein, Johannesburg, South Africa

songcas@ukzn.ac.za

ABSTRACT

Photodynamic therapy (PDT) utilizes light to activate special compounds known as photosensitizers (PSs) to produce reactive oxygen species (ROS) from oxygen that is present at the disease sites and cells. The penetration depth of human tissue by light is quite shallow. One of the photonics approaches in light delivery toward enhancing PDT includes using laser light sources and optic fiber delivery to reach deep-seated disease sites. Several innovations are available in the market for light distribution within the disease site at the end of the optic fiber. PDT has been enhanced by combination with other minimally invasive therapies such as photothermal therapy (PTT), sonodynamic therapy (SDT), magnetic hyperthermia therapy (MGH), radiotherapy (RT), cold atmospheric pressure plasma therapy (CAPP), and immunotherapy (IT), to name a few. Photonics often play well-defined roles in each of these combination therapies, resulting in synergistic enhancement against cancer and bacterial infections and an increasing scope of other applications. The current state of the art of PDT involves nanoconjugate systems that are loaded with copious amounts of the PS to improve the pharmacokinetics, delivery, targeting, and specificity of disease sites and cells. The purpose of the nanoconjugate approach is to induce very little or no immune response while the nanoconjugate is still in systemic circulation to selectively target the disease site and cells, where it is selectively taken up and retained by the disease cells. While an increasing number of modalities of the approach employ systems that respond to unique characteristics of the disease site and cell external and internal microenvironments to release the PS, an increasing number of nanoconjugates are stimulated by external stimuli to do so. The external stimuli reported in the literature include light, MGH, ultrasound (US), and X-rays. Therefore, photonics has a major role to play in stimulus-responsive PS release. Our research group has developed a number of nanoconjugate systems for PDT and combinations thereof with other minimally invasive technologies. For example, nanoconjugates combining PDT with PTT and those combining PDT with MGH have been prepared and are showing good results against cell lines in vitro. The appropriate literature update on photonics applications to potentiate PDT introduced in this paper focuses on three key applicators, namely basic, preclinical, and clinical research. The paper also introduces some of our research results of photonics applications in PDT, PTT, MGH, and combinations thereof. The paper concludes by highlighting state-of-the-art photonics devices in basic research and the clinic and recommendations on potential areas of further research and innovation. As part of these concluding remarks, the paper also comments on the future research directions in our research group based on the nanoconjugates we have developed and specific disease applications of national interest in South Africa.

INTRODUCTION

Light has been used in hospital physiotherapy and medicine for more than seven decades [1]. In contrast, according to Dr. Tomislav Meštrović, the light therapy approach itself dates back more than three thousand years [2]. Nowadays, light has found more nuanced therapeutic applications. For example, in PDT, light is used to photosensitize the generation of ROS in the disease microenvironment. ROS are molecular species derived from molecular oxygen that are highly reactive and, therefore, toxic. They include singlet excited state oxygen,

hydroxyl anions, radical anions, peroxide, and superoxide radicals and anions, that are generated from the type I mechanism, shown in Figure 1 using a Jablonski diagram.

Photonics in Photodynamic Therapy

According to Algorri et al. (2021), photonics in PDT is composed mainly of three approaches, which include irradiation using halogen lamps, irradiation with LEDs, and laser irradiation used in the laboratory and the clinic [3]. To enhance selectivity for the disease over normal host tissue, it is necessary to align the distribution and dosimetry of the light energy with the morphology of the disease. While this is difficult to achieve with non-coherent light sources such as halogen lamps and LEDs, coherent laser light sources are often equipped with specialized optic fiber for transmitting the laser light energy to the disease site. More importantly, however, these laser light transmission optic fibers are equipped with devices that distribute the light energy evenly over the disease, depending on the location, histology, and anatomy [4]. The trouble with optic fiber laser light energy transmission and delivery is that it is quite invasive. Researchers have come up with a number of non-invasive and minimally invasive technologies for delivering light energy to activate PSs in deep-lying diseases. These include SDT, MGH, and RT. Additionally, a novel innovation involving miniature implantable devices that are wirelessly activated to emit the desired light frequency from within the disease site has been reported [5]. Furthermore, photochemical internalization (PCI) potentiates PDT by incorporating organic dye PSs into the bilayer of endocytic liposomes, followed by endocytosis. Once inside the disease cells, the PSs are released by light activation, which causes photodynamic disruption of the endocytosed liposomal vesicle membrane bilayer into the cytosol [6].

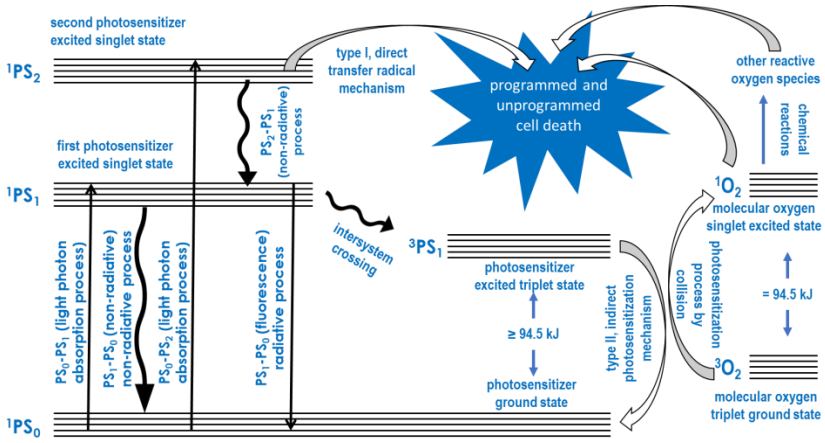

***Figure 1**: Jablonski diagram showing the mechanism of photodynamic therapy.*

Mechanism of Photodynamic Therapy

Upon light absorption, the PS is excited from its singlet ground state to the singlet excited states ($^1PS_0 \rightarrow {}^1PS_1$, $^1PS_0 \rightarrow {}^1PS_n$, n = 1, 2, …). Excitation to higher singlet excited states is almost always followed by non-radiative relaxation back to the first singlet excited state ($^1PS_n \rightarrow {}^1PS_1$), enhancing the population of the first singlet excited state ($^1PS_1$). Due to the enhanced population, the first singlet excited state relaxes by multiple mechanisms, including non-radiative intersystem crossing, fluorescence, and other non-radiative relaxations. The critical transition for PDT is the intersystem crossing ($^1PS_1 \rightarrow {}^3PS_1$) because it involves a spin state change that takes the PS to an excited triplet state from which radiative relaxation to the singlet ground state is forbidden. Because the excitation of molecular oxygen from its triplet ground state to its singlet excited state ($^3O_2 \rightarrow {}^1O_2$), which requires change from the triplet to the singlet state, has an equal energy differential and reverse spin state change, the energy transfer between the triplet state of the PS ($^3PS_1$) and molecular oxygen in its triplet ground state ($^3O_2$) occurs when the molecules collide, in a process known as photosensitization. The photosensitization of molecular oxygen from its triplet ground state to the singlet excited state ($^3PS_1 + {}^3O_2 \rightarrow {}^3PS_0 + {}^1O_2$) is an essential initial step in ROS production. Excited singlet state oxygen leads to other

ROS, such as hydroxyl and peroxide radicals and anions. Therefore, this process is made possible by two critical photonics factors. The first factor is the energy differential between the singlet excited state of molecular oxygen and its triplet ground state $\Delta E_{O2} = [E(^1O_2) - E(^3O_2)]$ and the energy differential between the triplet excited state of the PS and its singlet ground state $\Delta E_{PS} = [E(^3PS_1) - E(^1PS_0)]$. The energy differential between the PS species, ΔE_{PS}, must be equal to or marginally greater than the energy differential between the molecular oxygen species, ΔE_{O2}, which is equal to 94.5 kJ/mol ($\Delta E_{PS} \geq \Delta E_{O2} = 94.5$ kJ/mol). The second is the spin state differential between the ground and excited states. This renders the electronic transitions untenable for both the PS and molecular oxygen because a forbidden change between triplet and singlet spin states is required for each of these transitions. However, when the $^3PS_1$ and $^3O_2$ molecules collide, simultaneous energy transfer and triplet/singlet spin state change occurs.

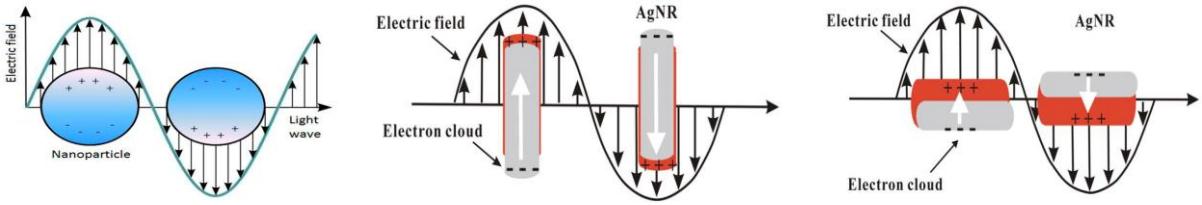

(a) spherical resonance (b) longitudinal resonance (c) transverse resonance

***Figure 2**: illustration of (a) the resonance mechanism for spherical nanostructures, (b) the tudinal surface plasmon resonance, and (c) transverse surface plasmon resonance. Reproduced from er et al. (2015) [7] and Jiang et al. (2014) [11] under the appropriate creative commons attribution licenses.*

Mechanism of Photothermal Therapy

Light is also used to generate therapeutic localized hyperthermia. For example, due to the local surface plasmonic resonance (LSPR) of their surface electrons, some nanoparticles absorb light and transform the light energy into heat. Therefore, when such nanoparticles are irradiated after they are embedded in the disease site or selectively taken up by the disease cells, they can generate heat there. The disease cells will therefore be killed provided the generated heat exceeds the threshold for the disease cells enough to overwhelm the biological response of heat shock proteins. The LSPR mechanism of these nanoparticles is shown in Figure 2. Light comprises perpendicularly orientated synchronous electric and magnetic field components with sinusoidal intensity variation. The sinusoidally changing electric and magnetic fields cause a coupled resonance of the nanoparticle surface electrons, thus absorbing the energy and converting it to heat. This energy conversion occurs mainly by hysteresis [8]. Theoretical analytical research [9,10] and empirical evaluation [11,12] have shown that the LSPR is more intense with longitudinal nanostructures than non-longitudinal ones. Hence the LSPR absorption band arising from longitudinal surface electron resonance is more intense compared to the absorption band arising from transverse surface electron resonance, which is arguably of the same magnitude as that of non-longitudinal nanostructures of similar diameter. Longitudinal nanostructured materials known for applications in photothermal hyperthermia include nanorods of gold, silver, iron oxide, and carbon nanotubes. Others include nanosheets of several chalcogenides, including manganese, molybdenum, and copper. The range of non-longitudinal structures includes metal nanostructures such as silver and gold, carbon structures such as graphene dots and fullerenes, and nanostructures of oxides of many metals.

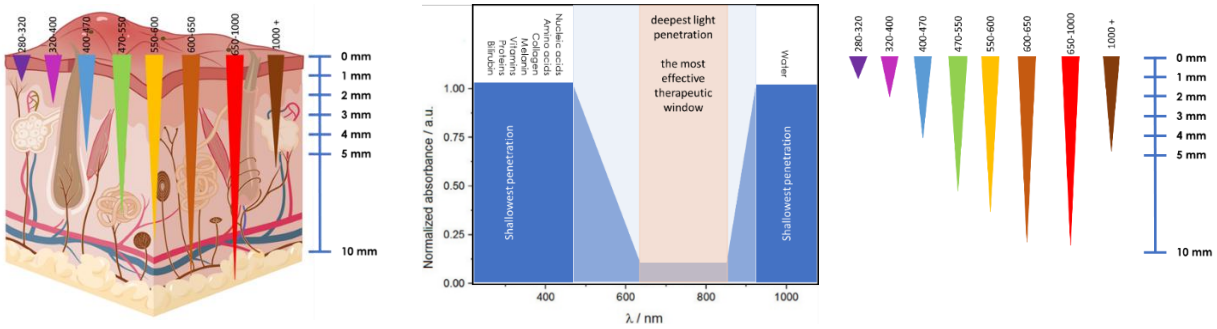

(a) light penetration through the skin

(b) therapeutic window

(c) deepest penetrating frequencies

Figure 3*: illustrations of the therapeutic window showing the deepest penetrating light frequencies and light propagation through the skin according to Rugguiero et al. (2013) [13].*

Biomedical Light Sources

For PDT and PTT, halogen lamps and light-emitting diode (LED) light sources are widely used. PDT and PTT irradiation was also accomplished using laser light sources, most of which generate low-intensity lasers for direct application or via transmission through optic fibers. For example, while we used an LED light source, the laser light source used for some of our PDT and PTT experiments was a tunable intensity dual-output frequency laser light source with optic fiber transmission and an output distribution device that delivered spherically shaped equal distribution. The first category of biomedical light sources and devices are those used in basic experimental research. Three important parameters are the intensity and frequency of the light and the portability of these devices. The frequency depends on the application, including the biomedical agents such as the PS nanoconjugate and plasmonic nanoparticles used. In cases of direct application to superficial and shallow disease, the frequency depends on the penetration depth of the tissue. As a result, near-infrared light sources are preferred because the maximum penetration depth is achieved in the near-infrared therapeutic window. The therapeutic window may be illustrated using Fig. 3, showing the variation of human tissue penetration with frequency. The second category of light sources are those used in clinical settings, referred to as medical lasers. The characteristics of medical lasers depend on specific clinical applications. Whereas some are used for light therapy, the characteristics of those used for PDT, and PTT, and combinations thereof also depend on the PS and the plasmonic nanoparticles used.

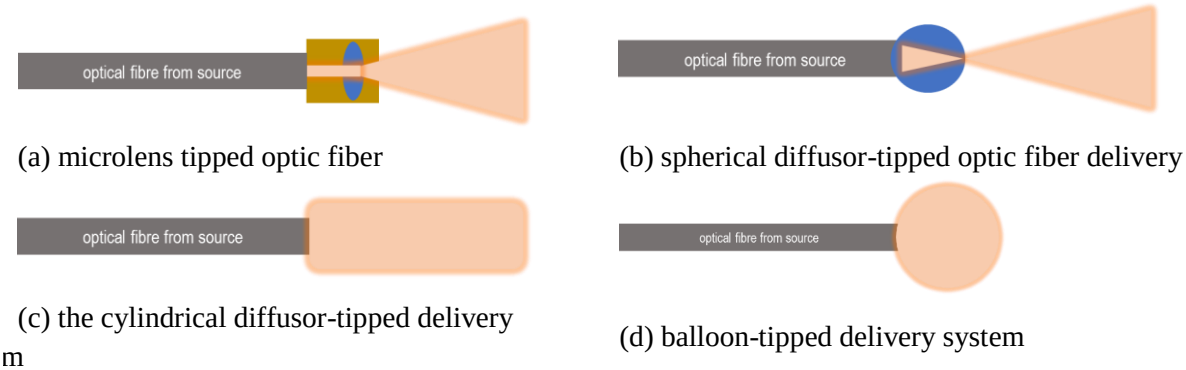

(a) microlens tipped optic fiber

(b) spherical diffusor-tipped optic fiber delivery

(c) the cylindrical diffusor-tipped delivery m

(d) balloon-tipped delivery system

Figure 4: *schematic illustration of microlens-tipped optic fiber, spherical diffusor-tipped optic fiber delivery, cylindrical diffusor-tipped delivery system, and balloon-tipped delivery system*

Laser Light Distribution Devices

Delivery of light to clinical disease or disease models in-vitro and in-vivo depends on the shape and size of the disease model container or disease site. Several light delivery devices are available in the market. While

overcoming the shallow depth of light penetration through human tissue to reach the disease site, optic fibers are tipped with lenses that distribute the energy of light evenly over a 2-dimensional plane (Fig. 4a). They are also tipped with a spherical diffusor to distribute the light over a spherical disease morphology (Fig. 4b). Cylindrical diffusor-tipped devices are useful for treating disease in tubular organs such as blood vessels and the gastrointestinal tract (Fig. 4c). The balloon-tipped diffusor is used for distributing light from within the internal cavities of organs such as the stomach and the bladder (Fig. 4d).

METHODS

Samples were irradiated using one of three light sources; a halogen lamp (tungsten halogen GE Quartzline lamp; 500 W, 560−780 nm), a light emitting diode array (164.51 J/cm^2, 660 nm), and laser light source (continuous-wave $NdYVO_4$ air-cooled NIR laser (2.5 ± 0.5 W/cm^2, 1064 nm).

Irradiation Using a Halogen Lamp

Initially, rudimentary photonics arrangements were used to irradiate our samples. For example, to evaluate the effect of protoporphyrin-IX and methylene blue-mediated aPDT against biofilm-forming multidrug-resistant *A. baumannii*, we irradiated the samples using a halogen lamp, filtering the heat from the lamp using a water bath, as shown in Fig. 5a [14]. This arrangement was also used to evaluate the aPDT effect of cationic porphyrin encapsulated gold nanorods on bacterial cell lines [15]. Samples were placed on an opaque surface at the bottom drawer of the device shown in Figure 5a, and the front lid was closed. The samples were irradiated from the rectangular irradiation hole at the top of the device. After irradiation, the hole was closed, and the samples were transferred to an incubator. Despite low power density and low light fluence, the use of the halogen lamp as a light source for PDT and PTT has been reported widely in the literature [16].

Irradiation Using a Light-Emitting Diode

Due to reduced excess heat, LED and laser light sources were also employed. For example, to overcome the cytotoxicity of common passivating agents, gold nanorods were passivated with gelatin. The as synthesized nanoconjugates were then irradiated with an LED in the PTT experiment [17]. Additionally, to overcome the poor water solubility of porphyrin dye PS molecules and their non-specific binding, ZnCuInS/ZnS quantum dots were conjugated with the PS meso-tetrakis(3-hydroxyphenyl)porphyrin. In the PDT experiment, the resulting nanoconjugate was irradiated with an LED light source, as shown in Figure 5a [18]. While the LED was effective and reproducible, irradiation quantification was still challenging.

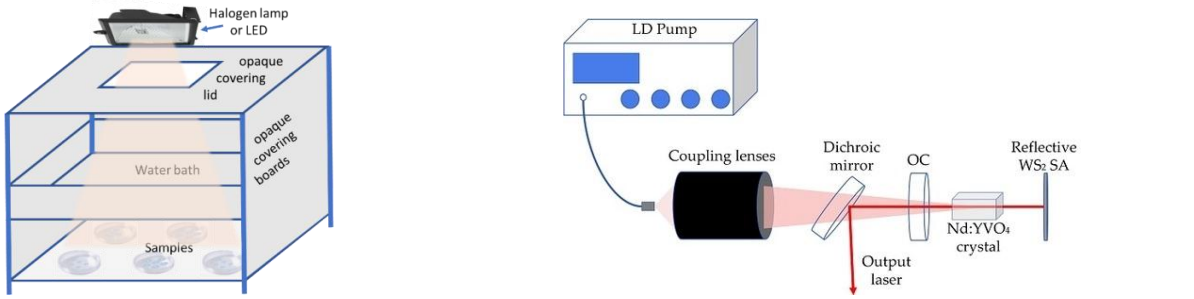

(a) rudimentary photonics arrangements ıally used to irradiate our samples for PDT in-vitro measurements.

(b) schematic showing the continuous-wave Nd:YVO4 air-ed NIR laser [19]. Reproduced from Wang et al. (2019) under the creative commons attribution license.

***Figure 5**: halogen lamp, LED, and Laser irradiation techniques.*

Irradiation Using a Continuous-Wave Optic Fiber-Transmitted Laser

In evaluating their effect against cancer metastasis in the proper axillary lymph nodes in mice, however, mPEG-passivated gold nanorods were irradiated with a continuous-wave optic fiber-transmitted laser, tipped

with a spherical diffuser (Fig. 4b) with a focusing diameter of up to 6 mm from a neodymium air-cooled NIR laser source [20]. Another advantage of using a tunable laser light source is that the desired output is set on the laser-generating device. These output settings may be reproducibly repeated many times. In addition, the laser light source is calibrated to a desired narrow monochromatic bandwidth to enable irradiation at specific absorption bands of the chromophores. This is important to isolate the absorption of the PS from the absorption of the nanoconjugate and vice versa, thus isolating the PDT from the PTT effect.

RESULTS

In the initial rudimentary irradiation using a halogen lamp, heat from the lamp was absorbed by the water bath at room temperature, with a depth of at least 120 mm. Therefore, the temperature of the medium-filled control samples was constant within ±2 ^{o}C. In the arrangement shown in Figure 5a, initially used with the halogen lamp, the water bath soon became of little value when the LED was used because the LED produced significantly less heat. Nevertheless, the water bath was retained to remove any heat from the lamp. In each case, the light energy was monitored using a light meter, adjusting the distance of the lamp from the samples as needed. The temperature was also monitored using a thermometer by continuously measuring the temperature of an identical control sample among the sample cell lines. This arrangement was not needed when using laser light. Additionally, the laser light source delivered reproducible energy with the same settings (power = 2.5 ± 0.5 W/cm2, □max = 1064 nm, and beam diameter = 0.6 mm) with a laser focus diameter of up to 0.6 cm) [**Ошибка! Закладка не определена.**].

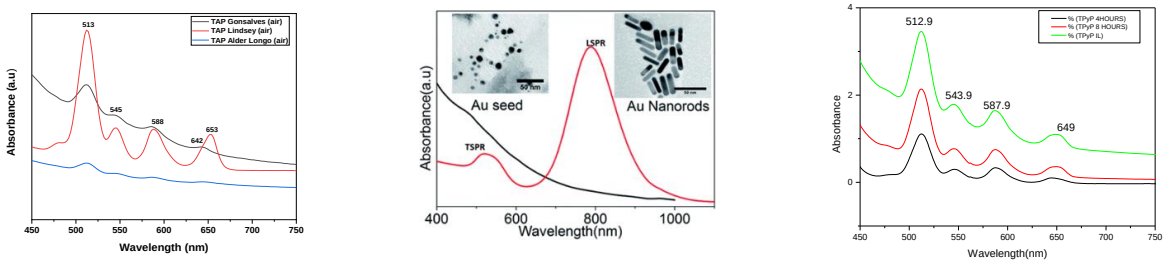

(a) Q-bands of 5,10,15,20-rakis(4-aminophenyl)porphyrin

(b) TSPR and LSPR absorption bands of the gold nanorods

(c) Q-bands of 5,10,15,20-tetrakis(4-4-pyridyl)porphyrin

***Figure 6**: different absorption of the PSs (a) TAP and (b) TPyP, and gold (c) nanorods. Reproduced from Hlapisi et al. (2021) [15] under the creative commons attribution license 4.0.*

CONCLUSION

Photonics has enabled several combinations of PDT, for example, with PTT, thus potentiating the technology. In all our experiments, irradiation with a halogen lamp and subsequently with an LED served their purpose well. However, the reproducibility of the laser light source and variable power settings presented significant advantages for PDT and PTT. Laser light power calibration curves were completed in minutes. There was no need for the filtration of heat from the light source. It is possible to isolate the PTT effect from the PDT effect by irradiating at the plasmonic resonance band because it is well separated from the PS Q bands. For example, it was possible to isolate the PTT response from the PDT response by irradiating at 800 nm, the longitudinal nanorod absorption where the porphyrin has no absorption. Similarly, irradiating at any of the Q bands (Q1 ~ 510 nm, Q2 ~ 550 nm, Q3 ~ 580, and Q4 ~ 655 nm) isolated the PDT response from the PTT response because the PS Q band absorptions are well separated from the nanorod longitudinal absorption (Fig. 6). To overcome the tissue penetration depth challenge, our group has embarked on studies of the combination of MHT with PDT. We first demonstrated the capping of iron oxide nanoparticles with a meso-tetra(4-hydroxyphenyl)porphyrin [21,22] and a porphyrin-capped layer of gold [23,24]. These materials exhibited aPDT and anticancer PDT against cell lines in-vitro. In-vivo studies using mouse models against cancer and bacterial infection have been initiated. A benchtop magnetic hyperthermia equipment was procured for

applications in the planned preclinical studies. Additionally, a dual-frequency tunable laser has been made available to be used for topical aPDT studies in-vivo using mouse models. Our group has plans to test the SDT ROS generation of the nanoconjugate systems thus far developed as we commence our debut into SDT. The current focus includes breast cancers and various bacteria, such as multidrug-resistant *S. Aureus* and *A. baumannii*, because they make a significant contribution to the South African national burden of disease. While located, arguably, at the tail end of the clinical PDT and PTT translation, the development of photonics devices offers avenues for novel innovations to support the clinical lobby in ways that can be anticipated from the photonics support for basic PDT and PTT research. One example of current device innovation already showing promise is the combination of PDT and PTT against superficial cancer, and possibly multidrug-resistant bacterial and fungal strains, is the microneedle technology [25].

Acknowledgments

The research was made possible by several grants from the National Research Foundation South Africa (105262, 149191, 129808, 129806, 129736, 114313, 118774, 129391) and the Council for Scientific and Industrial Research, South Africa (LREPA26, LREQA26, LRERA23, LRESA24, LRETA24).

[1] A. Liebert and H. Kiat, The history of light therapy in hospital physiotherapy and medicine with emphasis on Australia: Evolution into novel areas of practice. Physiother Theory Pract. 37, 3, 389-400, 2021.

[2] Downloaded on the 22nd April from https://www.news-medical.net/health/What-is-Light-Therapy.aspx

[3] J.F. Algorri, M. Ochoa, P. Roldán-Varona, L. Rodríguez-Cobo, J.M. López-Higuera, Light Technology for Efficient and Effective Photodynamic Therapy: A Critical Review. Cancers. 13, 3484, 2021.

[4] M.M. Kim, A. Darafsheh, Light Sources and Dosimetry Techniques for Photodynamic Therapy. Photochem Photobiol 96, 2, 280-294, 2020.

[5] A. Bansal, F. Yang, T. Xi, Y. Zhang, J.S. Ho, In vivo wireless photonic photodynamic therapy. Proc Natl Acad Sci USA 115, 7, 1469-1474.

[6] Berg, K.; Selbo, P.K.; Prasmickaite, L.; Tjelle, T.E.; Sandvig, K.; Moan, J.; Gaudernack, G.; Fodstad, Ø.; Kjølsrud, S.; Anholt, H.; Rodal, G.H.; Rodal, S.K. and Høgset. A.; Photochemical internalization: a novel technology for delivery of macromolecules into cytosol. *Cancer Research* **1999**, 59, 6, 1180-1183.

[7] S. Unser, I. Bruzas, J. He and L. Sagle, Localized Surface Plasmon Resonance Biosensing: Current Challenges and Approaches. Sens. (Basel) 15, 7,15684-15716, 2015.

[8] M.S. Nisar, S. Kang and X. Zhao, Photothermal Effect in Plasmonic Nanotip for LSPR Sensing. Sens. (Basel) 20, 3, 671, 2020.

[9] D.C. Tzarouchis, P. Ylä-Oijala, T. Ala-Nissila, and A. Sihvola, Shape effects on surface plasmons in spherical, cubic, and rod-shaped silver nanoparticles. Appl. Phys. A 122, 298, 2016.

[10] M. Shabaninezhad, G. Ramakrishna, Theoretical investigation of size, shape, and aspect ratio effect on the LSPR sensitivity of hollow-gold nanoshells. J. Chem. Phys. 150, 14, 144116, 2019.

[11] Z. Jiang, G. Wen, Y. Luo, X. Zhang, Q. Liu and A. Liang, A new silver nanorod SPR probe for detection of trace benzoyl peroxide. Sci Rep 4, 5323, 2014.

[12] K.R. Ryu, G.W. Kim, and J.W. Ha, Localized surface plasmon resonance inflection points for improved detection of chemisorption of 1-alkanethiols under total internal reflection scattering microscopy. Sci Rep 11, 12902, 2021.

[13] E. Ruggiero, S. Alonso-de Castro, A. Habtemariam and L. Salassa, Upconverting nanoparticles for the near infrared photoactivation of transition metal complexes: new opportunities and challenges in medicinal inorganic photochemistry, Dalton Trans. 45(33), 13012, 2016.

[14] Y.A. Anane, T. Apalata, S. Vasaikar, G.E. Okuthe and S.P. Songca, In vitro antimicrobial photodynamic inactivation of multidrug-resistant Acinetobacter baumannii biofilm using Protoporphyrin IX and Methylene blue. Photodiagnosis Photodyn Ther. 30, 101752, 2020.

[15] N. Hlapisi, T.S. Maliehe, O.S. Oluwafemi, S.P. Songca, L. Linganiso and T.E. Motaung, Antibacterial Activities of Cationic Porphyrins and Gold Nanorod Encapsulated Porphyrins on Bacterial Cell Lines. Pharmacogn. J. 13, 5, 1086-1096, 2020.

[16] Y.H. Lee, HW. Park, JH. Lee, S. H.W. Seo and S.Y. Lee, The photodynamic therapy on Streptococcus mutans biofilms using erythrosine and dental halogen curing unit. Int J Oral Sci. 4, 196–201, 2012.
[17] A.O. Oladipo, T.C. Lebepe, V. Ncapayi, N. Tsolekile, S. Parani, S.P. Songca, S. Mori, T. Kodama and O.S. Oluwafemi, The Therapeutic Effect of Second Near-Infrared Absorbing Gold Nanorods on Metastatic Lymph Nodes via Lymphatic Delivery System, Pharmaceutics 13, 1354, 2021.
[18] N. Tsolekile, S. Parani, E.F. de Macedo, T.C. Lebepe, R. Maluleke, V. Ncapayi, M.C. Matoetoe, S.P. Songca, K. Conceição, D.B. Tada and O.S. Oluwafemi, Photodynamic therapy and antibacterial activities of a novel synthesized quaternary Zn-Cu-In-S/ZnS QDs- mTHPP Porphyrin conjugate, Int J Nanomedicine 17, 5315-5325, 2022.
[19] T. Wang, Y. Wang, J. Wang, J. Bai, G. Li, R. Lou, and G. Cheng, 1.34 μm Q-Switched Nd:YVO4 Laser with a Reflective WS2 Saturable Absorber, Nanomaterials (Basel) 2019, 9, 9, 1200.
[20]Oladipo AO, Oluwafemi OS, Songca SP, Sukhbaatar S, Mori S, Okajima J, Komiya A, Maruyama S, Kodama T, 2017. A novel treatment for metastatic lymph nodes using lymphatic delivery and photothermal therapy. Nature Scientific Reports, 3(7):45454. Nature Scientific reports, 7, 45459.
[21] S.P. Songca, O.S. Oluwafemi, A. Eshilokun, A. Strydom, R. Tshikhudo, S. Debeila, T. Hillie, Functionalization and Characterisation of Porphyrin capped iron oxide-gold core-shell nanoparticles, Int. J. Basic Appl. Sci. 4, 2, 36-48, 2014.
[22] O.J. Fakayode, S.P. Songca and O.S. Oluwafemi, Facile Green Synthesis and Characterization of Water-Soluble Superparamagnetic Iron Oxide-Gold Porphyrin Conjugate for Improved Photodynamic Therapy, The Minerals, Metals and Materials Society, TMS 2017 146th Annual Meeting and Exhibition Supplemental Proceedings, The Minerals, Metals and Materials Series, 23-27.
[23] O.J. Fakayode, S.P. Songca, O.S. Oluwafemi, Singlet oxygen generation potential of thiolated methoxypolyethyleneglycol encapsulated superparamagnetic iron oxide nanoparticles-gold core-shell meso-tetrakis(4-hydroxyphenyl)porphyrin, Mater. Lett. 199, 37–40, 2017.
[24] B.M. Amos-Tautua, O.J. Fakayode, S. van Vuuren, S.P. Songca, O.S. Oluwafemi, Non-distorted visible light-absorbing thiol-PEGylated gold-coated superparamagnetic iron oxide nanoparticles–porphyrin conjugates and their inhibitory effects against nosocomial pathogens, MRS Commun., 9, 4, 1335-1342, 2019.
[25] M. Wang, X. Li, W. Du, M. Sun, G. Ling and P. Zhang. Microneedle-mediated treatment for superficial tumors by combining multiple strategies. Drug Deliv. and Transl. Res. 13, 1600–1620, 2023.

Научное издание

BRICS Workshop on Biophotonics-2023
Proceedings of BRICS Workshop

Edited by Polina A. Dyachenko, Qingming Luo,
Vanderlei Salvador Bagnato, Santhosh Chidangil,
Heidi Abrahamse and Valery V. Tuchin

SEPTEMBER 27 – 29, 2023

SARATOV

Семинар БРИКС по Биофотонике-2023

Сборник материалов семинара БРИКС
под редакцией Полины А. Дьяченко, Цинмин Ло,
Вандерлея Сальвадора Баньято, Сантоша Чидангила,
Хайди Абрахамс и Валерия В. Тучина

27 – 29 СЕНТЯБРЯ 2023 Г.

Подписано в печать 29.01.2023 г. Формат 60×84/16.
Усл.-печ. л. 12,5. Тираж 500 экз. Заказ № 312

Издательство «Саратовский источник»
г. Саратов, ул. Кутякова 138б, 3 этаж.
Тел. (8452) 52-05-93
E-mail: saristoch@bk.ru
Отпечатано в типографии «Саратовский источник»